Confined cell nematics submitted to an orientation field. Applications to differentiation.

Thibault Aryaksama

PSL UNIVERSITÉ PARIS

THÈSE DE DOCTORAT
DE L'UNIVERSITÉ PSL

Préparée à l'Institut Curie

Confined cell nematics submitted to an orientation field. Applications to differentiation.

Nématiques cellulaires actifs confinés et soumis à un champ d'orientation. Applications à la différentation.

Soutenue par

Thibault ARYAKSAMA

Le 23 Mars 2021

Ecole doctorale n° 564

Physique en Ile-de-France

Spécialité

Physique

Composition du jury :

Jean-François, JOANNY
Professeur, Collège de France
Président

Catherine, PICART
Professeur, Institut Polytechnique de Grenoble
Rapportrice

Stefano, GUIDO
Professeur, Università di Napoli
Rapporteur

Myriam, REFFAY-BEUGNON
Maître de conférence, Université de Paris
Examinatrice

Bruno, CADOT
Chargé de recherche, Institut de Myologie
Examinateur

Pascal, SILBERZAN
Directeur de recherche, Institut Curie – CNRS
Directeur de thèse

institut Curie

Confidentielle jusqu'au 23/03/2022

Confined cell nematics submitted to an orientation field. Application to differentiation.

Thibault Aryaksama

Merci.

Le déroulement de cette thèse, du premier jour jusqu'à la soutenance, en passant par la rédaction du manuscrit ici présent sera une épreuve dont je me souviendrai toute ma vie. Cette aventure passionnante fut jalonnée de haut et de bas, de moments de joie comme de déception, … mais surtout de rencontres. Aussi j'aimerai remercier toutes les personnes qui ont surmontées cette épreuve avec moi, que ce soit directement ou indirectement.

Je remercie du fond du cœur Pascal, mon directeur de thèse, qui a su me faire confiance dès que je suis arrivé en stage de recherche dans son équipe. Quatre ans, plus tard, j'ai beaucoup appris grâce à lui notamment sur le plan scientifique ou il a toujours su m'orienter. Je le remercie aussi pour sa disponibilité et son sens de l'écoute, deux qualités indispensables à un très bon directeur de thèse.

Je remercie les membres de mon jury de thèse, Jean-François Joanny, Catherine Picart, Stefano Guido, Myriam Reffay et Bruno Cadot d'avoir évalué mon travail. Je tiens aussi à remercier Myriam et Thomas qui ont pu suivre ma thèse de près lors de mes comités de thèse.

Je remercie également tous les membres de l'équipe Silberzan, passés et présent, qui m'ont aidés plus d'une fois sur les protocoles, la réalisation des expériences ou bien leurs analyse. Dans le désordre : Flora, Victor, Isabelle, Axel, Sylvie, Tobias, Sarah, Sarah, Trinish, Thomas, Mathilde, Nastassia, Caroline, Brice, Pierre, Xingming, … Je serai toujours partant pour une partie de pétanque ensemble.

Je remercie aussi tous les membres de l'UMR 168 pour les moments de partage.Par rapport à la thèse en elle-même, je remercie tout particulièrement Fanny et Aude pour les cellules, Eric et Remy d'avoir fabriqué ma machine et Laurence et Thuy pour la partie administrative.

Cette thèse n'aurait pas pu aboutir sans mes collaborateurs que je remercie chaleureusement. Tout d'abord, les physiciens théoriques, Jean-François, Thomas, Carles et surtout Louis avec qui j'ai pu longuement collaborer.Ensuite, les personnes qui m'ont aidé dans ma quête de C2C12 capables de se différencier, à savoir, Benoit, Myriam, Gaëtan, Bruno et Manh. Finalement, je remercie toutes les personnes des différentes plateformes, Guillaume à l'IPGG ou Olivier à la BDD.

Enfin, je remercie mes amis et les membres de ma famille pour m'avoir vidé la tête durant cette thèse. Je remercie surtout ma mère, mon phare dans l'océan. J'ai aussi une pensée pour mon père, qui aurait aimé être là et que je suis certain d'avoir rendu fier.

Finalement, je remercie la personne la plus importante à mes yeux, celle qui m'a fait devenir qui je suis au moment d'écrire ces lignes et dont je n'aurait pas assez de mots pour décrire ce que je pense. Merci Laure.

- Mais, c'est quoi la "glisse"?
- C'est tout à la fois, me répond Toutoune. C'est une question de position, de souplesse des chevilles, des hanches et des bras, mais aussi de volonté.

Je me suis rendu compte, bien plus tard, que la glisse était en fait une notion systémique. Je n'avais pas encore écrit *Le Macroscope*, qui serait publié en 1975. J'y étudie comment une approche tient compte de plusieurs facteurs et j'y démontre que toute propriété émerge de la dynamique des interactions de ces facteurs.

Joël de Rosnay, *Petit éloge du surf*, 2020

Abreviations

A
Ab = Antibody
ATP = Adenosine TriPhosphate

B
BMBC = Biochemistry, Molecular Biology and Cells platform
BSA = Bovine Serum Albumine

C
CG = Contact Guidance
μCG = microscale Contact Guidance
CI = Confidence Interval
CIL = Contact Inhibition of Locomotion
CIP = Contact Inhibition of Proliferation

D
DMEM = Dulbecco's Modified Eagle's Medium
DSHB = Developemental Studies Hybridoma Bank

E
ECM = ExtraCellular Matrix

F
FA = Focal Adhesion
FAK = Focal Adhesion Kinase
FBS = Foetal Bovine Serum
FFT = Fast Fourier Transform
FOV = Field Of View

G
mG = mesocale Guidance
GAG = GlycoAminoGlycan
GTP = Guanine TriPhosphate

H
HS = Horse Serum

I
ITS = Insulin-Transferrin- sodium Selenite

L
LIC = Line Integral Convolution
LINC = LInker of the Nucleoskeleton with the Cytoskeleton
LR = Left-Right

M
MHC = Myosin Heavy Chain
MLC = Myosin Light Chain
MMP = Matrix Metallo Protease
MRF = Muscle Regulatory Factor
xMSC = Mesenchymal Stem Cell (x = h: human, r: rat)
MT = MicroTubule
MTOC = MicroTubule-Organizing Center

N
NCC = Neural Crest Cells
NGS = Normal Goat Serum
NIH = National Institute of Health (USA)
NPC = Neural Progenitor Cells

P
PBME = Physico-Biology at Mesoscales
PBS = Phosphate Buffer Saline
PCR = Polymerase Chain Reaction
PDMS = PolyDiMethylSiloxane
PEG = PolyEthyleneGlycol
PFA = ParaFormAldhehyd
PG = ProteoGlycan
Pi = inorganic Phosphate
PIV = Particle Image Velocimetry
PNIPAAm = Poly(N-IsoPropylAcrylAmide)
PSC = Pluripotent Stem Cell (iPSC = induced PSC)

R
ROCK = Rho-assoCiated Protein Kinase
RT = Room Temperature

S
mSC = muscle Satellite Cells
SEM = Scanning Electron Microscopy
SHG = Second Harmonic Generation
SS = Saturation Solution

T
THG = Third Harmonic Generation

W
WT = Wild Type

Y
YAP = Yes-Associated Protein

Foreword

Cells in the body are surrounded by a complex environment made of fibrillar proteins called the Extracellular Matrix. Cells move freely in the environment but are submitted to strong geometrical constraints spanning several lenghtscales. Interactions between cells and their surrounding environment are crucial to understand biological problematics from cancer invasion to morphogenesis. In particular, collective migration of cells in such ECM environment is yet to be understood. This knowledge could be crucial for future application such as organogenesis.

This manuscript contains all the work done during my PhD under the supervision of Pascal Silberzan, in the lab Physico-Chimie Curie (UMR 168) of Institut Curie. I used a simple *in vitro* model of chemically patterned stripes on microabraded glass surfaces to understand the self-organization of spindle-shaped cells on such substrates. The experiments were compared to the previous study of a PhD of the team, Guillaume Duclos, and a theoretical model was build in close collaboration with Louis Brézin at Collège de France. I used the results of this study to perform the differentiation of C2C12 muscle precursors cells into fully grown myotubes. This method aimed at outperforming existing techniques.

This manuscript is divided in four chapters:

- Chapter I. is an introduction on the biology of cells and their interactions with their environment: substrate and surrounding cells. A particular focus is made on contact guidance and collective migration, two effects resulting from these interactions. A small part treats about the particular case of muscle cells, how to differentiate them and how the surrounding environment of cells can play a role in this differentiation. Lastly, the active nematics framework is presented together with examples of active nematic cells under geometric constraints. All parameters fine tuning the collective behaviours of such systems are put in regards between theoretical and experimental results.

- Chapter II. deals with protocols, materials and algorithms used during this thesis. Further developments and details could be found in Appendices A – C.

- Chapter III. exposes the results obtained when seeding nematic cells on multiscale substrates made of chemically patterned stripes of given width on top of perpendicular microabrasions. I show that for a given microabrasions "field" the stripe width is the control parameter of the system. Cells orientation can then be controlled from this parameter without affecting cellular flows. These results, in accordance with the results of G. Duclos, helped us build a model in the active gel framework with L. Brézin. Moreover, by fine tuning the geometry of our system, I was able to measure the so-called flow-alignment parameter. These results were completed by a small study on topological defects.

- Chapter IV. uses the previous results in order to enhance differentiation of C2C12 myoblasts in such substrates. I particularly focus on describing the spontaneous formation of a tridimensional "cord" of cells with unique architecture. The differentiation in this structure was quantitatively compared to results on geometries similar to what is found in the literature.

This work aims at be used by future students, the same I did with the work of Guillaume Duclos and its predecessor. This is meant for anyone who want to add their contribution to the building of knowledge on active matter and more generally to science.

Thibault Aryaksama,

03/02/2021

Keywords: active nematics, collective cell behaviour, contact guidance, multiscale, contact guidance, differentiation.

Table of contents

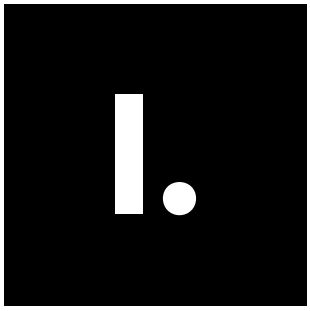

I. Introduction

1. Cell and tissues

1. 1. The cell

Cells are the smallest functional unit of living organisms. They are complex biological systems made of an arrangement of proteins that highly interact with each other. As live entities, they extract energy from their nutrient-rich surrounding medium and therefore they function out of equilibrium for most of their functions such as proliferation or migration.

1. 1. 1. Cytoskeleton and molecular motors

Cells are mostly composed of water encapsulated in a phospholipidic bilayer. Metabolic functions are compartmentalized in specific structures called organelles such as the mitochondria, the endoplasmic reticulum or the nucleus that contains the genetic information. Cell internal organization is dictated by the cytoskeleton, a meshwork of protein filaments. This structure is not a "passive skeleton" backbone but is a dynamical architecture that controls several cell functions across different timescales (from seconds to cell life time) and lenghtscales (from molecular to supracellular scale) such as internal molecule exchanges or cell migration. Actin microfilaments, intermediate filaments and microtubules are the three types of filaments that constitute this cytoskeleton, each of them having a specific function and unique mechanical properties [2,3]. All filaments result from the association of subunits to form supramolecular structures similar to polymers, the difference being that, here, the monomers are not bound covalently. The filaments assemble and disassemble, making these systems highly dynamical (Table 1 – 1).

Intermediate filaments are made of an association of 8 tetramers of coil-coiled helices of the protein family of keratins, vimentins, lamins, …[4] They are present both underneath the nuclear envelop and in the cytoplasm. They are mainly responsible for maintaining the cellular shape and withstanding mechanical stresses. They are also important to maintain cell-cell contacts.

Microtubules subunits are heterodimers of α-tubulin and β-tubulin. They assemble in protofilaments made of a succession of αβ-tubulin dimers and 13 of these filaments assemble again

in a hollow helical cylinder. Microtubules are very rigid and polar, the β-tubulin end is called the (+)-end and the other end, the (-)-end. All these filaments nucleate from the MicroTubule-Organizing Center (MTOC), close to the nucleus, elongating from their (-)-end towards their (+)-end which is close to the plasma membrane. They act as "tracks" for transport in the cytoplasm when they are associated with molecular motor proteins. An example is kinesin, a protein able to "walk" on microtubules in the (-) to (+) direction, carrying cargos to the plasma membrane. Other motors like dyneins move in the opposite direction.

	Actin	Intermediate filaments	Microtubules
Subunit	Globular actin	α-helix (keratins, vimentins or lamins)	αβ-tubulin heterodimer
Protofilament	-	2x coil-coiled helices (tetramers)	Chain of αβ-tubulin
Supramolecular structure	Double-stranded helix	Association of 8 tetramers	13 protofilaments into hollow helical cylinder
Polarity	Barbed end (+) → pointed end (-)	Apolar	β-ended (+) → α-ended (-)
Diameter	5 – 9 nm	10 nm	25 nm
Principal functions	Cell shape, locomotion, division	Cell mechanical integrity, cell-cell contact	Cytoplasmic transport, organelles organization, division

Table 1 – 1. Principal features of the cytoskeleton filaments: actin, intermediate filaments and microtubules [2].

Actin filaments are critical in the present work because they are involved in several mechanobiological pathways [5]. They are arranged in a double-stranded helix made of several globular actin proteins (Fig. 1 – 1A). These filaments are polarized: actin monomers are added at the "barbed end" (or (+)-end), while they are removed at the "pointed end" (or (-)-end). Depending on the rate of polymerization/depolymerization at both ends, actin filaments are able to extend at a certain speed and produce a net force of several pN [6]. The persistence length of actin filaments is around 10 μm, making them quasi-stiff rods at the scale of a cell. The maximal force a single filament can exert depends on its length but larger forces can be retrieved when many filaments assemble together in particular organizations mediated by cross-linkers (Fig. 1 – 1B). The *actin*

cortex lying underneath the plasma membrane helps cells maintain their shape, it is formed of a homogeneous network of crosslinked actin filaments. The l*amelippodium*, made of branched actin filaments, protrudes at the front edge of a moving cell. Ahead of it, *filopodia* are spiky parallel bundles of actin able to sense mechanically the cell environment [7] and to allow a fast physical response. Finally, *stress fibers* are contractile bundles of antiparallel actin filaments associated with myosin molecular motors [8–10]. Myosins comprise a head domain that binds to the actin filament, and a long tail domain. Hydrolysis of ATP changes the conformation of the myosin head-to-tail domain and consequently triggers a mechanical force. Two myosins can dimerize by their tail in a two-headed myosin filament that can crosslink two different actin filaments, thus creating contractility in the acto-myosin network.

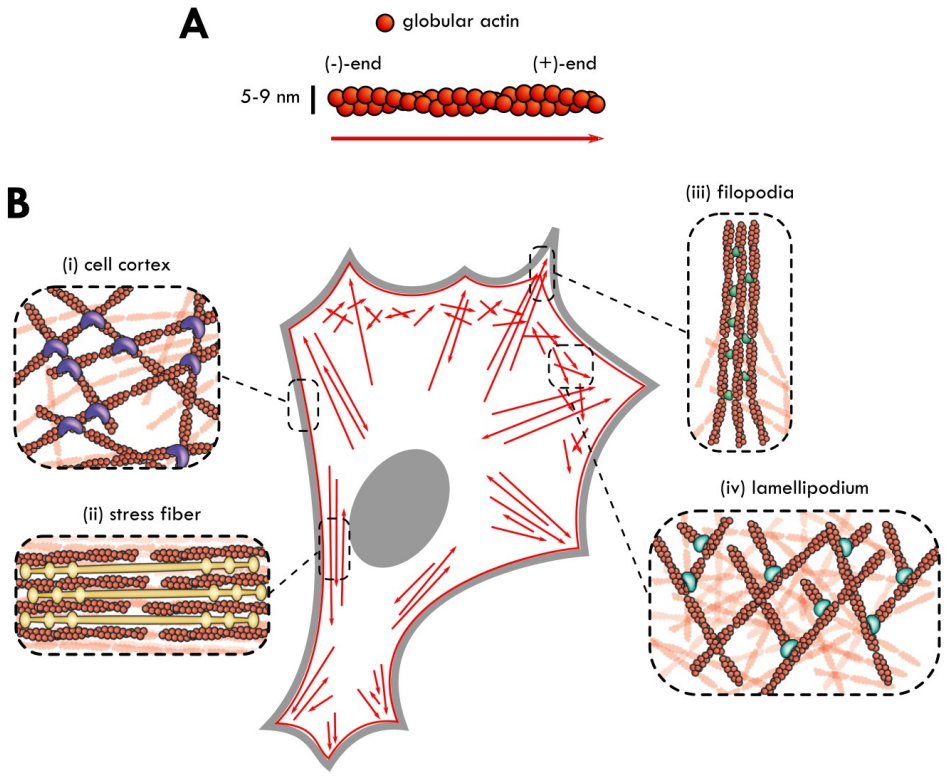

Figure 1 – 1. Actin cytoskeleton. (**A**) Actin filament is made of globular actin subunits that arrange in a double-stranded right-handed helix. This filament is polar, new monomers being added at the (+)-end (or "barbed" end) and monomers being depolymerized at the (-)-end (or "pointed" end). (**B**) Actin cytoskeleton can have several organizations depending on the mechanical function it achieves (i) cell cortex: homogeneous network (typical crosslinker: filamin) (ii) stress fiber: antiparallel contractile bundle (typical crosslinker: myosin II) (iii) filopodium: non-contractile parallel bundle (typical crosslinker: fascin) (iv) lamellipodium: branched network (typical crosslinker: Arp2/3 complex). Adapted from [2,3].

The structure of the cytoskeleton and more precisely the actin organization is key to understanding how cells can exert mechanical forces. As these forces are applied to a substrate, another key element to take in account is the cell environment and particularly the extracellular matrix.

1. 1. 2. The extracellular matrix

In vivo, cells are surrounded by a complex environment, the extracellular matrix (ECM) produced by specialized cells [2,11,12]. This matrix maintains the physical integrity of tissues but it also provides chemical and mechanical cues that can trigger signaling pathways in cells and promote cell fates [13,14]. Its composition is different from tissue to tissue, thus displaying a various range of forms: from rock hard teeth or bones to soft epidermia or transparent cornea. Although compositions may differ, two main classes of proteins play a major role in this matrix (Fig. 1 – 2A):

(i) Proteoglycans (PG) are non-branched proteins made of glycoaminoglycan (GAG) chains and a core protein. These proteins assemble in large complex polymers, for instance as big as a bacterium for aggrecan. Due to their molecular structure, these proteins are highly hydrophilic and negatively charged, thus retaining a large amount of water and ions. For that reason, they form a hydrogel that surrounds cells. They can retain soluble factors such as TGF-β or chemokines and withstand compressive stresses.

(ii) Fibrous proteins, as their name suggest, are fibrillar proteins that structure the ECM and with which cells will mainly interact. We list below the main players:

- *Collagen* is the most abundant protein in the ECM and accounts for up to 30% of total proteins in the human body. Although 28 classes of collagen molecules have been identified so far [15], usually one type predominates in a specific tissue. These molecules mostly control the ECM physical properties. Collagen molecules are triple helix molecules of 1.5 nm diameter that can assemble in fibrils (10 – 500 nm) that can further assemble in fibers (0.5 – 20 μm) surrounding the cells (Fig. 1 – 2B). In most connective tissues, these fibers are randomly oriented. However, in some specialized tissues that need to withstand mechanical tension along a particular direction, they show particular organizations. For example, collagen fibers in tendons are all parallel to each other.

- *Elastin* gives elasticity to the tissue, being able to be stretched up to 150%. It prevents tissues to be torn apart by high strains.

- *Fibronectin* is a protein associated with cell adhesion and remodeling of the ECM. This protein is mainly secreted by fibroblasts that shape it at their surfaces into fibers of tens of micrometers long, parallel to their actin cytoskeleton.

- *Laminin* is a particular ECM protein lying mostly in the basal lamina[a] of epithelia [16]. Laminins are essential in embryogenesis and organogenesis by triggering pathways for differentiation.

Each of these components and many more contribute to the physical structure of the ECM. A change from the "normal" ECM state can lead to various diseases such as muscular distrophia, atherosclerosis or chronic inflammations [12,17]. Its mechanical properties are highly impacted by the types and ratio of these proteins but also by the details of its architecture and the interaction between proteins and embedded cells. Indeed, fibroblasts constantly remodel the ECM by degrading it with secreted proteases such as matrix metallo proteases (MMP), and/or by secreting new fibronectin fibers guided by preexisting fibrillar structures. Altogether, ECM should not be viewed as a mere passive scaffold but as a dynamical structure that can be remodeled in presence of biochemical factors or mechanical stresses.

In the last years, tissue engineers have tried to reconstitute controlled ECM from purified components and retrieve some of its physico-chemical properties [18–21] such as stiffness, fibers structure [22,23] or molecular composition [24,25] (Fig. 1 – 2C). More recent strategies rely on culturing fibroblasts on artificial scaffolds in order to guide them to secrete functional ECMs. It is then necessary to recapitulate a multiscale environment, with defined stiffness and chemical spatio-temporal organization to achieve this goal.

a Basal lamina is a particular type of ECM that lies under epithelial tissues which are strongly anchored to it.

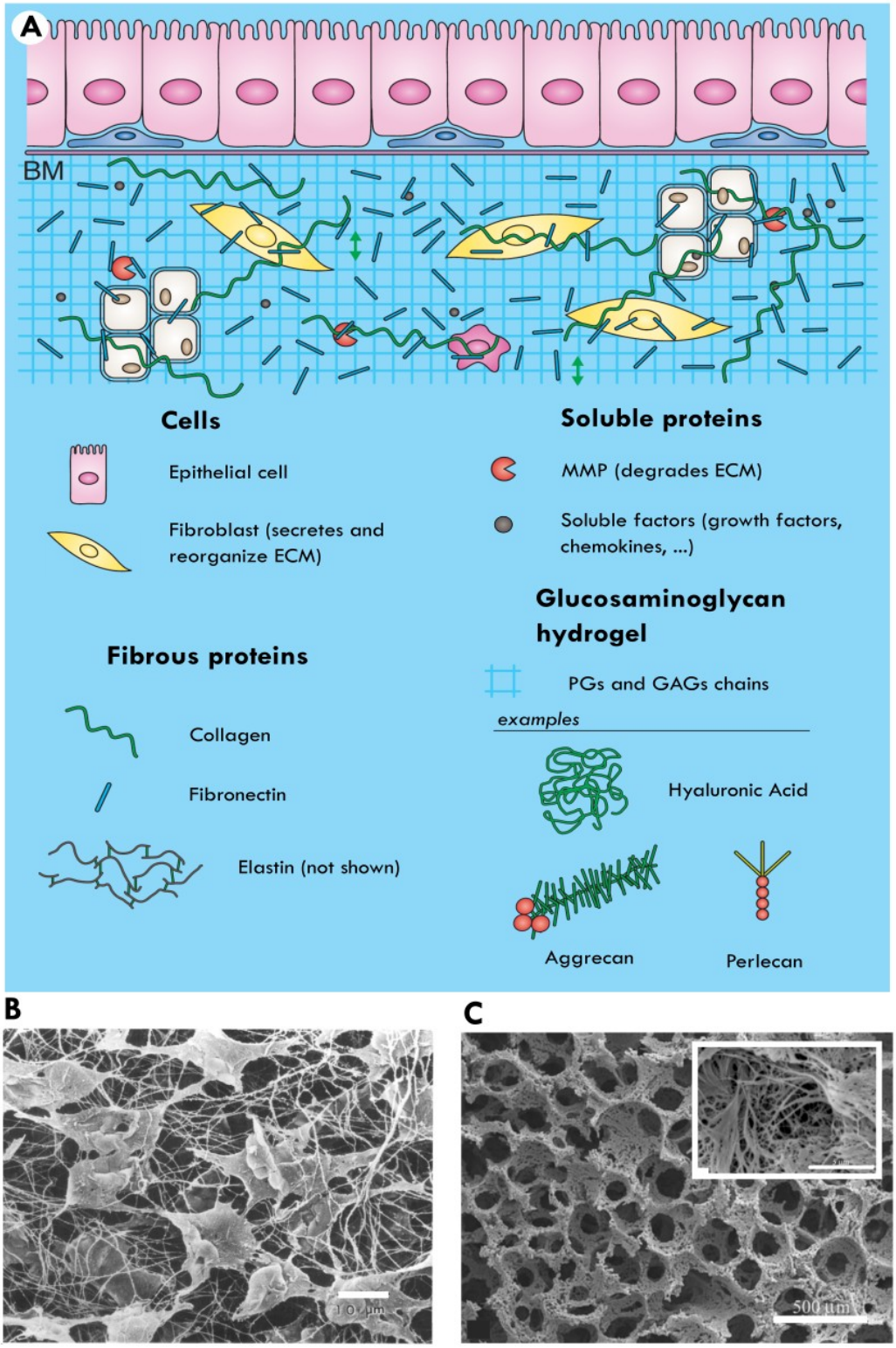

Figure 1 – 2. Extracellular matrix. (**A**) ECM major components and organization. Adapted from [11]. (**B**) Fibroblasts surrounded by collagens fibers in cornea oberserved in SEM [26]. Scale bar = 10 µm. (**C**) Engineered medium constituted of electrospun fibers of polylactic acid designed to mimic the ECM multiscale environment (micron-size pore made of nanofibers) [27]. Observation under SEM. Scale bar = 500 µm. Insert: zoom on the structure (scale bar = 5 µm).

1. 2. Cells interacting with their physical environment

Although cell behaviours – migration, division, apoptosis, differentiation, survival – are largely monitored by soluble chemical factors that regulate cascades of biochemical reactions in the cell, this picture is not complete and the importance of the spatio-temporal physical environment has also to be taken into account. Cells' physical interactions with their environment, such as alignment along fibers of collagen or migration into constrictions, can occur across multiple lengthscales that we detail in the following.

1. 2. 1. Molecular scale: cell-matrix adhesions and actin cytoskeleton reorganization

Cells adhesive interactions with their substrate are essential not only for their survival but also with respect to various cell behaviors such as migration, where cells propel themselves forward. Cell interactions with ECM are mediated by specific transmembrane proteins called integrins [2,28,29] (Fig. 1 – 3A). Integrins are heterodimer proteins made of two subunits α and β that exist in several isoforms. The heads of the subunits interact with ECM in their extracellular domain while their tails interact with proteins in the cytoplasm. The initial adhesive bound between integrins and the ECM, called a focal contact, has a typical size of 100 nm and is too weak to allow a cell to stably attach. For that reason, mature stable adhesion sites, the focal adhesions (FAs), must assemble hundreds of focal contacts. Mature FAs have an elliptical shape and their long (respectively small) axis ranges from 1 to 10 μm (respectively 2 μm). Assembly of mature focal adhesions takes several minutes during which linker proteins like vinculin or talin bind the β-tail of the integrins to the actin cytoskeleton. This increases actin tension and/or triggers biochemical pathways, leading to an amplification of the mechanical input signal [30,31].

Focal complexes also bind focal adhesions kinases (FAK) that are upstream of several signaling pathways, including those that remodel the actin cytoskeleton [32]. This remodeling is largely mediated by small GTPases of the Rho family, such as Cdc42, Rac and Rho [33,34]. Cdc42 and Rac activate the formation of filopodia and lamellipodium respectively. Rho activates the bundling of

actin and myosins by either phosphorylating Myosin Light Chain (MLC, or the tail domain) or inhibiting MLC phosphatases (Fig. 1 – 3B). It allows maturation of stress fibers that increases both cell contractility and adhesion. The action of these proteins is well exemplified when cells build up adhesion on a substrate [35] (Fig. 1 – 3C): cells first produce filopodia to anchor on the substrate, then they extend a lamelippodium, strengthen their adhesions and finally create more stress fibers.

On another line, nucleus deformations induced by cell adhesion have been shown recently to provide direct transduction of mechanical stresses. Indeed, particular actin stress fibers, the actin cap, are directly attached to the nuclear envelop via the LINC complex. Under tension caused by adhesion, this actin cap compresses the nucleus which may affect chromatin organization and gene expression [36,37]. Nuclear compression also leads to the localization of the Yes-Associated Protein (YAP) into the nucleus, which enhances the activation of genes responsible for cell proliferation [38–40].

1. 2. 2. Cellular scale: contact guidance

Interactions of the cells with their physical environment through the previously described structures lead to various changes in cell behaviours. In the present thesis, we are particularly interested in directed migration induced by topography of the substrate, a phenomenon first reported by Harisson in 1912 [41] and formally named "contact guidance" (CG) by Weiss in 1945 [42]. If there is a preferred topographical direction – an "easy" direction[b] –, cells that follow contact guidance elongate in this direction, and consequently migrate in the direction of the substrate anisotropy. It is common to quantify the impact of CG by measuring one or several observables: cell orientation or direction of locomotion compared to the easy direction, or cell elongation/aspect ratio (Fig. 1 – 4A).

Although this phenomenon has been studied for a long time, some of its underlying mechanisms are still unclear [43–48]. Indeed, *in vivo*, cells are surrounded by the complex meshwork of fibers described above, that can direct the cells if properly oriented.

b We will refer to the preferred direction of orientation of cells as the "easy axis" or "easy direction" in accordance with the terminology used to describe the preferred anchoring direction of liquid crystals to a wall or surface [1] (see I. 2.).

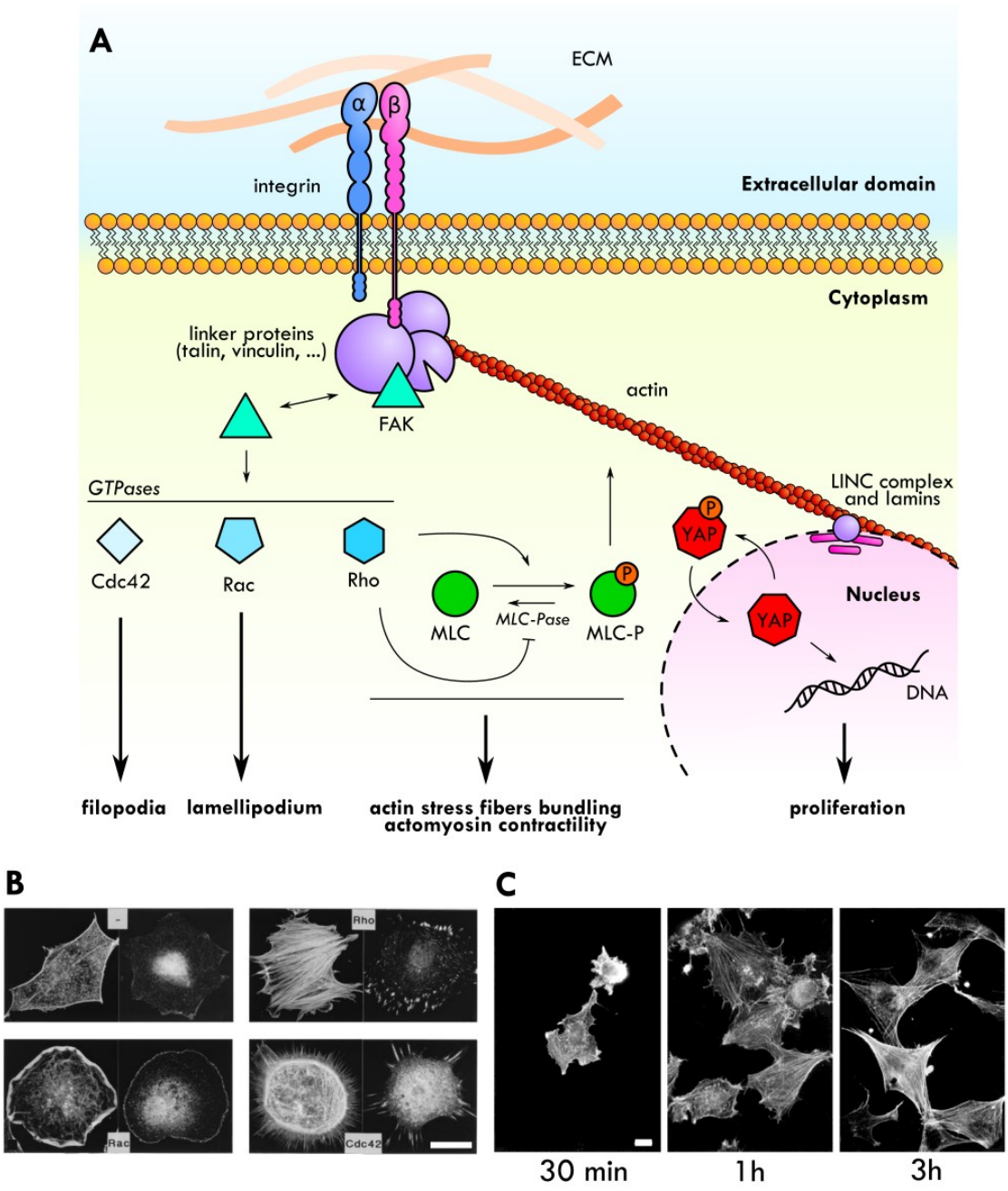

Figure 1 – 3. Cell-substrate interactions. (**A**) Schematics of the main pathways involved in mechanotransduction. Integrins bind ECM proteins and cytoplasmic β-tail domain attach to actin through linker proteins such as talin. The focal adhesion build-up is controlled by FAKs, upstream of various pathways involving GTPases that modulate the actin cytoskeleton architecture. Rho activates actomyosin contractility. Mechanical forces can be transmitted to the nucleus via YAP or LINC complex. (**B**) Changes in actin cytoskeleton morphology of 3T3 fibroblasts when GTPases are activated (i) WT adherent cells (ii) Rac activated cells extend lamelippodia (iii) Rho activated cells create more stress fibers (iv) Cdc42 activated cells elongate filopodia [33]. Left panels: actin, right panels: vinculin. Scale bar = 25 µm. (**C**) Cytoskeleton dynamical changes as 3T3 cells build adhesions to the substrate [35] (actin is stained). At first, cells extend filopodia and lamelippodia to explore their environment and spread. As focal adhesions mature, more actin stress fibers appear. Scale bar = 5 µm.

In vitro, CG can be quantified by plating cells on well-controlled micron-size topographies that are obtained by photolithography techniques. Several substrate topographies have been tested in the literature, such as ridges/grooves, pits, anisotropic pillars [49], wrinkled surfaces [50,51], mono-directional abraded substrates [52,53], … A similar CG effect occurs on chemically patterned attractive/repellent lines alternated on the substrate [46,48]. In any case, culturing cells on such substrates have led to the identification of two components that play a role in contact guidance: protrusions in the form of filopodia (Fig. 1 – 4B) and adhesions, particularly FAs (Fig. 1 – 4C). Here we exemplify principles of single cell CG by describing it on castelated substrates, characterized by their ridge width, their groove width and their groove depth (Fig. 1 – 5A).

Mechanisms of contact guidance

As explained previously, CG involves protrusions and adhesions to the substrate. The mechanisms that intended to explain CG first focused on either one of these two players. However, modern views understand that CG arises from a complex interplay between protrusions and adhesions. The balance between these mechanisms is questioned in Box 1.

A first mechanism of alignment relies on adhesions. Ohara & Buck in 1979 postulated that CG is related to mature elliptical Focal Adhesions (FAs) being physically constrained on ridges smaller than their long axis length (10 μm) [54]. Maximum CG would be achieved for a width range that constrains FAs to orient parallel to the ridges [55,56] (Fig. 1 – 5B). For ridges much thinner than FAs size, mature FAs cannot form, while on wide ridges, FAs orient randomly. Alignment of mature FAs triggers the formation of actomyosin bundles and stress fibers that ultimately lead to cell shape orientation in the easy direction. This effect is also at play for cells on chemically patterned lines.

CG has also been interpreted as the result of a biased exploration of cell's environment by oriented protrusions. Dunn & Heath in 1976 considered cell protrusions as rigid rod-like organelles that cannot be bent [57]. When encountering a discontinuity, a wall, a curvature, … these organelles shorten because of the geometrical constraints (Fig. 1 – 5C). As a consequence, cells are not able to generate enough traction forces to move in that direction. Favored cell protrusions will then form preferentially along the easy direction that allows adhesion/migration. Indeed, it has been observed

experimentally that cells form more protrusions in the easy direction [58,59]. A complementary observation is that cells avoid to bridge gaps with protrusions and prefer maximizing their contact area with the substrate [60].

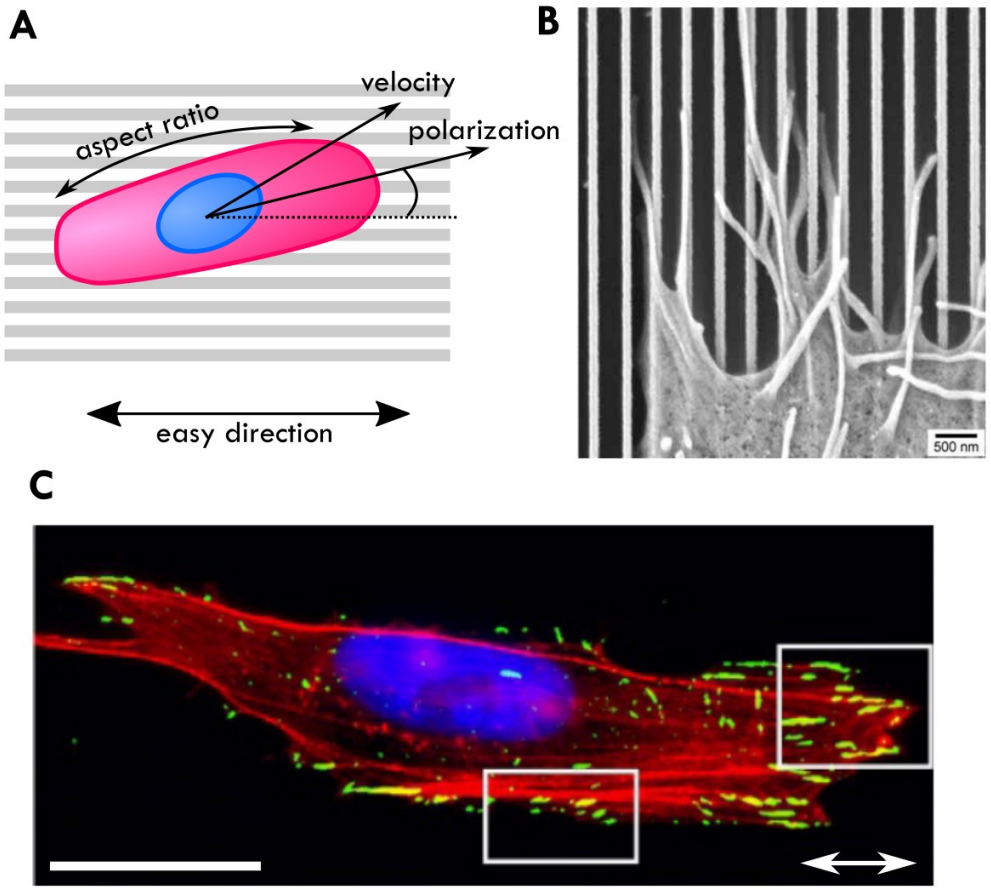

Figure 1 – 4. Contact guidance of single cells. (**A**) Schematic of a single cell during contact guidance. Three main measurements can be done to evaluate CG impact: cell orientation compared to easy direction, cell velocity and cell aspect ratio. Gray lines represent the micro-scale guiding cue, it can be topography with an alternance of grooves and ridges or chemical with a succession of adhesive/non adhesive patterned lines. (**B**) Filopodia are the organelles that sense the topography of the substrate [58]. Human cornea epithelial cell and its filopodia on a nanogrooved substrate observed in SEM. In white are the top of the nanogrooves. Scale bar = 500 nm. (**C**) A MDA-MB-231 breast cancer cell on grooves/ridges pattern aligns and elongates in the direction of the easy direction [55]. Elliptical focal adhesions are constrained by ridges/grooves and have to follow the easy direction (double white arrow). Ridges/grooves size: 400/400 nm. Red: actin; green: vinculin; blue: nucleus; scale bar = 20 µm.

Complementary with the two previous mechanisms, Curtis et al. [61] hypothesized that cells concentrate actin at sharp discontinuities which favors the creation of adhesions and stress fibers in the easy direction. Thus, on corrugated substrates, increasing the depth increases CG because the sharp corners prevent cells to contact the bottom surface [58,62–64] (Fig. 1 – 5A). That is why on deep

topographies, cells tend to stay on top of the ridges and adapt their shape along them, showing a very strong CG. In contrast, sinus-like topographies decrease the CG effect because cells can more easily adjust their shape to the whole surface [65,66].

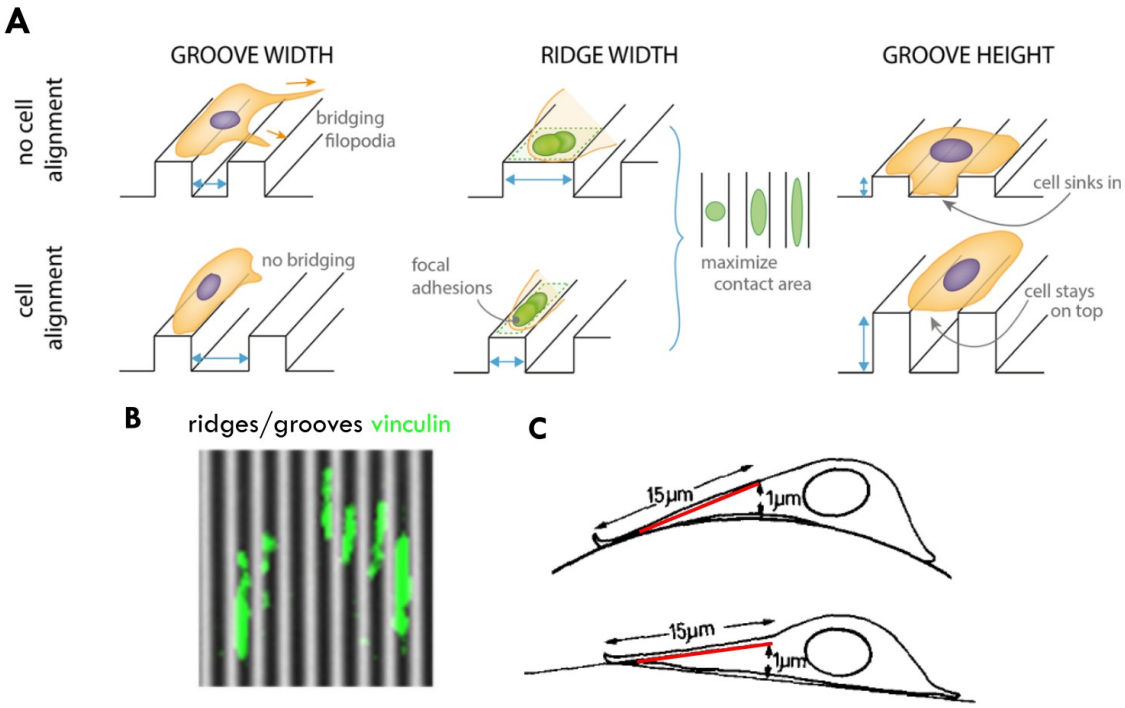

Figure 1 – 5. Some possible mechanisms for contact guidance. (**A**) Corrugated topographies can be defined by their groove width, ridge width and groove depth [48]. Changing these parameters involves adhesions and protrusions and allows to probe mechanisms at stake in CG. (**B**) CG involves that mature FAs are aligned with ridges/grooves direction [55]. Here, FAs are geometrically constrained on top of ridges. Ridges/grooves (400/400 nm width) are observed on phase contrast (top of the ridges is darker), vinculin is in green. (**C**) Dunn & Heath considered protrusions as stiff-rods [57]. On highly curved substrates or when cells face an edge, protrusions (in red) cannot extend sufficiently or create mature adhesions. Cells will then form protrusions and adhesions in the only possible free direction and therefore reorient.

Box 1. Questioning the balance between adhesions and contractility in contact guidance

We understand that CG arises from a combination of tension in the actin cytoskeleton and adhesions. As described previously, adhesions favor the formation of actin filaments assembling in contractile stress fibers that allow traction forces to be exerted on the substrate. However, the essential role of adhesions and contractility in the mechanism leading to CG can be questioned.

Indeed, CG may be triggered in the absence of adhesion proteins [71], or when there is not enough tension in the cytoskeleton to mature FAs. [69] (Fig. 1 – 6). Indeed, CG may be triggered by plasma membrane deformations or actin cytoskeleton dynamics only. For example, plasma membrane can follow ECM fibers in a wetting-like process [70]. Here, guidance in the easy direction is associated with the formation of actin protrusions that deform the cell in this direction. This wetting mechanism is independent of the cell contractility [67,68] as inhibitors of actin contractility such as blebbistatin or Y27632 did not affected CG.

This indicates that CG may not be dependent on the formation of strong adhesions and subsequent stress fibers needed for cell motility. It is more likely a consequence of geometrical constraints restraining cell protrusions on

"tracks". As a consequence, cells have no other choice than adapt to these particular constraints and remodel their cytoskeleton along the easy direction.

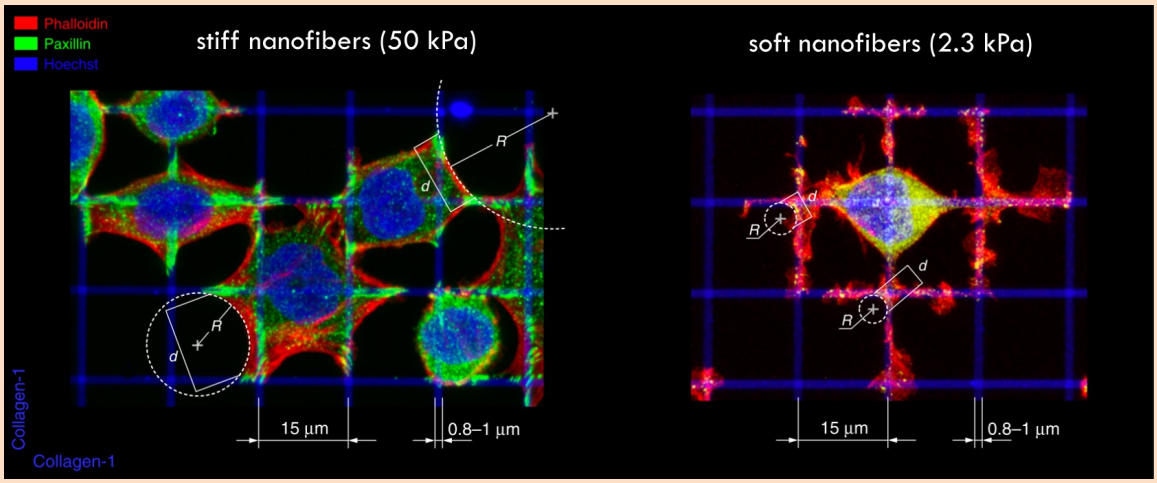

Figure 1 – 6. Two modes of contact guidance. Depending on substrate stifness, cells can display CG following different mechanisms involving either adhesions or actin cytoskeleton. (**Left**) On stiff substrates (50 kPa), cells spread by building focal adhesions and stress fibers. This is made possible because traction forces are strong enough to tense actin. (**Right**) On soft substrates (2.3 kPa), traction forces are too low to build strong adhesions. Cells spread as a fluid wets a substrate. Independently of any contractility-based mechanism. Adapted from [69].

Collective contact guidance

CG of cell assemblies has been much less studied than single cell's. In tissues, cells cannot be considered as individual units but are surrounded by and interact with other cells. Different studies have shown that single cells that display CG do not necessarily display CG in confluent monolayers[c] and vice-versa [62,63,66,72,73]. This is particularly true with epithelial cells that have strong cell-cell adhesions. For example, clustered MDCK cells showed no or little alignment with underlying nanogrooves in particular in the center of clusters where there were more cell-cell contacts, while individual MDCK cells oriented very well [62] (Fig. 1 – 7A). Inversely, in another study on nanogrooves [66], individual C2C12 cells do not show CG but orient when grown at confluence (Fig. 1 – 7B).

Collective CG results from a competition between cell-substrate and cell-cell interactions. It has been suggested that in confluent monolayer, CG can propagate from cell-cell interactions [73]. On

c Confluence is defined as the state where all cells are touching each other.

substrates for which a fraction of the surface has been nanostructured while the other part remained featureless, ARPE-19 cells (epithelial cells) show a propagation of their orientation direction (Fig. 1 – 7C). On the CG half-space, cells were oriented with the easy direction while on the flat half-space, this orientation propagated up to a certain distance from the boundary. This orientation was not directly due to the underlying substrate but resulted from cell-cell interactions, that propagated over several cell sizes.

All these studies demonstrate the complex interplay between CG and cell-cell interactions in tissues. Collective migration of cells should then be taken in account when observing a collection of cells on substrate that can show CG.

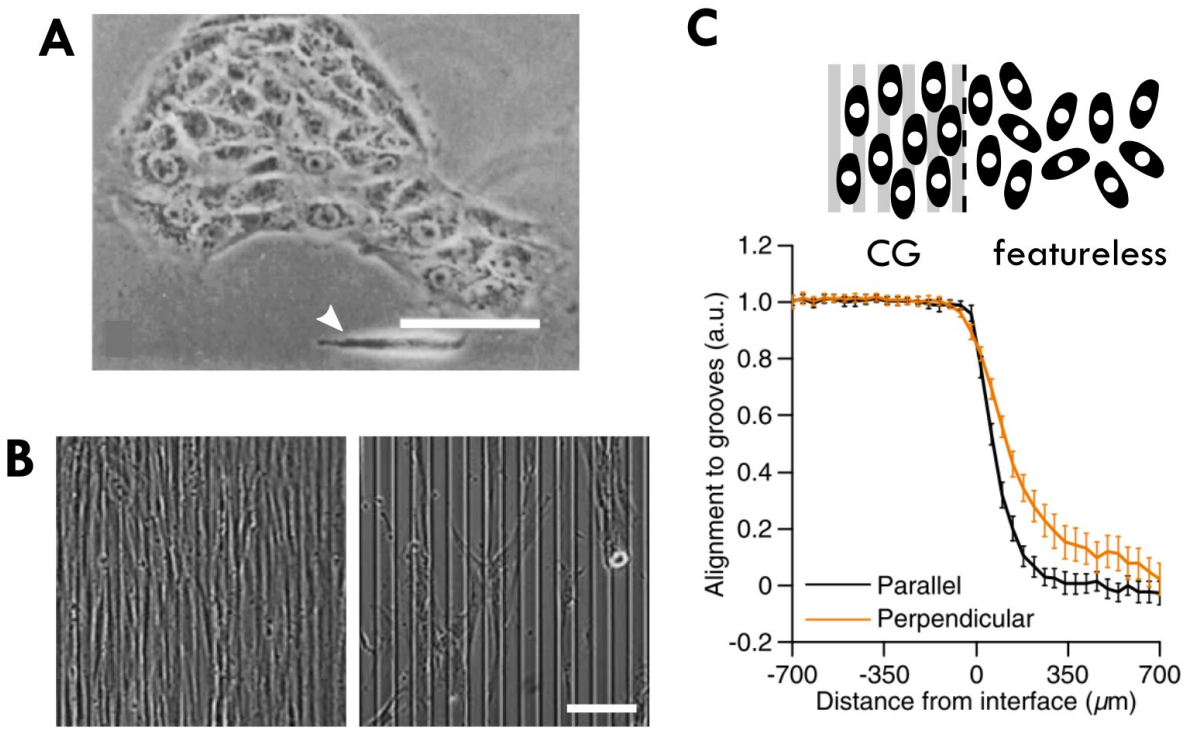

Figure 1 – 7. Collective contact guidance. (**A**) MDCK cells in cluster on top of ridge/groove nanotopography (210/210 nm width, 210 nm depth). Individual cells show alignment with the topography (white arrows). In contrary, cells in clusters are randomly oriented especially at the center where cells have more neighbors. Nanotopography is on the horizontal direction. Scale bar = 30 µm. Adapted from [62]. (**B**) Dermal fibroblasts on ridges/groove topography (25/25 µm width, 780 nm depth). Confluent cells (left) are aligned with the topography while subconfluent scattered cells (right) are not. Scale bar = 100 µm. Adapted from [63]. (**C**) On a hybrid surface made of half sinusoidal nanotography space (pitch 1 µm, depth 150 nm) and half featureless space (schematics), ARPE-19 cells on the flat half near the boundary show similar orientation as those on the CG half. This order propagates over several cell sizes due to cell-cell interactions. Adapted from [73].

1. 2. 3. Tissue scale: collective migration

The collective behaviour of cells may be very different from the one of single cells. Indeed, in organs, cells of different types coexist and act together. Interactions between cells can be direct from cell to cell or mediated by a medium like the ECM [74]. They lead to collective behaviours at the supracellular scale in various processes such as wound closure or tumor invasion. For simplification, we will only deal with behaviours emerging from autonomous cell properties and leave aside collective behaviours that require the existence of supracellular structures like actin cables. An extensive literature on collective migration exists [75–78], some of it focusing also on the physical models that will be discussed in more details in part I. 2. [79,80]. Here we present the basic biological and physical concepts necessary to understand the emergence of collective migration.

Cell-cell and cell-substrate physical interactions lead to collective migration

It is necessary to remind here the key players at stake during single cell migration. The proteins involved in locomotion have been described above. Cells propel forward by adhering to the substrate and pulling on it. This generates cell-substrate traction forces as well as friction forces that oppose the motion. From a physical point of view, cell motion can be described by its velocity and its polarization vectors. Velocity accounts for the speed and direction of motion while polarization defines the cell body orientation[d] (Fig. 1 – 8A). In the absence of any external signal, cells move randomly on the substrate. In the presence of other cells, cell-cell interactions are to be taken in account. Here we exemplify two major cell-cell interactions that can lead to collective migration: weak repulsive interactions via contact inhibition of locomotion (CIL) and strong attractive interactions through cadherins mediated adhesions in epithelial tissues.

Contact inhibition of locomotion was first described by Abercrombie et al. [81], in these terms, “when a contact is formed, further movement in the direction of the contacting cell tends to be inhibited” (Fig. 1 – 8B). At low cell density, CIL tends to scatter cells. In contrary, in packed clusters, CIL effectively “cages” the cells by their neighbours when they are far from the boundaries

d The polarization vector will then point in the direction of migration.

and "freezes" their motion. That is why a loss of CIL is involved in tumor invasion: cancerous cells at the edge of the tumor lose CIL with healthy cells, and are then able to invade the tissue [82]. However, in some cases, CIL can lead to collective migration (Fig. 1 – 8C), for example in the migration of neural crest cells (NCC) in zebrafish embryos. In this case, chemotaxis combines with heterogeneous CIL and NCC cells move as a cluster [83,84].

Epithelial cell assemblies form cohesive tissues because of strong cell-cell adhesions. Because of these bonds, a force acting locally may propagate over a relatively large distance in the tissue. It is common to look at epithelial collective migration by performing the so-called "wound healing" experiment. Briefly, cells are grown to confluence in a space limited by a "wall". At the beginning of the experiment, the wall is removed so that the monolayer can invade the free space [85]. In this case, it has been shown that the traction forces are larger at the edge of the tissue and generate tensile stress in the bulk via cell-cell junctions [86]. As a consequence, velocities correlate more in strongly adhesive tissues than in weakly adhesive ones [87]. For example, MDCK (epithelial tissue) and NRK (fibroblasts) cell velocities from the edges of an invading monolayer were correlated over 200 μm and 50 μm respectively [88] (Fig. 1 – 8D).

Box 2. The role of cell proliferation in collective migration

Because collective migration is a mesoscopic phenomenon, it is common to set aside the role of cell divisions. A trivial effect of proliferation is the increase of cell density with time. As cell density increases, the system ultimately "freezes" in a process reminiscent of a glass transition [92]. This "jamming" phenomenon is the result of the interplay between cell motility, adhesions strength and density [89].
However, before the system jams, a more detailed description of collective migration should include how cell divisions influence the velocities of the surrounding cells and inversely how local forces orient the cell division axis. On the one hand, cell divisions can generate long-range flows across several cell sizes in the tissue [94] that lead to its fluidization [95]. On the other hand, the cells division axis is set by surrounding forces [90,91], generated by the neighbouring cells. Altogether these mechanisms can lead to emergent phenomena. For example, MDCK cells proliferating in a cell-adhesive disk form a 3D rim at the edge because increasing cell density favors edge cells to form another layer [93].

Collective migration in confined environments

In vivo, migrating tissues are surrounded by a complex 3D environment that imposes physical constraints on them. Advances in photolithography over the past decades have helped scientists design experiments *in vivo* where cell monolayers are confined in well-defined patterns

aiming at mimicking some of these *in vitro* structures. Here, we give examples of emerging collective behaviours in two well-studied geometries *in vitro*, disks and stripes, as well as some *in vivo* observations of collective migration. The particular case of active "nematic" spindle-shaped cells in such mesoscale patterns will be discussed later in part I. 2. 3.

In vitro patterns are well-defined and characterized by the typical length of the system: the diameter for disks and the width for stripes. If the size of the pattern is smaller than the intrinsic correlation length of the cells, cell assemblies can show correlated motion. For cells confined in disks, global rotational motion appears only for diameters smaller than the natural correlation length of MDCK, around 170 μm [96] (Fig. 1 – 9A). In stripes during wound healing experiment[e], cells flow in the direction of the free space and are aligned with the edges for widths smaller than the cell correlation length [97,98] (Fig. 1 – 9B). In both cases, if the lengthscale of the system is larger than the intrinsic correlation length, local flows may appear in the form of swirls. As explained before, in these systems, cell-cell interactions mediated by E-Cadherins and the actin cytoskeleton are very important. A downregulation of E-Cadherins that bind the cells together, impairs the rotational motion in disks.

In vivo, the ECM offers a complex environment spanning different lengthscales. For instance, observations in mouse epidermis [99,100] (Fig. 1 – 9C,D) show that cells from melanomas invade the stroma along ECM collagen fibers, blood vessels, striated muscles or even nerves, that create geometrical constraints of dozens of micrometers. Another *in vivo* observation in zebrafish embryos is the existence of cell-repulsive ECM bands of versican that guide the collective migration of neural crest cells clusters towards placodal cells. Strikingly, these confining bands seem adjusted to the size of the cell cluster which would promote efficient directed motion during morphogenesis (Fig. 1 – 9E). Both *in vitro* and *in vivo* examples of collective migration in confined environments show that these geometrical constraints act as a guide for directed motion and are involved in phenomena such as morphogenetic events or tumor invasion.

e In this particular wound-healing experiment, the free space is patterned with mesoscale non-adhesive stripes oriented perpendicularly with the initial wall direction.

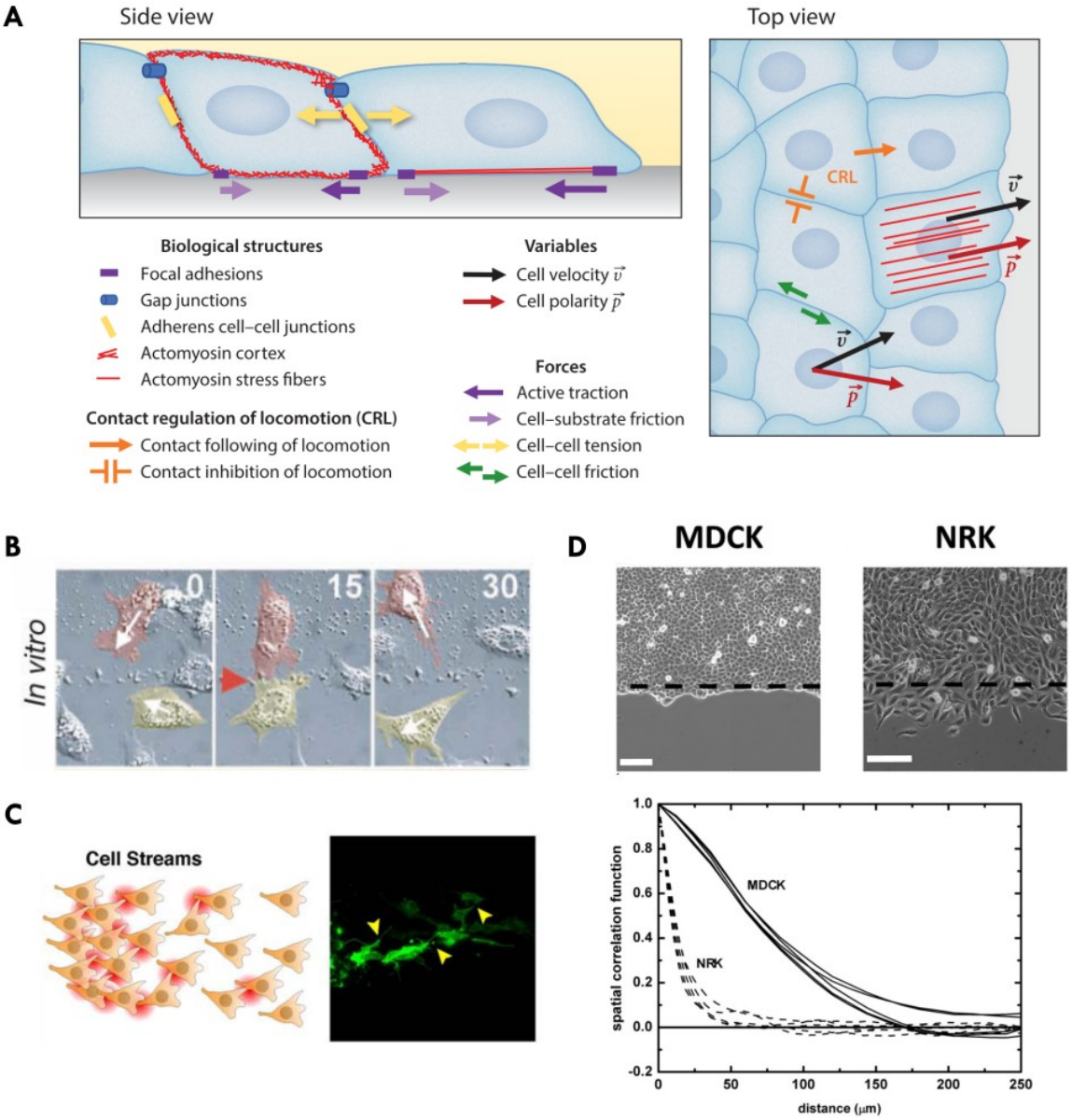

Figure 1 – 8. Collective migration of cells. (**A**) Cells in tissues interact with their substrate and other cells through physico-chemical signals and biological regulation mechanisms. From a physics perspective, tissues are described by both velocity and polarization [80]. (**B**) Contact inhibition of locomotion (CIL): when two cells meet, they repolarize away from the contact point [83]. On top right: time (in min); white arrows: direction of migration; red arrow: contact point. (**C**) In particular cases, CIL can make assemblies of cells move in streams [82]. Right panel: image of cells in such streams. (**D**) Epithelial (MDCK) and fibroblastic (NRK) tissues do not have the same spatial correlation when invading the free space in wound healing experiment. This is due to differences in cell-cell adhesion strength [88]. Scale bar = 100 μm.

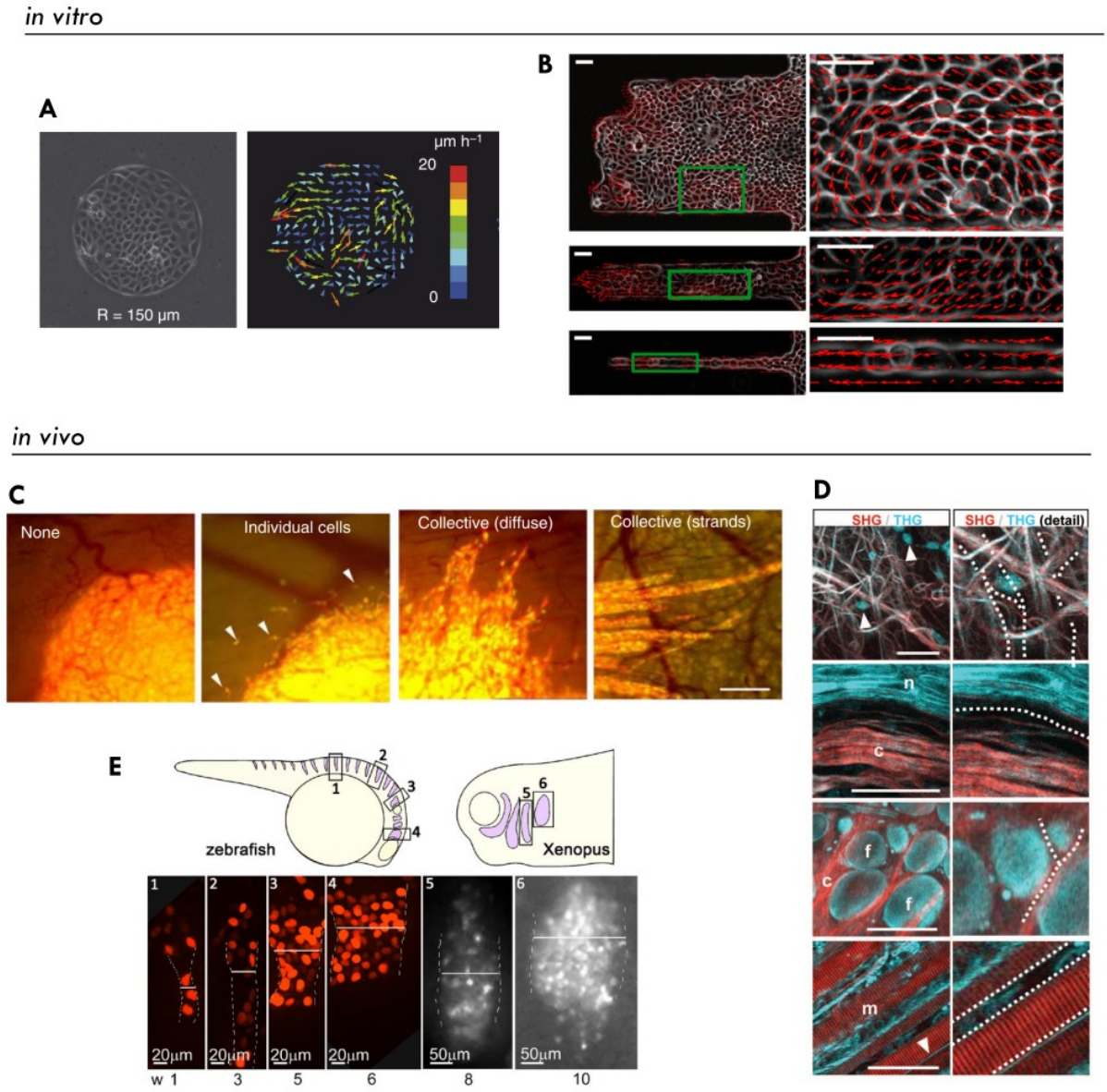

Figure 1 – 9. Collective cell migration in confined environments. *in vitro* (**A**) MDCK cells confined in disks display rotating motion. For disks larger than the orientation correlation length, vortices appear [93]. (**B**) MDCK cells in stripes during wound healing experiment have a directed motion towards free space. For large stripes, vortices appear [97]. Scale bar = 50 μm. | *in vivo* (**C**) Different invasion modes of HT1080 cells in skin-fold chambers monitored by epifluorescence microscopy [99]. From left to right: no invasion, individual cells invading space, collective migration with a leader cell, collective migration in well-defined strands. Sale bar = 250 μm. (**D**) Native dermis imaged with second and third harmonic generation (SHG/THG) unravels the complex cellular environment and its geometrical constraints [100]. From top to bottom: random and aligned collagen fibers (c), nerves (n), fat cells (f), striated muscles (m). Space available for tumor invasion is highlighted by dotted lines. Scale bars = 50 μm. (**E**) NCC cell clusters (nucleus stained) in zebrafish and xenopus embryo migrate in confined stream lines of different widths [101].

1. 2. 4. Competition between cellular contact guidance and supracellular guiding cue

Since the geometrical constraints imposed by the ECM span a wide range of lengthscales, we question here the consequences on cell migration of guiding topographies of different lengthscales. Such combinations can be set in a controlled way *in vitro*. For example one can combine wide population-scale tracks with subcellular scale grooves. In this example, the smaller topographical structures tend to orient the cells in their direction via CG, we will refer to this effect as microscale contact guidance (μCG). Wider confinement tend to orient the whole tissue population and will be refereed as mesoscale guidance (mG). Several studies have put in competition μCG and mG through different approaches (Table 1 – 2). We will refer to "parallel geometries" for setups where μCG and mG are aligned and "perpendicular geometries" for setups where they are perpendicular (Fig. 1 – 10A).

Reference	Cells	Microscale contact guidance (μCG)	Mesoscale guidance (mG)	Observations
Cha, 2017 [102]	C2C12	Electrospun fibers (∅ < 1 μm)	Patterned lines (100/200 μm)	Longer myotubes on parallel geometries
Gilchrist, 2014 [103]	hMSC	Grooves (2 μm)	Stripes (125 – 1250 μm)	Transition in cell orientation for widths > 500 μm
Kim, 2014 [104]	hMSC	Grooves (0.35 μm)	Sinusoidal substrate (λ = 30/100 μm)	Synergistic effect on osteoblasts differentiation and adhesion to native tissue
López-Bosque, 2013 [105]	rMSC	Grooves (0.05 μm)	Grooves (10 μm)	Best cell alignment on parallel geometries*
Moffa, 2014 [106]	HUVEC	Electrospun fibers (∅ 0.24 μm)	Grooves (15 – 100 μm)	Synergistic effect on cell orientation, area, vinculin expression, ...
Nam, 2016 [107]	MCF10A/ PIK3CA	Grooves (0.8 μm)	Patterned lines (30 – 120 μm)	Faster and more persistent cell migration on parallel geometries*
Werner, 2018 [108]	hMSC	Fibrillar collagen (∅ 0.1 – 0.2 μm)	Cylinders (∅ 0.25 – 5 μm)	Transition in cell orientation for cylinder diameter > 1000 μm

Table 1 – 2. Studies of substrates with subcellular lengthscale (μCG) in competition with micrometric geometric constraints (mG) and their effect on adherent cells (*parallel geometries = both smaller and larger lengthscales aligned).

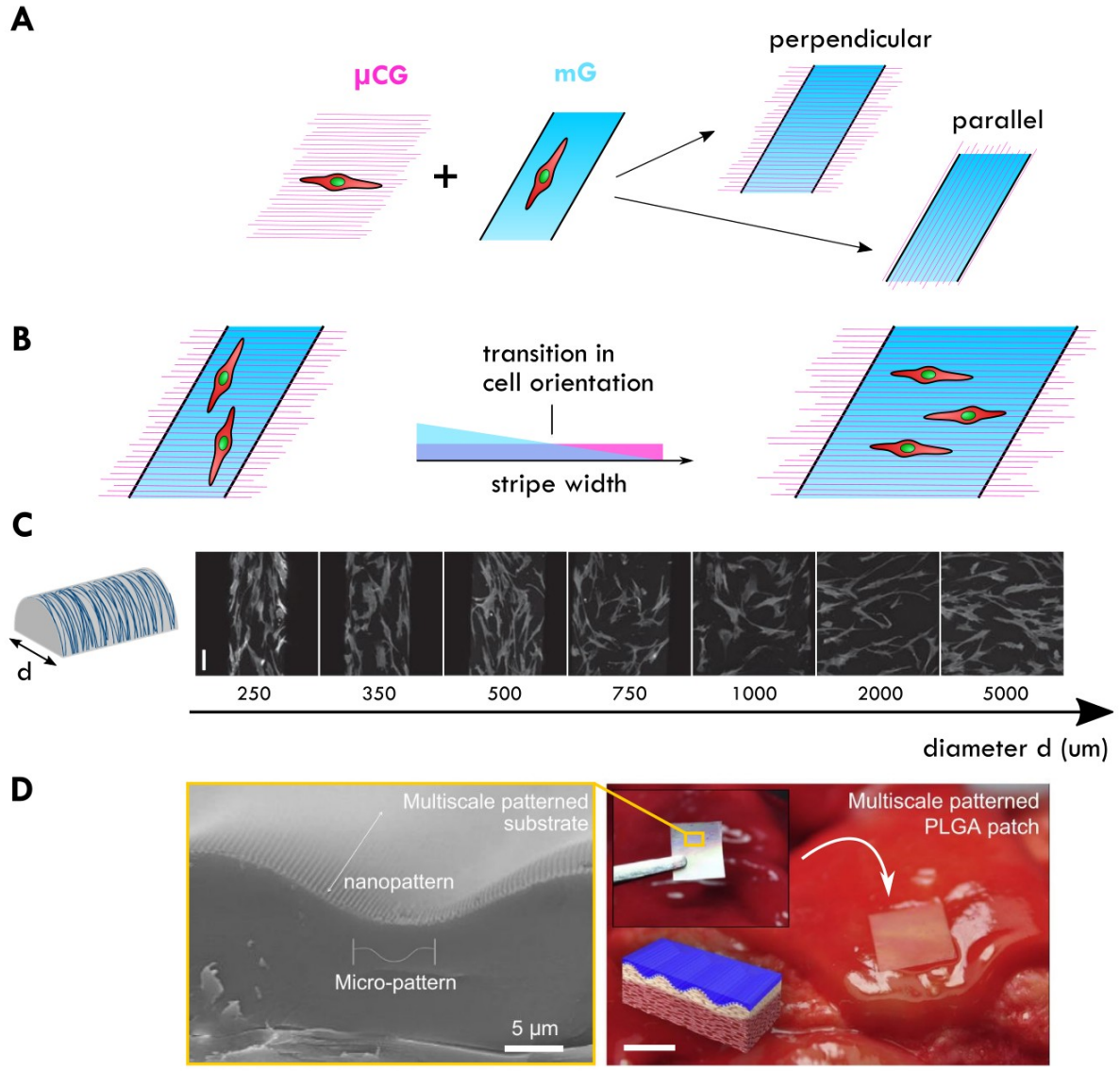

Figure 1 – 10. Competing physical cues for cell alignment. (**A**) Schematics of two orientational cues of different lengthscales. μCG orients cells with microscale topogaphy (pink). mG orients cells because of geometrical constraints (mG). The two extreme cases for competition between these two cues are "perpendicular" and "parallel" geometries. (**B**) Schematics of the competing effects of μCG (pink) and mG (blue) on cellular orientation for perpendicular geometry. For a given μCG, a transition in cell orientation occurs at a particular mG width. Indeed, mesoscale stripes constraint cells in their direction overriding μCG effect for thinner widths. In contrary, for wider stripes μCG effects impose cell orientation. (**C**) Images of hMSCs on cylindrical substrates coated with electrospun nanofibers (horizontal direction) and with increasing curvature [108]. Cells follow the effect described before, the cylindrical confinement induced by the finite perimeter playing the role of mG. Scale bar = 100 μm. (**D**) SEM image of a multiscale patterned substrate (left) [104]. On such substrate, μCG/mG orient synergistically cells parallel to each other. Moreover, mG topography allows maximal contact area between the cell patch and the soft intestinal tissue (right). Scale bar = 5 μm (left); 1 cm (right).

On perpendicular geometries for a given μCG cue, one of the two modes of guidance prevails depending on the width of mG (Fig. 1 – 10B,C). For very small widths, mG controls cell orientation because of mesoscale confinement while for very large widths, cells will follow μCG as if they were in bulk [103,108] (except close to the edges). With parallel geometries, a synergistic effect appears [105–107], cells are more prone to align and migrate in the imposed easy direction. However, the effect of mG appears to be dominant. For instance, for migrating HUVEC cells, the parallel μCG only slightly, although significantly, increases migration speed, persistence as well as vinculin expression [106].

So far, only few attempts have been made to use synergistic effects of multiscale substrates to direct tissue self-organization. In terms of application, this route could be a promising way to manufacture cellular patches with a better integration for tissue repair [104] (Fig. 1 – 10D) or to promote differentiation of tissues such as muscles [102] that require a particular elongated architecture.

1. 3. A particular tissue: the muscle

In this thesis, we have investigated the collective migration effects induced by multiscale substrates and how they could enhance the differentiation of C2C12 myoblasts into mature muscles fibers. Here we present the general architecture of muscles, how they form and what factors play on their differentiation. We also present the state of the art of the impact of topography on C2C12 differentiation *in vitro* that will be compared to our study in Chapter IV.

1. 3. 1. Biology of the muscle

Muscle hierarchical structure

Muscle tissues are present in all animals. They represent 40% of body mass in human and they produce forces to induce locomotion movement or internal organ contractions. There are three

principal types of muscles: smooth muscles are responsible for organ deformation for example vasoconstriction, cardiac striated muscles for heart beating and skeletal muscles for locomotion. Only skeletal muscles are under conscious control via moto-neurons. They are of particular interest for us because of their architecture and the way they form and regenerate.

The base unit of skeletal muscles is the muscle fiber or myofiber. It is a syncytium containing hundreds of nuclei. It possesses a remarkably well organized actomyosin structure that uses ATP molecules as a source of energy to contract and produce mechanical forces. Diversity in muscle shapes and functions comes from the different arrangements these fibers can take [109]. Some muscles can contain hundreds of fibers (like the tensor tympani, an eardrum muscle) and others millions (like the medial gastrocnemius, a calf muscle). Some are elongated (like leg muscles), useful for fast contraction, and others thicker, that allow more force generation (like phalanx muscles). To fully generate forces and maintain mechanical integrity, myofibers are connected together hierarchically via successive layers of connective tissue made of ECM, blood vessels and nerves (Fig. 1 – 11A, B). The outer layer, the epimysium, is thick and separates muscles from each others. Myofibers are arranged in bundles, the fascicles, of around 500 μm diameter (in humans) and surrounded by the perimysium. Between fascicles lie blood vessels that bring energy supply and oxygen but also nerves, essential for muscle contraction. Finally, each myofiber is surrounded by an endomysium layer.

In humans, myofibers are usually 50 μm thick and are composed of thousands of myofibril units, 1 to 2 μm in diameter (Fig. 1 – 11C). Each myofibril is separated from each other by sarcomeric reticulum and few mitochondrias. They are composed of a very periodic alternation of light (I-band) and dark bands (A-band). A-bands are due to the presence of myosin microfilaments, an assembly of hundreds of myosins coupled tail-to-tail. These myosin microfilaments are evenly spaced in this zone in a crystal-like structure by intermediate filaments structures. Lighter I-bands correspond to zones containing actin filaments. The middle of I-band is called a Z-disk and the structure between two Z-disks is called a sarcomere that has an exact length of 2.2 μm in its relaxed state (Fig 1 – 11D). Hydrolysis of ATP bends myosin heads and reduces sarcomere length which induces muscle contraction and mechanical forces. Generated forces add-up in the whole muscle, tense the tendons linked to bones and create motion via a leverage effect.

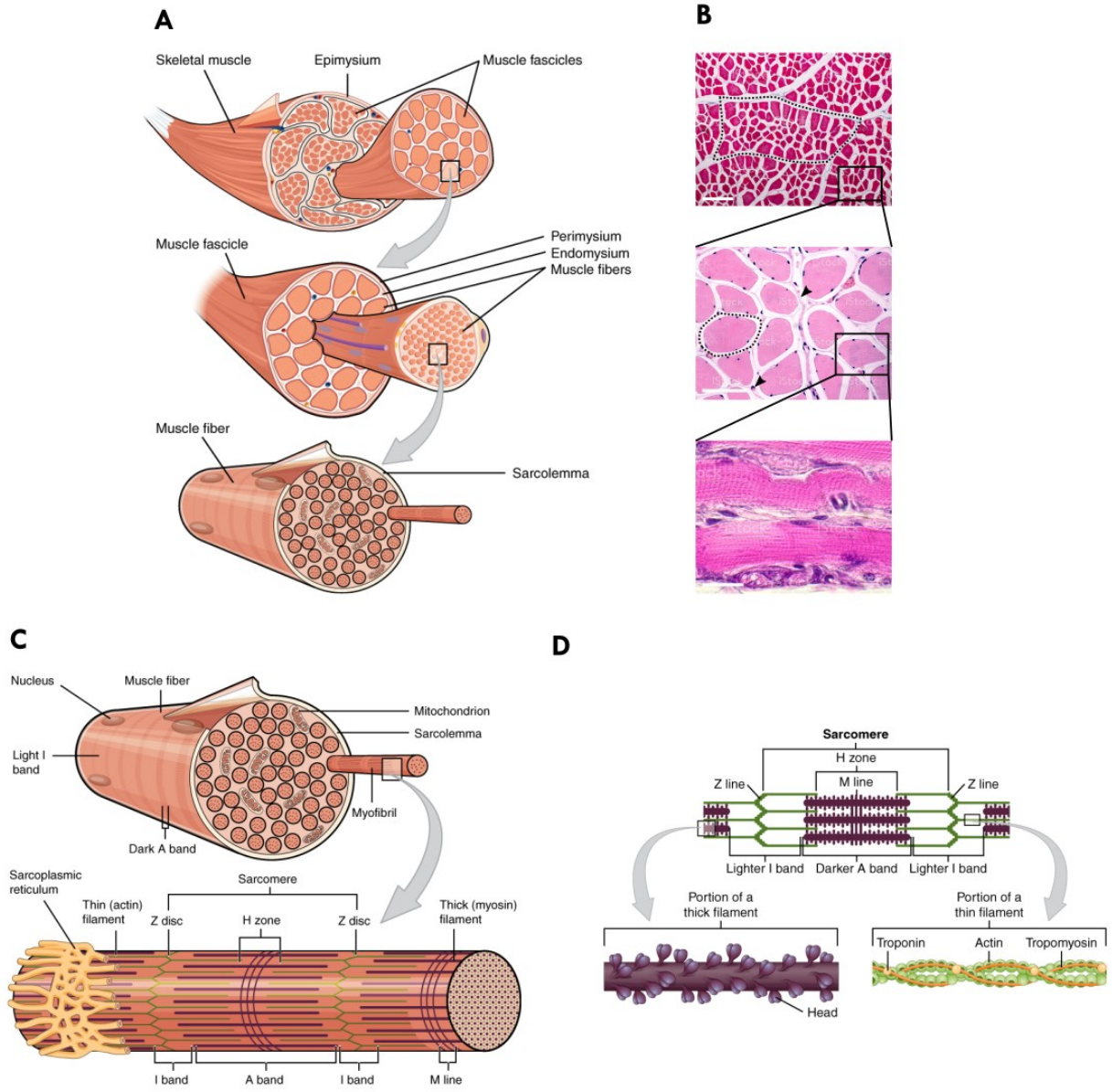

Figure 1 – 11. Muscle hierarchical structure. (**A**) Muscle fibers are arranged in bundles, the fascicles that are packed together to form the muscle. Muscles fibers, fascicles and muscles are surrounded by a layer of ECM, epimysium, perimysium and endomysium respectively. (**B**) Photos of muscle sections (credit: iStockPhoto). From top to bottom: muscle fascicles (dotted line), scale bar = 100 µm; muscles fibers (dotted line), blood vessel (arrows), scale bar = 50 µm; sarcomeres in muscle fibers, scale bar = 50 µm. (**C**) Muscles fibers are composed of hundreds of myofibrils containing sarcomere units. (**D**) schematics of a sarcomere and its actomyosin arrangement. All schematics are adapted from [110].

Myogenesis

In the embryo, muscle tissues form from the mesoderm during pregnancy [111]. After birth, the whole adult muscle mass has been generated and myofibers can only grow thicker or be repaired by specialized stem-cell like cells, the muscle satellite cells (mSC). These cells are often studied as a model for *in vitro* myogenesis due to their high stemness [2,112,113]. mSCs differentiate progressively into fully mature myofibers by triggering successively the expression of myogenic regulatory factors (MRFs) (Fig. 1 – 12). The first step in myogenesis is the expression of Myf5 followed by MyoD. Cells expressing MyoD – the myoblasts – acquire a spindle-like shape and stop proliferating, they reduce their motility and ultimately begin to fuse end-to-end with other myoblasts into nascent myotubes. At this point, they express the late differentiation markers, myogenin (MyoG) and Mrf4. Muscle myosins are also expressed and their long chain (Myosin Heavy Chain MHC) is often used to observe differentiated myotubes. Late differentiation stages from myotubes to mature myofibers involve several nuclear motion [114] up to the point where nuclei are equally distributed close to the plasma membrane of the myofiber leaving space for the growth of the sarcomeres.

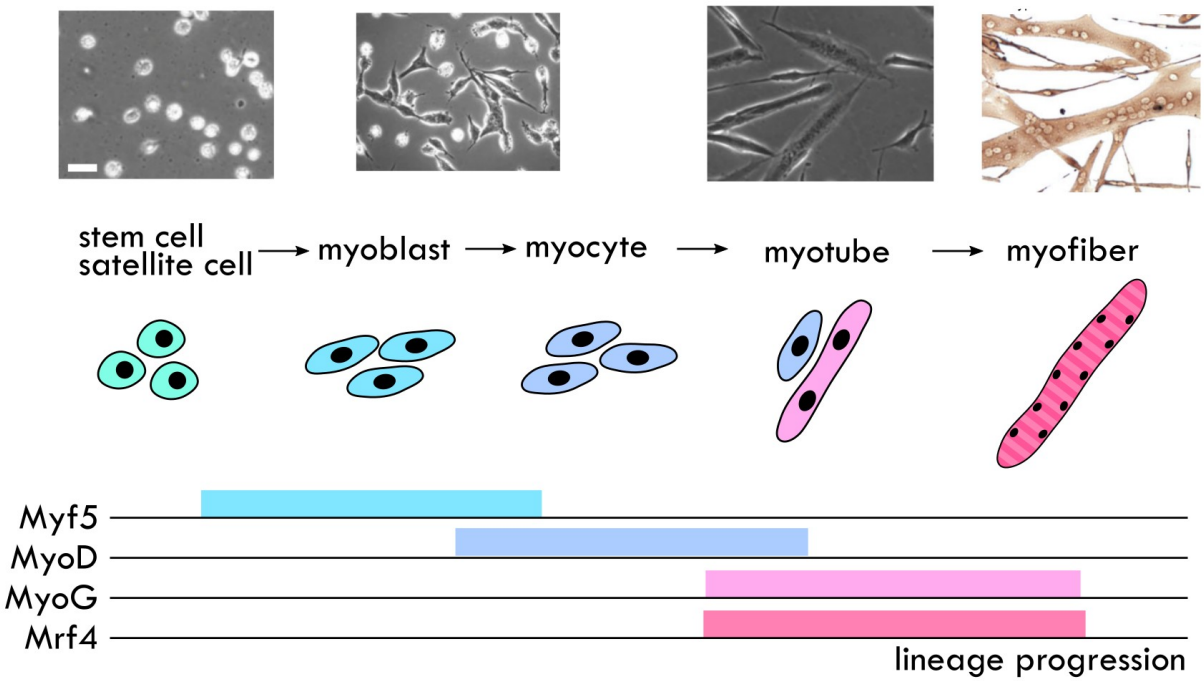

Figure 1 – 12. Myogenesis. To develop into fully mature muscle fiber, satellite cells goes trough several shape changes correlated with the activation of the different muscle regulatory factors (MRFs). Adapted from [113,115]. Scale bar = 50 µm.

Physical factors affect myoblasts differentiation

In vivo, MRFs expression is triggered by cascades of chemical signaling[f]. However, beside these chemical factors, physical cues due to cell environment also affect myogenesis. Myoblasts undergo a radical shape change during differentiation into myotubes: from an elliptical to a very elongated shape. Myotubes result from the end-to-end fusion of myoblasts and differentiation is therefore favored by cell alignment. Indeed, cell-cell contacts through N-cadherins [116] and high cell aspect ratio [117] have been shown to upregulate the fusion of myoblasts.

Cell-substrate interactions also play a major role in the differentiation of myoblasts. We focus here on two key players: laminin and substrate stiffness. Cells cultured on laminin, which is present in the native basal membrane of muscle tissue, differentiate more efficiently[g] than cells plated on other substrates [118,119]. Substrate stiffness is an important parameter regarding further maturation of myotubes. Indeed, C2C12 cells cultured on soft substrates with tissue-like stiffness (12 kPa) or on top of other C2C12 cells, develop into mature striated myofibers [13,120] more efficiently than when plated on rigid substrates.

All of these parameters have to be taken into account for a good myoblast differentiation *in vitro*. In our example, the best substrate would have a stiffness close to the one of myoblasts, be coated with ECM proteins like laminin and structured to enhance myoblasts alignment and fusion.

1. 3. 2. *In vitro* myogenesis

Box 3. On tissue engineering

Tissue engineering aims at generating a part or an entire functional organ *de novo*, to repair damaged tissues or be used as disease models [130]. In particular, several studies have focused on cardiac or skeletal muscle engineering [126–128]. Here, we present the main strategies used for tissue engineering. Most of the attempts made so far have used stem cells, either from donors or using autologous cells that have been reprogrammed (iPSCs).
The simplest idea is to stimulate tissue self-healing by adding growth factors or directly transplant new stem cells in the tissue *in vivo* for instance at the locus of a heart infarct. However, this strategy shows poor cell survival,

f *In vitro*, we induce differentiation by replacing the cell medium by a medium containing factors triggering differentiation.

g The efficiency of differentiation is often quantified by the expression of particular MRFs or the amount of fused myoblasts.

emphasizing that a good control of the cell's environment similar to its healthy standard, is crucial for tissue repair.
To cope with this issue and mimic 3D environment, some strategies rely on scaffolds made of biocompatible materials [122] that guide tissue self-organization. Scaffolds can be used to generate a tissue *in vitro*, or can be directly implanted *in vivo* to enhance tissue repair. Nonetheless, the risk of the scaffold being rejected by the host body exists. To avoid this, most scaffolds are designed to be degraded at the same speed as the tissue regenerates.
Another strategy to avoid rejection problems is to mature scaffold-free explants *ex vivo* then implant them in the host body [121]. For example, hierarchical structures can be assembled by growing differentiated monolayers on thermoresponsive polymers such as PNIPAAm[h,129]. A simpler method consists in engineering substrates that guide tissue architecture. This favors self-organization and differentiation into the desired organ [123–125]. This is the strategy we have followed of this thesis to generate 3D muscle tissue from chemically patterned multiscale substrates (see Chapter IV.).

In Table 1 – 3, we review some examples on how the physical environment of cells can direct C2C12 myogenesis. In all these studies, several observables are used to characterize the efficiency of differentiation. Fusion and maturation indices are a simple way to quantify differentiation: the fusion index accounts for the number of nuclei in fused myotubes versus the overall nuclei population, the maturation index measures the number of myotubes containing five or more nuclei versus all the myotubes. To make these measurements, cells are stained with proteins of mature muscles: Myosin Heavy Chain (MHC) or α-actinin, a sarcomeric protein. The last kind of analysis is gene expression quantification, especially MRFs that is performed with real-time qPCR. Cell alignment and elongation are also important because they favor the end-to-end fusion of myoblasts. Of note, the nuclei are also aligned and elongated in the direction of the cell shape.

h PNIPAAm is a polymer that is cell-adhesive above 33°C and cell-repellent below. Tissue engineers use this particular effect to grow cell tissues in 37°C incubators and detach them from their plating substrate when removed from the incubator. Harvested cells sheets can then be assembled hierarchically.

References	Substrate material	Coating	Geometry	Observations
Contact guidance by topography (μCG)				
Shimizu, 2009 [140]	PDMS	laminin	Microabrasions (Ra = 0.03 – 0.56 μm)	No influence on differentiation
Greco, 2013 [51]	PEDOT:PSS (1 GPa)	-	Wrinkles (λ = 1 - 2 μm)	More differentiation, elongated myotubes Co-culture with nHDF fibroblasts
Grigola, 2014 [66]	PDMS	fibronectin	Sinus (λ = 0.28 – 2 μm)	Better alignment in confluent cultures
Mesoscale guidance by geometrical constraints (mG)				
Engler, 2004 [120]	PA (1 – 20 kPa)	collagen	Lines (100 μm)	Optimal stiffness for differentiation (12 kPa) Striation for cells cultured on other cells
Yamamoto, 2008 [141]	Glass	-	Microgrooves (5 – 120 μm)	Optimal cell alignment for 20 μm grooves width Elongated and orientated nuclei Myofibrils appearance
Nagamine, 2010 [142]	Glass then fibrin	-	Lines (100 – 800 μm)	Misalignment of cells on larger lines Long term synchronized contractions
Zatti, 2012 [131]	PA (15 kPa)	laminin	Lines (100 – 500 μm)	Increased fusion index with line width Paracrine soluble factors essential for differentiation
Sun, 2013 [132]	PDMS	fibronectin	Lines (20 – 200 μm)	Longer myotubes for lines width larger than 50 μm Misalignment of cells on larger lines Myotubes differentiate over myoblast layer
Denes, 2019 [133]	Gelatin	-	Lines (10 μm)	Enhancement of sarcomeric gene expression
Combination of physical guiding cues				
Jana, 2014 [134]	Chitosan - PCL	-	Lines (50 – 100 μm) + electrospun fibers (∅ 100 – 150 nm)	Synergistic effect of parallel substrates on differentiation
Cha, 2017 [102]	PCL	-	Lines (100/200 μm) + electrospun fibers (∅ < 1 μm)	Longer myotubes on parallel substrates

References	Substrate material	Coating	Geometry	Observations
Yeo, 2019 [135]	PCL + alginate (10 kPa)	-	Strut (∅ 340 µm) + electrospun fibers (∅ 0.3 µm)	Better nuclear, cell elongation and muscle gene related expression on parallel substrates
Bajaj, 2011 [136]	PE (Petri dish)	fibronectin	Lines (20 – 300 µm), torus (⌀ = 40 – 200 µm) or lines + torus	Hybrid patterns (lines + torus) give better fusion and maturation indexes
Ahmed, 2010 [137]	PDMS (1 MPa)	fibronectin	Lines (30 µm) + stretching	Stretching of the substrates Better differentiation for lines at 45° compared to strain
3D approaches				
Fujita, 2009 [138]	PDMS	laminin	Silk sutures 18 mm apart	Cylindrical bundles of myotubes Sarcomeric structures
Neal, 2014 [139]	Gelatin then fibrin	-	Hollow cylinder (⌀ = 254 – 1016 µm)	Muscles fascicle with several myotubes Sarcomeric structures

Table 1 – 3. Studies of *in vitro* myogenesis of C2C12 cells using physical factors to direct differentiation. All substrates with guiding cues showed better cell alignment and elongation than flat substrates.

Myoblasts cultured on flat substrates organize in randomly oriented domains. To enhance cell alignment, the strategies based on a combination of µCG and mG as described in I. 1. 2. 4. have been used on myoblasts. µCG and mG separately, favor alignment and appearance of elongated and aligned myotubes. Microscale contact guidance is obtained by engineering nano/micro topography or micropatterns like sinus waves [66], abrasions [140] or wrinkles [51] (Fig 1 – 13A). Mesoscale guidance is implemented with patterned substrates with stripes of adhesion proteins in an otherwise cell-repellent substrate (Fig. 1 – 13B). Myotube differentiation is highly impacted by the stripe width. Thin stripes allow better alignment and the appearance of sarcomeric structures [133,141]. Wider stripes show a spontaneous orientation of the myotubes at a finite angle with the mG stripes, which limits their elongation [142]. Strikingly, in mG stripes the cells self organize in such a way that the differentiated myotubes sit on a layer of myoblasts [132], which may improve their differentiation [120]. Furthermore, a synergistic parallel combination of µCG and mG always outperformed µCG or mG alone, in term of cell alignment, fusion index but also MRFs gene expression [102,134,135] (Fig. 1 – 13C).

All of these studies have focused on describing better ways to generate muscle tissue *in vitro*. Nowadays, tissue engineers aim at letting cells self-organize by only directing them via geometrical constraints [144]. Although, morphogenetic rules are unclear because of the numerous parameters to take into account, general physical principles involved in cell collective migration and self-organization can be understood by theoretical modeling based on cell properties and symmetry arguments.

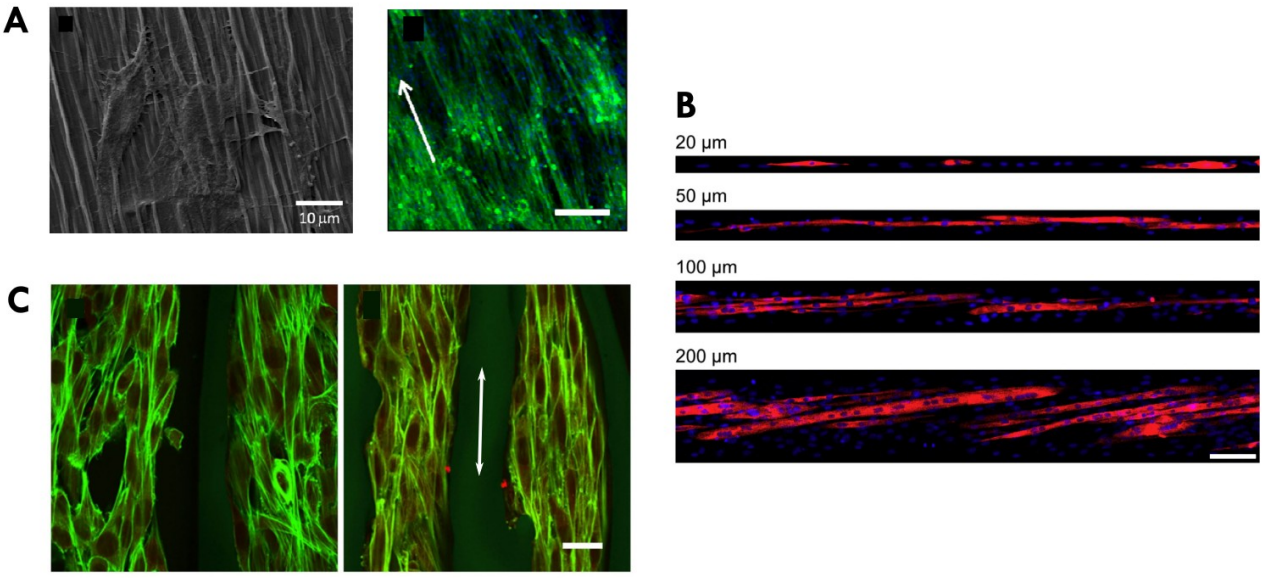

Figure 1 – 13. Directing myogenesis by engineering physical environment. (**A**) Substrate anisotropy (here microwrikles) can enhance myogenesis, cells being aligned by contact guidance (µCG) [51]. Left: microwrinkle observed in SEM, scale bar = 10 µm; right: actin-stained C2C12 monolayer, µCG direction is shown by the white arrow. Scale bar = 200 µm. (**B**) Chemically patterned stripes help myogenesis by aligning myoblasts because of cells confinement (mG) [132]. Myosins are imaged in red (MHC) and nuclei in blue (DAPI). Scale bars = 100 µm (XY); 10 µm (XZ). (**C**) Multiscale substrates with parallel geometry for µCG/mG show enhanced alignment and differentiation of C2C12 [134]. Left: mG only; right: parallel substrates, µCG direction shown by the double arrow. Green: actin; red: MHC. On the right image, cells appears more yellow, meaning a greater expression of differentiation marker MHC. Scale bar = 20 µm.

2. Active cellular nematics

2. 1. Active matter

In complement with the classical biology approach of cells and tissues, a coarse grained physical continuum approach has been proposed to describe tissues. In the next part, we will develop the key elements used for such description.

2. 1. 1. Definition and examples

Regardless of the involved lengthscales, biological objects such as actomyosin networks, cells or tissues can be viewed physically as a material. Such a description belongs to the more general framework of active matter. Active matter refers to an out-of-equilibrium system containing an ensemble of objects able to convert chemical energy from their environment into motion or force. In such systems, collective behaviors can spontaneously emerge, in contrast with passive matter where they would be the consequence of an external cue. These emergent behaviours cannot be predicted by the sum of the individual behaviours as the interactions between objects are an essential feature of these systems. This definition of active matter applies to many different systems of various sizes: animals groups, tissues, colloids, cells, bacteria and down to acto-myosin system (Fig. 1 – 14).

2. 1. 2. Theories of active matter

A large theoretical effort has been developed in the last 20 years to describe active matter. In the present cases, cells are submitted to three types of forces: friction forces that result from cell-substrate interactions; cell-cell interaction forces that arise for example when two cells slides laterally to each other; and active forces. In a closed system, these three forces cancel.

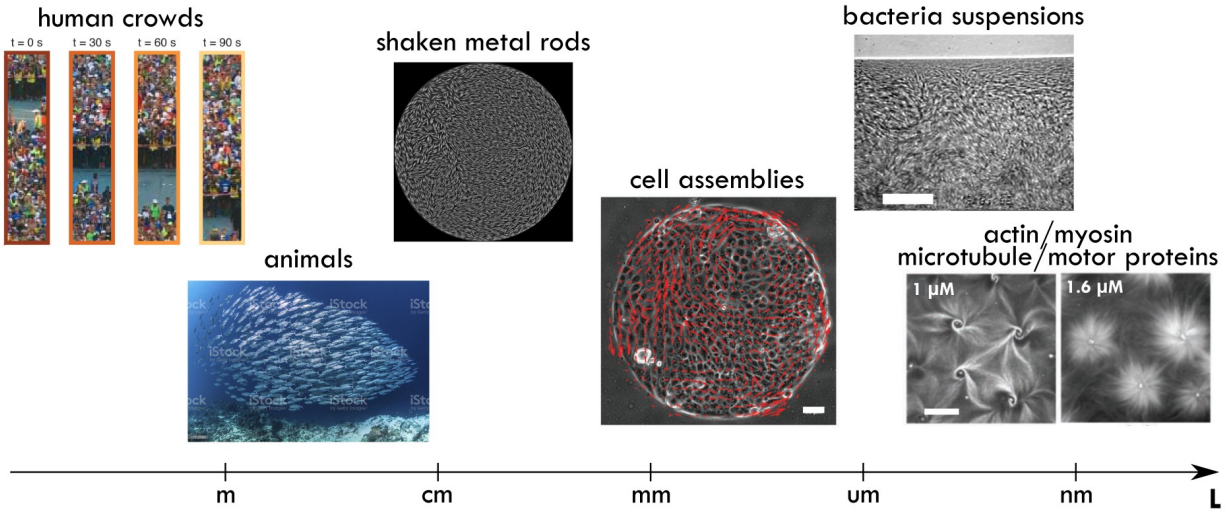

Figure 1 – 14. Different classes of active systems across lengthscales. From left to right: human crowd in Chicago marathon have polarized motion [145] (human = 1.7 m); fish shoal swim in a compact ball to frighten predators, (fish = 20 cm) (credit: iPhotoStock); copper rods vertically shaken display giant number fluctuations [146] (rod = 1 cm); MDCK cells confined in a disk spontaneously rotate altogether [96] (scale bar = 50 μm); bacteria suspensions have turbulent dynamics at low Reynolds number [147] (scale bar = 35 μm); microtubule/kinesin system form patterns such as asters [148]. Concentration of motor protein (a proxy for activity) is indicated in top left corner, scale bar = 100 μm.

Theories of active matter deal with two fundamental quantities: the velocity **v** and the polarization **p**. Velocity is a vector that represents cell displacement. Cells move because of their active components such as the actomyosin machinery. The definition of polarization depends on the model used. One of the biological definition of polarization is the nucleus-Golgi apparatus vector. A simpler way to define it is the direction of elongation of the cell[i,j]. For an isolated cell, this direction can be easily identified. However, for tissues, this observation can be more difficult. Often, cell polarization in tissues does not align with velocity. The aligning process between the velocity and the polarization is crucial to understand cell collective behaviour. On isolated cells, **v** and **p** align because cells repolarize in their direction of migration. However, in tissues, external factors such as CIL can lead to a mismatch between these vectors that gives rise to emergent collective migration.

There is a large literature on physical models for collective migration [77,79,80,149,150]. Among common models used for describing cell assemblies we can cite the Vicsek [151] and Toner-Tu

i As elongation of the cell gives only a direction, in this definition, polarization vector must point in the direction of the cell motion.

j In other models, the polarization can also be defined by the force dipole exerted by cell traction forces when they migrate.

[152] theories, that take in account the influence of the vicinity on the velocity; the cellular Potts models [153], that use a lattice representation of particles; vertex/Voronoi models, that consider the edges of the cells. Each model is well suited to specific types of problems, for example vertex models are well-suited to study epithelial tissues. However, we will only detail the model we use in our thesis that is based on a coarse-grained continuum description of the system that does not take into account each cell specificity but treat the whole system as a material. These "active gel models" are based on hydrodynamic equations and liquid crystals theory.

2. 2. Active nematic liquid crystals

Continuum descriptions of tissues are based on a hydrodynamic theory adapted to anisotropic particles. Therefore, some basic knowledge on liquid crystals is necessary. In this part, we give the main theoretical results necessary to Chapter III. without detailing the calculation. More details can be found in the book of De Gennes and Prost [1] for passive nematic description and in the following reviews [154–157] for active nematohydrodynamic models.

2. 2. 1. Distortions in passive nematic liquid crystals

Liquid crystal phases are states of matter between liquid and crystal [1]. Nematics are a particular case of liquid crystals where elongated molecules show no long-range positional order but a long-range alignment direction. We note **p** the director vector. For nematics the symmetry **p** = -**p** applies (Fig. 1 – 15A). In the following, vectors will be denoted in bold. The tensorial notation will be used for their components (as well as those for tensors).

Frank-Oseen energy

In its nematic state, all particles are aligned in principle. We now consider distorsions in the alignment of this liquid crystal. The free energy density f_d associated with the distortion, called the Frank-Oseen energy should obey some conditions. First, it should account for the symmetry of the

system **p** = -**p**. Second, terms linear in ∇**p** vanish and only terms that are invariant by rotation stay. Given these considerations, the Frank-Oseen energy density reads:

$$f_d = \frac{1}{2} K_s (\nabla \cdot \boldsymbol{p})^2 + \frac{1}{2} K_t (\boldsymbol{p} \cdot \nabla \times \boldsymbol{p})^2 + \frac{1}{2} K_b (\boldsymbol{p} \times \nabla \times \boldsymbol{p})^2 \quad (1.1.)$$

The Frank constants K_s, K_b and K_t are associated with the three possible types of deformations of the director, respectively splay, bend and twist (Fig. 1 – 15B). These constants are necessarily positive in order for the energy to reach a minimum. They have the unit of a force. For simplifications, it is usual to make the so-called "one constant approximation" where all Frank constants are equal to K. Thus the free energy density reads:

$$f_d = \frac{1}{2} K [(\nabla \cdot \boldsymbol{p})^2 + (\nabla \times \boldsymbol{p})^2] \quad (1.2.)$$

Topological defects

We have presented so far smooth distortions of the director field. However, localized variations of the director can appear in the liquid crystal. These regions are called disclinations or topological defects. They are characterized by monitoring the total angle change Ω of the director when a line surrounding the defect is followed in the trigonometric direction, so that Ω = 2πm. They are characterized by a topological charge m that is an integer or a half-integer. For nematics, ±1 defects are not stable and only ±1/2 defects can be observed (Fig. 1 – 15C).

2. 2. 2. Fréedericksz transition in passive liquid crystals

Molecular field

The equilibrium state of the nematic director in bulk is the result of a minimization of the distortion energy $F_d = \int f_d d\boldsymbol{r}$. Small variations of this energy should be null, so that we can

apply the Euler-Lagrange theorem that gives $\delta F_d = \int h_\beta \delta p_\beta d\boldsymbol{r}$ where δp_β is a small variation of the director field and the Lagrange multiplier h_β is the *molecular field* given by

$$h_\beta \equiv \frac{-\partial F_d}{\partial p_\beta} + \partial_\alpha \left(\frac{\partial F_d}{\partial (\partial_\alpha p_\beta)} \right) = -A(\boldsymbol{r}) p_\beta \quad (1.\ 3.)$$

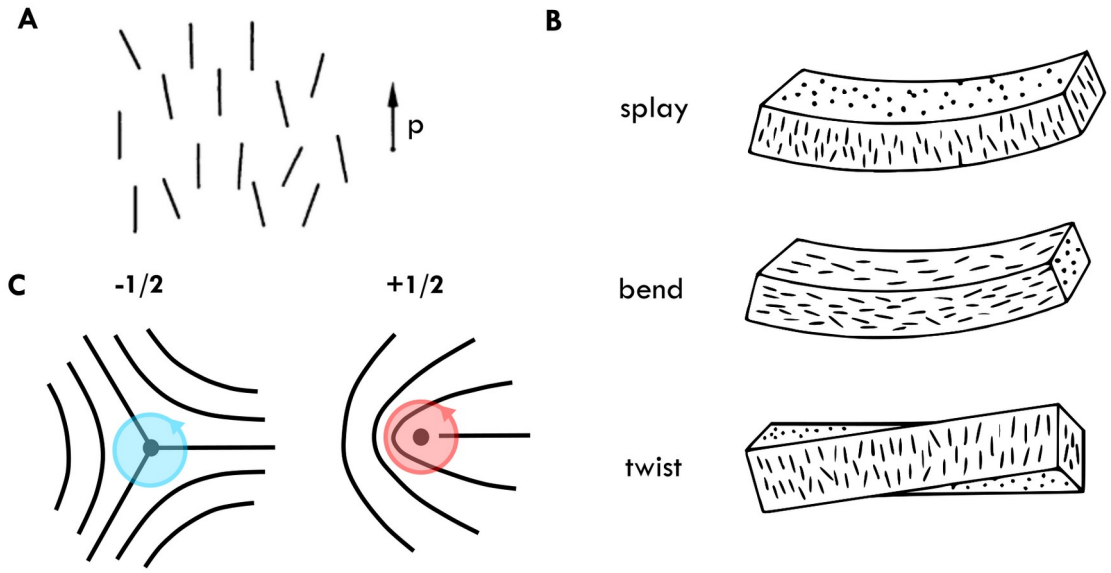

Figure 1 – 15. Passive nematics. (**A**) Nematic liquid crystals are characterized by no long-range positional order but a long-range alignment described by a director **p**. (**B**) Three possible distortions of the nematic phase, here the "perfect" cases are schematized: splay, bend and twist. Adapted from [1]. (**C**) Two possible stable topological defects in nematic phases: -1/2 and +1/2. Black lines represent the direction of orientation of the molecules.

The consequence of this expression is that at equilibrium, the nematic director must follow the molecular field in order to minimize the energy of the system. For the one-constant approximation, injecting (1. 2.) into (1. 3.) gives a simpler expression of the molecular field

$$\boldsymbol{h} = K \nabla^2 \boldsymbol{p} = h_\perp \boldsymbol{p} + h_\parallel \boldsymbol{p} \quad (1.\ 4.)$$

In two dimensions, this expression reduces as parallel and perpendicular contributions with the director **p**. Parallel contribution $h_\parallel$ is not useful for our purpose being only a scaling factor of the nematic director ($p^2 = 1$). However, equation (1. 3.) shows that for an equilibrium molecular field, a small distortion alters the free energy. Thus, all deviations from the equilibrium state are included in the perpendicular contribution of the molecular field $h_\perp$. This is in particular the case for deviations

caused by activity. If we note θ the angle between the director and the horizontal direction (x-axis), we can write

$$h_{\perp} = K \nabla^2 \theta \quad (1.5.)$$

Applied magnetic field

Boundaries can orient nematic phases. The direction of orientation at the boundary is called the *easy direction*. This can be a crystallographic axis if the substrate is a crystal or the direction of abrasion of a glass substrate. Unlike a conventional fluid, if a nematic fills the space between two substrates of different easy directions, it can transmit torques. This means a restoring force is created in the fluid and the state of the nematic director is a balance between these forces.

Some nematics are diamagnetic meaning that we can apply an external magnetic field **H** to orient the molecules in the direction of the field in the bulk. The applied magnetic torque then depends on the magnetic susceptibility χ of the liquid crystal, and adds a magnetic contribution h_M to the molecular field

$$\boldsymbol{h_M} = \chi (\boldsymbol{p} \cdot \boldsymbol{H}) \boldsymbol{H} \quad (1.6.)$$

When surface torques and magnetic torques compete in aligning nematic particles, one can show by minimizing the free energy of the system that the effect of the boundary vanishes exponentially away from the surface. The transition in orientation occurs over a distance ξ called the *magnetic coherence length*

$$\xi = \sqrt{\frac{K}{\chi H^2}} \quad (1.7.)$$

Fréedericksz transition

We now consider a liquid crystal between two parallel plates separated by a distance L where we apply a transverse magnetic field **H** (Fig. 1 – 16A). In this calculation, we consider that the easy axis is along the plate surfaces and that the applied field is normal to them. The Fréedericksz transition is the transition from the "aligned state", where the nematic director aligns everywhere

with the easy axis, to the "distorted state" where the magnetic field distorts the director in the bulk. It is a balance between the surface and the magnetic torques. The transition occurs at a critical field that can be calculated by considering a variation of the aligned state $p = p_0 + \delta p$. The perturbation can be analyzed in Fourier series, so that

$$\delta \boldsymbol{p} = \sum_q \delta p_q \sin(qz) \quad where \quad q = m\frac{\pi}{L}, \quad m \in \mathbb{N} \quad (1.\ 8.)$$

Given the expression of the Frank-Oseen energy (1. 1.) and the magnetic energy derived from (1. 6.), the free energy of the system reads

$$f = d(f_d + f_M) = \frac{L}{4}\sum_q \delta p_q^2 (Kq^2 - \chi H^2) \quad (1.\ 9.)$$

This free energy should be positive for the aligned state to be stable. Given this condition, we can calculate the critical field for the first distortion mode (m = 1)

$$H_c = \frac{\pi}{L}\sqrt{\left(\frac{K}{\chi}\right)} \quad (1.\ 10.)$$

The distorted state will appear for a critical field H_c and the coherence length will be L/π[k]. This transition can be monitored by measuring the angle $\theta(0)$ at the mid plane of the two plates (Fig. 1 – 16B). It is a second-order transition since there is no discontinuity of the angle in the vicinity of the transition. It is found that $\theta(0) \propto \sqrt{(H - H_c)}$ at a given width or that $\theta(0) \propto \sqrt{(L - L_c)}$ for a given field.

Symmetry of the solutions and "pincement" phenomenon

We develop equations (1. 2.), (1. 4.) and (1. 6.) for the system described previously and represented in Fig. 1 – 16. The equation for the orientation of the nematic director orientation θ in such 2D system is given by [158]

$$\xi^2 \frac{\partial^2 \theta}{\partial x^2} + \frac{1}{2}\sin 2\theta = 0 \quad (1.\ 11.)$$

where ξ is the magnetic coherence length given in equation (1. 7.).

k The Fréedericksz transition can also be observed with a constant magnetic field and variable distance between the plates. This is the original system used by Fréedericksz to describe the phenomenon in 1927 [143].

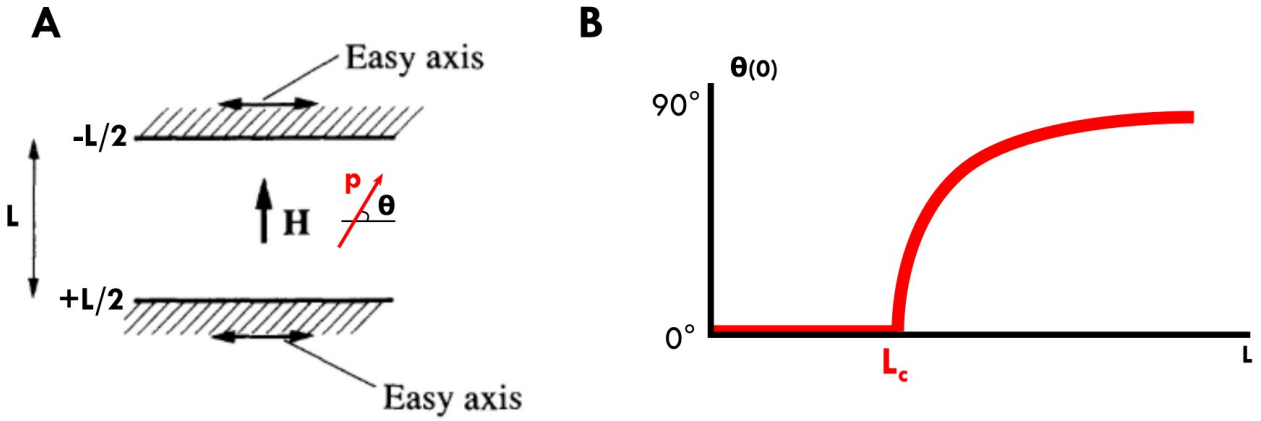

Figure 1 – 16. Fréedericksz transition. (**A**) Schematics of the system used to observe the Fréedericksz transition. The nematic phase is placed between two plates separated by a distance L. A magnetic field **H** is applied perpendicularly to the plates surfaces. Here, the easy axis is parallel to the plates surfaces. (**B**) Nematic director angle in the midplane between the two plates depending on the external field strength. An increasing width L will cause the nematic phase to distort above a critical width L_c. If $L < L_c$, torques applied by the surfaces are strong enough to keep the nematic director unchanged.

Integrating this equation, the general analytical solution for the Fréedericksz transition reads

$$\frac{1}{2}L = \xi\, K_{elliptic}(\sin\theta_{max}) \quad (1.12.)$$

where $K_{elliptic}$ is the complete elliptic integral of first kind [159] and θ_{max} is the maximal angle distortion of the nematic director that can be observed midway between the two plates. $K_{elliptic}$ being an even function, the nematic symmetry of the solution is respected. Moreover, two mirror solutions of the director field are possible (Fig. 1 – 17A): in the (+) configuration (respectively (-)), the director goes from 0° to θ_{max} (respectively $-\theta_{max}$) from the plate edge towards the middle. The two solutions depicted in Fig. 1 – 17A are equally probable.

These distortions occur within domains of orientation between the two plates. If the magnetic field is perfectly oriented perpendicular to the plates, these domains will be equally distributed. The regions between two domains (+) and (-) are called "walls". Interestingly, as the field increases, these walls become thinner and eventually separate into a pair of ±1/2 defects (Fig. 1 – 17B) in a transition called a "pincement" [160].

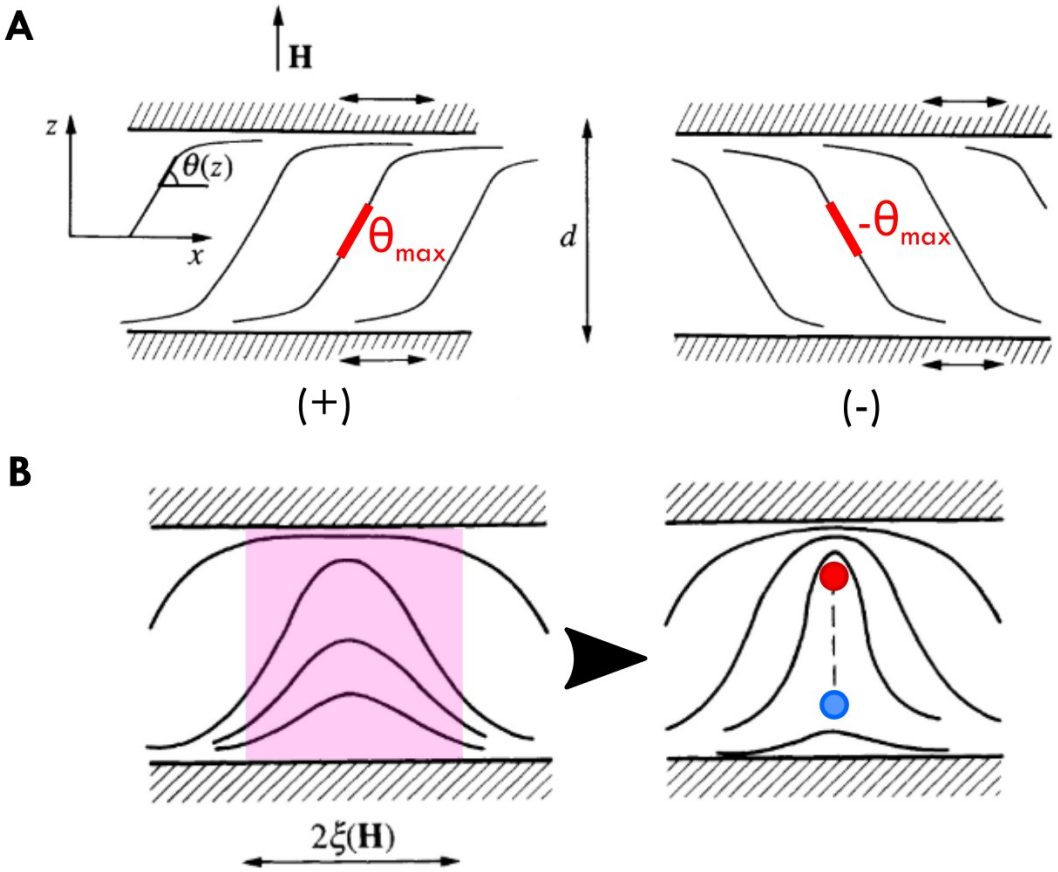

Figure 1 – 17. "Pincement" phenomenon. (**A**) Two possible states of distortion of the nematic director during the Fréedericksz transition. The easy axis is parallel to the plates and a perpendicular magnetic field H is applied. Adapted from [160] (**B**) The two distortion states are separated by "walls" (in pink). If the field **H** is strong enough, walls can break into a pair of +1/2 (red) and -1/2 (blue) defects. Adapted from [1]. The direction of the director is represented by black lines.

This passive description of nematics provides a good description of systems that contain elongated particles or molecules. However since the cells used in the present thesis are out of equilibrium, their activity has to be included in the description.

2. 2. 3. Hydrodynamic model: active gel theory

The theory of active gels was first used to describe gels of proteins and molecular motors that consume ATP to produce forces or displacements. However, since the symmetries are similar, this theory can also be applied to tissues. We will refer to the system as a gel. Compared to the passive case, an active term has to be added. The present description is based on the review of Marchetti et

al. [156]. Calculations are beyond the scope of this introduction. So we only describe the approach of the theory and give the main results.

Activity creates entropy

We first consider the system at thermal equilibrium with no heat exchange. The Onsager approach builds a thermodynamic out-of-equilibrium model based on the entropy production rate $T\dot{S}$ of the system. Part of the entropy production comes from passive features of the system such as density ρ and polarization **p**. However, as our system contains living entities, we also have to take into account local injection of energy in the form of activity that converts chemical energy into mechanical energy. We note Δμ the energy consumed by one cell per nutrient molecule and r the reactive coefficient. Thus, the energy per unit volume associated to the activity of the system is -rΔμ. Taking into account all these elements and given conservation laws of density and momentum, the entropy production reads

$$T\dot{S} = \int_r dr\left[\sigma_{\alpha\beta} u_{\alpha\beta} + P_\alpha h_\alpha + r\Delta\mu\right] \quad (1.\ 13.)$$

In the terminology of Onsager, this entropy is written as the sum of "flux" times "force" terms (Table 1 – 4). In equation (1. 13.), the term $\sigma_{\alpha\beta} u_{\alpha\beta}$ is related to the hydrodynamics of the system: stresses and velocities. Note that the strain-rate tensor $u_{\alpha\beta}$ writes as $u_{\alpha\beta} = \frac{1}{2}(\partial_\alpha v_\beta + \partial_\beta v_\alpha)$. The term $P_\alpha h_\alpha$ is linked to the polarization and the nematic state of the system. The term $r\Delta\mu$ is the activity that we have described above. All these terms have a time-reversal signature that describes their change of sign when time is reversed.

Flux			Force	Time signature
Stress tensor	$\sigma_{\alpha\beta}$	$u_{\alpha\beta}$	Strain-rate tensor	-1
Comoving and corotational derivative of polarization	P_α	h_α	Molecular field	+1
Reaction rate of advancement	r	Δμ	Reaction energy consumption	+1

Table 1 – 4. Forces, fluxes and time symmetries of the quantities of the system.

Coupling coefficients and constitutive equations

In the Onsager approach, forces and fluxes are coupled close to the equilibrium. Given the laws of thermodynamics, the entropy production rate should be positive. Consequently, forces and fluxes couple with specific rules. Fluxes coupled with forces of the same time signature contribute to the entropy production, they are dissipative. In contrary, fluxes and forces with an opposite time signature are anti-coupled and do not contribute to the entropy production. They are reactive. These couplings between forces and fluxes and the corresponding coupling parameters are schematized in Fig. 1 – 18.

Classical coupling parameters already present in the passive nematohydrodynamic theory are the viscosity η, that converts stress into velocity, the rotational viscosity γ, that accounts for changes in polarization and the flow-alignement coefficient ν that expresses how stresses create a polarization change. The activity coefficient ζ arises from the activity of the system. The sign of this coefficient allows us to define two main classes of active systems: ζ negative corresponds to a contractile stress while a positive value gives rise to an extensile stress. The other active coefficient λ and ε are more difficult to understand physically. However, they are less important for our purpose and often included in an effective activity coefficient ζ^*.

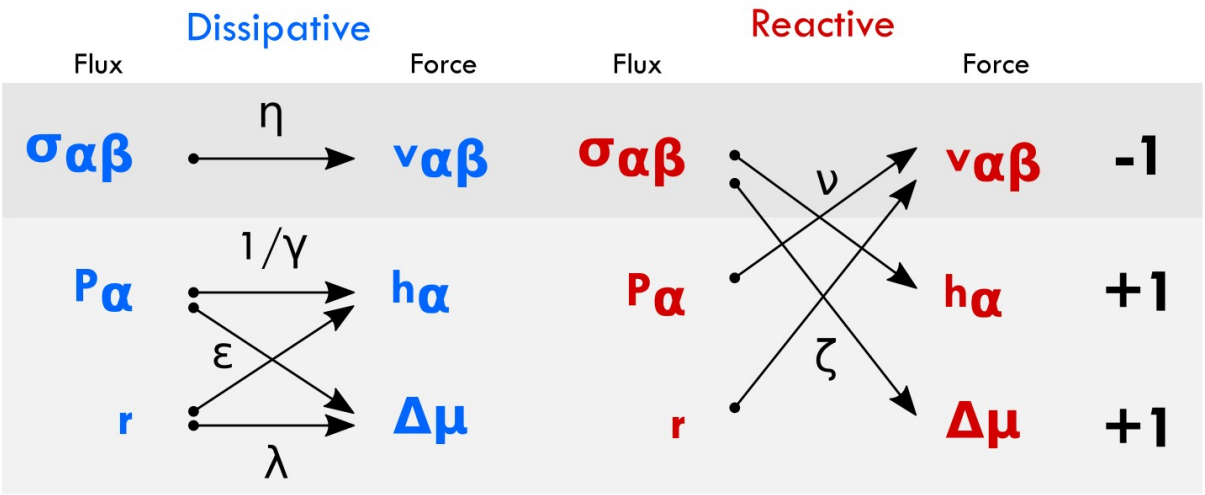

Figure 1 – 18. Coupling coefficient of "fluxes" and "forces" in the Onsager approach. Fluxes (on the left of schematics) are coupled with forces (on the right). Dissipative (respectively reactive) parts of fluxes are coupled between fluxes/forces of same (respectively opposite) time signature.

Using equations (1. 2.), (1. 13.) and developing all contributions, we can now write the constitutive equations for the active gel

$$\begin{aligned}\sigma_{\alpha\beta} &= \sigma_{\alpha\beta}^{passive} + \sigma_{\alpha\beta}^{active} \\ &= [2\eta u_{\alpha\beta} + \frac{\nu}{2}(p_\alpha h_\beta + p_\beta h_\alpha - \frac{2}{3} p_\gamma h_\gamma \delta_{\alpha\beta})] + [-\zeta \Delta\mu\, p_\alpha p_\beta]\end{aligned} \quad (1.\ 14.)$$

$$P_\alpha = \frac{h_\alpha}{\gamma} - \nu\, p_\beta u_{\alpha\beta} \quad (1.\ 15.)$$

The classical constitutive equations for flowing passive nematic phases are retrieved by these equations if the activity coefficient ζ is set to zero. The activity in the system arises only in equation (1. 14.) as an active stress. As explained before, this active stress comes from the local consumption of nutrients that is transformed into mechanical energy. Another consequence is that this activity distorts locally the orientation of the nematic director. As flows and polarization are coupled by equation (1. 15.), this results in local flows.

Altogether, these equations show that polarization, flows and activity are intimately coupled by coefficients (shear viscosity η, rotationnal viscosity γ, activity ζ, …) linked to intrinsic components of the system. On cells and more generally on any kind of active systems, it will be possible to tune the dynamic response by playing on these components, for example with drugs targeting actomyosin contractility, a proxy for activity, such as blebbistatin.

2. 3. Dynamics of active nematic phases

2. 3. 1. Flows and topological defects

In nematohydrodynamics, flows and polarity are strongly coupled. Adding activity in the system allows injection of energy that results in flows. This has a strong consequence: perfectly ordered active nematic phases are unstable in presence of fluctuations. For a system larger than the active length $l_a \propto \sqrt{(\frac{K}{|\zeta\Delta\mu|})}$, distortions of the nematic order are created and amplified. They ultimately lead to the formation of a pair of ±1/2 defects that move apart because of the system activity [161] (Fig. 1 – 19A). Flow dynamics are then closely related to activity and to the number of

defects [162–164]. Indeed, the theory of active gels shows that because of their particular shape, +1/2 defects self-propel and generate a pair of counter-rotating vortices on each side of their main axis. Motion of these defects then tend to "stir" the nematic phase. This results in a disordered state and even turbulent states in particular cases. Such turbulence of active nematics have been studied *in vitro* with HBEC cells [165]. Altogether, these disordered flowing nematic systems are under the control of activity. An increase in activity gives rise to more defects and more flows.

In the presence of friction, flows are damped over the friction length $l_f \propto \sqrt{(\frac{\eta}{\xi_f})}$ where ξ_f is a friction coefficient. Theoretical results and simulations show that tuning this parameter from low to high friction, allows the nematic to behave as "wet" where interactions are mediated by hydrodynamics to "dry" where flows are screened [166] (Fig. 1 – 19B). For "wet" states where friction is negligible, defects display swirls and creation/annihilation events described above. In this situation, the area of the vortices scale as l_a^2. For "dry" states where the friction length l_f is low, instabilities and flows are damped over distances so small that they cannot develop. When l_a and l_f become comparable, vortices and defects organize in lattices. Particular configurations of these ordered phases can lead to laning events where antiparallel streams coexist. Such laning phases have been observed *in vitro* in a microtubule/kinesin system [167] (Fig. 1 – 19C).

The interplay between activity and friction through defects is involved in tissue homeostasis of cellular active nematics. Experimentally, it was observed that Neural Progenitor Cells (NPC) accumulate at the tip of +1/2 defects, forming 3D mounds [168] (Fig. 1 – 19D). This is due to activity in the system: the counter-rotating vortices around the +1/2 defects create flows towards their core. However this observation alone is not sufficient to model the cell accumulation. Indeed if the friction is isotropic, the flows are symmetric on both sides of the defect and no accumulation can occur. However an anisotropic friction resulting from the cell shape gives rise to an asymmetric flow profile: cells flow to the front of the defect faster than they escape at its back, which results in cell accumulation at the core of the defect. For symmetry reasons, this cell accumulation is not possible for -1/2 defects which has been confirmed both with experiments and simulations. Complementary with these observations, measurements of traction forces in a system of MDCK cells show that +1/2 defects accumulate stresses at their core which ultimately leads to extrusion

and apoptosis [169]. Again, this observation was supported by an active gel model were +1/2 defects were shown to exert more compressive stresses at their core.

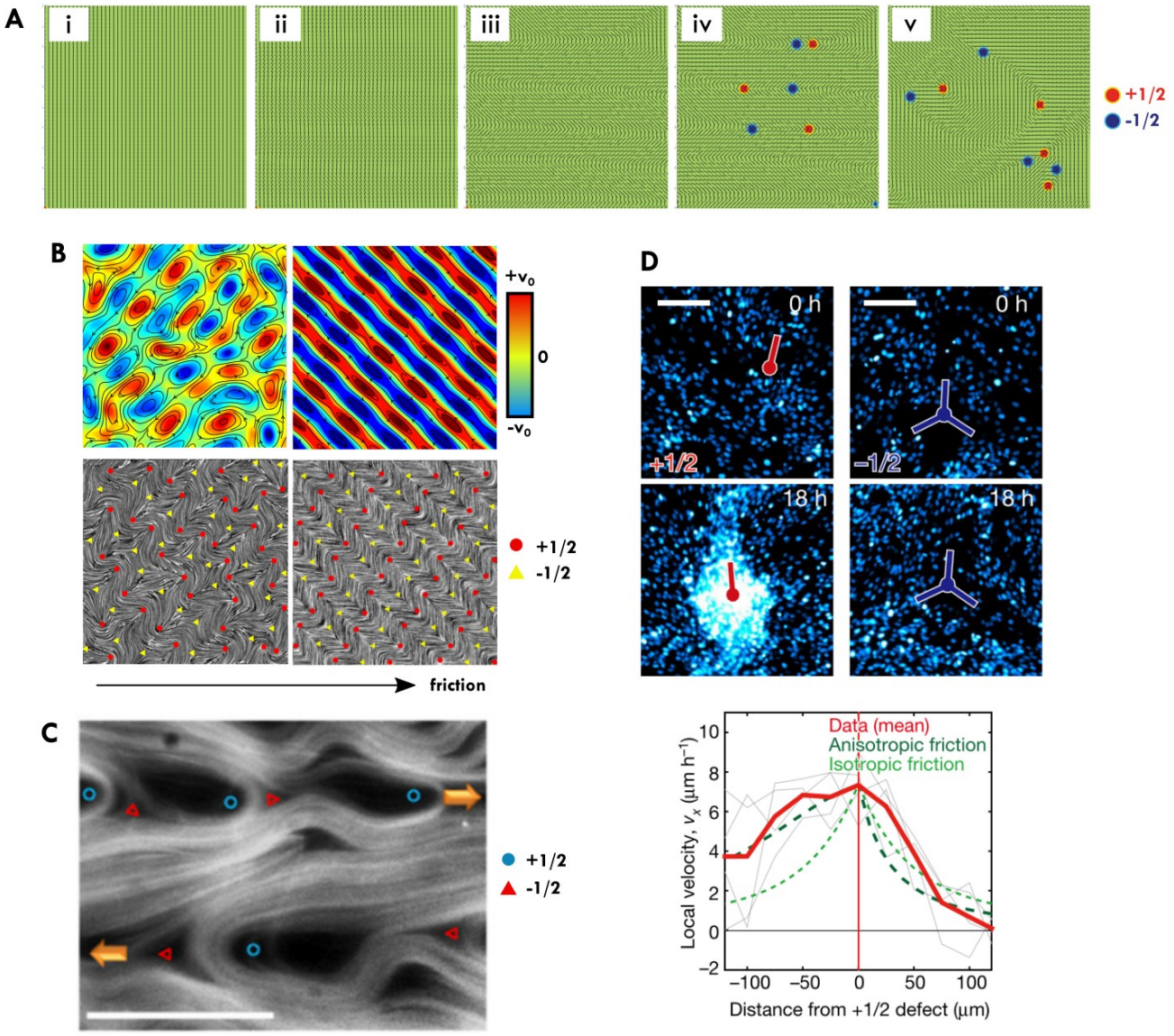

Figure 1 – 19. Dynamics of active nematic phases. (**A**) Simulated ordered active nematic phases spontaneously distort and create defect pairs [161]. From left to right: time evolution of the orientation field. Red: +1/2, blue: -1/2. (**B**) Defects create flows vortices damped by friction. By controlling friction in the system, it is possible to go from a state with disordered flows (left) to state with laning flows (right). Shown: simulations for increasing friction. Top: color codes for speed; black line: current lines. Bottom: nematic orientation shown in LIC; defects are shown by symbols. Adapted from [166] (**C**) Experimental observation of laning phases in a microtubule/kinesin system marked in fluorescence, showing ordered defects (symbols) [167]. Scale bars = 100 μm. (**D**) +1/2 defects tend to concentrate NPC cells at their tip. Nuclei are fluorescently labeled. Scale bar = 100 μm. Bottom: local velocity along the direction of a +1/2 defect. Data and model with anisotropic friction show an asymmetric velocity profile responsible for cell accumulation. Adapted from [168].

The existence of nematic spontaneous flows is therefore closely related to activity and friction and their corresponding lengthscales. A possible way to modulate these flows is therefore to confine the system into particular geometries that control the number of defects as well as their localization.

2. 3. 2. Confining in circular geometries

A circular geometry with a parallel anchoring condition at the boundaries imposes a +1 topological charge to the system. However, as mentioned earlier, in nematic phases, only ±1/2 defects are stable. The minimal defect configuration in disk geometry is thus two +1/2 defects. These disks then control the defects' distribution and therefore the cellular flows. Their spatial distribution depends on their activity and of the value of R_0, thus active nematics confined in disks can exhibit very different dynamics.

After seeding RPE1 cells on disks patterns of 250 to 400 μm radius R_0, initial ±1/2 defects annihilate by pairs leaving at confluence two facing +1/2 defects [170] (Fig. 1 – 20A). These defects sit on average at a given distance from the edges that results from a minimization of the Frank-Oseen energy. Experiments with other cells (C2C12, 3T3) or under drug treatment (blebbistatin) confirmed this is a passive-like effect even if cells are active. For C2C12 cells in such disks patterns, it is possible to observe signatures of activity by reducing the radius of the disk below l_a [171]. In this configuration, C2C12 cells display an orthoradial rotational velocity similar to what have been observed for MDCK cells (see I. 1. 2. 3.). As density increases, these flows lead to spiraling motions. For long experimental times, an aster configuration with a +1 defect is left at its center. This configuration favors radial flows towards the center. High compressive stresses have also been reported in the center of the disk. Similarly to what happens at the tip of +1/2 defects, this increases cell accumulation and extrusions. This phenomenon ultimately leads to the formation of a cell mound at the center of the disk (Fig. 1 – 20C).

Parameters such as activity in experimental disks systems can be difficult to control. However, simulations in such disks of given radius R_0 show that these systems can be driven in others dynamical states if activity is increased [172] (Fig. 1 – 20B). We described previously, "dipolar

state" where two facing defects were dynamically frozen because of the system symmetry and low activity. Increasing the activity allows a transition to a "circulating state" where the two defects rotate together around one big vortex in the center of the disk that breaks the symmetry. Ultimately, if activity is large enough, a "turbulent state" with multiple randomly distributed defects, similar to what exists in monolayers, can be reached.

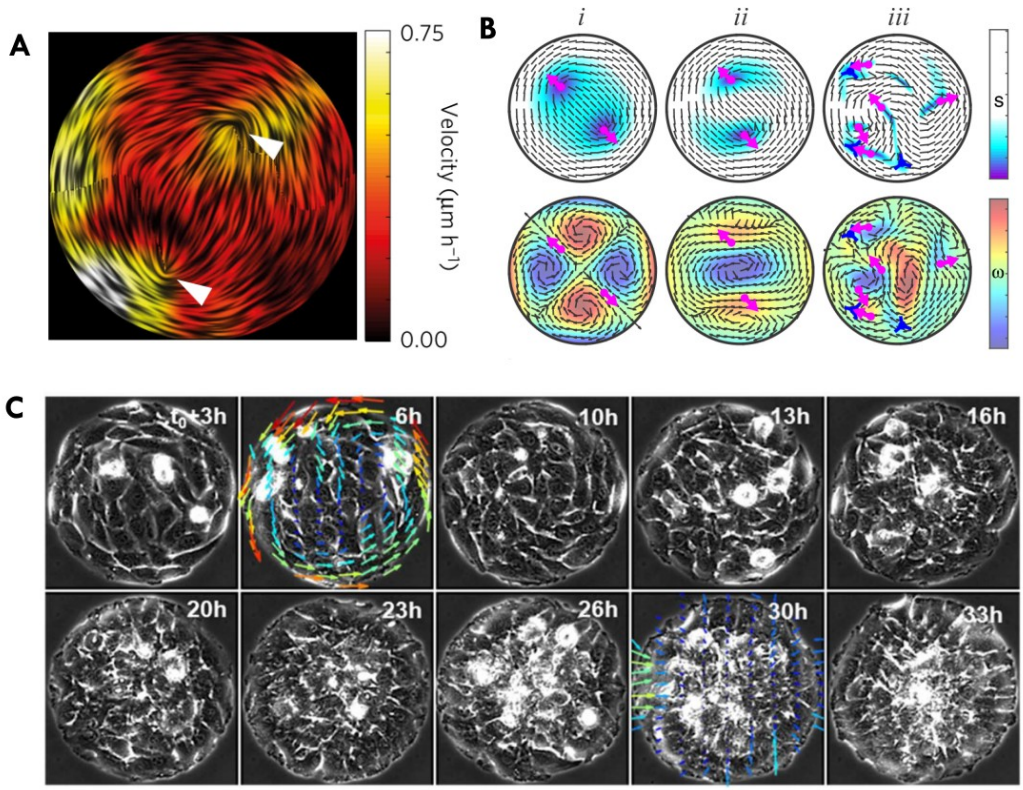

Figure 1 – 20. Cellular active nematics confined in disks. (**A**) Disk geometry imposes a +1 topological defect that splits in two +1/2 defects (white arrows) facing each other [170]. Disk diameter = 350 μm. (**B**) Hydrodynamic regime can be controlled by activity of the system. From low to high activity: (i) dipolar state with two facing +1/2 defects and four vortices (ii) circulating state with two rotating +1/2 defects and three vortices (iii) turbulent state with many defects and vortices [172]. (**C**) For small disk, spiraling monolayer will ultimately form an aster (+1 defect) by extruding a 3D mound [171]. Phase contrast images over time. Disk diameter = 100 μm.

The geometry of confinement in disks allows a control of the number and distribution of defects. However, these systems' geometry intrinsically impose a +1 charge, in order to study situations free of defects, one may consider infinite stripes of given width L.

2. 3. 3. Confining in stripe geometries

We consider here infinite stripes along a y-axis direction, of width L. Boundaries of the stripe are set to ±L/2 on a x-axis direction (Fig. 1 – 21A). The stripe width is the control parameter and all phenomena will be considered unidimensional across this width. For example, the orientation of 3T3 cells will depend on the stripe width [173] (Fig. 1 – 21B). For stripes larger than the correlation length of cells on flat substrates, nematic domains of random orientation separated by topological defects are observed. For thinner stripes with parallel anchoring condition, cells align together in the direction of stripes. This order arises from the edges and propagates toward the center of the stripe as density increases with time. In contrast, other types of cells develop a marked tilt with the stripe direction while keeping a perfect nematic order. This tilt can only be explained by cell activity [174].

Spontaneous shear flows of active cellular nematics in stripes

As we have seen, a gradient of orientation between the edges of the stripe and its middle promotes cellular shear flows. A theoretical study by Voituriez et al. [175] predicts a transition from a static nematic ordered state to a spontaneously flowing state presenting a tilt in orientation. We can write the equation for the total stress in the stripes σ^{t}_{xy} given equation (1. 14.) in 2D. The angle between the director **p** and the x-axis is noted θ. We considered also force balance in y-axis $\partial_x \sigma_{xy}=0$. The total stress then reads

$$\sigma^{t}_{xy}=0=\eta\,\partial_x v_y-\frac{\zeta\,\Delta\mu}{2}\sin 2\theta+\frac{\nu}{2}\left(h_{\parallel}\sin 2\theta+h_{\perp}\cos 2\theta\right)-\frac{h_{\perp}}{2} \quad (1.\ 16.)$$

Projection of P_α following the equation (1. 15.) on each axis, gives

$$0=\frac{h_{\parallel}}{\gamma}-\frac{\nu}{2}\partial_x v_y\sin 2\theta \quad ; \quad 0=\frac{h_{\perp}}{\gamma}-\frac{\partial_x v_y}{2}\left(\nu\cos 2\theta-1\right) \quad (1.\ 17.)$$

Gradient of velocity $\partial_x v_y$ and the parallel contribution of the molecular field $h_{\parallel}$ were eliminated. We considered a free-slip boundary condition so that $\sigma_{xy}(x=\pm L/2)=0$. Given the equation (1. 15.) for the perpendicular contribution of the molecular field, the evolution of the angle across the width of the stripe can be written as

$$\partial_x^2\theta=\frac{\zeta\,\Delta\mu\sin 2\theta\,(\nu\cos 2\theta-1)}{K\left(\frac{4\eta}{\gamma}+\nu^2-2\nu\cos 2\theta+1\right)}=\phi_0(\theta) \quad (1.18.)$$

This equation has no simple solutions for the angle θ. However, if we look at small perturbations of the angle θ' = π/2 - θ around the ordered state configuration, we can linearize the equation (1. 18.). Doing so sets a critical length L_c where the first mode of deformation is possible. The exact expression of L_c is given by

$$L_c^2=\frac{\pi^2 K\left(\frac{4\eta}{\gamma}+(\nu+1)^2\right)}{-2\zeta\,\Delta\mu(\nu+1)} \quad (1.19.)$$

We call this transition by analogy, an *active Fréedericksz transition*, the active molecular field playing here the role of the magnetic field. If the stripe width is smaller than L_c, anchoring effects dominate over active ones and the system does not flow. For widths larger than L_c, activity creates a gradient of orientation in the nematic order coupled with the appearance of shear flows (Fig 1 – 21A).

Further calculations in the linear domain allow to determine angle and shear flows in this system. Expression of the angle θ and the shear velocity v_y read

$$\theta=\frac{\pi}{2}+\theta_0\sqrt{\left(\frac{L-L_c}{L_c}\right)}\cos\left(\frac{\pi x}{L}\right)+O\left(\frac{L-L_c}{L_c}\right) \quad (1.20.)$$

$$v_y=\frac{2\theta_0\pi K}{L_c(\nu+1)\gamma}\sqrt{\left(\frac{L-L_c}{L_c}\right)}\sin\left(\frac{\pi x}{L_c}\right)+O\left(\frac{L-L_c}{L_c}\right) \quad (1.21.)$$

where $\theta_0=\pm 2\sqrt{\left(\frac{(\nu+1)\left(\frac{4\eta}{\gamma}+(\nu+1)^2\right)}{\frac{4\eta}{\gamma}(1+4\nu)+1+\nu^2(3+4\nu)}\right)}$ is a function of passive hydrodynamic coupling parameters η, γ and ν. Expression of θ and v_y then scales as $\sqrt{(L-L_c)}$ close to the transition.

The flow-alignment parameter ν

Independently of the nature of the system, the flow transition only occurs in the regime where $|\nu| > 1$, called the flow-aligning regime[1]. This result is the same for passive nematics that flow [1]. In particular, cells far from the boundaries of a large stripe should orient at an angle θ_L fixed by the flow-alignment parameter so that

$$\cos 2\theta_L = \frac{1}{\nu} \quad (1.\ 22.)$$

Cells orienting at this angle are not under the influence of hydrodynamic torques of the boundaries. It is possible to use this property to measure ν in passive nematic systems under Couette flows for example [176].

In our active system, there is a strong interplay between the flow-alignment parameter and activity. Looking at equation (1. 19.), the flowing state exists only if $\zeta(\nu + 1)$ is negative. Two cases are possible:

- if $\zeta < 0$ and $\nu > -1$: the system is contractile with disk-like particles. This means the director tends to align perpendicularly to the shear.

- if $\zeta > 0$ and $\nu < -1$: the system is extensile with rod-like particles. In this case the director aligns parallelly to the shear flows. We will be in this case for the rest of this thesis.

Recent theoretical studies emphasize the role of flow-alignment parameter ν in such active systems. This parameter should be considered together with activity ζ and friction ξ_f. For a given friction in stripes, the activity and the flow-alignment parameter set different flow regimes: no flows, turbulent flows or intermediate states where the nematic director distort periodically [177]. In the same line, when activity is high enough to generate flows, an increase of friction leads to the appearance of laning states in flow-aligning regimes only [178]. On flow-tumbling regimes, active nematic phases show the appearance of defects that lead to either turbulent states or uncommon states such as bounded defects pairs moving together in a given direction.

1 The regime where $|\nu| < 1$ is called a flow-tumbling state, where no alignment of the director is stable.

Experimental validation of the active Fréedericksz transition

While described theoretically fifteen years ago, the active Fréedericksz transition has been observed only recently by Duclos et al. [174] with C2C12 and RPE1 spindle-shaped cells on cell-adhesive stripes. Cell orientation and cellular flows were measured in the middle and at the edges of the stripes. By looking at the cellular angle in the middle of the stripes $\theta(x = 0)$ or the shear flow velocity $v_y(x = \pm L/2)$, the active Fréedericksz transition length L_c was measured to be 50 μm for RPE1 and 30 μm for C2C12 (Fig. 1 – 21C). Above the transition length, cells display an orientation gradient towards the center of the stripe and shear flows that decayed 40 μm from the edges. Experimental data also matched the theoretical scaling law of θ and v_y in $\sqrt{(L-L_c)}$. Contrary to C2C12 and RPE1 cells, 3T3 cells failed to produce flows at any width either because their activity is too low or the friction with the substrate is too large. Similarly, adding blebbistatin in the medium killed the shear flows because of reduced activity. Moreover, two unpredicted observations arise from the experiments. First, the angle tilt is always oriented in the same direction, emphasizing a chirality in this biological system. Secondly, significant convergent flows v_x towards the stripe center were measured, a feature not predicted by the theory. Their existence can be explained by the proliferation of the cells.

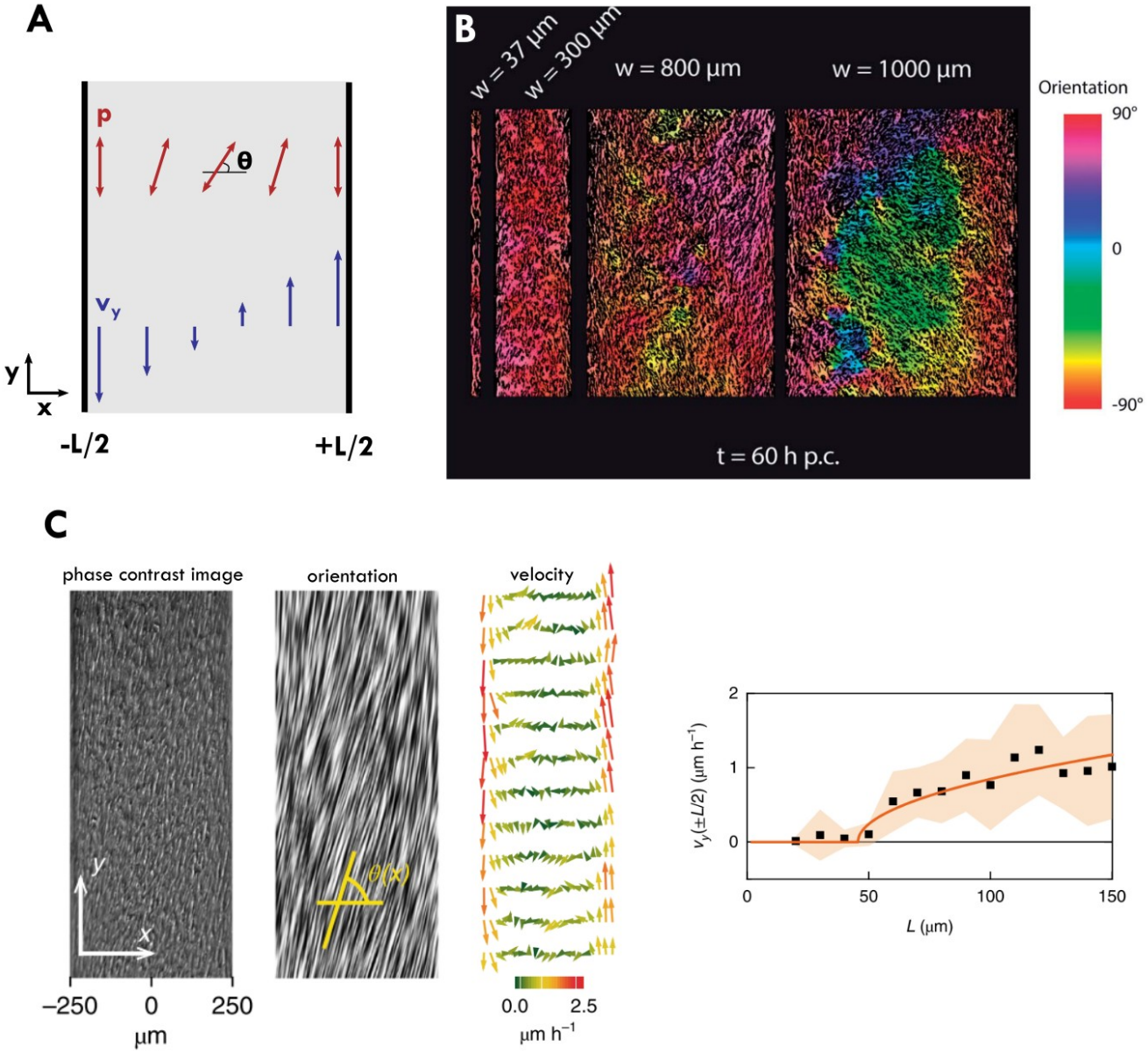

Figure 1 – 21. Cellular active nematics confined in stripes. (**A**) Schematics of the stripes confining active cellular nematics. Theory matches the experimental data of a spontaneous flow transition similar to an active Fréedericksz transition [175]. Red: cell orientation; blue: velocity in y-direction. (**B**) Phase-contrast images of 3T3 cells in chemically patterned stripes of given width. The nematic order is conserved if the stripe width is smaller than the cell correlation length [173]. Orientation is colorcoded. (**C**) Experimental validation of the theory of active Fréedericksz transition [174]. From left to right: phase contrast image of a RPE1 monolayer in a 500 µm wide stripe; LIC representation of the same stripe; cellular flows. Right panel: cell velocity at stripe edges for increasing stripe width, spontaneous flows appear for stripes 50 µm wide (black points). The transition in velocity is compatible with the predicted scaling law $v_y(\pm L/2) \propto \sqrt{(L - L_c)}$ (red line).

This study on active cellular nematics shows that cell collective motion can be controlled by geometrical conditions. In the case of C2C12 plated on stripes, shear flows would only appear for stripes wider than 30 μm. In this case, the mechanisms involved in collective migration of cells on similar mesoscales are well-known (I. 1. 2. 3.) as well as single cell migration on microtopographies (I. 1. 2. 2.). However, the mechanisms of collective motion on multiscales substrates have not been strongly studied yet (I. 1. 2. 4.).

In the present thesis we propose to study collective migration on such multiscale substrates (I. 2. 1.). More precisely, we use a simple *in vitro* model made of chemically patterned stripes, similar to Duclos et al. [174] but with the addition of perpendicular microabrasions. We use the results of passive nematic liquid crystals (I. 2. 2. 1.) and hydrodynamics of active cellular nematics (I. 2. 2. 3.) and compare them to our study to decipher the coupling between passive and active effects in our system in Chapter III. This work was performed in close collaboration with Louis Brézin and Jean-François Joanny that developed the theoretical models.

The competition between collective cell migration and contact guidance results in cellular self-organization which favors myogenic differentiation (I. 1. 3.). On multiscale substrates, the cells are well aligned and form oriented layers in three-dimension which is known to promote efficient differentiation. In Chapter IV. we discuss this approach in more details. The results are promising as we set a simple method to form physiologically relevant supracellular structures of myotubes, reminiscent of muscles fascicles. We hope this thesis finds echoes in the developing field of tissue engineering.

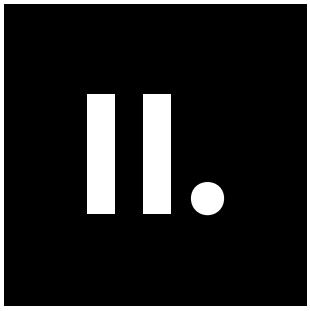

II. Material and methods

1. Cell culture

1. 1. Cell lines

We chose several "nematic" cell lines that have the particularity to be elongated when plated on an adhesive substrate such as glass or the plastic of cell culture flasks. Cells have a typical length of 50 μm and a width around 10 μm. We used the following immortalized cell lines, easy to culture:

- **C2C12**: subclone of the distrophic mouse (*mus musculus*) muscle cells isolated by Yaffe & Saxel [179]. They have low cell-cell adhesions, thus are able to easily pile up and form 3D structures. As explained in Chapter I. 1. 3., these cells can differentiate and fuse two-by-two when the monolayer is dense enough, resulting in the formation of long myotubes, the precursor of muscles. Note that the C2C12 cell line we used in our experiments characterizing nematic phases (Chapter III.) does not differentiate because of the large number of passages that have selected a proliferative phenotype.

- **NIH/3T3**: embryonic fibroblasts cells from the NIH Swiss mouse (*mus musculus*) [180]. These cells have the particularity to show high autologous contact inhibition. Still, they have an elongated shape suited for our active nematic experiment. They will be used as a control because of their poorly active behaviour.

We used either wild type (WT) or stable cell lines for which the actin is labeled with mCherry in order to avoid imaging abrasions in phase contrast. The C2C12 cell line has been modified by the Curie BMBC platform using Crispr technique thanks to Aude Battistella and Fanny Cayrac. The other cells were already present in our stocks before the beginning of this thesis and already used in previous studies of the team [173,174]: 3T3 from Karine Laud-Duval (Inserm – U830).

We cultured all our cells in Dulbecco's Modified Eagle's Medium (DMEM) supplemented with 10% of Foetal Bovine Serum (FBS) and 1% of penicillin/streptomycin antibiotics. Cells were incubated at 37°C, 5% CO2 and 90% humidity controlled environments.

1. 2. Drugs

Several drugs were used to perturb the system. If not precised, the drug was added before the video timelapse was taken. To add the drug, 1 mL of the culture medium was collected, mixed well with the correct amount of drug then added back in the culture medium. This way we ensure the drug is homogeneously mixed in the medium. Drugs we used:

- para,nitro-blebbistatin (Cayman Chemical): an inhibitor of myosin II that reduces cell contracility and activity. We used this drug in the range 1 μM to 5 μM on C2C12 cells. We used thus a non-phototoxic drug rather than the classical blebbistatin [181] because the cells were exposed to light for several days in our experiments.

- Y27632 (Sigma-Aldrich): an inhibitor or the ROCK pathway that also affects the cell contractility. We used a concentration of 10 μM.

1. 3. C2C12 differentiation

We used differentiation protocols that can be found in the literature (see Chapter I. 1. 3. 2. for references) on our C2C12 cells. Discussion and details on the exact protocol can be found in Chapter IV. 2. 1. Here we present briefly how we differentiate C2C12 into myotubes (Fig. 2 – 1). First, we made sure we used cells with very low passage number, less than 20, that were more likely to express myoD and differentiate further. Before seeding the cells, we incubated laminin (1 – 2 mg/mL) 1:100 in PBS at 37°C for at least 4h on the patterned glass substrates. Then we plated C2C12 cells at low density and incubated them in proliferation medium (DMEM + 10% FBS with penicillin/streptomycin). After several days (typically 2 – 3 days), once the confluence was about 60-70%, we changed the medium to differentiation medium (DMEM + 2% HS + 1% ITS with penicillin/streptomycin). We renewed the differentiation medium every two days.

After two to three days, differentiated cells start to appear. In phase-contrast microscopy, they are often formed on top of undifferentiated cells and appeared bigger and more elongated. At four days, fused multinucleated myotubes are clearly visible. These structures keep growing in

length during the next days. We always stopped our experiment the fifth day after changing to differentiation medium. Ultimately, we fixed and stained the cells.

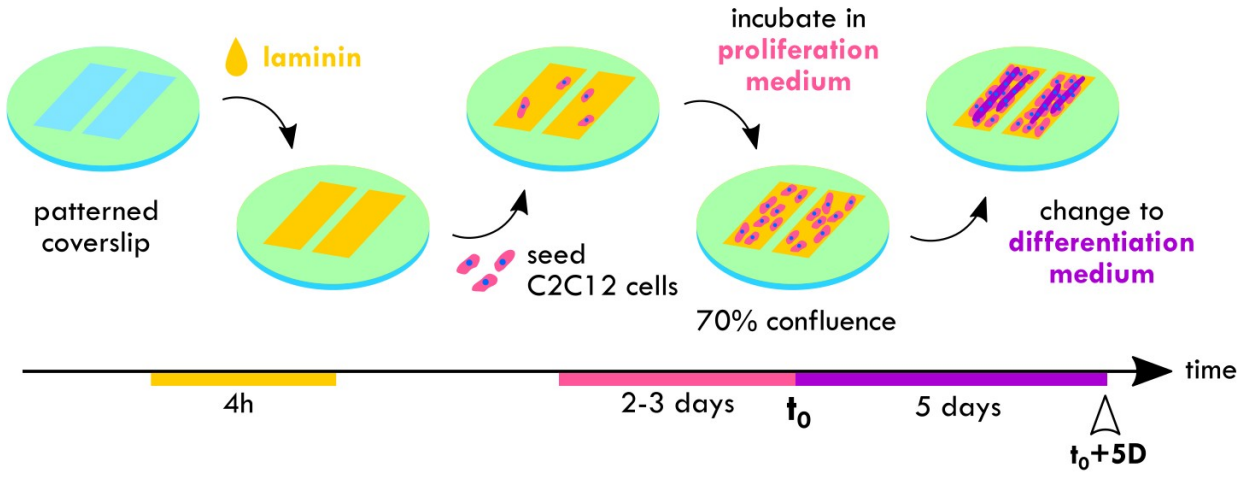

Figure 2 – 1. Protocol for C2C12 differentiation. We coat the coverslips with laminin (1 – 2 mg/mL) 1:100 for 4h at 37°C. Then we seed the C2C12 cells and let them proliferate in proliferation medium (DMEM + 10% FBS + penicillin/streptomycin). After several days, when cells reach 70% confluence, we switch to differentiation medium (DMEM + 2% HS + 1% ITS + penicillin/streptomycin). We fix and stain our samples for observation after 5 days (white arrow).

1. 4. Immunostaining

For observation of specific proteins in fixed cells, we stained the proteins of interest with fluorescent dyes coupled with antibodies. More details of the immunostaining protocol can be found in Appendix A. 1. We first fixed the samples with 4% PFA for 15 min. Then we permeabilized the cell membrane with Triton x100 0.1% for 20 min. We saturated the antibody binding sites with a saturation solution of PBS + 2.5% NGS added with 0.1% BSA for 45 min. We added the primary antibody in saturation solution to our samples and let them incubate at least 2h at room temperature or overnight at 4°C. We then added the secondary fluorescent antibody for 30 min. Nuclei were labeled with DAPI 1:1000 for 15 min. All these steps were separated by 3x5 min washing steps in PBS.

To observe myotubes we stained specifically Myosin Heavy Chain (MHC) that is the myosin II domain that binds to sarcomeric actin. Typical dilutions for the antibodies we used are 1:50 for

the MF20 primary antibody (DSHB) against MHC and 1:500 for the secondary antibody, more often Alexa 546 goat-anti-mouse (Thermo Fisher Scientific).

2. Substrates

We aimed at producing substrates where two guiding geometrical cues of different lengthscales compete to orient cells. To do so, we chose to microabrade glass surfaces along a given direction and chemically pattern cell-adhesive mesoscale stripes at a controlled angle with the microabrasions. Here we present the methods used to produce these multiscale substrates.

2. 1. Surface abrasions

To combine chemically patterned stripes with microtopography, we initially considered to use classical soft lithography techniques. However, as this patterning required chemical processes, we needed substrates able to withstand chemical treatment. Because we used organic solvents, this excluded all the main polymers used in soft lithography. We also could have used glass etching, however this technique while feasible at micrometer scale [141], requires an optimization of the etching process and special chemistry. We decided to use a "poor-man" method by making abrasions on a glass surface with sandpaper, a method already used in the literature for studying contact guidance of cardiac cells [52,53]. This method is compatible with our chemical patterns.

Coverslips were unidirectionnaly abraded over a sandpaper of controlled grain size (Fig. 2 – 2). To do so, we applied pressure on the coverslip while doing back-and-forth movements over the sandpaper. At first, we did the abrasions manually. However, this method was poorly reproducible and did not allow us to control the size and depth of our microabrasions. To achieve more control and reproducibility in our experiments, we designed a device with the help of Eric Nicoleau of the workshop of Institut Curie. More details on the device design and how we fine tuned the parameters for making controlled microabrasions are discussed in Chapter III. 1. The main parameters that controlled the abrasions' lengthscales were the applied pressure, the sandpaper

grain size and the number of passages of the sandpaper over the coverslip surface. This led us to the protocol described in Appendix A. 2.

Briefly, the device is composed of a horizontal rail that guides a cart in making unidirectionnal motion. This cart is itself on a vertical rail perpendicular to the horizontal rail to ensure perfect alignment between the surface of the horizontal rail and the bottom of the cart. The cart can be loaded with weights to change the pressure that is applied to the coverslip. We glued the sandpaper on the horizontal rail surface. The glass coverlip was glued to the bottom of the cart. We put the sandpaper and the coverslip in contact and made back-and-forth motion that abraded the coverslips unidirectionnaly. With this protocol, we ensured the topography of the abrasions was reproducible. We also checked the topographical features using a mechanical profilometer. For the conditions we used, a $4.2 \cdot 10^4$ Pa applied pressure and 100 passages, abrasions were on average 200 nm deep with interabrasion distance ranging from millimeters to hundreds of micrometers.

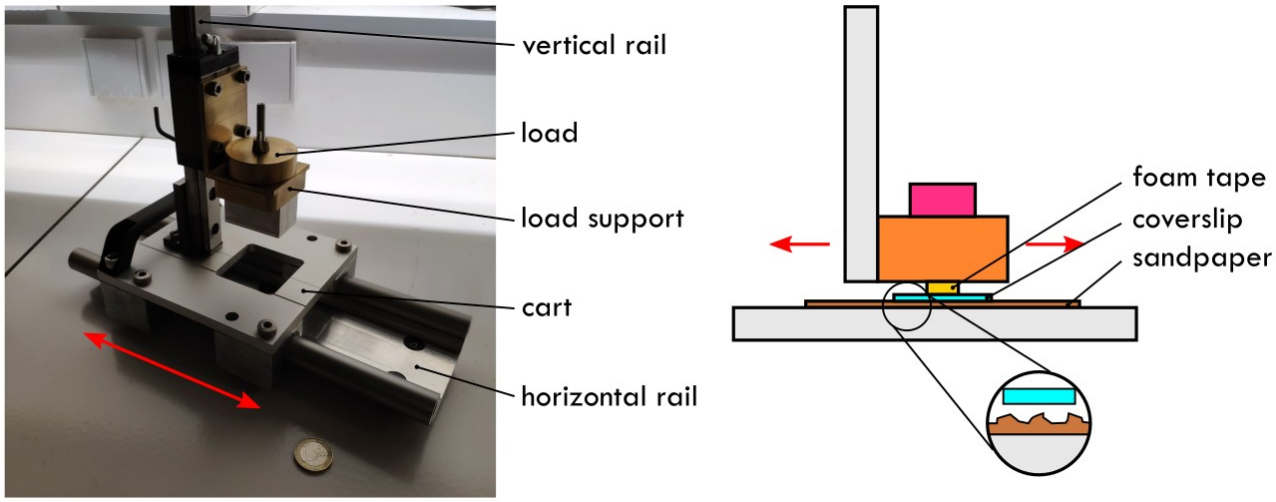

Figure 2 – 2. Principle of surface abrasions with sandpaper. The device for making microabrasions (left) is made of a horizontal rail guiding a cart in back-and-forth motions. The coverslip is glued under a load placed on the cart. The cart is attached to a vertical rail to achieve perfect alignment between the coverslip and the bottom of the horizontal rail were sandpaper is attached (right). Back-and-forth motions between contacting glass coverlip and sandpaper creates the microabrasions. 1€ coin for scale.

2. 2. Micropatterning

We chemically patterned glass surfaces after abrasions so that cells adhere only on the stripes we wanted to impose (Fig. 2 – 3). As our experiments take several days, we needed a robust surface chemistry that is not altered by the cells. We used an optimized protocol we routinely use in our lab based on a polyacrylamid/polyethyleneglycol polymer gel attached covalently to the glass [93,170,173,174,182,183]. The detailed protocol can be found in Appendix A. 3.

Briefly, we first cleaned the glass surfaces to remove impurities. Then we covalently attached allyltrichlorosilane to the silanol groups of the glass. An acrylamide layer was then attached to the silane. Finally a layer of PEG was grown on the acrylamide layer. Due to PEG chains, this coating is cell-repellent. To pattern these surfaces, we used photolithography. We first spincoated a layer of photoresist on the coated subtrates. Then we illuminated the resin through a mask with UV light, developed the resin so that it dissolved in the illuminated zones. We finally removed the unprotected PEG chains with air plasma and dissolved the remaining resist in acetone. This led to cell-adhesive glass surface patterns surrounded by a cell-repellent layer. The coating lasted for several weeks in culture conditions without being altered by the cells. These substrates could even be reused a few times for other experiments, in our case not more than twice. Interestingly, these patterns can be combined with our previously abraded substrates.

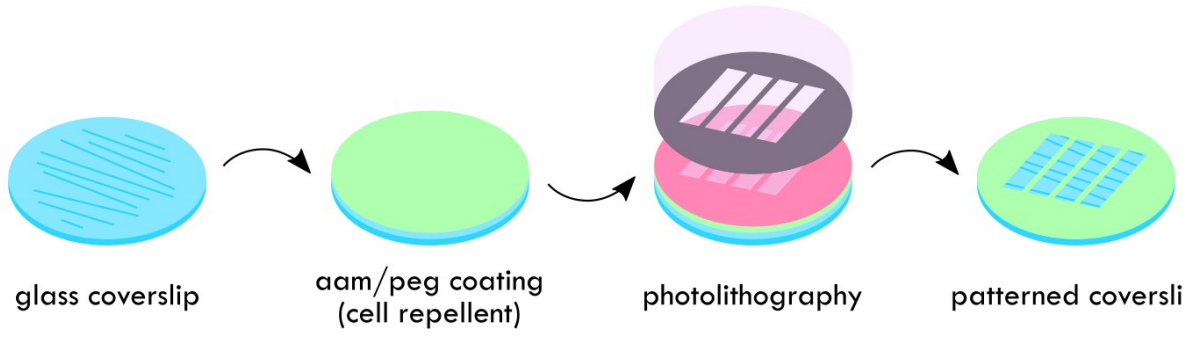

Figure 2 – 3. Mesocale patterning protocol of glass coverslips. A repellent layer made of aam/peg is coated then removed on zones illuminated by photolithography. Cell-adhesive glass is left on patterns, surrounded by the cell-repellent layer. Ultimately, glass can be coated with adhesion proteins like laminin.

3. Microscopy

3. 1. Timelapse microscopy

We used timelapse microscopy to image living cells. We acquired phase contrast images on an inverted microscope, either a Leica DM-IRB or an Olympus IX-71 equiped with an incubator (37°C, 5% CO2 and 90% humidity). We also made timelapse movies of fluorescently labeled cells with the same set-ups. We imaged our cells at 10x magnification every 15 min for several days. The experiments were computer-controlled using Metamorph software.

3. 2. Confocal microscopy

To get tridimensionnal images, we used confocal microscopy techniques to study our system so the focal plane can be displaced across the z-axis and "slices" can be made in the z-direction. There are two main kinds of confocal microscopes:

- In *laser scanning microscopes* (LSM), a laser excites a small volume of the sample through a pinhole, get the emitted light back and scans the whole sample. This technique has a high resolution in all directions. However due to the scanning process, this has two main drawbacks. First it is very time-consuming and only small FOVs can be imaged. Secondly, the high intensity of light can be phototoxic to the cells. For these reasons, this technique is well-suited for fixed samples.

- *Spinning-disk microscopes* have more or less the same principle as the LSM except there are many pinholes gathered in a rotating disk. This allows to image several volumes of the sample at the same time, thus a whole focal plane, by rotating the disk. These microscopes have a good temporal resolution at the expense of spatial resolution. They are then more suited to image living samples. The z-resolution is only fixed by the optical features of the system, for the wavelength and objective we used, this resolution was 0.46 μm.

We mostly used the Nikon spinning-disk of the PICT@BDD imaging platform to image large FOVs with good enough spatial resolution, in order to distinguish cellular layers. We used a 20x oil objective with large numerical aperture.

3. 3. Characteristics of used microscopes

This table gather all the characteristics of the microscopes we used during this thesis.

Microscope	Type	Camera	Objective	Size of FOV	pixel/µm
Olympus	Inverted microscope	Retiga 4000R	10x air	2048 x 2048	0.747
Leica	Inverted microscope	Retiga 6000	10x air	1379 x 1104 (bin 2)	0.918 (bin 2)
Nikon (PICT@BDD)	Spinning-disk	CoolSNAP HQ2	20x oil	1392 x 1040	0.322 (in XY)

Table 2 – 1. Microscope characteristics.

4. Image and data analysis

We explain here the main methods used for our data analysis. The main ideas of each method will be described in this part. However, more details on each algorithm or analysis could be found in corresponding parts indicated in the text. The codes used in this thesis are gathered on GitHub repository (https://github.com/taryaksama/multiscale-substrates).

4. 1. Cell orientation

We computed cellular orientation using the Fiji plugin named "OrientationJ" [184,185]. It is based on the computation of the structure tensor $J_{\alpha\beta}(x,y)=\int_{\sigma}\nabla_{\alpha}I\nabla_{\beta}I$, from the pixel intensity I on the specified gaussian window of size σ. We took σ = 30 pixels which corresponds approximately to a cell size. Once the structure tensor is computed, diagonalization of J gives two eigenvectors that point in the directions of maximal and minimal gradient of intensity and thus the direction of anisotropy. This is encoded on each pixel of a resulting image.

As we considered our stripe patterns infinite, we needed to have information on cell orientation across their width. We then computed orientation images with Matlab. The details of

this analysis can be found in Chapter III. 2. 1. and are illustrated in Fig. 2 – 4. Basically, we averaged angles comprised in a window of width dw = 32 pixels over the experiment time and over the long axis of stripes. This value of 32 pixels was taken because it is again approximately the size of a cell and also because the PIV algorithm uses windows of 32 pixels. We also used an overlap of 50% between consecutive subwindows. Note that because we measured angles, averaging the dataset was not trivial, for example, angles of 10° and 350° should fall in the same bin. This requires wrapping our data correctly. For that reason, we used the Circular Statistics Toolbox of Matlab [186] than contains all circular functions suited for our problem. More details on circular statistics and algorithms used for calculating average angles are present on Appendix B. and C.1.

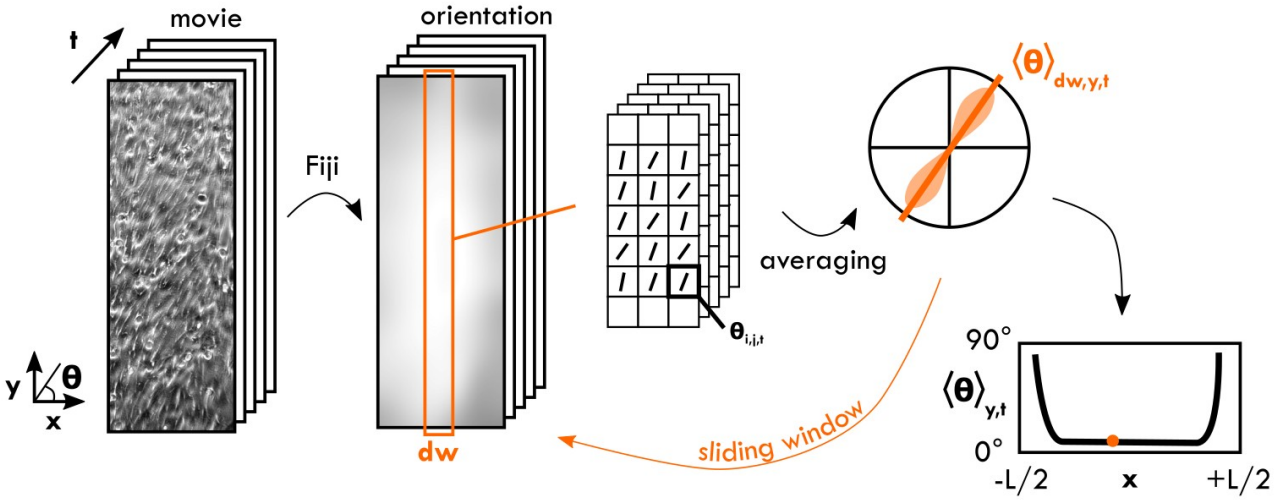

Figure 2 – 4. Schematics of orientation analysis algorithm. Cell orientation is calculated from the movies using the Fiji plugin "OrientationJ". Each pixel of the image is associated with an orientation. These orientations are averaged in time and y-direction within a sliding window of width dw = 32 pixels. This gives ultimately an average angle profile over the stripes width.

4. 2. Particle Image Velocimetry (PIV)

For the reasons described earlier, we did not track the displacement of every cell individually but we used a global approach. Indeed, density in our system was so high that we cannot track or even distinguish each cell. We mapped cell displacements in stripes using Particle Image Velocimetry (PIV), a technique well implemented in our group [88,187]. This coarse-grained approach gives results adapted to the mesoscale we are looking at. We used the Matlab plugin *matpiv* [188]. This technique

calculates the cross-correlation between consecutive subwindows of an image and computes the most probable displacements. Each subwindow has a given size, in our case, we used 32 pixels, the same as in orientation analysis. As explained before, we imaged our system every 15 minutes. Thus the analysis subwindow should be calibrated on the maximal cell displacement dw ~ $v_{max} \cdot dt$. Looking at images, between two time frames, cells do not move more than one cell length in a 15 minutes interval, so that we could set dw = 32 pixels[a]. Finally we set an overlap of 50% between consecutive subwindows. By recovering all the subwindows, we can retrieve a velocity map that was further analyzed with Matlab to extract features such as velocity profiles and velocity average values. More details on the analysis can be found in Chapter III. 2. 2. and are illustrated in Fig. 2 – 5.

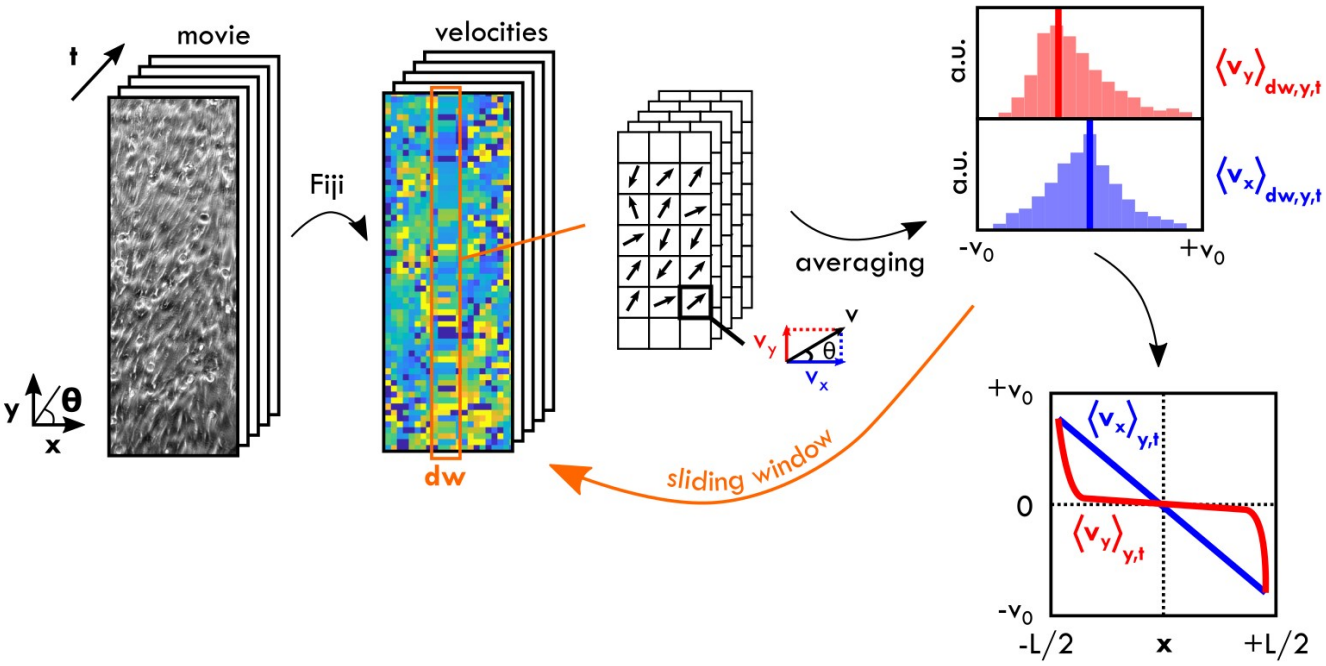

Figure 2 – 5. Schematics of orientation analysis algorithm. Cell speed is calculated from the movies using the Matlab plugin *matpiv*. Velocity vectors **v** are decomposed between their x-axis or y-axis component and treated separately. Norm of **v** is also calculated. Velocities are then averaged over time and y-direction in subwindows of width dw = 32 pixels. Ultimately, we computed the profiles of v_x and v_y over the stripes' widths.

a The size of the window should be a multiple of 2 for *matpiv* to run optimally.

4. 3. Topological defects

We detected and characterized the topological defects following the algorithm of DeCamp et al. [165,189]. More details on the algorithm we used can be found in Appendix C. 3. Briefly, the positions of defects were found by computing the local order parameter of the orientation $Q_{loc}=\sqrt{(\langle\cos 2\theta\rangle_\sigma^2+\langle\sin 2\theta\rangle_\sigma^2)}$ over a window of size σ = 30 pixels. Defects sit in the regions of low order parameter. Charge and orientation can be found by calculating the change of angle around the defect center in the trigonometric direction. This algorithm gives good results for mapping the defects' positions and charges. It allowed us to make statistics over hundreds of observations, a process that would be time-consuming if done manually.

4. 4. Myotube features

In the experiments described in Chapter IV. 2., we want to characterize the state of the differentiation process and the features of the myotubes. We followed manually the protocol illustrated in Fig. 2 – 6. After acquiring images of fixed cells with the spinning-disk microscope, we counted the number of nuclei within each stripes using the DAPI channel. Then, we characterized the features of the myotubes by drawing a mask around them with a graphic tablet and fitting them with an ellipse. The long-axis (resp. short-axis) of the ellipse gave the myotube length (resp. width). Finally, we counted the number of nuclei in each previously defined myotubes. All these steps were semi-automatized using Fiji macros.

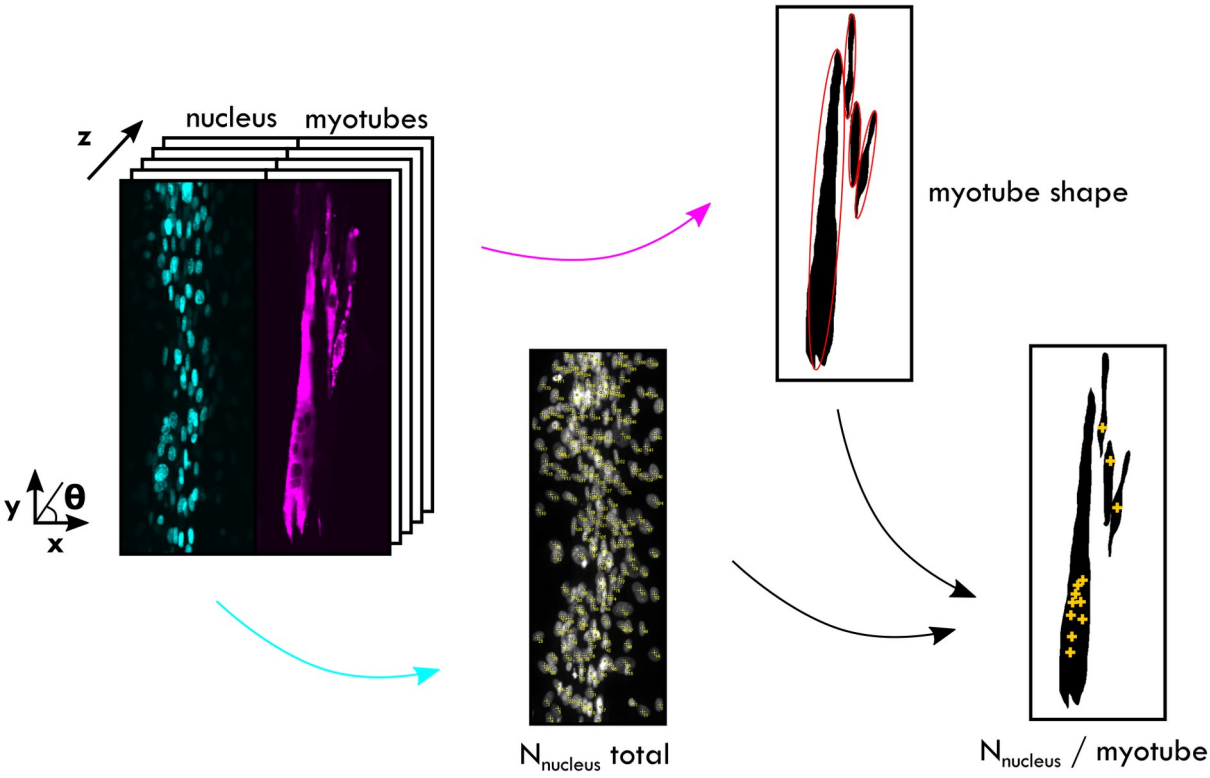

Figure 2 – 6. Myotube process of analysis. After spinning-disk images of myotubes (magenta) and nuclei (blue) were taken, cell nuclei were manually counted. The myotubes contours were hand-drawn with a graphic tablet to extract their long and short axis length via an ellipse fitting. Finally, the nuclei in each myotube were counted. All these parameters will be used in Chapter IV. 2.

5. Statistical analysis

5. 1. Active cellular nematics

For active cellular nematics on substrates with mesoscale stripes and miscroscale abrasions, experiments were performed in six or twelve well plates with different conditions for each well. Conditions could be different mesoscale stripes width, drug addition, … Experiments were reproduced at least twice for each condition and duplicates were made within the same experimental plate. Due to the variability in the observations, we had to average our datasets with a binning procedure. The detailed process can be found in Appendix C. 2. Briefly, the dataset comprising stripes with various widths, was binned according to stripes width. For example, all

stripes with widths ranging from 100 to 200 μm (then 200 to 300 μm, …) were grouped together. In each of these groups, we averaged measured quantities such as orientation or speed profiles.

5. 2. C2C12 differentiation in myotubes

For C2C12 differentiation into myotubes, experiments were reproduced for each conditions at least 2 times. To minimize biological variability, each set of conditions meant to be compared were seeded with C2C12 cells the same day. We tried to image at least 2 stripes per experimental plate. Each stripe is composed of several FOVs stitched together so that the stripe length (in y-direction) is at least 0.5 mm.

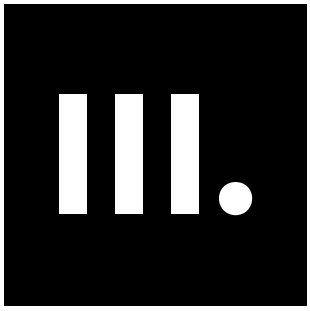

III. Controlling supracellular assemblies with multiscale geometrical constraints

In the present chapter, we study the competition between microabrasions modeled as an external field and mesoscale patterned stripes. Results of this study will be directly compared to the results of Duclos et al.[174] on non-abraded patterned stripes. We first describe the set up used to make reproducible microabrasions on glass substrates. Then we describe the transition in cell orientation for stripes of increasing width combined with microabrasions. We show that we can use these results to estimate the flow-alignment parameter ν of C2C12 nematics cells. Finally we discuss the topological defects occurrence and positioning in such systems.

1. Dynamic of monolayers on abraded substrates

1. 1. Abrasions

In the line of the work of Duclos et al., we wanted to combine chemically patterned stripes and microscale topography. However, as the chemical patterning required the use of organic solvents, we could not use the classical soft lithography techniques based on polymers such as PDMS, to make the microabrasions. We then decided to make the topography by directly abrading the glass substrates, a technique already used in several studies[52,53]. The principle is simple, we abraded glass coverslips with sandpaper following the protocol described in Chapter II. 2. 2 and Appendix A. 2. The first experimental protocol was set in the laboratory by Flora Ascione and improved during the course of this thesis. Here we focus on how we chose the optimal parameters used in the upcoming experiments of this chapter.

As a first attempt to make abraded substrates, we used coverslips that we pressed on the sandpaper manually then abraded in one direction. This method was not reproducible, mostly because of the unknown pressure applied with the finger. To cope with this issue, we designed a device together with Eric Nicoleau from the mechanical workshop of Institut Curie (Fig. 3 – 1). Three main requirements drove the design of the device. First, the glass coverslip should slide unidirectionally over the sandpaper. Second, the glass coverslip and the sandpaper should be as parallel as possible during abrasion. Third, we should be able to control the applied pressure. By

fulfilling all these requirements, we were able to make reproducible microabrasions on 20 mm diameter glass coverslips.

The device was composed of a horizontal rail (igus drylin® W) guiding a cart. The sandpaper was glued with double-sided tape at the bottom of the rail while the glass coverslip, glued under the cart, slided over it. A pressure was applied on the coverslip via a load that could be modulated. The coverslip was attached to the load via a soft foam tape pad (tesa® 4957) so that the load weight was evenly distributed over the coverslip surface. To ensure perfect alignment during the abrasion process, the load support was attached to a vertical rail perpendicular to the horizontal rail. The load support was able to slide on the vertical rail (NSK NH series) via a ball-bearing system (NSK NAH series) so that the load was supported by the coverslip.

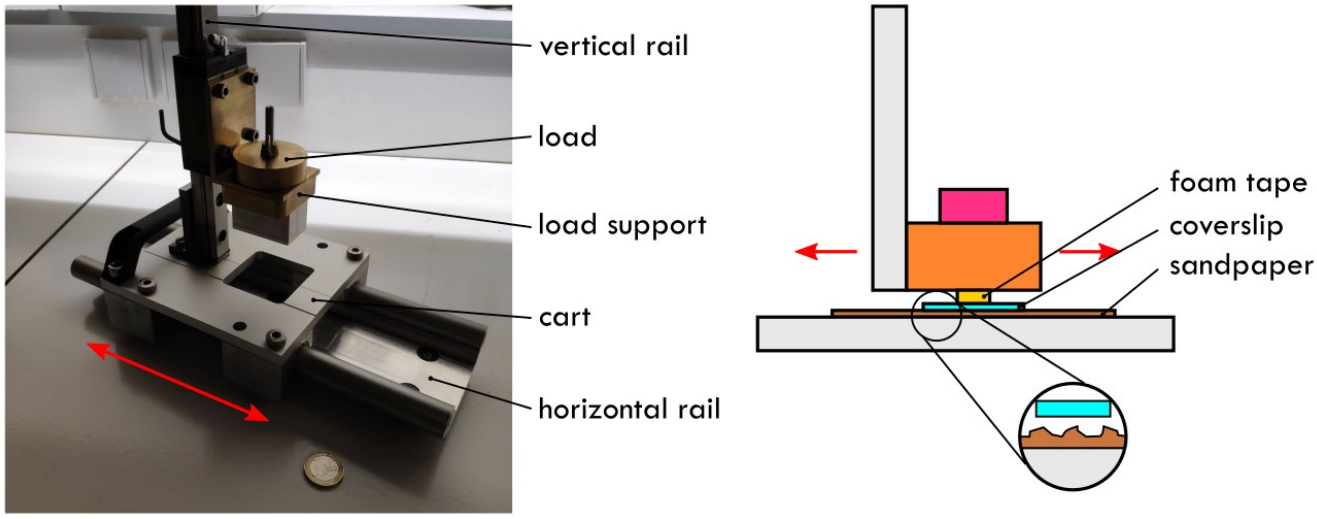

Figure 3 – 1. Abrasion machine. Picture of the abrasion device (left) and schematic in lateral view (right). Sandpaper is glued on the horizontal rail. Coverslip is glued via a foam tape under the load support, that can slide on a vertical rail with a ball-bearing system. A back-and-forth motion (red arrows) along the horizontal rail direction allows unidirectional abrasion of the coverslip. 1€ coin for scale.

We used well calibrated sandpaper (South Bay Tech) made from grains of silicon carbide (SiC), a material harder than glass. These sandpapers span several rugosities, denoted as "grit" that correspond to the mean particle size on the paper. Sandpapers with large particle size (grit 180, particle diameter 82 μm), made few big and deep abrasions that sometimes cut the coverslips. These abrasions were not evenly distributed and the resulting depth was inhomogeneous. In the contrary,

sandpapers with small particle size (grit 1000, particle diameter 10.3 µm) made very shallow abrasions. Finally, we chose an intermediate sandpaper grit 600, with average particle size of 16 µm that gave the best balance between abrasion depth and density (Fig. 3 – 2). Profilometer estimations gave us a rugosity of around 200 nm deep with a distribution of "peaks" interdistance ranging from millimeters up to tens of nanometers.

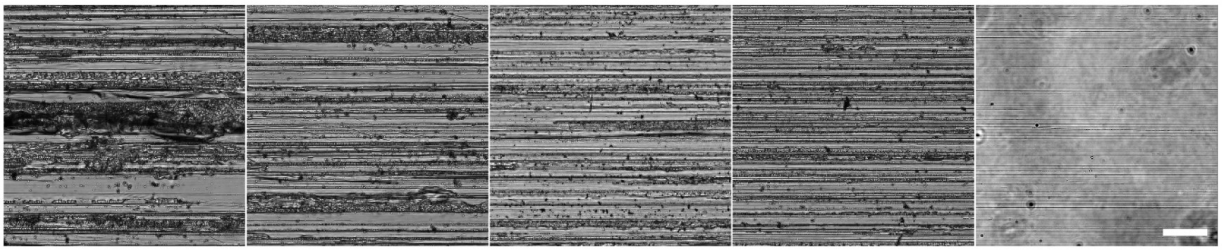

grit	180	240	320	600	1000
particule Ø (um)	82	53	36	16	10.3

Figure 3 – 2. Abrasions with respect to sandpaper grit. Phase-contrast images of glass surfaces abraded with sandpapers of different grits. Sandpapers with big particles create large and dispersed valleys while sandapers with small particles made few shallow abrasions. Sandpaper grit 600 gives the best microabrasions distribution and size. Glass coverslips were abraded under a pressure of 53 kPa, for 10 passages. Scale bar = 100 µm.

The size of the foam tape was important because it ensured that all the weight was evenly distributed on the surface of the coverslip during abrasion. The applied pressure P can be simply calculated by P = mg/S where g is the gravity of Earth, m the mass of the load and S the surface of the foam tape. On small surfaces, concentrated pressures tended to break the coverslip while on large surfaces, pressure seemed to apply only close to the edges most likely because of the back-and-forth motion. We had to find a compromise and chose foam tape patches of 10 mm diameter and 20 mm diameter round coverslips (Fig. 3 – 3).

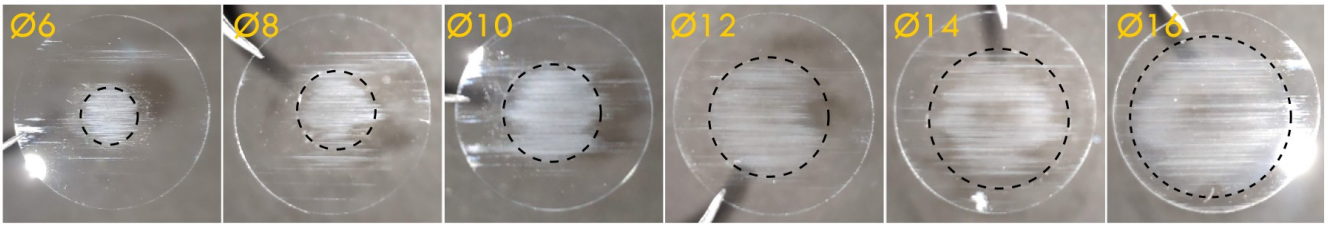

Figure 3 – 3. Abrasions with respect to foam tape size. Photos of ⌀20 glass coverslips abraded with different foam tape size (thus different pressure) for a load of 200g and 100 passages. Smallest foam tape concentrate the pressure at the center of the coverslip that can break it. Largest foam tape creates unevenly distributed abrasions. Dashed line: foam tape position.

With our optimal conditions for making the abrasions, only two ways were possible to modulate the surface topography. First we varied the load, thus the pressure applied to the coverslip surface. The support alone weights 225g and we could add up to 400g of load so that the applied pressure ranged from 28 to 78 kPa. The second parameter we could monitor was the number of back-and-forth motions, denoted as "passages".

We measured the topography of the substrates with a mechanical profilometer while varying the two parameters described above. We then quantified rugosity in accordance to standards used in tribology[190]. Using the profile of heights, we calculated the rugosity Ra as

$$Ra = \frac{1}{L}\int_0^L |z(x)|\,dx$$

We measured Ra over a distance of L = 3 mm, at three different spots on the coverslip, for different loads and numbers of passages (Fig. 3 – 4). Over this distance, we sampled 59922 surface points so that the lateral sampling was approximately 0.05 µm. We observed that the biggest changes occurred when the number of passages varied. Pressure above 30 kPa had only a small impact on Ra in the tested range. Nevertheless, high pressures with a high number of passage showed a decrease of Ra, probably because the surface started to be degraded.

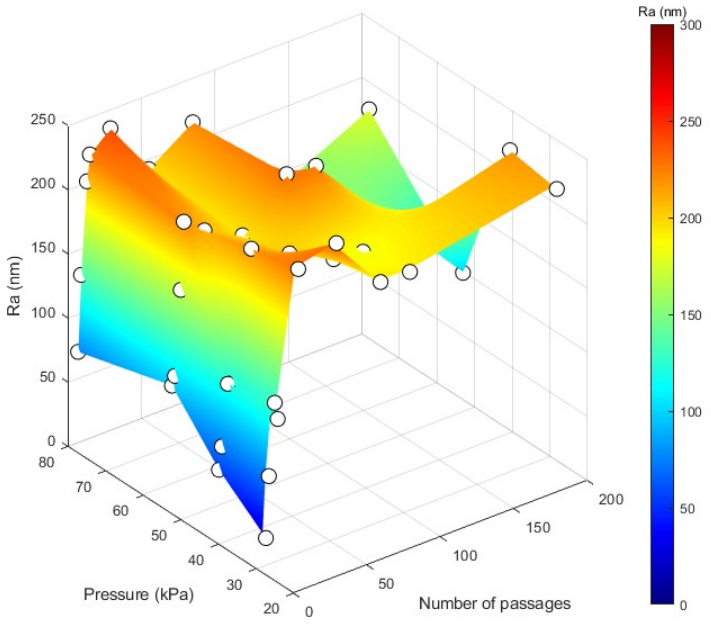

Figure 3 – 4. Rugosity Ra versus load or number of passages. The rugosity Ra quickly increases with the number of passages of the sandpaper, up to a plateau value. The applied pressure has little influence on Ra.

We then evaluated the spatial distribution of abrasions. We first qualitatively described the topography by looking at pictures taken in phase-contrast microscopy (Fig. 3 – 5A). As the passage number increased, microabrasions were denser. We estimated the spacing between abrasions by calculating the FFT of images taken with phase-contrast microscopy (Fig. 3 – 5B,C). We observed a wide range of spatial frequencies in our samples rather than a favored distance between "peaks". Characteristic spatial frequencies ranged from 0 to around 70 μm^{-1}, thus spanning several lengthscales. However, due to the resolution of our images, we were not able to assess features smaller than the pixel size, 0.33 µm.

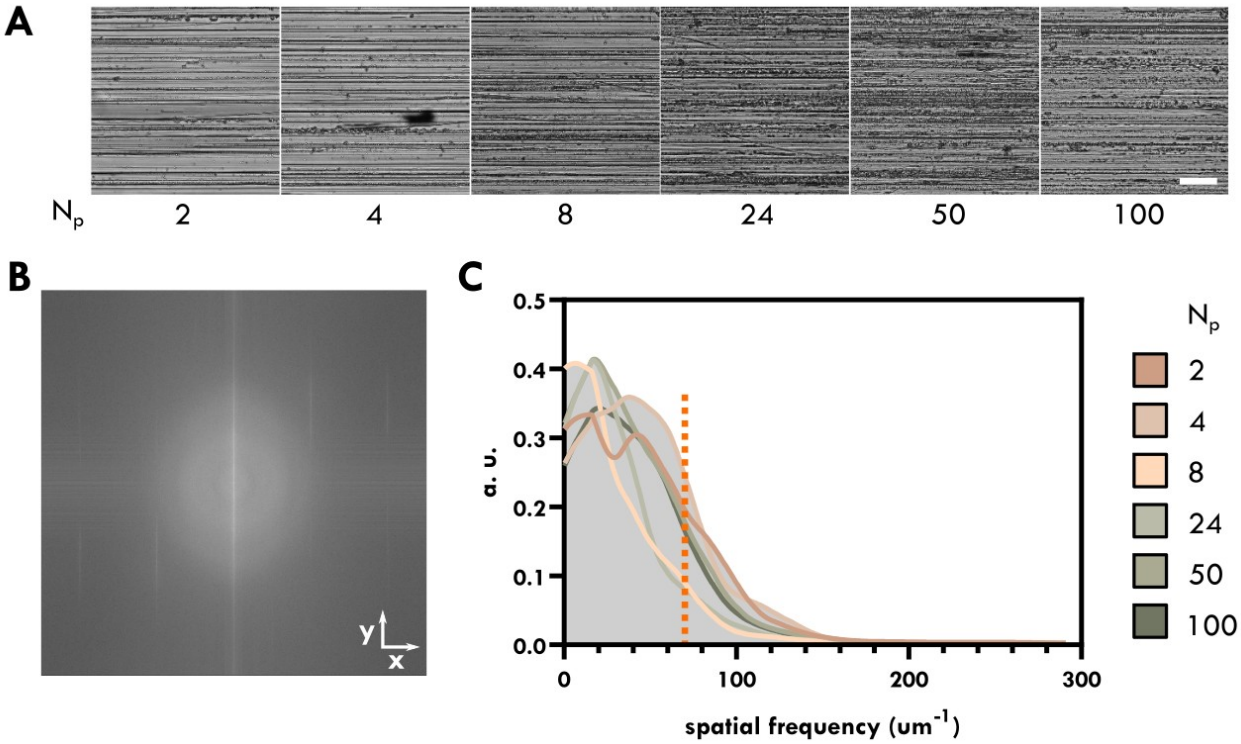

Figure 3 – 5. Spatial distribution of abrasions. (**A**) Phase-contrast images of microabraded glass coverslips for different number of passages N_p. The applied pressure is 53 kPa. Scale bar = 100 µm. (**B**) 2D FFT of a phase-contrast image of an abraded coverslip (N_p = 100). (**C**) FFT along the direction perpendicular to the microabrasions (y-direction). There is a wide distribution of spatial frequencies with a cutoff frequency (dashed orange line) around 70 μm^{-1}.

Altogether, we managed to make cheap, fast and reproducible topographical textures on glass coverslips by using sandpaper and a dedicated device. We quantified the control parameters and showed that the number of passages of the sandpaper over the coverslip had a significant impact on the topography. For the rest of the study, we always used the same parameters: a pressure of 53 kPa and 100 passages. This ensured reproducible microabrasions of typically 200 nm depth and spanning typical lenghtscales larger than dozens of nanometers, in the same range as classical contact guidance cues. For that reason, we called these microabrasions µCG, similarly to what we have done in Chapter I. 1. 2. 4.

1. 2. Cell monolayers

We seeded C2C12 cells on the previously characterized abraded surfaces and measured their orientation and velocity with time. We first looked at cell orientation in the monolayer (Fig. 3 – 6A,B). On non-abraded substrates, cells organized in nematic domains randomly oriented while they followed the topography direction ("easy" direction, that we set as the x-axis) on abraded substrates by contact guidance. We quantified how cells were oriented by calculating the order parameter Q defined by $Q=\sqrt{(\langle\cos 2\theta\rangle^2+\langle\sin 2\theta\rangle^2)}$ over the whole image (Fig. 3 – 6C). An order parameter close to 1 means that cells are perfectly aligned while if Q is null, cells are randomly oriented. We compared the monolayers with and without abrasions. On abraded substrates, the orientation of the cells increased as their density increased. After confluence, they were perfectly oriented (Q = 1). On non-abraded substrates, the order parameter remained low even after confluence even though the cells were locally well oriented. This is due to the organization in domains that are themselves uncorrelated.

We investigated the cells' motions in the monolayers using PIV. The average speed of cells ranged from 6 to 12 μm/h, independently on the presence of abrasions on the substrate (Fig. 3 – 7A). Starting below confluence, we observed an increase of speed then a decrease after confluence, the system evolving towards a jammed state. We then measured the x and y component of the velocity field (Fig. 3 – 7B). On non-abraded substrates, these two components were similar as the system is isotropic. On abraded substrates, cell speeds were higher in the easy direction than perpendicular to it. As the presence of abrasions did not affect the average cell speed compared to non-abraded substrates, we conclude that abrasions favor cell migration in the direction of the easy axis.

Altogether, these results show a clear contact guidance of cells on abraded substrates. We model this oriented topography as a microscale field that orient individual cell bodies.

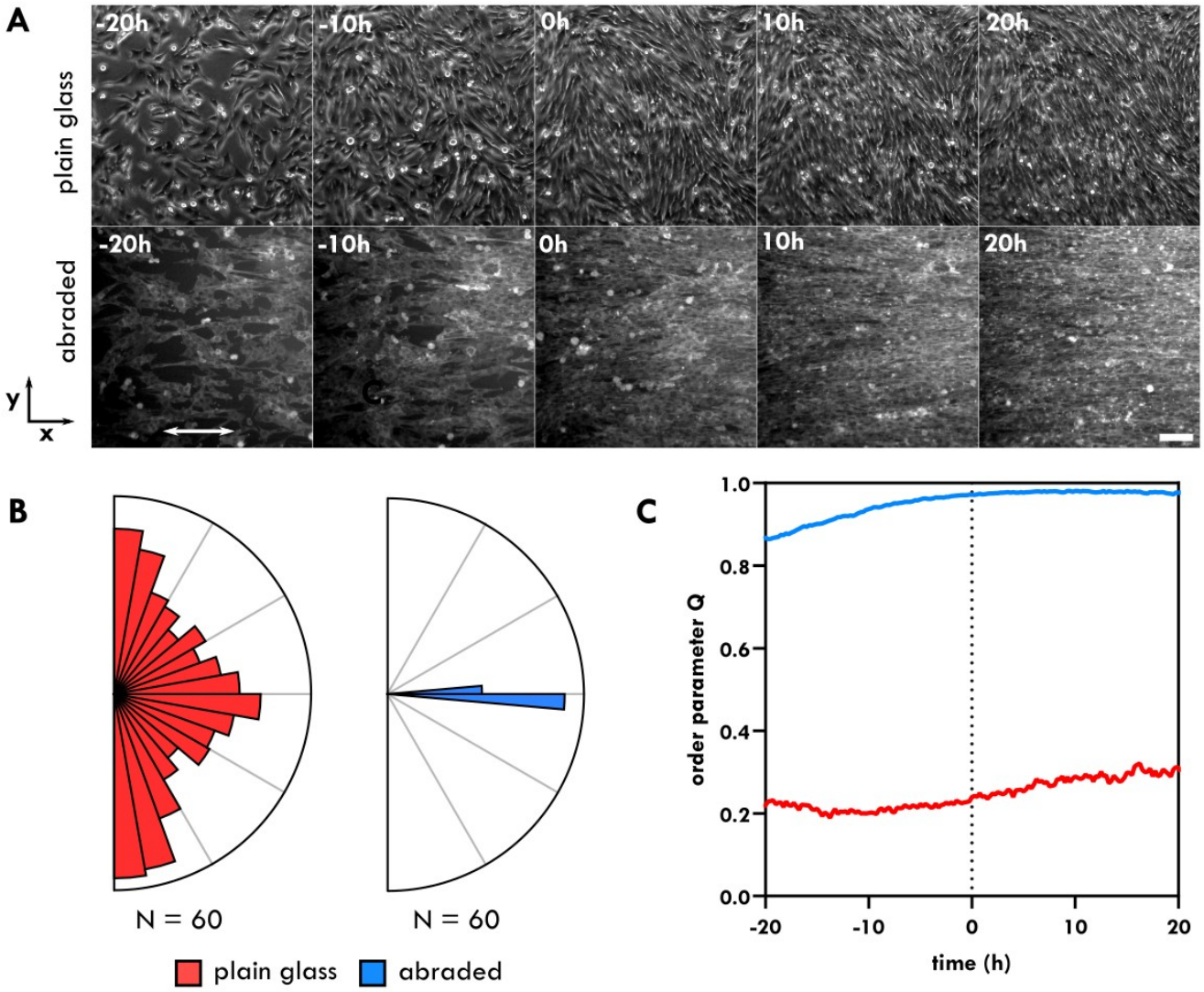

Figure 3 – 6. Cell orientation in the monolayer. (**A**) Images of C2C12 monolayers on non-abraded (top) and abraded substrates (bottom) over the duration of the experiment. On plain glass, cells form domains of oriented cells separated by topological defects. On abraded substrates, cells follow the topography by contact guidance. Cells are observed on phase-contrast (resp. fluorescent actin in mCherry) on non-abraded (resp. abraded) substrates. Scale bar = 100 µm. (**B**) Cell average orientation in the monolayer for several FOVs. Cells randomly orient on plain glass but follow the easy direction on abraded substrates. (**C**) Order parameter Q in monolayers over time. Q is 1 on abraded substrates that show perfect orientation. This value drops on non-abraded substrates because of randomly oriented nematic domains. Time t = 0h corresponds to confluence. Red: plain glass; blue: abraded substrates.

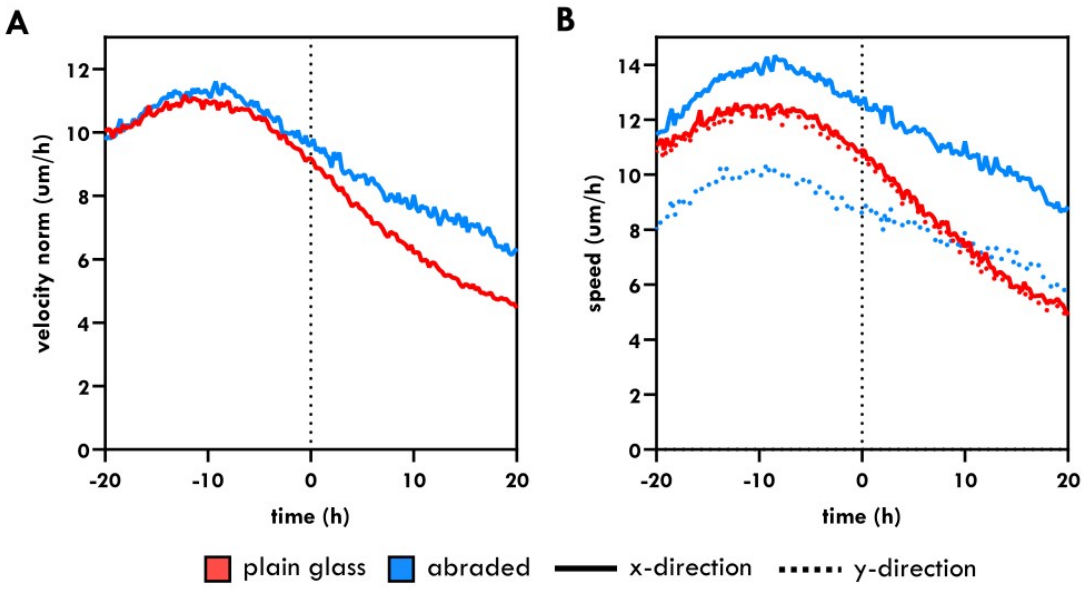

Figure 3 – 7. Cell velocity in the monolayer. (**A**) Average speed over time. On both substrates, cell speed decreases after confluence towards a jammed state. However, velocities are comparable and range from 6 to 12 µm/h. (**B**) Speeds in x and y directions over time. On abraded substrates, cells flow at different speed in the perpendicular direction. Time t = 0h corresponds to confluence. Red: plain glass; blue: abraded substrates; solid line: x-direction; dashed line: y-direction.

2. Analysis pipeline

Before we start to discuss our observations, it is useful to explain and discuss the analysis pipeline that has been setup. This pipeline follows the protocols described in II. 3. where the overall approach is explained.

2. 1. Notations

We set here the notations and conventions that will be used in the rest of this chapter (Fig. 3 – 8). Our system is made of chemically patterned mesoscale stripes (mG) on top of microabrasions of the glass coverslip (µCG). The term "stripe" will always refer to the mesoscale pattern. This pattern is meant to act on the whole population via collective flows. Stripes are infinite in the y-direction and have a finite width L in the x-direction. Beside the stripes, subcellular microabrasions may be

present. For simplicity, we will denote them as "abrasions". Abrasions favor alignment of cells individually via contact guidance.

Two particular positions are important for our analysis. The middle of stripes x = 0 will be refereed as "$_{mid}$". The edges of stripes x = ±L/2 will be refereed as "$_{edge}$". Finally, the overall system will be called "stripes" or "stripes with abrasions" depending on the presence or not of microabrasions.

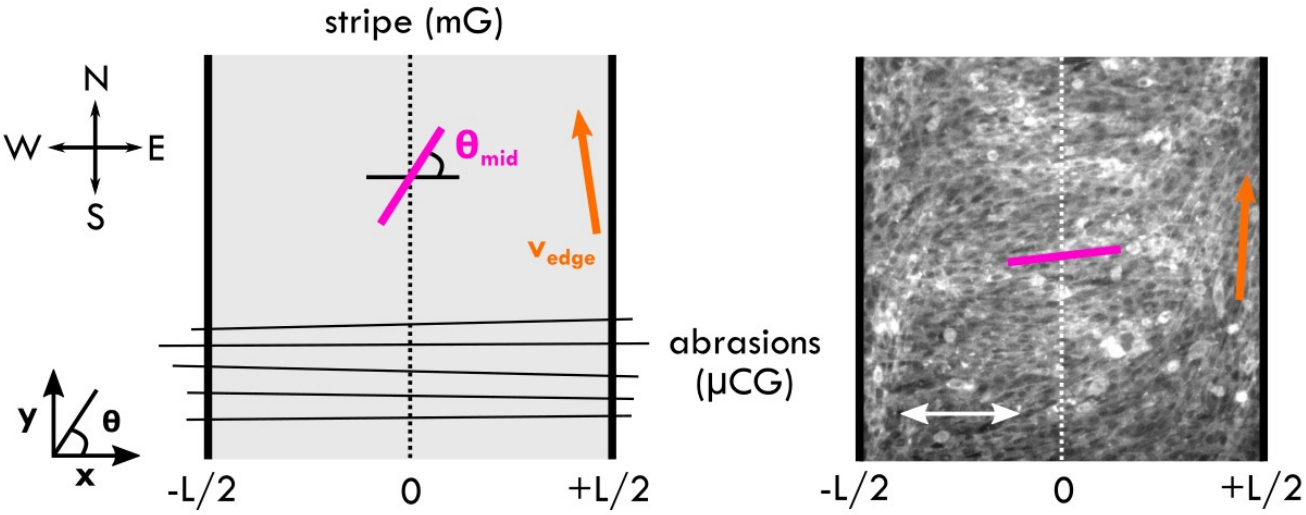

Figure 3 – 8. Notations. Schematics (left) and fluorescence image (right) of a stripe with abrasions. We call "stripe" the mesoscale chemical pattern. This pattern acts as a mG field on the overall cell population. The stripe is infinite in the y-direction and has a width L in the x-direction. The angle with the x-axis is noted θ. We called "abrasions" the microtopography. This topography acts as a μCG on individual cells. There are two particular positions in the stripes, the middle x = 0 (denoted "$_{mid}$") and the edges x = ±L/2 (denoted "$_{edge}$"). On the image: actin is labeled; double arrow indicates microabrasions direction; width of the stripe = 553 μm.

Images in our experiments were acquired every 15 minutes for at least 5 hours after confluence, before the cells started to form multiple layers. To extract the quantities we are interested in, cellular orientation and velocity, we needed an analysis pipeline. To reduce biological variability, we averaged our experiment along the direction of the stripes (y-axis), over time, and for several FOVs. We exemplify below how we computed cellular orientation and velocity profiles. In this example, the stripe is 296 μm wide.

2. 2. Cellular orientation

We computed local cellular orientations θ from images of the cells. We excluded all FOVs with defects to keep only images with a clear orientation (Fig. 3 – 9A). We used the method described in Chapter II. 4. 1. to compute the orientation field (Fig. 3 – 9B). Orientation of cells ranged from -90° to 90° where a ±90° angle accounts for a parallel alignment of the cells with the stripe's direction. From the angle map, we computed the local order parameter Q_{loc} over a window of size 32 pixels (Fig. 3 – 9C). As expected, all cells were perfectly aligned locally, so that Q_{loc} is very close to 1 everywhere.

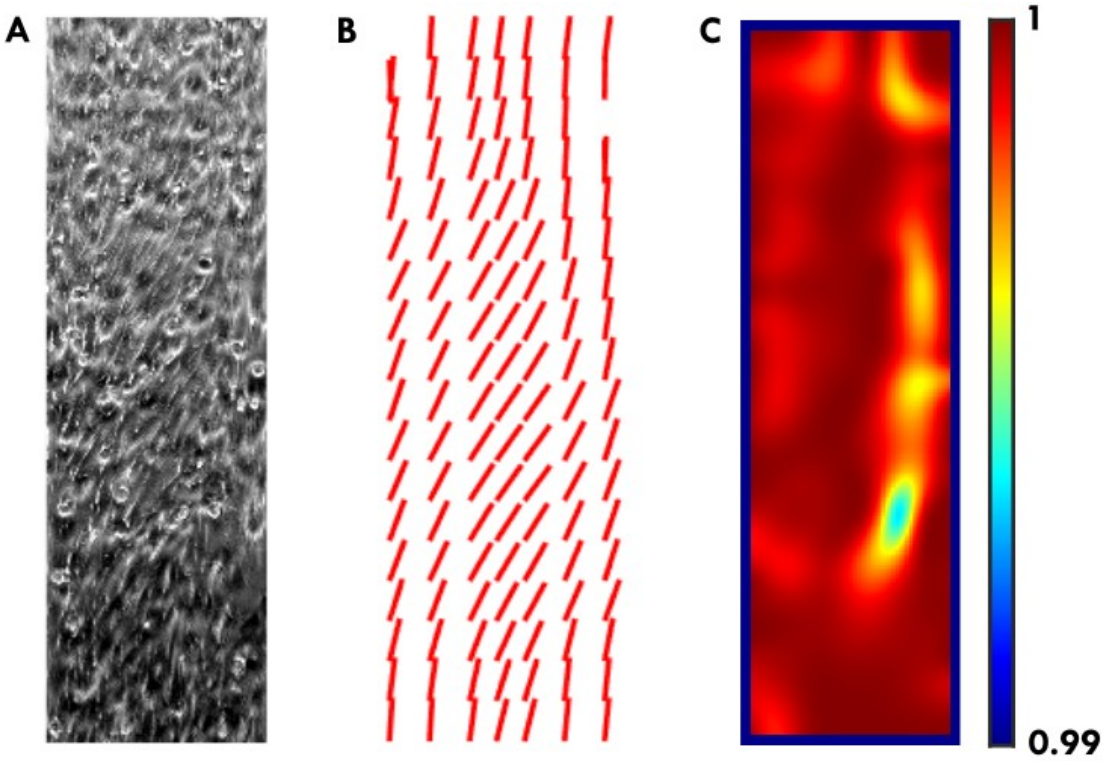

Figure 3 – 9. Cell orientation in stripes. (**A**) Phase-contrast image of a stripe seeded with C2C12 cells at confluence. (**B**) Orientation of cells of the previous image. We can see that cells at the edges nearly follows the stripe's direction while cells in the middle of the stripe develop a tilt. (**C**) Order parameter map of the previous image for a window of σ = 32 px. Values are very close to 1 meaning that cells are locally aligned. Width of the stripe = 296 µm.

As we studied mean-field effects, we averaged the orientation field over time and over the direction of the stripe (y-axis). All the movies started at confluence and stopped before a second layer formed, around 5h after confluence. Histograms of the angles at a given position along the x-

axis were measured over time and showed that the average angle remained the same as the experiment went on (Fig. 3 – 10A). As a consequence, we averaged the cell angle over time and along the y-axis and computed angular profiles across the stripe width (Fig. 3 – 10B).

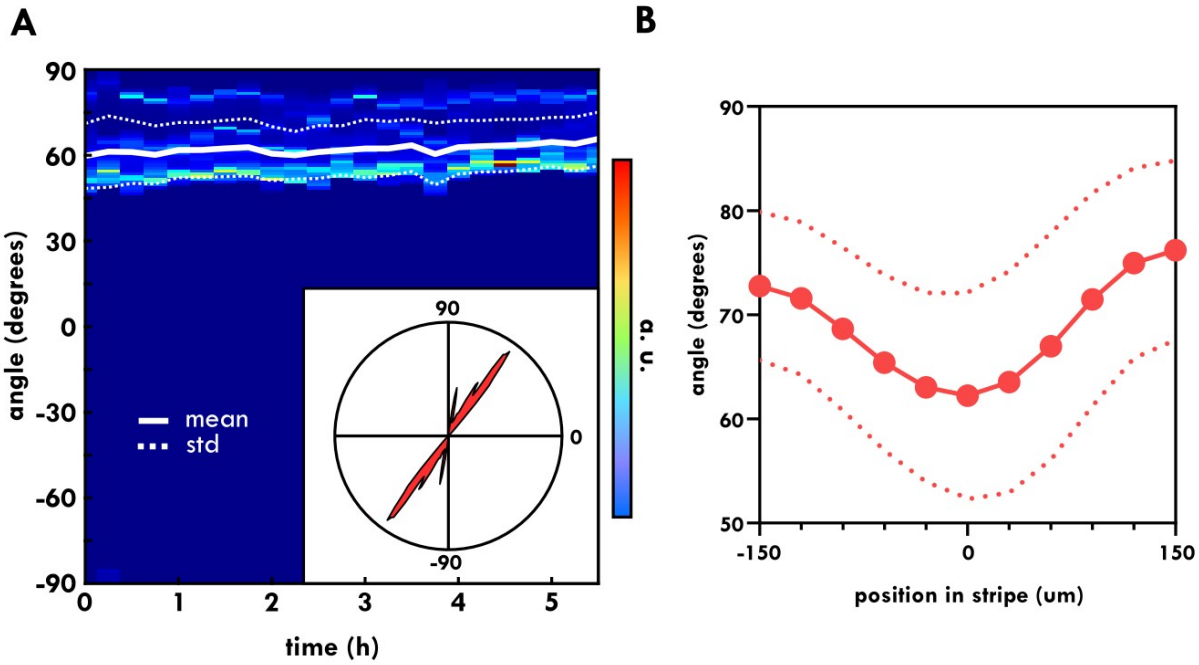

Figure 3 – 10. Evolution of angle at the middle of stripes over time. (**A**) Histogram of angles in the middle of the stripe showed in Figure 3 – 9A over time. The angle is constant over the time of the experiment. Insert: polar histogram of the same experiment averaged over time. (**B**) Cellular orientation averaged over y-axis and time according to the position in the stripe. In this case, cellular angle does not follow the stripe direction in the middle of the stripe. Solid line: mean value of angle; dashed line: standard deviation.

2. 3. Cellular flows

From the theory of active nematics we know that a gradient of orientation gives rise to flows (see Chapter I. 2. 2.). Indeed, we observed a shear flow whose direction was compatible with an extensile nematic, a positive angle[a] creating a "downstream" flow at the left edge and an "upstream" flow at the right edge (i.e. $v_y(-L/2)<0$ and $v_y(+L/2)>0$). We followed the dynamics in the monolayer using PIV and computed the results following the protocol explained in Chapter II. 4. 2. Speeds were locally computed in boxes of size σ = 32 px (that corresponds to 24 – 30 µm depending on the

a By "positive angle" we mean a director in the direction SW-NE in our images. Inversely, a "negative angle" would be a director in the direction SE-NW.

camera used), with 50% overlap. Notwithstanding fluctuations, the speed was the same all along the stripe, meaning that all cells moved (Fig. 3 – 11A). The velocity was decomposed along its x-axis contribution v_x (Fig. 3 – 11B) and its y-axis contribution v_y (Fig. 3 – 11C). The contribution v_x was called "convergent" velocity because cells flow towards the center of the stripes. The contribution v_y was called "shear" velocity.

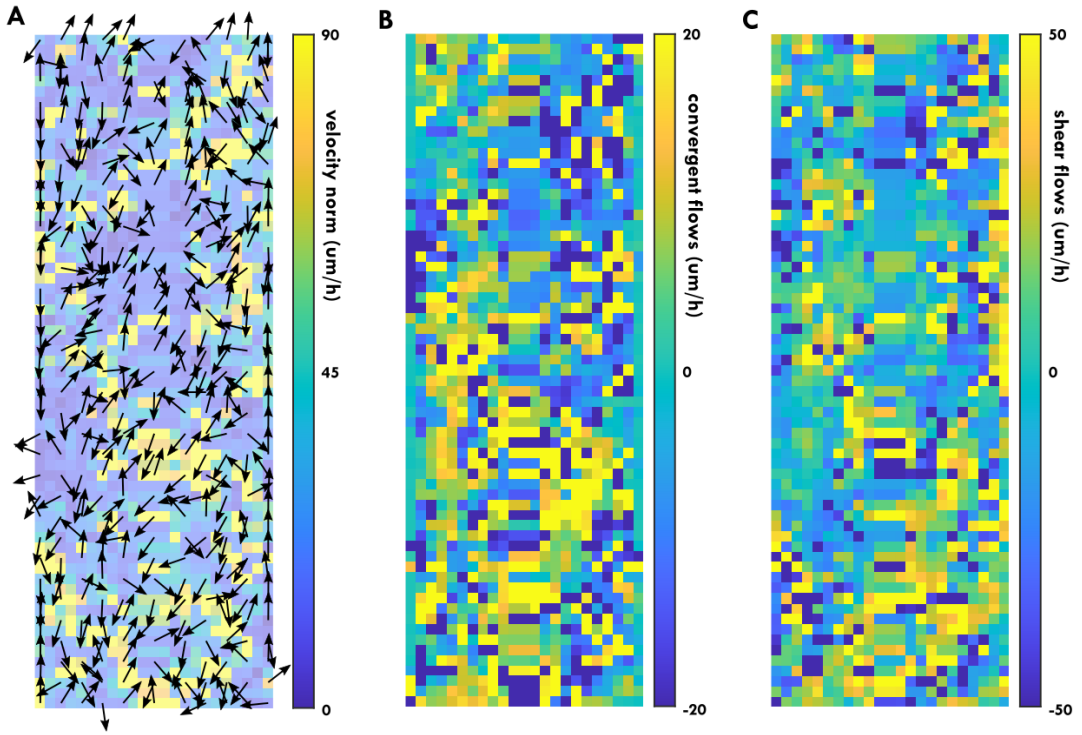

Figure 3 – 11. Cellular flows in stripes. (**A**) Instantaneous velocity observed as black arrows for its direction, and colormap for its norm 5 hours after confluence. (**B**) x-axis component of velocities (convergent flows) and (**C**) y-axis component of velocities (shear flows) for the stripe shown in Figure 3 – 9A. PIV is computed over two successive images taken 15 minutes apart.

We averaged flows for the experimental duration to remove noise in the analysis. We first noted that the speed decreased over time, and cells evolved towards a jamming transition at long times (Fig. 3 – 12A). However for the duration of our experiment, around 5h, the variations in speed were smaller than 10% and we assumed that the velocity norm remained constant. Thus, the profiles of velocities were comparable over time. By averaging along the stripe direction (y-axis), we calculated the convergent and shear flow profiles over the course of the experiment and observed no

significant changes (Fig. 3 – 12B). Finally, averaging over time and y-direction, we were able to measure cellular flow profiles across x-direction in stripes (Fig. 3 – 12C).

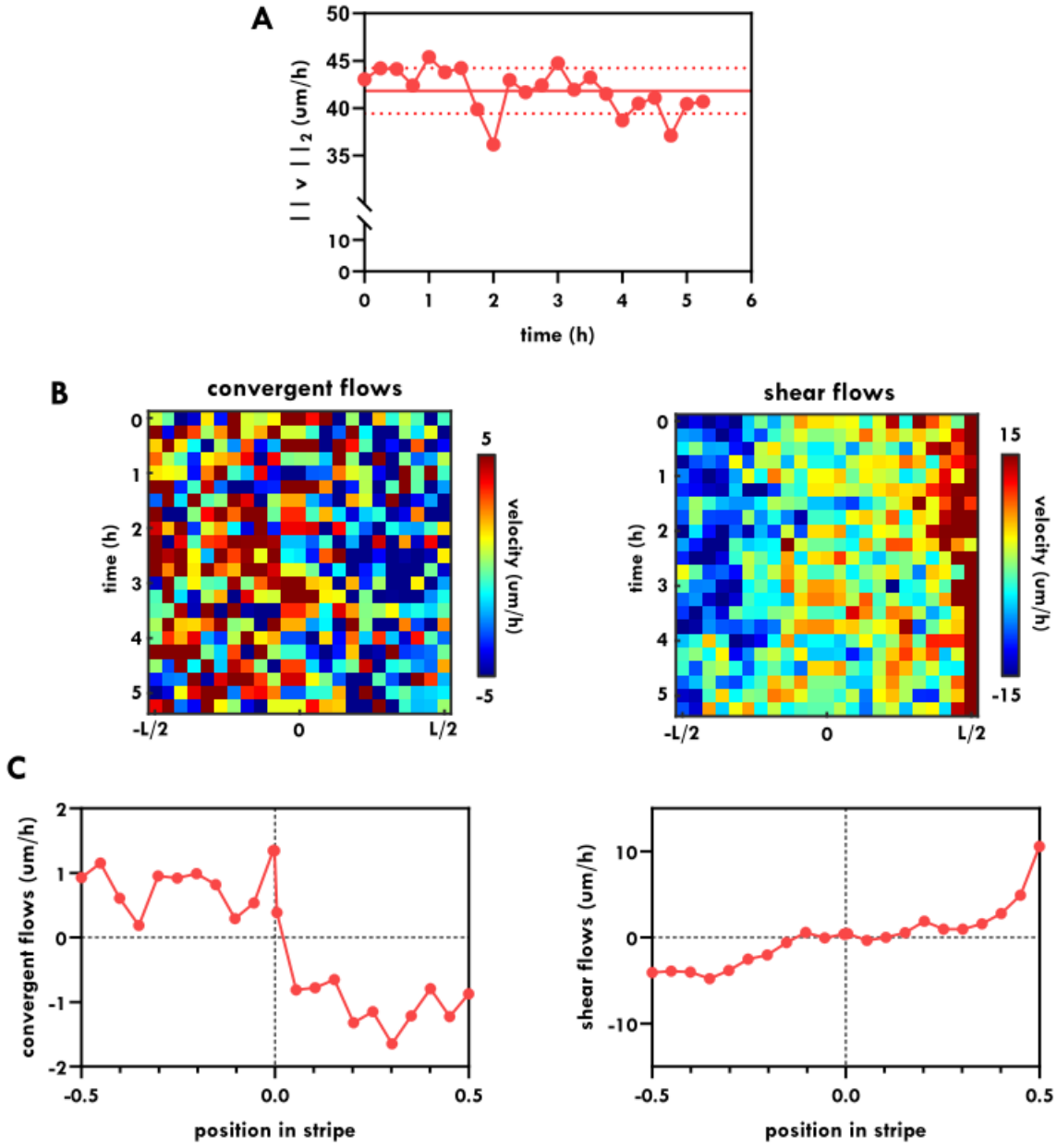

Figure 3 – 12. Evolution of cellular flows over time for a single FOV. (**A**) The mean speed decreases only by 10% over the course of the experiment (around 5h). We assumed it is constant. Solid line: average value over time; dashed line: standard deviation. (**B**) Convergent and shear flow profiles averaged over the y-axis do not significantly change during the timecourse of the experiment. (**C**) Convergent and shear flow, averaged over y-axis and time, versus the normalized width of the stripe. We observed cellular flows going towards the center of the stripe and shear flows close to the edges.

We took a closer look at the speed distributions at the edges and at the middle of stripes (Fig. 3 – 13). For convergent flows, we saw opposite mean values of the speed at the boundaries meaning cells flew inwards symmetrically. These distributions spread over ±10 μm/h. At the center, the distribution was bimodal as cells flew in opposite directions so that the average value is zero. Shear flows distribution were similar to convergent flows except they spread more. At the edges, their mean value was $v_y(-L/2) = -4.4 \pm 22.8$ μm/h (resp. $v_y(+L/2) = 11.5 \pm 26.4$ μm/h) for the example given. At the center, a bimodal distribution was observed.

Due to the spread of these distributions and for readability purpose, we decided not to show errorbars in the following of this chapter. Velocity profiles were calculated using the average values of these distributions.

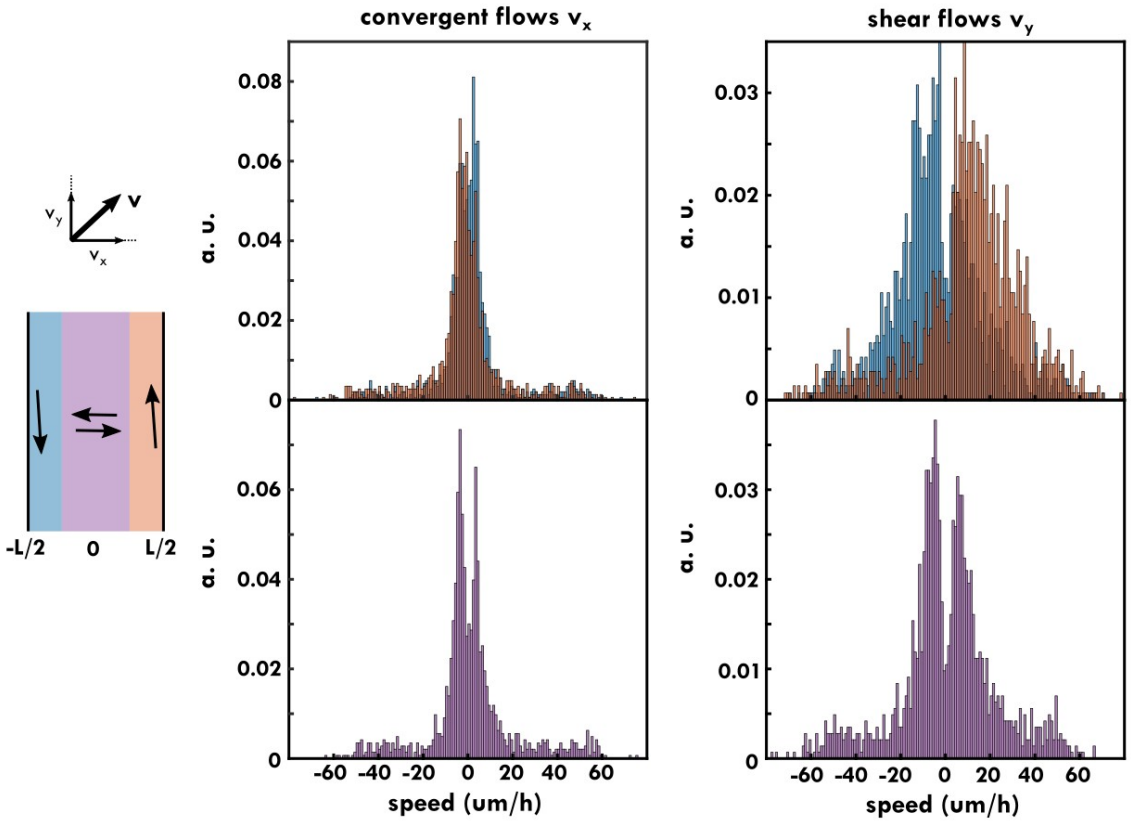

Figure 3 – 13. Distributions of speed. Convergent and shear flows distribution of speeds for the exemplified FOV. At the edges of the stripe (blue: left edge; orange: right edge), a unimodal distribution shows that cells flow in a given direction while in the center (purple: center) two populations of cells flow in opposite directions.

We have so far dealt with orientation and velocity profiles for a single FOV. We repeated our measurements up to 30 times in our experiments and averaged all these profiles. We binned the average profiles across the width, following the protocol explained in Chapter II. 5. 1. and detailed in Appendix C. 2. Orientation and velocity profiles were averaged and compared together and with the previous results of Duclos et al.[174]

3. Supracellular assemblies on multiscale substrates

3. 1. Mesoscale to microscale transition

To study the cells' collective response to antagonistic alignment cues at different lengthscales, we patterned mesoscale cell-adhesive stripes perpendicularly to a microabraded surface following the protocol described in Chapter II. 2. 2. 2. In an analogy with the classical Fréedericksz transition, the microscale topography acted as the magnetic field.

3. 1. 1. Cellular angle evolution with stripe width

We looked at the middle angle in stripes of increasing width (Fig. 3 – 14). For non-abraded substrates, the middle angle tilted away from the stripe direction as the stripe width increased. For large stripes, this angle seemed to saturate at the angle $\theta_\infty = 59°$. For abraded substrates, we observed a clear transition in orientation at a width L_c from the direction of the stripes imposed by mG (±90°) to an alignment with microabrasions by μCG (0°).

As a first approximation, we assumed that chirality effects were negligible in our system and eluded them by measuring cos(2θ) instead of θ. This way, we combined the two branches in one, which was easier to read and interpret. A more detailed discussion on chirality in our system can be found in III. 4. 4. The value cos(2θ) then varied from -1 for cells aligned with the stripes' direction to +1 for cells perpendicular to it. We estimated the value of the transition by a sigmoid fit (Fig. 3 –

15A). We found a length L_c = 274 µm (95% CI = 268 – 281 µm). For abraded stripes wider than L_c, the orientation in the middle is totally imposed by µCG effects, cells lying at 0°.

The cells' angle at the edges followed the same trend. For non-abraded substrates, this angle slightly decreased from 90° for very thin stripes to 80° for large ones, following middle angle tilt. For abraded substrates, this angle changed from 90° to θ_∞ = 62° for stripes larger than L_c (Fig. 3 – 15B).

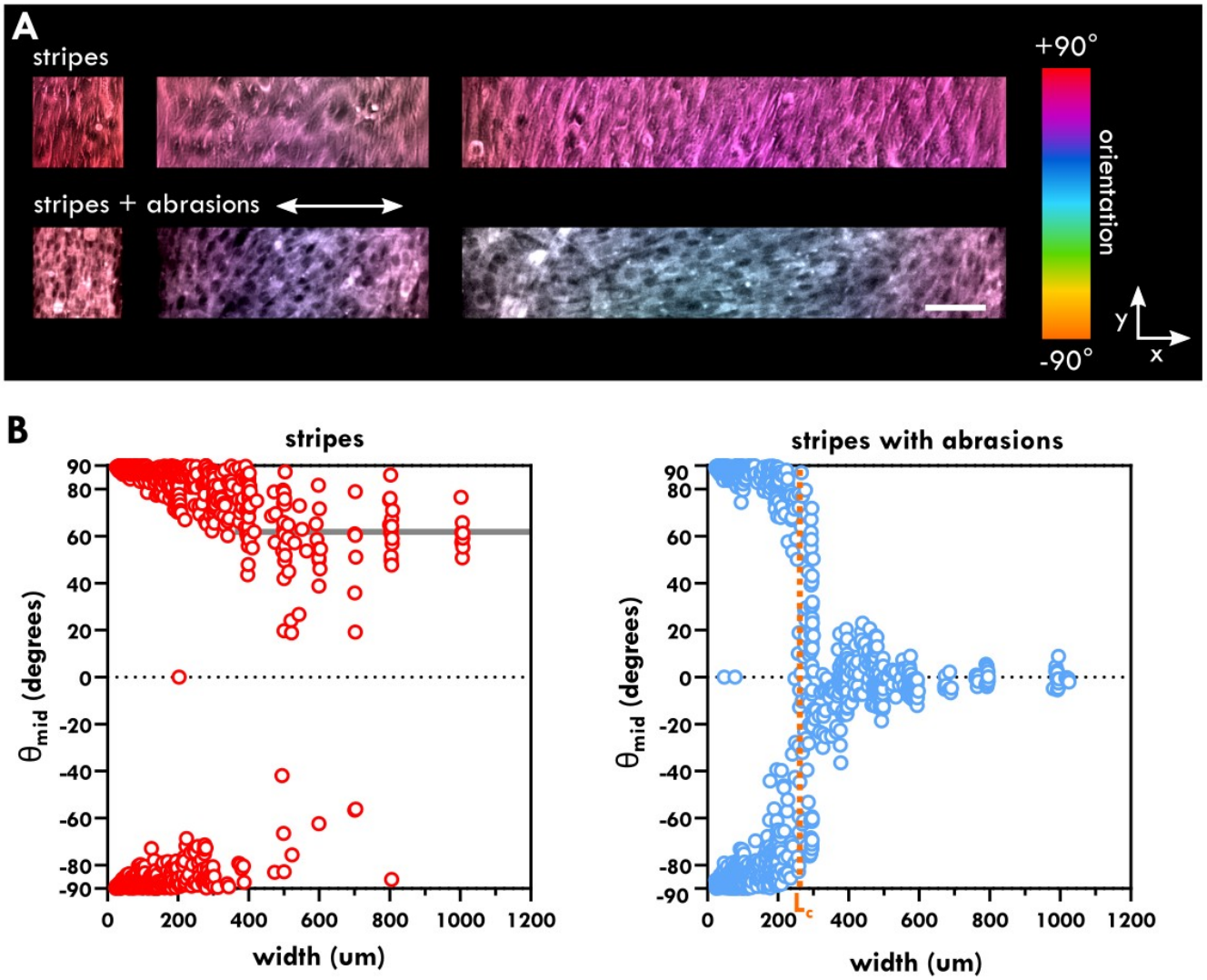

Figure 3 – 14. Transition in cell orientation for stripes of increasing width. (**A**) Images of C2C12 cells in stripes and stripes with perpendicular abrasions. On non-abraded substrates, cells in the middle of the stripes show an increasing tilt with stripe width. For abraded substrates, a clear transition in orientation appears at a stripe width L_c. The direction of abrasions is indicated by the double-arrow. Colors code for the orientation, scale bar = 50 µm. (**B**) Evolution of cell angle in the middle θ_{mid} for stripes of increasing width. On stripes with abrasions, a transition from mesoscale to microscale mode of guidance appears at L_c = 274 µm (95% CI = 268 – 281 µm, orange line). The two branches correspond to the two possible chirality of the nematic. Red: featureless stripes, blue: stripes with abrasions.

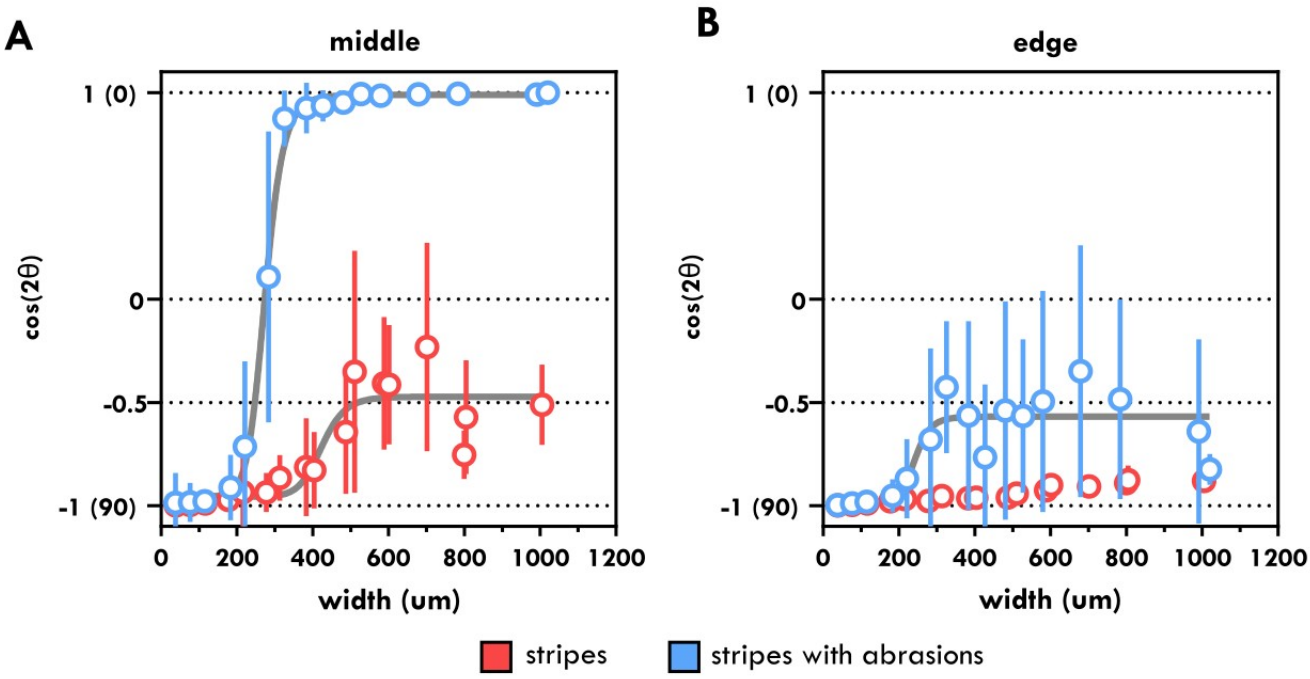

Figure 3 – 15. Evolution of middle and edge cellular angles for stripes of increasing width. Cellular orientation at the middle (**A**) and edges (**B**) of stripes of increasing width for non-abraded (red) and abraded substrates (blue). For large non-abraded stripes, cells in the middle tilt at a constant angle $\theta_\infty^{(stripes)} = 59°$. For abraded stripes, we observe a clear transition in orientation for widths larger than $L_c = 274$ µm (95% CI = 268 – 281 µm). Cells at the edges try to accommodate the middle orientation by shifting at $\theta_\infty^{(abrasions)} = 62°$ from their parallel anchoring. Grey line: sigmoid fit.

The change of angle from the edges towards the center was also seen across profiles[b] of orientation (Fig. 3 – 16A). Looking at profiles of angles, for non-abraded stripes we again observed the tilt of the cells at the middle of the stripes. For abraded stripes, we observed the transition described before. We measured the length across which the change in orientation from the edges to the center of stripes occurs and called it "coherence length", in analogy with the passive Fréedericksz transition (Fig. 3 – 16C). We fitted a sigmoid along the profile to get this value (Fig. 3 – 16B). Note that we excluded all fits that have a determination coefficient r^2 below 0.8. For non-abraded substrates, the coherence length increased with the stripe width and increases with it. In contrary, for abraded substrates, this length was constant with a value $\xi = 70 \pm 36$ µm. Interestingly, this value was consistent with a "classical" Fréedericksz transition since $\xi \cdot \pi = 219$ µm of the same order as the transition width $L_c = 274$ µm (see Chapter I. 2. 2. 2.).

b From now on, we will refer as "profile" for a quantity observed along the x-axis. For our stripes, all quantities are averaged over y-axis and time when we observed profiles.

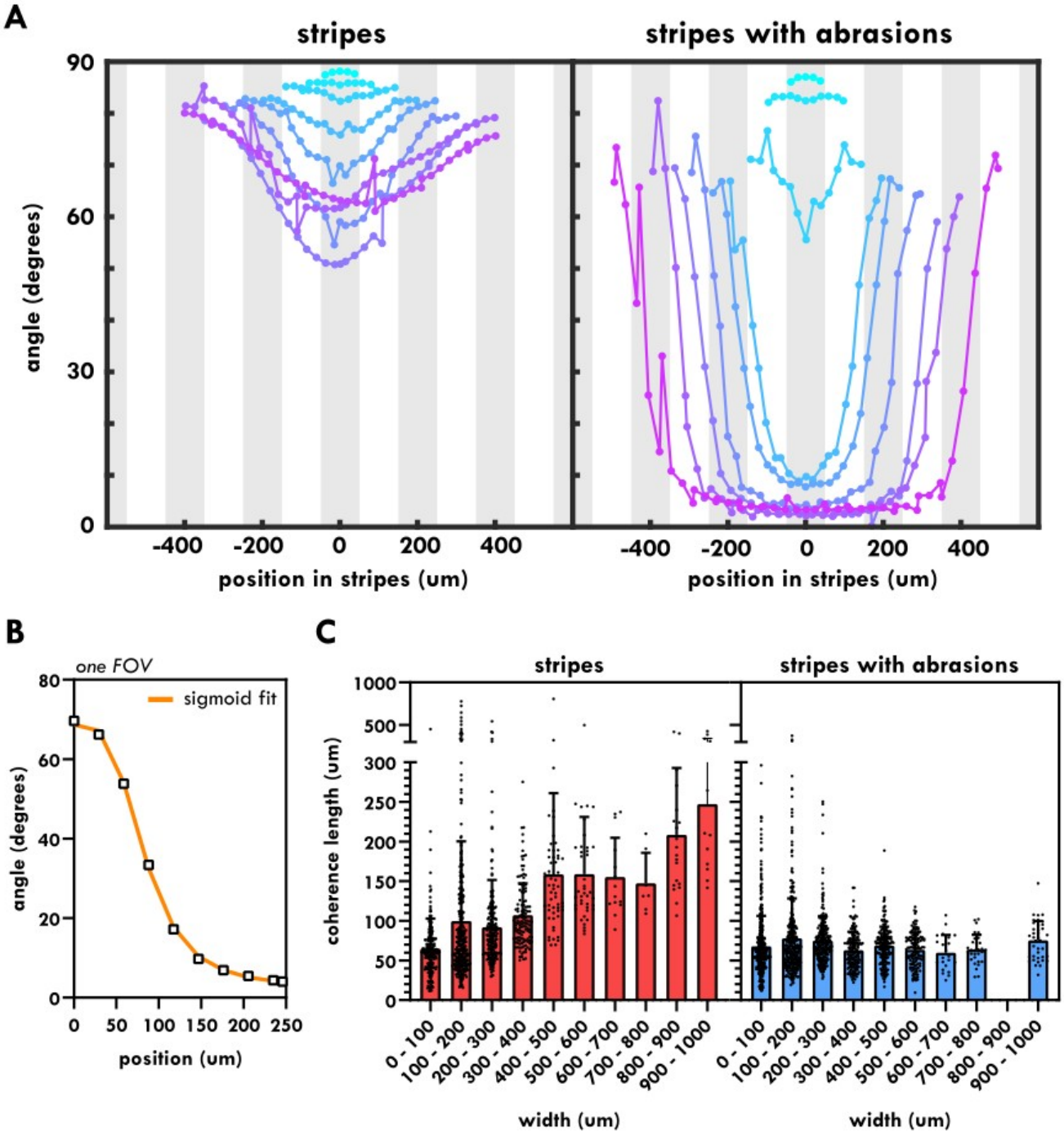

Figure 3 – 16. Profile of angles. (**A**) Cellular orientation across stripe width. We retrieve previous observations of Figure 3 – 15. (**B**) Coherence length is measured by a sigmoid fitting of the angles from stripes edge to the center. Here an example for one FOV (stripes with abrasions) of L = 500 μm is shown. (**C**) On stripes, coherence length increases with the width. For stripes with abrasions, it is approximately constant at ξ = 70 ± 36 μm.

3. 1. 2. Flow profiles

We measured the flow profiles for stripes of increasing widths. Here again, it is convenient to decompose the velocity into convergent and shear flows. Convergent flow profiles followed the same trend for all stripes' widths (Fig. 3 – 17A). They were symmetrical around the stripes' center with cells flowing inward. Maxima of the velocity were reached close to the edges. They increased with the stripes' width. We measured the slopes of the profiles around the center of the stripes by a linear fit (Fig. 3 – 17B,C). Of note, we systematically observed a small discontinuity of the flows around x=0, so that we fitted each stripe side independently. This discontinuity was not observed with the other tested cell lines (3T3 cells), we have no explanation for it. We excluded all fits with determination coefficients r^2 smaller than 0.7. For non-abraded stripes, this slope remained the same for all stripes' widths excepted for the thinner stripes where the measurement is less precise due to the small number of points in the profile. In contrary, for abraded stripes, the slope decreased with the width of the stripes. The presence of convergent flows was also observed in the experimental study of Duclos et al. and explained by mass balance $\partial_x v_x = -k$ where k is the rate of division/apoptosis $k = k_d - k_a$ in our system. The fact that we observed similar values and trends for k on both substrates suggests that these convergent flows are not directly linked to the system's activity.

Shear flow profiles were similar for all stripes' widths with or without abrasions (Fig. 3 – 18A). The shear decreased from its maximal value at the edges to reach zero at the center of the stripes. The maximal speed of the shear at the edges was similar whether the stripes were abraded or not.

The change from this maximal value at the edges to zero in the stripes center occurred within a length λ called the screening length. This length can be defined as $\lambda^2 \propto \eta/\xi_f$ with η the viscosity of the tissue and ξ_f is a friction constant per unit area modeling the dissipative interactions with the substrate. We measured this length by fitting a decaying exponential (Fig. 3 – 18B). We excluded all fits with determination coefficients r^2 below 0.9. This length had a mean value of $\lambda = 26 \pm 11$ µm

(resp. 22 ± 14 um) for non-abraded substrates (resp. abraded substrates) (Fig. 3 – 18C) both values being comparable to the one reported in Duclos et al. for C2C12 cells (λ = 12 ± 2 µm).

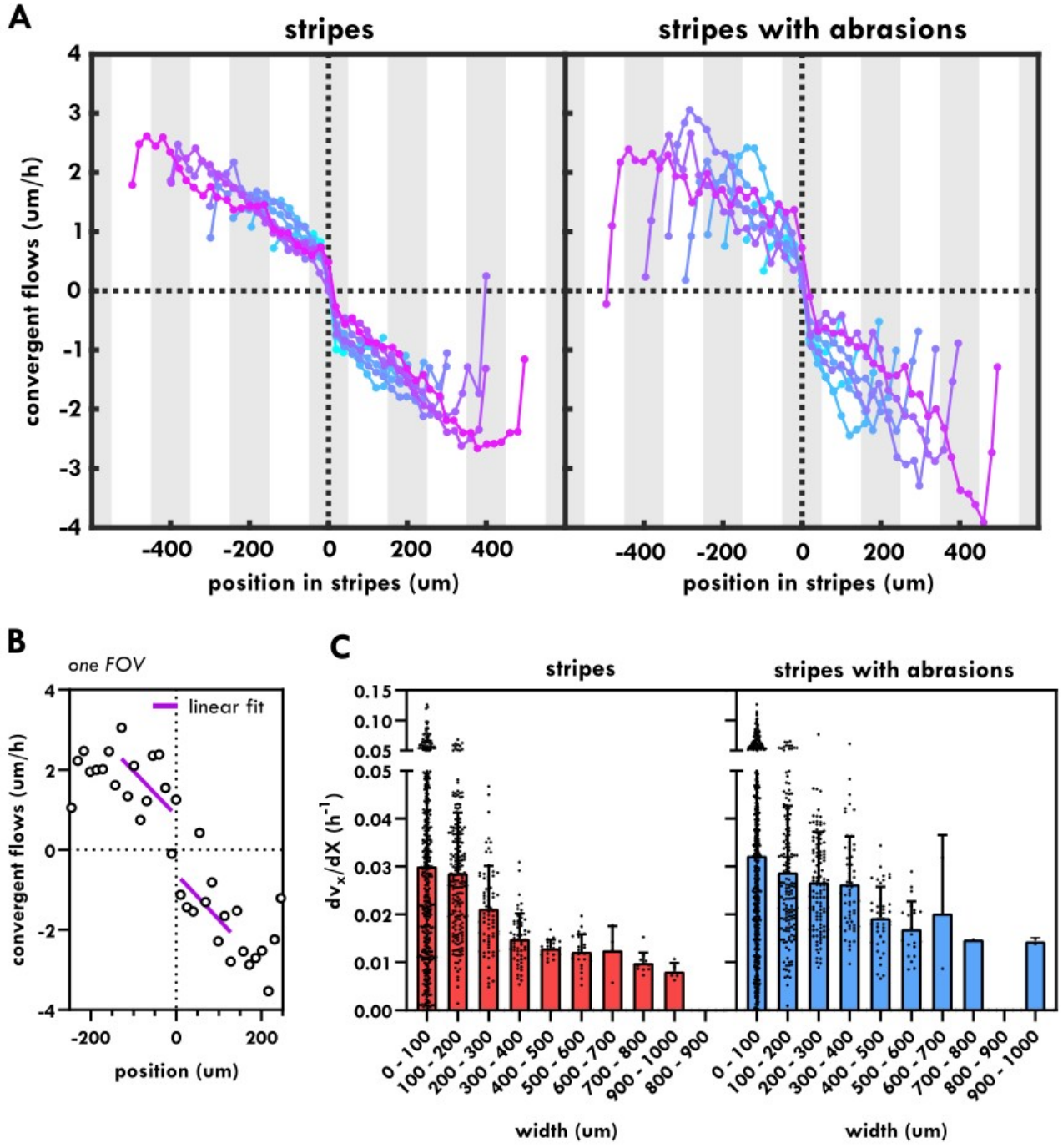

Figure 3 – 17. Convergent flow profiles. (**A**) Convergent cellular flows v_x for stripes of increasing width. Cells flow towards the center of stripes. (**B**) Slopes of convergent flow profiles is fitted with a linear function. Here is shown an example for a stripe of L = 491 µm. (**C**) Slopes of convergent flow profiles decrease with stripes' width. They are more likely related to the rate of division and extrusion (k_d – k_a) in the stripes.

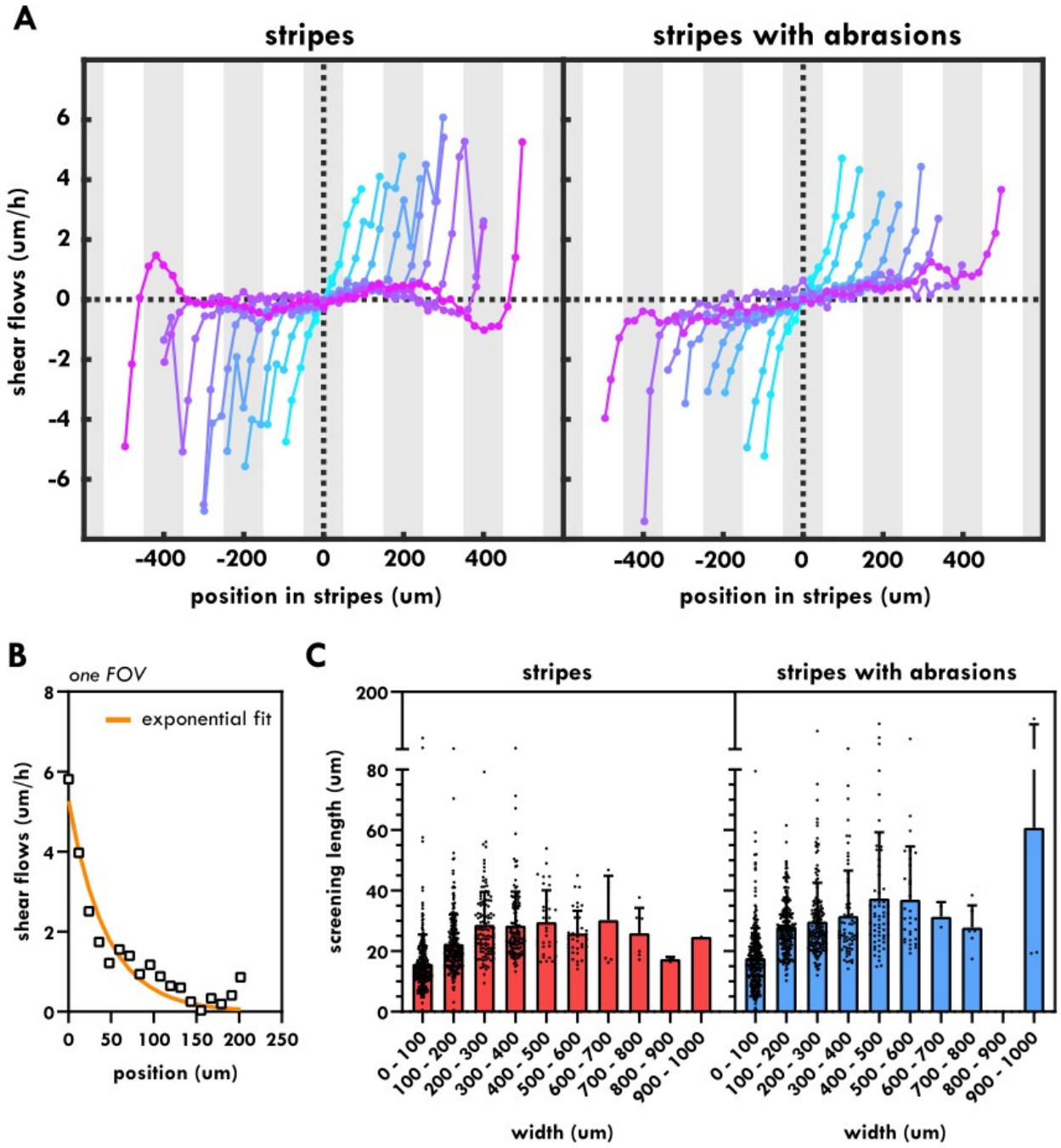

Figure 3 – 18. Shear flow profiles. (**A**) Shear cellular flows v_y for stripes of increasing width. Shear flows have a maximal speed at the edges and decay to zero towards the center of stripes. (**B**) Screening length λ measured by fitting a decaying exponential for one FOV. (**C**) Screening length for stripes of different widths. The mean values of friction length is λ = 26 ± 11 µm (resp. λ = 22 ± 14 µm) for stripes (resp. stripes with abrasions).

Altogether, our results describe a change in orientation from mesoscale-guiding constraints to microscale contact guidance at L_c = 274 µm, with no consequences on the dynamical aspects since cellular flows are only weakly impacted by this transition. We conclude that this transition likely

results from geometrical effects due to the competition between the multiscale guiding cues. For these reasons, we decided to call this a "geometrical transition". For stripes larger than L_c, the torques applied at the boundaries are overridden by abrasions-induced contact guidance effects, similarly to what has been described in Chapter I. 2. 4. However the shape of this transition is not described by the theoretical Fréedericksz expression that predicts close to the transition $\theta_{mid} \sim v_{y,edge} \sim \sqrt{\frac{(L-L_c)}{L_c}}$ [175]. In our case, the transition is much steeper than this theoretical expression, being even close to a discontinuous transition.

3. 2. Modulation of cell activity

3. 2. 1. Contractility inhibitors

We tested the nature of the geometrical transition by changing the cells' contractility. We used a derivative of the myosin inhibitor blebbistatin[c] at different concentrations (1.5 µM or 3 µM) between 5 and 10 hours after confluence, when the shear flows were well established. We followed the impact of drug addition for five more hours. We measured θ_{mid} and $v_{y,edge}$ before and after drug addition. Cell orientation was not impacted by the addition of the drug (Fig. 3 – 19B). In contrary, cellular shear flows were significantly reduced by the addition of the drug (Fig. 3 – 19A,D). This reduction of the shear flows was also observed on non-abraded substrates. Very interestingly, every time the drug was added, cells in the monolayers seemed to "contract" resulting in a systematic inversion of the shear flows inside the stripes. Indeed, the nematic director of cells did not change but cells then moved slightly inwards following the orientation of this director. From a macroscopic point of view, we then saw a change from an extensile to a contractile phenotype following the drug addition.

c We used non-phototoxic para,nitro-blebbistatin as described in Chapter II. 1. 2. but for simplicity, we will refer to it as "blebbistatin".

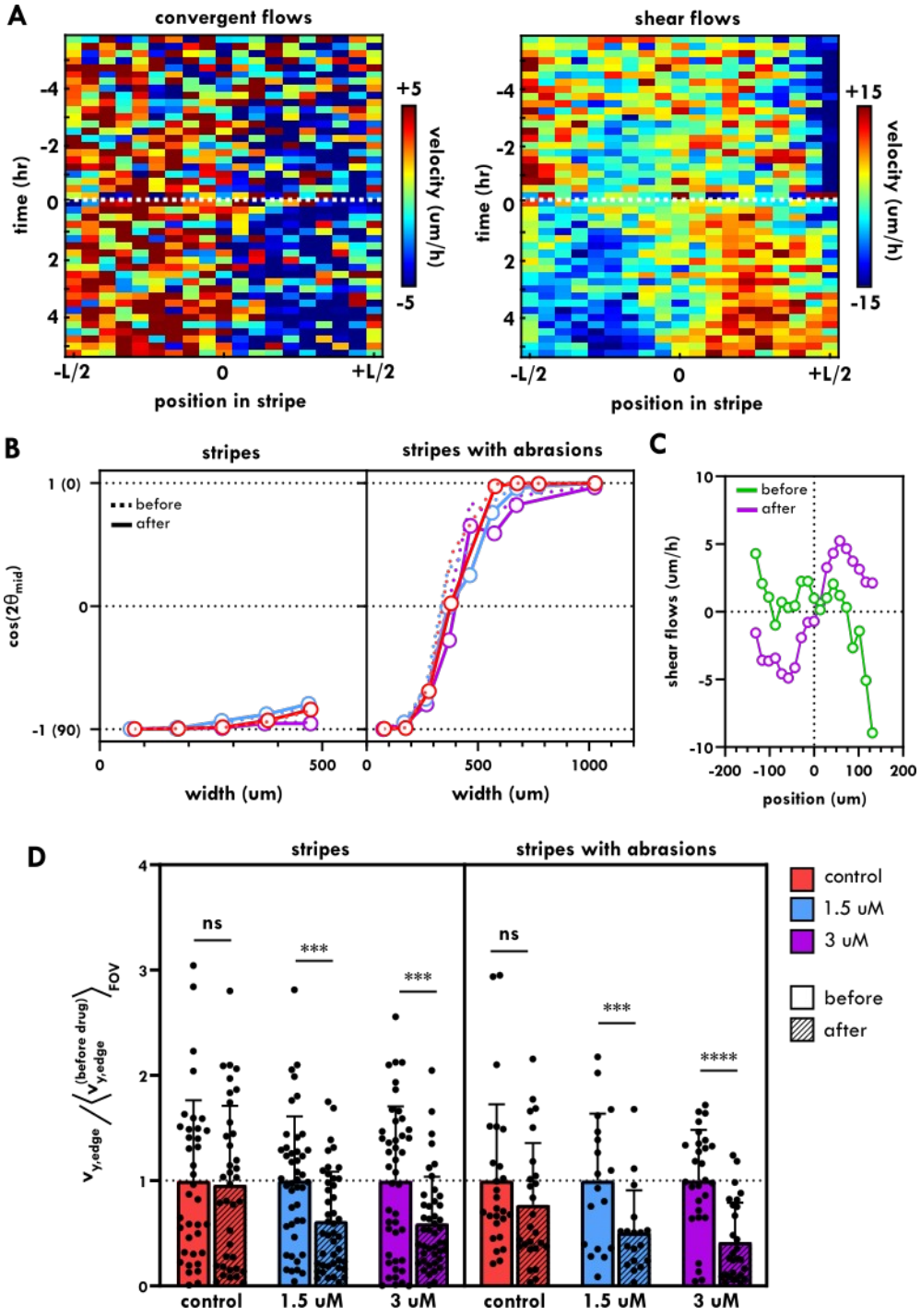

Figure 3 – 19. Effect of the addition of blebbistatin during the course of an experiment. (**A**) Velocity profiles during the experiment for a stripe with abrasions of 263 µm. We added 3 µM of blebbistatin a t = 0h. Left: convergent flows; right: shear flows. (**B**) Middle angle θ_{mid} for stripes of increasing width. There are no changes in cell orientation with drug addition. Dashed line: before drug; plain line: after drug. (**C**) Shear flow profiles before (green) and after (purple) 3uM blebbistatin addition, on the previous exemplified FOV. (**D**) Changes in $v_{y,edge}$ before and after blebbistatin addition. Speeds decrease significantly with drug addition. The speeds before drug addition are normalized by their mean value. Plain bars: before drug addition; dashed bars: after drug addition. Red: control; blue: 1.5 uM blebbistatin; purple: 3 uM blebbisatin.

Because the cellular orientation did not change in response to the inhibition of contractility, we conclude that the geometrical transition was not directly ruled by activity but by geometrical constraints only. Indeed, changes in the shear flows velocities did not result in changes in orientation. Thus μCG mode of guidance overrode cellular flows dynamic and active effects.

We did other experiments by adding blebbistatin or Y27632 three to six hours before starting the experiment. Concentration of these inhibitors were respectively 2 μM and 10 μM. In this case, we observed a small but significant shift of the geometrical transition compared to control conditions (Fig. 3 – 21A): $L_c^{(blebb)}$ = 314 μm (95% CI 307 – 322 μm) for blebbistatin-treated samples and $L_c^{(Y27632)}$ = 365 μm (95% CI 357 – 373 μm) for Y27632-treated samples. This shift in the transition was not associated with a decrease in shear flow speeds (at +L/2) and thus the activity (Fig. 3 – 21B). Shear flows speeds for drug-treated samples were not significantly different from control sample.

These observations appear to be in contradiction with what we observed when we added the drug during the experiment. However, the drug may have other effects than the decrease in contractility, for example a decreased friction with the substrate, a change in the flow-alignment parameter or a change in cell shape. At long timescales, it is possible that cells self-organize to adapt these changes of conditions.

3. 2. 2. Non-active cells: NIH-3T3

We finally tested the passive nature of the geometrical transition by using NIH-3T3 cells. These cells do not develop a spontaneous flow transition nor a tilt angle on non-abraded stripes either because they are not very active or because their friction with the substrate is too high[174].

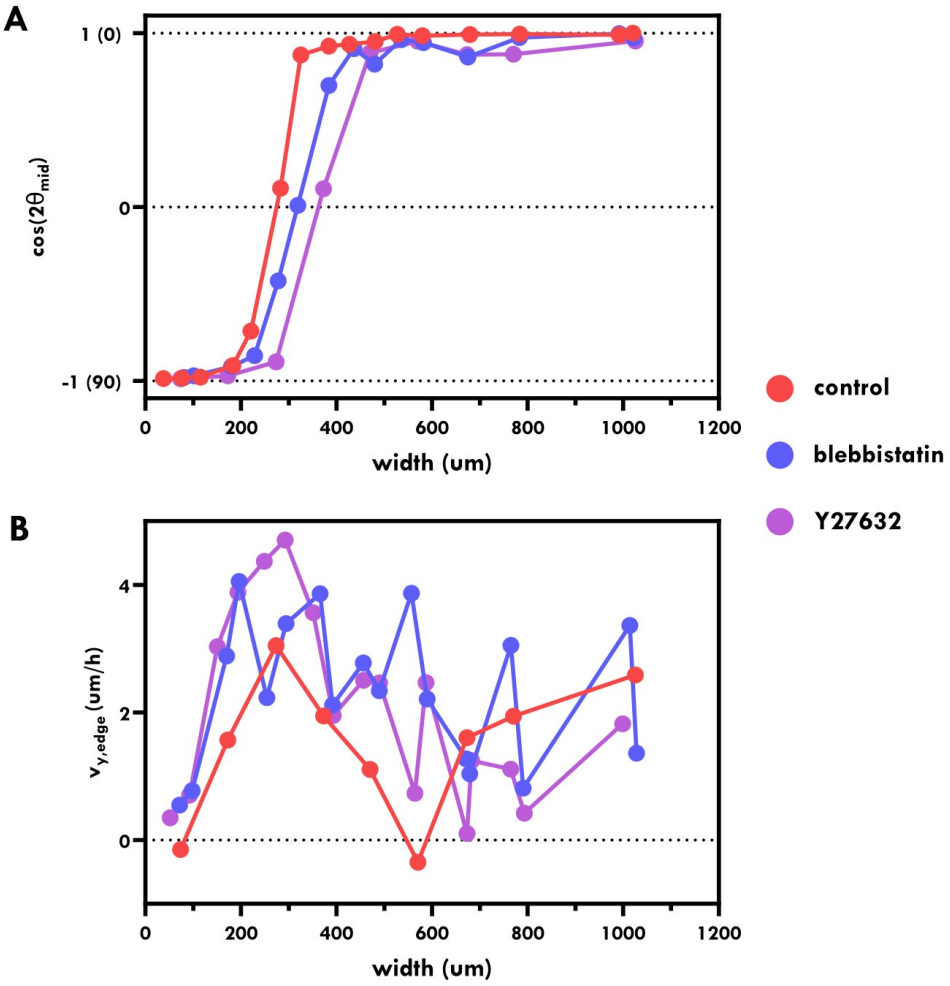

Figure 3 – 21. Effect of drug treatments decreasing cell activity on the geometrical transition. Cell orientation θ_{mid} (**A**) and shear flows $v_{y,edge}$ (**B**) for stripes of increasing width and for sample treated with 2 µM blebbistatin and 10 µM Y27632. The transition is significantly shifted from $L_c^{(control)}$ = 274 µm to $L_c^{(blebb)}$ = 314 µm and $L_c^{(Y27632)}$ = 365 µm while shear flows are not significantly impacted.

On non-abraded stripes, cellular orientation in the middle and edges of stripes remained strictly parallel to the edges similarly to what has been observed by Duclos et al. In contrast, for stripes with abrasions, the geometrical transition was observed for L_c = 552 µm (95% CI 523 – 581 µm) while cells at the edges remained parallel to the mesocale stripes (Fig. 3 – 22). The existence of the geometric transition for such low activity cells confirmed that µCG effects impose the orientation of the cells for wide enough stripes, independently of the system activity that mostly control cellular flows. Here again, the geometrical transition seems to be discontinuous unlike the classical Fréedericksz transition.

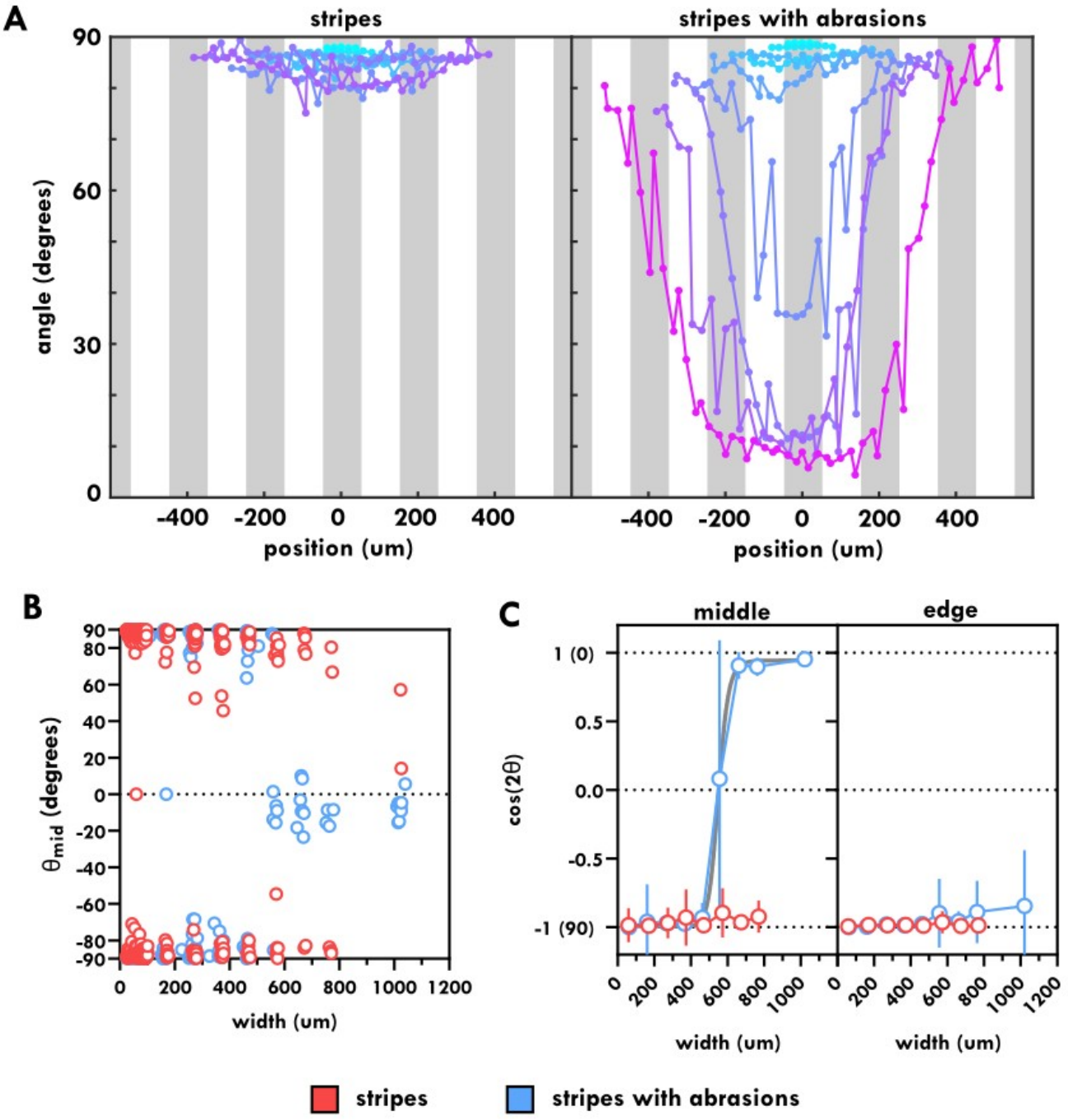

Figure 3 – 22. 3T3 cells orientation on multiscale substrates. (**A**) Cell orientation profiles for 3T3 cells. On non-abraded stripes, cells orient close to the direction of the stripe. Left: stripes; right: stripes with abrasions. (**B**,**C**) Middle and edge angle for stripes of increasing width. On abraded stripes, a geometrical transition is observed for $L_{c,p}$ = 552 μm. Red: stripes; blue: stripes with abrasions; gray line: sigmoid fit.

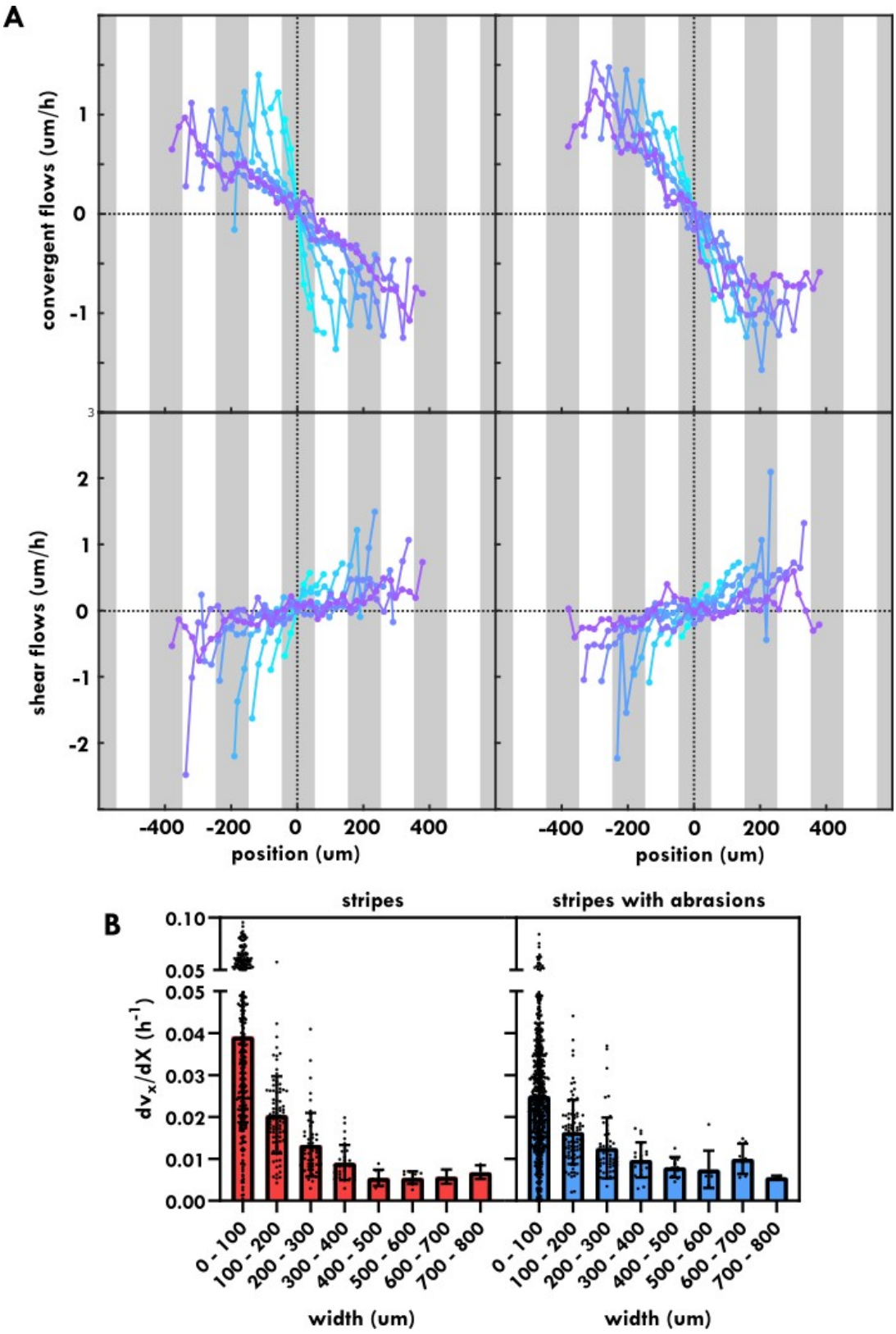

Figure 3 – 23. 3T3 cells flows. (**A**) Convergent (top) and shear flows (bottom) profiles for 3T3 cells on stripes and stripes with abrasions. Left: stripes; right: stripes with abrasions. (**B**) Slope of convergent flows for stripes of increasing width.

Flow profiles for these cells followed the same trends between stripes and stripes with abrasions. Convergent flows profiles were similar to those of C2C12 cells confirming that they result from cell division/extrusion rate and not from cell activity. The slope in convergent flows changed very significantly for non-abraded stripes whereas the effect was not as strong in presence of abrasions. Shear flow speeds were less than 2 μm/h on average for both substrates which underlines the low activity of such cells, much smaller than what we found for C212 cells.

All these observations confirm the passive nature of the geometric transition. Cellular orientation is affected only because of μCG independently of cellular flows and system activity.

3. 3. Active transition

We focus here on small widths between 20 and 200 μm where the active Fréedericksz transition has been observed previously by Duclos et al.[174] For C2C12, the transition length was reported to be $L_{c,a}$ = 30 ± 4 μm. In this analysis, we kept only the FOVs with a clear shear flow profile that is to say, FOVs with shear flows at the edges (±L/2) of opposite sign. We looked at the shear flows speed at the edges $v_y(\pm L/2)$ as well as at the angle in the middle of stripes θ_{mid} and their evolution with stripes' widths (Fig. 3 – 24A,B).

The biological variability was very large and prevented us from estimating a transition directly. On binned data (binning box = 10 μm), we observed that at widths smaller than $L_{c,a}$ = 90 μm, the middle angle θ_{mid} and shear speeds $v_{y,edge}$ were close to zero. This confirmed the existence of a transition but, unfortunately, the scatter of the data that come from different experiments is still too large to estimate a critical width and even more to verify the shape of the transition for widths larger than $L_{c,a}$. In these conditions, we cannot reliably compare substrates with and without abrasions or compare our experiments and those of Duclos et al.

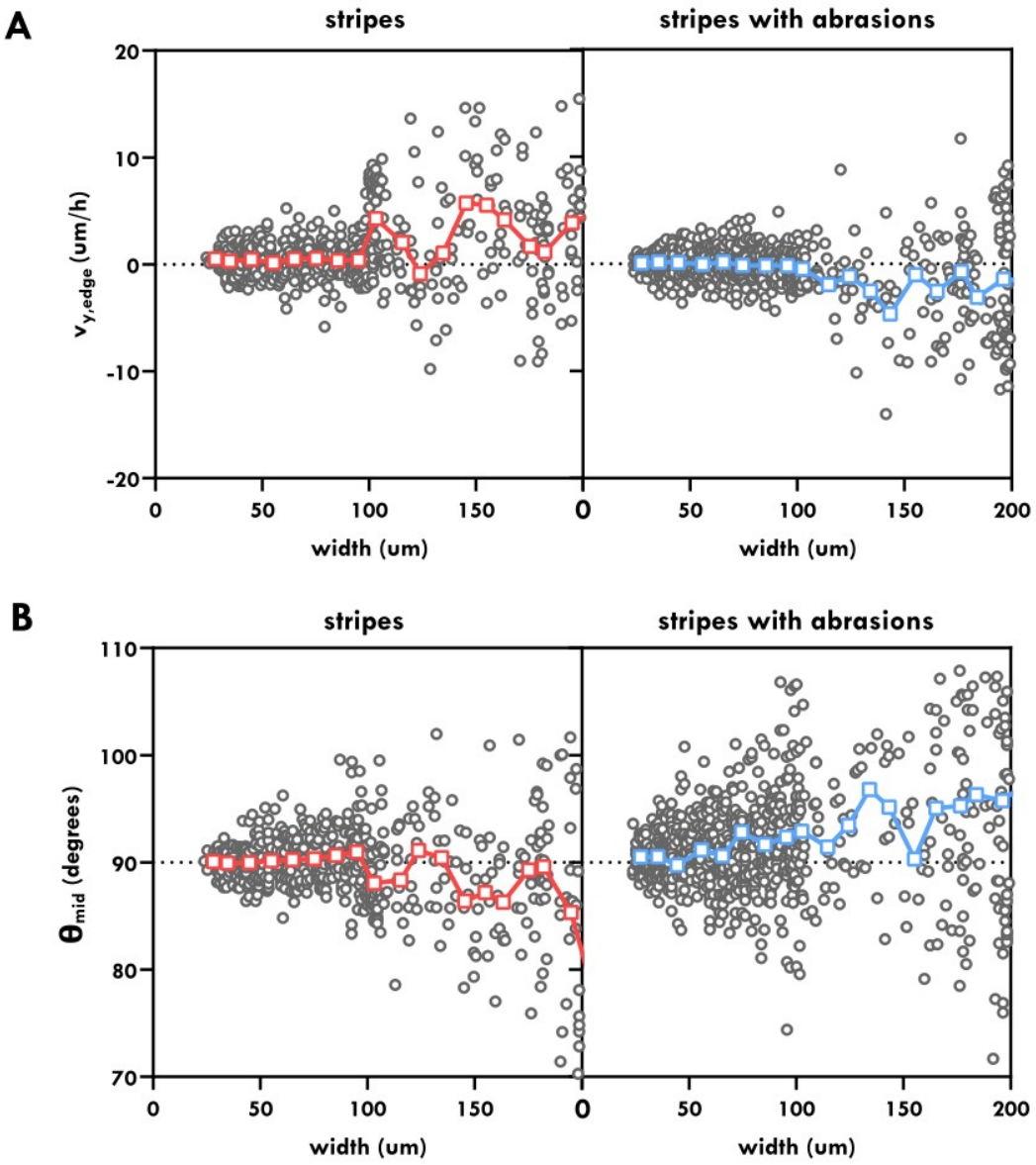

Figure 3 – 24. Active transition. Evolution of the shear velocity at edges (**A**) and middle cell angle θmid (**B**) for stripes of small width (20 – 200 µm). The binning box of our dataset is 10 µm. The high biological variability makes the measurement of an active transition difficult. Nevertheless, on both substrates, we remark the middle angle and the speed at the edge are close to zero at small widths. Red; stripes; blue: stripes with abrasions.

3. 4. Oblique microabrasions field

In this part, we vary the effective field resulting from the topography. Changing the topography in our system is difficult and it would be hard to compare two differently abraded substrates together. Therefore, we decided to use another approach by tilting the abrasion field by

an angle α compared to the x-axis. The field **H** can be decomposed in a parallel (to the stripe direction) contribution $H_{\parallel}$ and a perpendicular contribution $H_{\perp}$, so that

$$\begin{aligned} H_{\perp} &= H_0 \cos\alpha \\ H_{\parallel} &= H_0 \sin\alpha \end{aligned} \quad \text{with } -90° < \alpha < +90°$$

As we were looking for mean-field effects across the x-axis, we could tune $H_{\perp}$ from 0 to H_0 by simply varying the angle α (Fig. 3 – 25A).

We looked at the evolution of the middle angle with the stripes' width at various angles α between the stripe and the microabrasions (Fig. 3 – 25B). For thin stripes, cells oriented parallel to the edges while for wide stripes they seemed to orient parallel to the μCG field. However, contrary to the perpendicular case, there is no abrupt transition between these two modes of guidance but a smooth evolution with no critical width.

We measured θ_{mid} in stripes and varied the angle α between 0° and ±90°, the latter corresponding to the stripes direction (Fig. 3 – 25C,D). For thin stripes, the cells' orientation stayed close to 90° and this orientation was independent of the abrasions direction. For large stripes, in the regime where cells are oriented with μCG in the middle of the stripes, θ_{mid} was very close to α but there was a small deviation of cell orientation from the direction imposed by μCG. This result is very different from passive systems where nematics would completely follow the direction of the field after the Fréedericksz transition. Here this deviation reflects a coupling between the alignment induced by the microscale field and flows generated by activity of the system. We now proceed to discuss these results within the framework of active matter presented earlier.

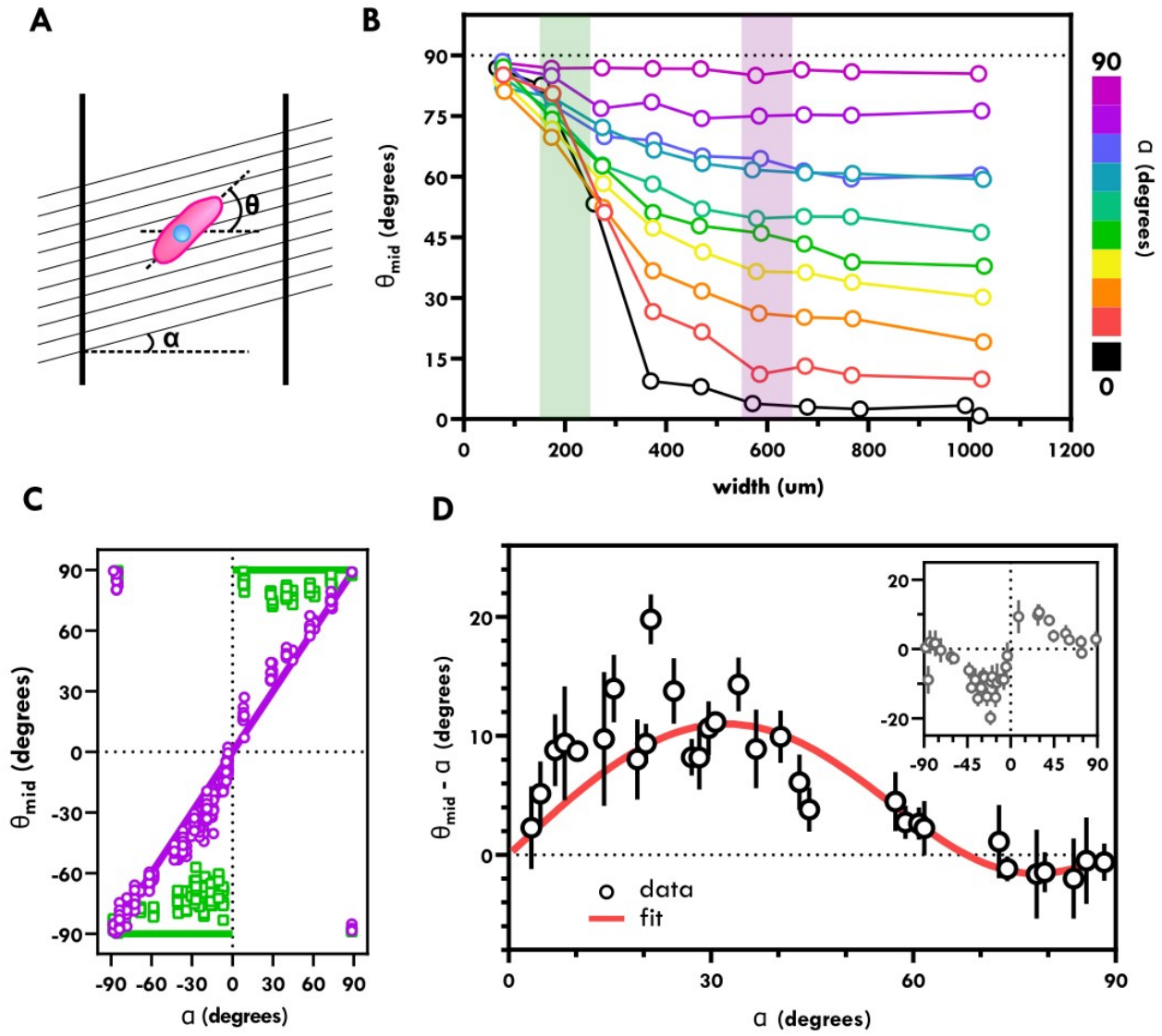

Figure 3 – 25. Tilting the direction between microabrasions and stripe direction. (**A**) Abrasions make an angle α with the x-axis. Cellular orientation is given by the angle θ. (**B**) Evolution of cell angle in the middle of the stripes versus the width of stripes for various angles α. (**C**) Evolution of the cell angle in the middle of the stripes versus the abrasion angle α. Colors corresponds to the stripes' widths highlighted in (B). For thin stripes (150<L<250 μm), cells orient close to 90° while for wide stripes (550<L<650 μm), cells globally follow the general abrasions direction although they slightly deviate from it. Purple line: θ = α; green line: θ = 90°. (**D**) Evolution of the deviation of θ_{mid} from abrasion direction α versus the abrasion angle α wrapped between 0° and 90° (insert: between -90°< α <90°). With our model, we deduced a value of the flow-alignment parameter ν = -1.4. Red curve: fit with our model. These results are taken for widths far from the active and geometric transitions (width range = 550 – 650 μm).

4. Theoretical model

4. 1. Model of active Fréedericksz transition with an applied field

4. 1. 1. Perpendicular microabrasions

To understand the effect of an applied field on active nematics, Louis Brézin and Jean-François Joanny have developed an active gel theory (see Chapter I. 2. 2. and thesis of Louis Brézin[191]). We used the notations of Figure 3 – 8 for the problem description. In all the following, quantities related to the active Fréedericksz transition described in I. 2. 3. 3. are noted with an index "$_a$". Similarly, quantities related to the "passive" transition described in I. 2. 2. 2. resulting from the analogy with the magnetic field are noted with an index "$_p$". Finally, quantities related to the multiscale system are noted with an index "H".

The nematic phase has a distortion energy density given by (1. 2.).

$$f_d = \frac{1}{2} K [(\nabla \cdot \boldsymbol{p})^2 + (\nabla \times \boldsymbol{p})^2] \quad (1.\ 2.)$$

In analogy with adding a magnetic field in the passive case (see I. 2. 2. 2.), the abrasion field adds a contribution to this free energy density that reads

$$f_H = \frac{-\chi}{2} (p \cdot H)^2 \quad (3.\ 1.)$$

By adding the contributions of distortions (1. 5.) and the microabrasions field (3. 1.) then by minimizing the free energy $F = \int (f_d + f_H) d\boldsymbol{r}$, the perpendicular contribution of the molecular field is rewritten as

$$h_\perp = K \partial_x^2 \theta - \frac{\chi}{2} \sin(2\theta) H^2 \quad (3.\ 2.)$$

With this modified molecular field, a perturbation analysis gives the first stable mode of the transition

$$q_{c,H}^2 = \frac{-2\xi \Delta\mu (\nu+1)}{K(4\frac{\eta}{\gamma} + (\nu+1)^2)} + \frac{\chi H^2}{K} = \pi^2 (\frac{1}{L_{c,a}^2} + \frac{1}{L_{c,p}^2}) = \pi^2 \frac{1}{L_{c,H}^2} \quad (3.\ 3.)$$

where $L_{c,a}$ is the active Fréedericksz transition width described by Duclos et al. in (1. 19.) and $L_{c,p}$ is the passive Fréedericksz transition width of equation (1. 10.).

As a consequence, the transition length $L_{c,H}$ in stripes with abrasions is expected to be smaller than the transition length $L_{c,a}$ in non-abraded stripes. As the shear flows result from cell's activity, they are not directly modified by the presence of the abrasions. Only the cells' orientation is modified because the molecular field $h_\perp$ is affected by the field. It changes the orientation gradient and impacts therefore the shear flow indirectly through the coupling of the equations. In the theoretical model, equation (1. 20.) and (1. 21.) are only slightly modified close to the transition

$$\theta=\frac{\pi}{2}+\theta_{0,H}\sqrt{\frac{L-L_{c,H}}{L_{c,H}}}\cos\left(\frac{\pi x}{L}\right)+O\left(L-L_{c,H}\right) \quad (3.\ 4.)$$

$$v_y=\frac{2\theta_{0,H}\pi K}{\left(L_{c,a}(\nu+1)\gamma\right)}\left(\frac{L_{c,H}}{L_{c,a}}\right)\sqrt{\frac{L-L_{c,H}}{L_{c,H}}}\sin\left(\frac{\pi x}{L_{c,H}}\right)+O\left(L-L_{c,H}\right) \quad (3.\ 5.)$$

$$\text{with} \quad \theta_{0,H}=\sqrt{\left(\frac{\left(\frac{4\eta}{\gamma}+(\nu+1)^2\right)^2-\frac{2\zeta\Delta\mu}{\chi H^2}(\nu+1)\left(\frac{4\eta}{\gamma}+(\nu+1)\right)^2}{\left(\frac{4\eta}{\gamma}+(\nu+1)^2\right)^2-\frac{2\zeta\Delta\mu}{\chi H^2}\left(\frac{4\eta}{\gamma}(1+4\nu)+1+\nu^2(3+4\nu)\right)}\right)}$$

Thus, we expect the orientation and shear flows in the presence of the abrasions to still scale as $\sqrt{\left(L-L_{c,H}\right)}$ as in the active Fréedericksz transition in absence of field.

4. 1. 2. Oblique microabrasions

In our system, active shear flows compete with passive μCG to guide the cells' orientation. We showed that we were able to impose a cellular orientation with microabrasions that overrode the active contribution materialized by shear flows. In the model, the perpendicular contribution of the molecular field (3. 2.) for an oblique microabrasion field reads

$$h_\perp=K\partial_x^2\theta+\frac{\chi H^2}{2}\sin\left(\alpha-\theta\right) \quad (3.\ 6.)$$

Calculations using (3. 6.) in equations (1. 16.) and (1. 17.) give an expression of θ(x) that depends on α. Because of activity, the orientation of the cells in the middle of the stripes θ_{mid} did not follow

exactly the abrasions direction α. In the limit where the mode of guidance imposed by abrasions is dominant in front of the activity $\left(\frac{\zeta \Delta \mu}{\chi H^2} \ll 1\right)$, the difference $\theta_{mid} - \alpha$ could be written as

$$\theta_{mid} - \alpha = \frac{-\zeta \Delta \mu}{\chi H^2} \frac{\sin 2\alpha \left(\nu \cos 2\alpha - 1\right)}{4\frac{\eta}{\gamma} + \nu^2 - 2\nu \cos 2\alpha + 1} + O\left(\left(\frac{\zeta \Delta \mu}{\chi H^2}\right)^2\right) \quad (3.\ 7.)$$

The activity creates a shift in cell orientation with the imposed direction even for widths larger than $L_{c,H}$. Given the expression of (3. 7.), it is then possible to measure the flow-alignment parameter ν in our system by taking advantage of the competition between active and geometric modes of guidance. This measurement should be robust as the crossing point $\theta_{mid} - \alpha = 0$ is independent of the other parameters of the system so that $\cos(2\alpha) = 1/\nu$.

4. 2. Comparison between model and experiments

From our experiments in III. 3. 1. (Fig. 3 – 14), we identify a new transition in orientation for L_c = 274 µm. This geometric transition is more related to contact guidance effects than to collective migration of cells. As the stripes' width increases, cell orientations in the bulk are less influenced by the torques created by boundaries and orient following the underlying microtopography. However, the identified transition is not a classical Fréedericksz transition as it shows a clear discontinuity.

For that reason we could not compare the theoretical variations of the middle angle $\theta \propto \theta_{0,H} \sqrt{\left(\frac{L - L_{c,H}}{L_{c,H}}\right)}$ to the experimental observations close to the transition. Deviations from this expected theoretical law may be due to a large surface friction with the surface.

Our experiments with drugs lowering contractility and with non-active NIH-3T3 cells support the hypothesis that this transition is independent of the activity of the cells. Indeed, in these cases, the geometrical transition was observed even if shear flows were decreased or almost null. The transition could not arise from contractility effects but only by contact guidance which is a phenomenon that does not require cell contractility[67,68].

From similar experiments on non-abraded stripes, Duclos et al. reported a value of the active Fréedericksz transition of $L_{c,a}$ of 30 ± 4 μm. In our case, for non-abraded stripes, we could not reasonably estimate a critical length because of the large variability of the measurements at small widths (Fig. 3 – 24). Nonetheless, for widths smaller than $L_{c,a}$ = 90 μm, middle angle as well as shear flows were close to zero. Similarly, on abraded stripes, $L_{c,H}$ cannot be measured and a comparison with the active Fréedericksz transition can only be speculated.

The signature of activity in our multiscale system was evidenced by studying the effect of an oblique field making an angle α with the stripes' direction. In that case, the cells orientation did not follow exactly the orientation imposed by the microabrasions. We fitted the equation (3. 6.) to measure the hydrodynamic parameters in our system (Fig. 3 – 25D). Unfortunately we were not able to access all the parameters as the fitting procedure did not converge. We therefore fixed the value of η/γ to 1 as is commonly admitted. Given this assumption, we found the ratio between activity and abrasion field $\frac{\zeta \Delta\mu}{\chi H^2}$ = 1.18 ± 0.04, slightly larger than the assumption of the model $(\frac{\zeta \Delta\mu}{\chi H^2} \ll 1)$ which could explain the difference with the expected behaviour of the Fréedericksz transition. The most valuable result was the measurement of the flow-alignment parameter ν that we found equal to ν = -1.4 ± 0.08[d]. For an extensile nematics like ours, we expect $\zeta > 0$ and $\nu < -1$ which applies to a rod-like behaviour of the nematic particles that tends to align parallel to the shear flows. Our measurement is compatible with this affirmation.

This result is similar to the behaviour of nematics under a constant shear. The flow-alignment parameter that couples flows and orientation can then be determined by measuring the angle when stresses exerted by flows and stresses exerted by the distortions of the nematic director perfectly balance, given by $\cos(2\theta_\infty) = 1/\nu$ [1,176]. For our active nematics where shear flows arise from activity, we already measured θ_∞ in III. 3. 1. 1. For non-abraded wide stripes, the middle angle saturated at θ_∞ = 59°, thus ν = -2.1 (95%CI = -2.8 – -1.7) (Fig. 3 – 15A), close to the previous value and in accordance with our model.

d This value of ν does not depend on our hypothesis $\eta/\gamma = 1$.

To our knowledge, the parameter ν was only measured once experimentally during the elongation of the *Drosophilia* wing[192]. Its value was comprised between -10 and -1 which is in accordance with our measurements. More recently, there has been a regain of interest in the flow-alignment parameter as it controls some features of active nematic dynamics. Along with activity and friction, a flow-aligning or flow-tumbling state may lead to the appearance of laning phases or the existence of bounded defects pairs[177,178,193]. Our strategy can be used to measure the flow-alignment parameter ν for other cell types, for example for cells developing turbulent dynamics like HT1080[165] or 3T3 cells that do not present shear flows.

4. 4. A word on chirality

We address in this section the apparent chirality in our system that we have eluded in previous parts but that has been observed by Duclos et al.[174] Chirality could be defined in two ways: either by the direction of the cells θ_{mid} in the middle of the stripes or by the signs of the shear flows at the edges $v_y(\pm L/2)$. Given these two criteria, four cases are possible (Fig. 3 – 26A). Cellular orientations θ_{mid} in the direction SW-NE (resp. SE-NW) are called "positive" (resp. "negative") cases. Together with cell orientation, a positive (resp. negative) shear flows at +L/2 for a "positive" angle is associated with an extensile (resp. contractile) system.

We counted the number of FOVs for each chirality cases in our experiments (Fig. 3 – 26B,C). For both abraded and non-abraded stripes, there were much less contractile cases than extensile cases, in accordance with our previous observations that our system was extensile. For non-abraded stripes, cells oriented mostly in the positive direction and this bias increased with the stripes' width. Positive cases accounted for 80% of the observed FOVs on non-abraded stripes[e], close to the results of Duclos et al. that observed more than 90% of positive cases. For abraded stripes, the situation was more balanced as 40% of FOVs were in the positive case. We concluded that μCG effects override the collective migration effects responsible for chirality in non-abraded stripes.

e In Figure 3 – 25C, we removed stripes which width ranging from 0 and 100 μm because the biological noise for these stripe is too high.

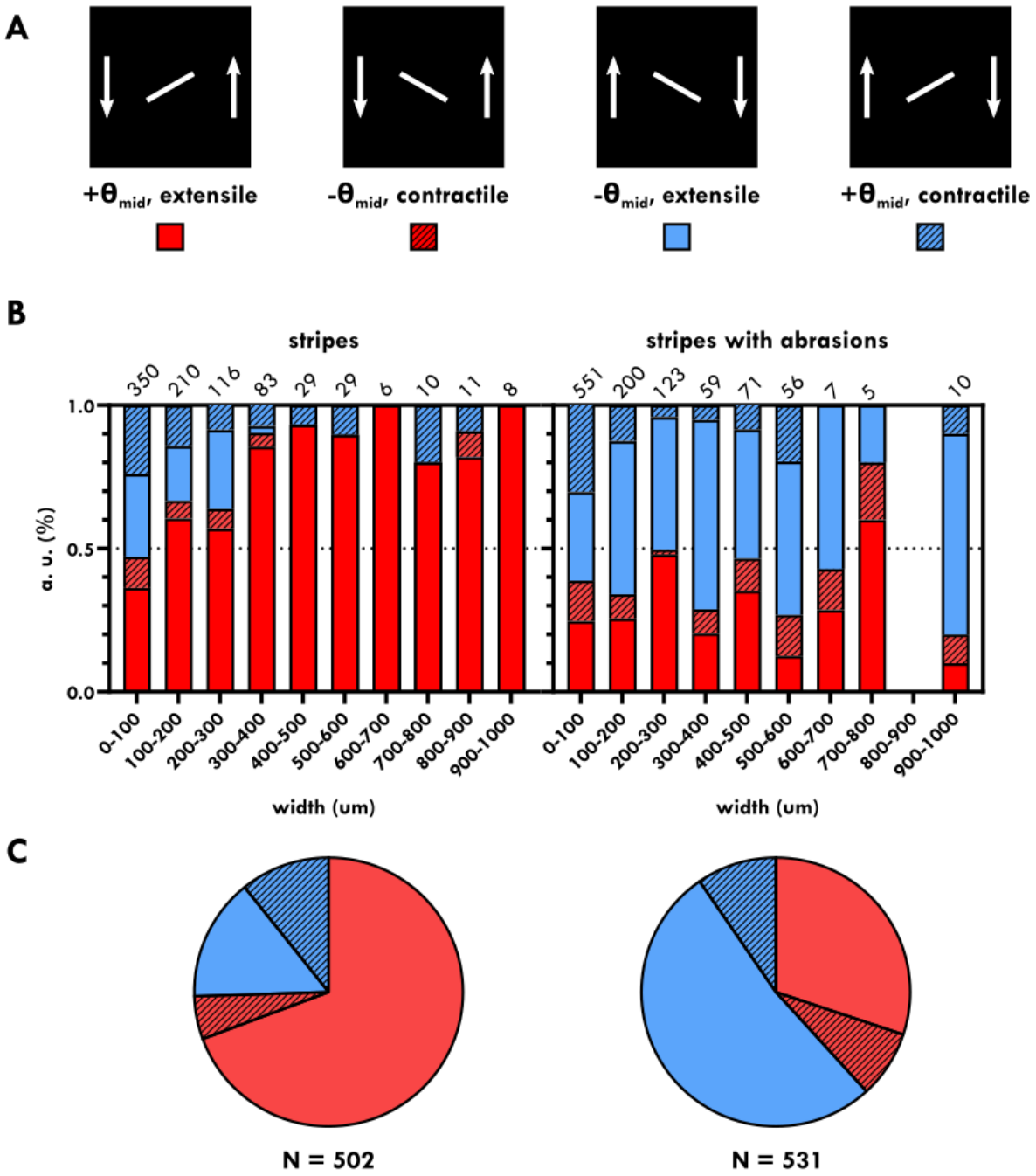

Figure 3 – 26. Chirality. (**A**) Different chirality cases in stripes. “Positive” (resp. “negative”) cases are cells in middle oriented along the SW-NE (resp. SE-NW) direction. In addition, the system is “extensile” (resp. contractile) if the shear flow at +L/2 is positive for a “positive” (resp. “negative”) case. Proportion of FOVs in each cases given the stripe width (**B**) or taken altogether for stripes larger than 100 µm width (**C**). On stripes, 80% of cases are positive while on stripes with abrasions, this proportion drops to 40%.

5. Topological defects

5. 1. Defect position and orientation

To complete our study, we focused on FOVs containing topological defects that were excluded manually from the previous analysis. Following our previous notations, we observed defects only in stripes with nearly perpendicular abrasions ($\alpha < 10°$). We observed 163 FOVs (resp. 322 FOVs) on non-abraded stripes (resp. abraded stripes) to make the statistics. We used the algorithm described in II. 4. 3. to analyze the charge and position of the defects in stripes with and without abrasions (Fig 3 – 27A). On non-abraded stripes, there were no defects for stripes thinner than 300 μm (Fig. 3 – 27B). On abraded stripes, only few defects appeared for stripes thinner than L_c where cells were all aligned in the direction of the stripes. These defects were distributed across the width of the stripe. For wider stripes, two different behaviours could be observed depending on the presence of the abrasions (Fig. 3 – 27C). On non-abraded stripes, defects distributed across the whole width, between +L/2 and -L/2. In contrast, on stripes with abrasions they were positioned at a constant distance L_d = 70 ± 40 μm from the edge. This distance was in the same order of magnitude as the coherence length ξ = 70 ± 36 μm measured on stripes with abrasions (III. 3. 2.). This region of the stripe is where the orientation gradient is the strongest as cells need to accommodate to the orientation imposed by the mG or μCG cues.

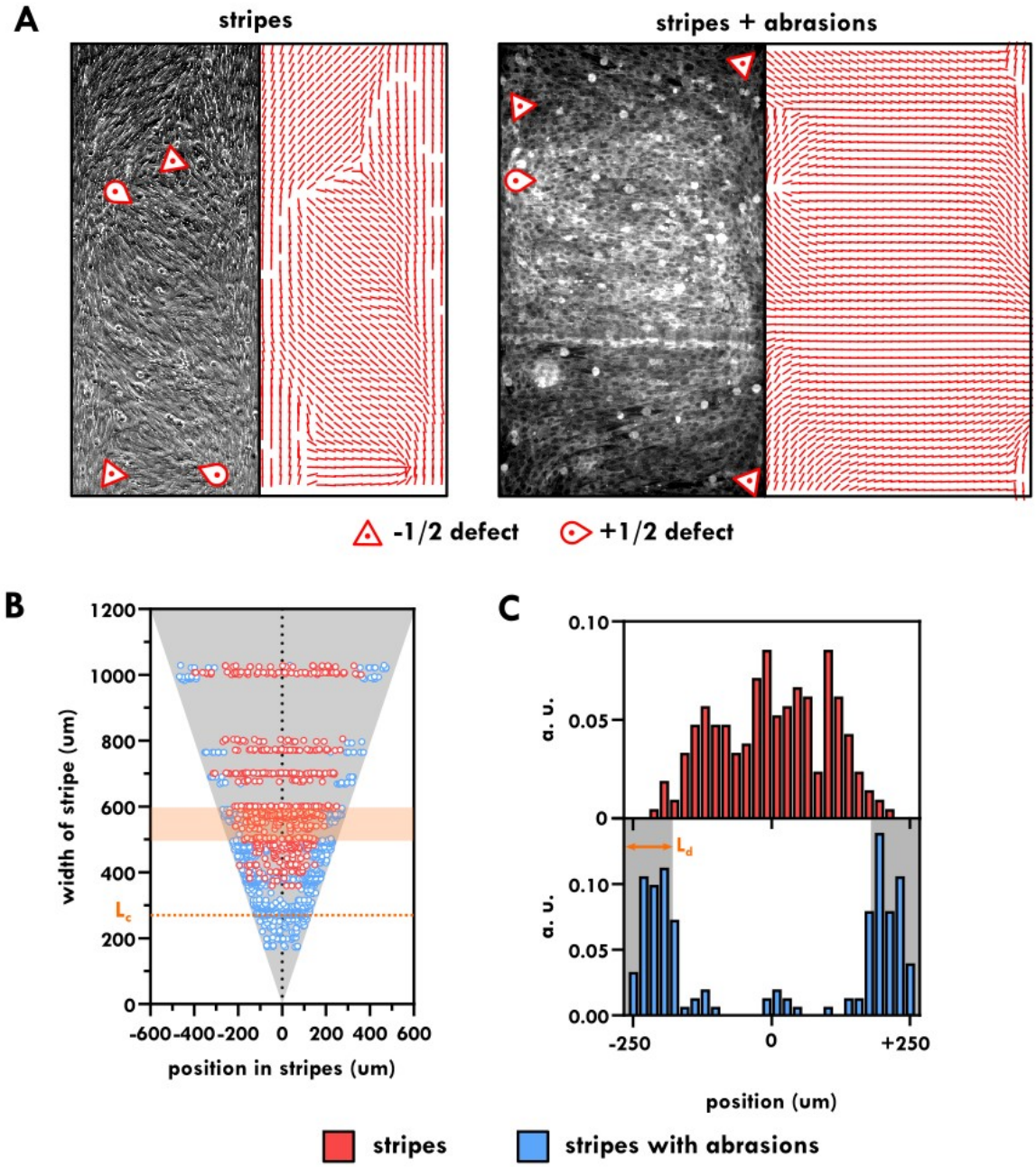

Figure 3 – 27. Defects in stripes. (**A**) Example of topological defects in system of stripes (left) and stripes with abrasions (right). Left images are snapshots of the C2C12 monolayer (stripes: phase-contrast; stripes and abrasions: actin marked). Right images represent the nematic director in the monolayer. Defects position and orientation are marked by the triangle (-1/2 defect) or the comet (+1/2 defect) symbols. Width: stripes = 600 μm; stripes with abrasions = 572 μm. (**B**) Position of defects along x-axis for stripes of increasing width. Dashed line y = 0 represents the middle of the stripe. (**C**) Distribution of defects position (normalized) across the width of stripes for stripes widths ranging from 500 to 600 μm (orange highlighted region in B). On plain stripes, defects can be found across all the width while on abraded substrates they are positioned at a distance L_d = 70 ± 40 μm from the edges. Red: stripes; blue: stripes with abrasions.

5. 2. Statistical occurrence

We looked at the proportion of both types of defects in our system. As we considered infinite stripes, the total charge should be zero and the number of defects of opposite charges should be balanced. We considered each FOV as an independent experiment. Most of the time, stripes in a FOV were around 1 mm long. On plain stripes, the number of ±1/2 defects per FOV was well balanced while on abraded stripes, there were slightly more -1/2 defects per FOV than +1/2 defects (Fig. 3 – 28A). We went in further details by looking at the number of defects per FOV (Fig. 3 – 28B). Strikingly, on non-abraded stripes, the probability to have an even number of defects per FOV was favored, most likely because the overall charge could cancel by pairs of ±1/2 defects in this configuration. On abraded substrates, a small number of defects per FOV was the most probable situation.

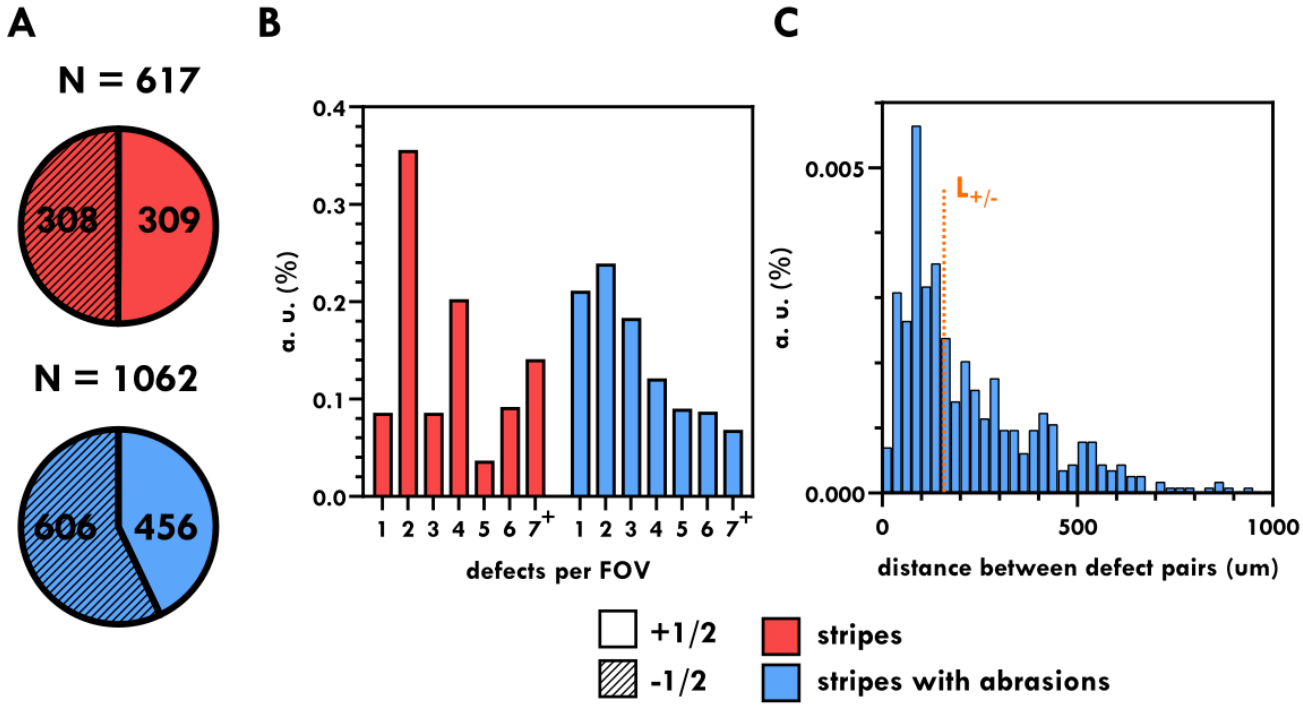

Figure 3 – 28. Defect occurrence. (**A**) Overall proportion of defects (plain: +1/2; dashed lines: -1/2) in featureless and abraded stripes. (**B**) Proportion of defects per FOV. On stripes, even number of defects per FOV is favored. Red: stripes; blue: stripes with abrasions. Number of FOVs with defects: featureless stripes = 163; abraded stripes = 322. (**C**) Distribution of distance in y-axis between defects of opposite charge. These defects were separated by $L_{+/-}$ = 158 ± 181 µm (N = 453 pairs of opposite charge defects).

On abraded stripes, defects mostly alternated in the y-direction as 83% of defects were in pairs of opposite charge ($N_{+/-}$ = 453 vs. $N_{+/+,-/-}$ = 94). In these pairs, defects were separated by a median distance $L_{+/-}$ = 158 ± 181 μm (Fig. 3 – 28C). We next focused on FOVs with an even number of defects that were the most probable on stripes. We noted these configurations pP:nN where P and N are the number of +1/2 and -1/2 defect respectively, for example a p1:n0 configuration is a FOV with one +1/2 defect and no -1/2 defect. On both substrates, configurations with two defects occurred mostly in pair of opposite defects (p1:n1) facing each other (Fig. 3 – 29A,B). This configuration allowed to accommodate in the simplest way the quasi parallel anchoring at the edges and the imposed direction of μCG at the center of the stripes. It also copes with locally extensile antiparallel shear flows close to the edges created by the nematic orientation gradient. This phenomenon looked similar to "pincement" described in I. 2. 2. 1. [160], where two domains of cells of opposite orientations are separated by a pair of ±1/2 defects. We finally looked at configurations with four defects. As we could expect, (p2:n2) configurations were favored (Fig. 3 – 29A,C). Among these configurations, the most interesting ones were square configurations were defects of opposite signs alternated in y-direction (Fig. 3 – 29D). Indeed, four defects configurations should be quite rare, however, the one with minimal distortion energy should be the square one with alternated defects. Even if they accounted for only 7 out of 39 FOVs[f] with four defects configuration, the spatial distribution of the defects was quite robust. Taking the origin at the center of the square, we saw an alternation of defects of opposite charge. In y-direction, defects were separated in average by 313 ± 123 μm. Each horizontal pair separated domains of perfectly aligned cells.

Such an analysis of the distribution of defects is complementary with our previous results and may allow a better understanding of the influence of geometrical constraints on active nematics orientation and flows. This could ultimately lead to phenomena such as cell extrusions close to +1/2 defect cores [169,194].

f Other four-defect configurations are not "squares" and look more like a kite.

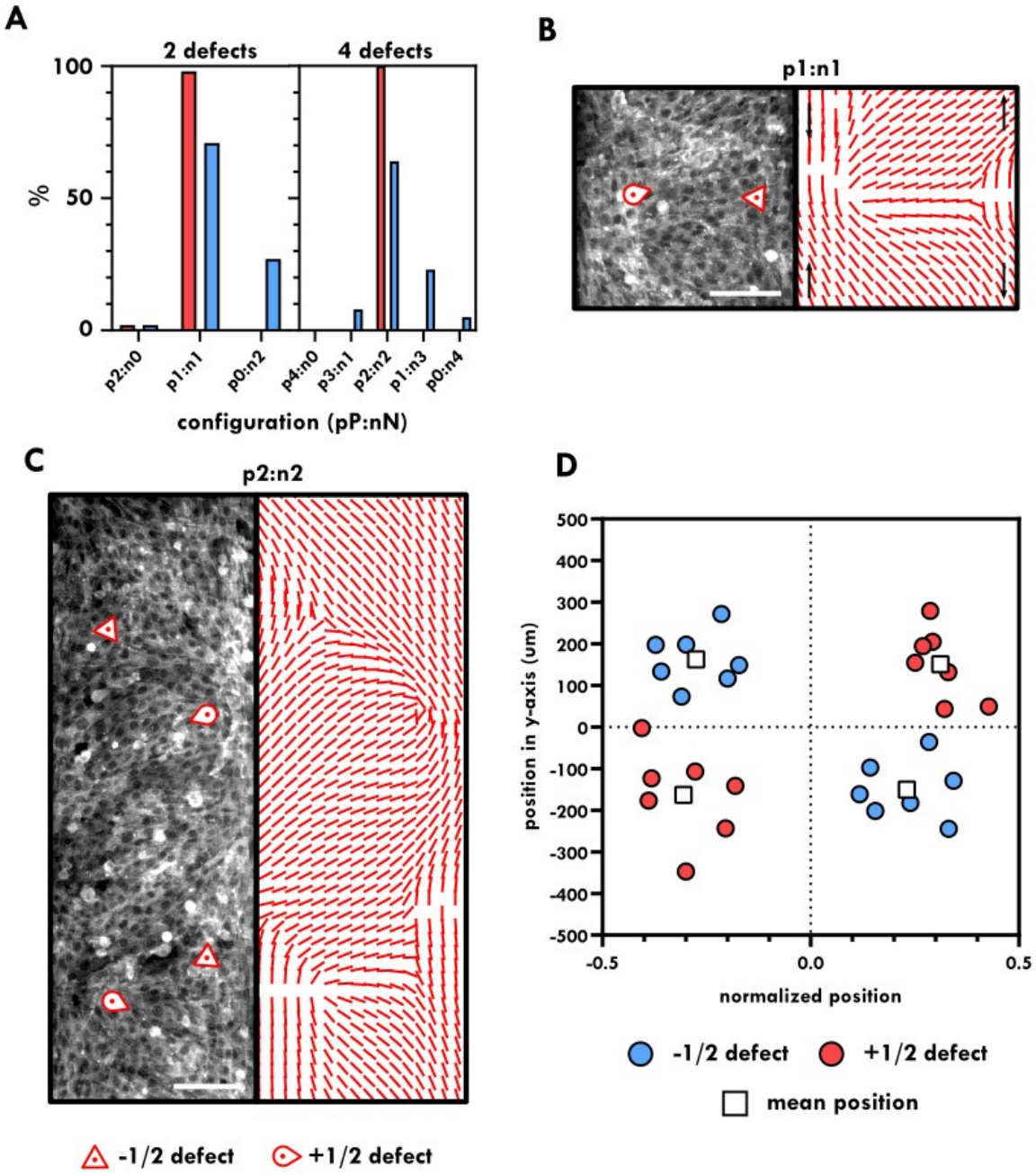

Figure 3 – 29. Defects configurations in stripes with abrasions. (**A**) Statistical occurrence of defects configurations. Configurations are denoted as pP:nN where P (resp. N) is the number of +1/2 (resp. -1/2) defects. The system favors configurations with an even number of defects. Example of stripes showing the most favored configurations (**B**) (p1:n1) and (**C**) (p2:n2). Left: actin-marked images of cells; right: map of orientation on the same images. Defects are marked with a triangle (-1/2) or comet (+1/2) symbol. Scale bar = 100 µm. (**D**) Position of defects in FOVs presenting a square configuration. The positions are calculated related to the center of the square placed on the origin of the graph. Defects of opposite charges are alternated and separated in y-direction by 313 ± 123 µm. Each horizontal pair of defects separate a perfectly aligned nematic domain. Red: +1/2 defect; blue: -1/2 defects; square: mean position.

6. Conclusion

We put in competition two modes of cellular guidance at different scales. We combined mesoscale stripes (mG) with reproducible microtopographies (μCG) obtained by abrading the glass coverslips. To do so, we designed a dedicated device together with the workshop of Institut Curie. Abraded coverslips surfaces were characterized and optimal conditions resulted in topographies 200 nm deep with interabrasions distances ranging from 100 nm to millimeter scales.

We seeded cells on both abraded and non-abraded patterned stripes and measured cells' orientation in the middle of stripes and shear flows close to their edges versus the stripes' width. On abraded stripes, we observed a marked change in cell orientation as we increased the stripes' width. For thin stripes, cells oriented along the direction of mG while on wider stripes, they oriented along the μCG. This transition occurred for L_c = 274 μm. The value of this transition was not altered by the addition of an inhibitor of contractility such as blebbistatin, even if shear flows speeds were reduced. Furthermore, poorly active 3T3 cells showed a similar transition for L_c = 52 μm. This shows that this transition was the result of geometrical effects caused by the μCG, independently of the activity. In this sense, it was reminiscent of the passive Fréedericksz transition but without showing the shape that is usually associated to it. First order Fréedericksz transitions have been theoretically predicted if the anchoring transition is weak[195] but we have no evidence that this in the case here. The strong interaction with the surface may also play an important role.

For thinner stripes on both substrates, we obtained results compatible with the active Fréedericksz transition described by Duclos et al. However, the variability in our data was too large to accurately measure a transition width.

We then modified the microabrasions field by varying the angle between the abrasions and the stripes. Far from the two previously described transitions, cells slightly deviated from the direction of μCG. This behaviour was the result of a competition between passive and active effects that we modeled via an active gel theory developed by Louis Brézin and Jean-François Joanny. The fit of this model with our data allowed us to measure experimentally the flow-alignment parameter

ν. The value of $\nu = -1.4$ was compatible with our extensile system. To the extent of our knowledge, it is the first time this value was directly measured in cellular nematics. As this parameter controls dynamical flows patterns in such nematic phases, our setup could be used to measure ν for other cell types showing different dynamical behaviour than C2C12 cells.

We completed our study by a qualitative analysis of topological defects on abraded stripes. These defects were distributed at a distance $L_d = 72$ µm from the stripes edges, where the orientation gradient was the strongest. Defects were mostly present by pairs in configurations reminiscent of the "pincement" phenomenon.

IV.

IV. Enhanced differentiation of myoblasts on multiscale substrates

This chapter develops a possible application of a phenomenon directly arising from the competition between the two perpendicular guiding cues of our previous system. So far, we studied cell collective behaviour at short timescales. In this chapter, we focus on the long timescales when cell density increases. As time goes by, convergent flows result in a 3D "cell cord" at the middle of the stripe. We will first discuss its architecture and the possible mechanisms of its formation. These cords favor cell alignment, that in turn may enhance C2C12 myoblasts differentiation. Results will be analyzed by quantifying the myogenesis state in our system and comparing it to experiments performed in featureless stripes and stripes with parallel μCG/mG guiding cues. These setups have already been described in Chapter I. 1. 2. 4.

1. Formation of 3D cellular cord

1. 1. Cell multilayering from 2D patterns

We used a setup slightly different from Chapter III. to induce competition between μCG and mG (Fig. 4 – 1). mG was still imposed by the width L of the main track but rather than abrasions, μCG was induced by micropatterned lines within these mesoscale tracks. The micro-lines were characterized by their width (noted b) and their spacing (noted a) which were chosen in such a way that cells could bridge over several lines. We named our patterns as follows:

- Adhesive featureless stripes like we used in Chapter III. were noted "S". This condition was meant to be compared with the literature and as a control.

- Patterns with μCG cues were refereed as PERP (resp. PARR) for perpendicular (resp. parallel) microscale/mesoscale guiding cues.

- For the LADDER pattern, the μCG cue was at the center but a small adhesive band existed at 40 μm from the edge of the stripe.

We made several trials to determine which pattern between PERP and LADDER was the closest to recapitulate the collective behaviour we saw in Chapter III. We first thought LADDER was the best because it allowed the parallel anchoring at the edges. However, after several observations, we switched to PERP that allowed an easier formation of the cell cord. Nonetheless, the collective

behaviour of cells on these two substrates is quite similar and led to similar cell cords after several hours. In the following experiments, the pattern used will be precised.

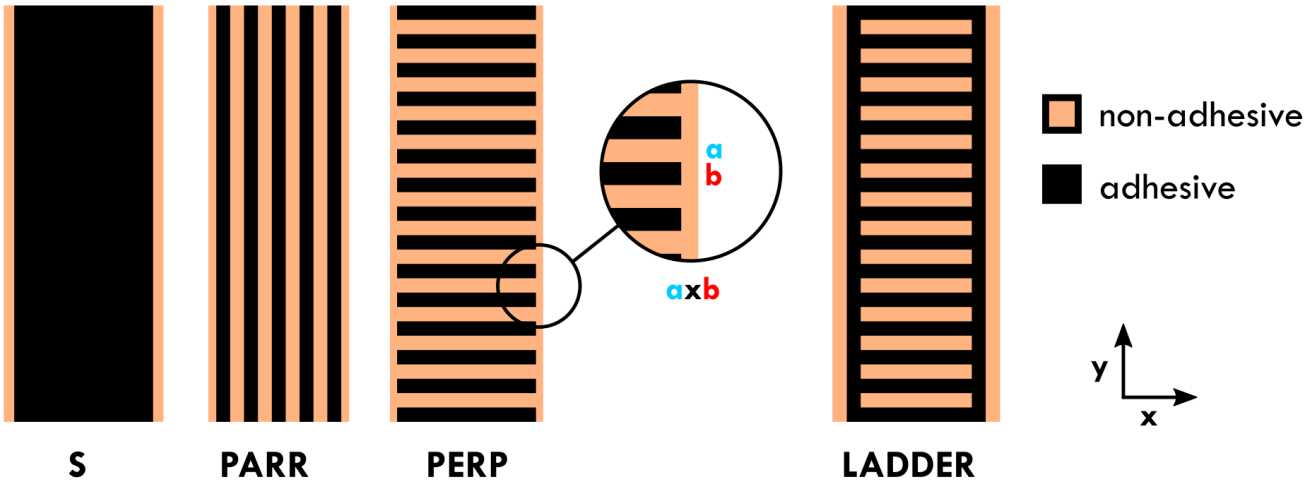

Figure 4 – 1. Patterns. Different patterns used in our experiments. Black parts are cell-adhesive parts. The microscale guidance cue geometry is denoted as in the insert.

As a first observation, we seeded C2C12 cells on PERP5x10 patterns. Cells started to form multilayers around 15h after confluence. The second layer formed at the edges of the stripes and progressed towards its center. Cells ultimately met at the center of the stripe to form a "cell cord" after 2 – 3 days (Fig. 4 – 2A). With phase contrast images, it was difficult to measure cell orientation in the cord but we could measure the decrease of the cord width with time (Fig. 4 – 2B). This cell cord formation was intimately related to the convergent flows described previously. Indeed, edge cells of the first layer oriented more and more along the μCG direction as the experiment went on. This effect was even stronger for PERP10x10 patterns where edge cells were totally pointing inward (Fig. 4 – 2C).

Cell cord formation is a direct consequence of the convergent flows. The conflict of orientations at the edges of the stripes could be the starting point of multilayering in the present case. By mixing a small amount of fluorescent C2C12 cells in WT C2C12 tissues, we could observe that layers lay perpendicularly on top of each other (Fig. 4 – 3A,C). The film of the experiment indeed suggested that cells went in the upper layer close to the edges, in accordance with our

hypothesis on the role of the edges. The second layer then moved actively via the convergent flows. Strikingly, the cells in the second layer moved perpendicularly to their long axis (Fig. 4 – 3B).

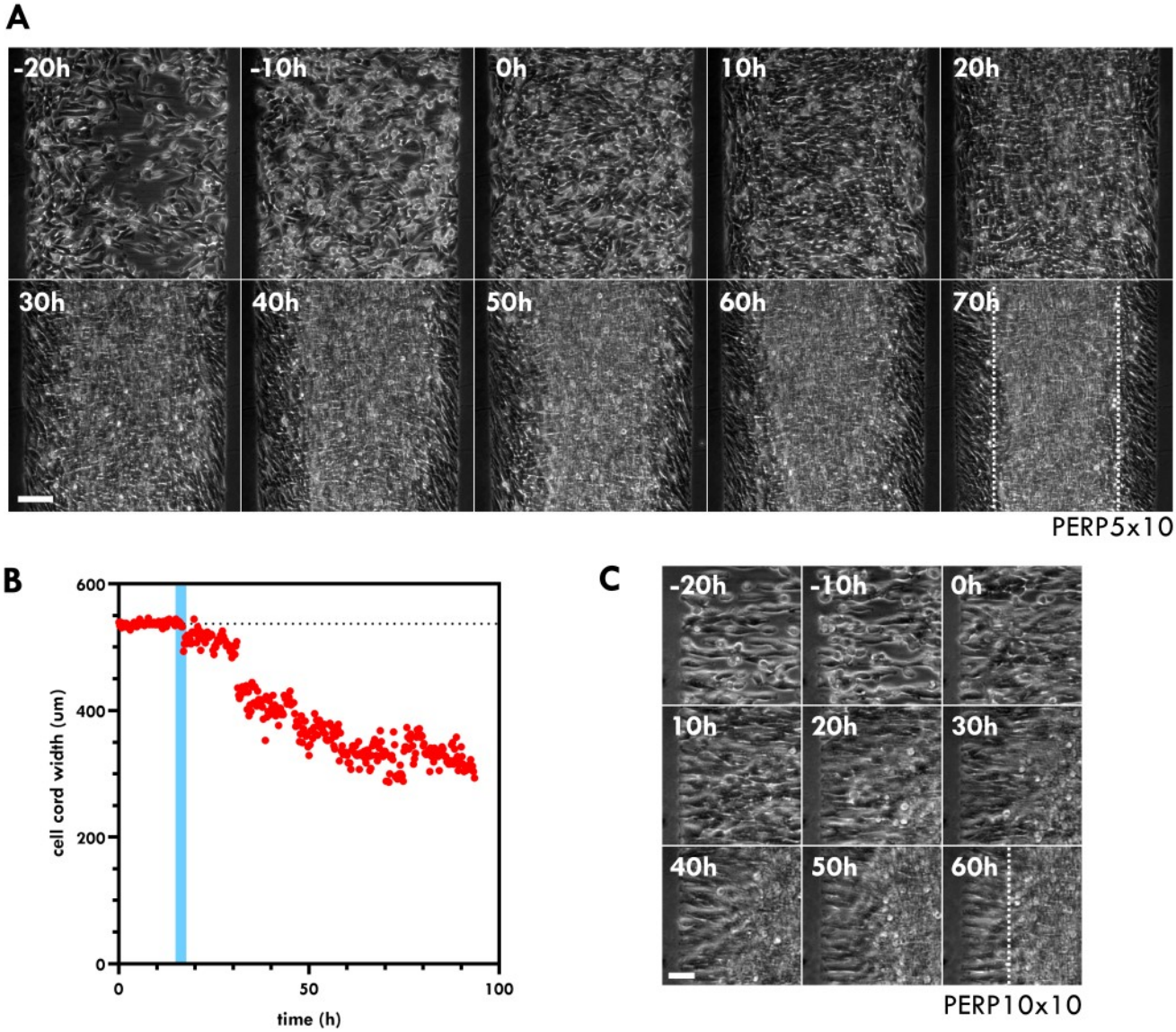

Figure 4 – 2. Formation of the cell cord. Timelapse of C2C12 cells seeded on the PERP5x10 (**A**) or PERP 10x10 (**C**) pattern observed in phase-contrast microscopy. A cell cord progressively form in the middle of the stripes, it appears in a clearer color. Time t = 0h corresponds to confluence. Dashed line: cell cord. Scale bar = 50 µm. (**B**) Cell cord width versus time. Starting from a stripe pattern of 555 µm, the 3D cell cord reaches a width of around 330 µm after 60h. Blue band: confluence; dashed line: stripe width.

Ongoing work in our lab [196] as well as studies in the literature [168,169] suggest that in unrestricted cell sheets, multilayering arises at the tip of +1/2 defects that tend to accumulate cells, favor cell extrusion and direct flows towards their tail in extensile systems. We have shown

previously in III. 5. that these defects sit close to the edges. Further work should help understand how this correlates with the formation of the cell cord.

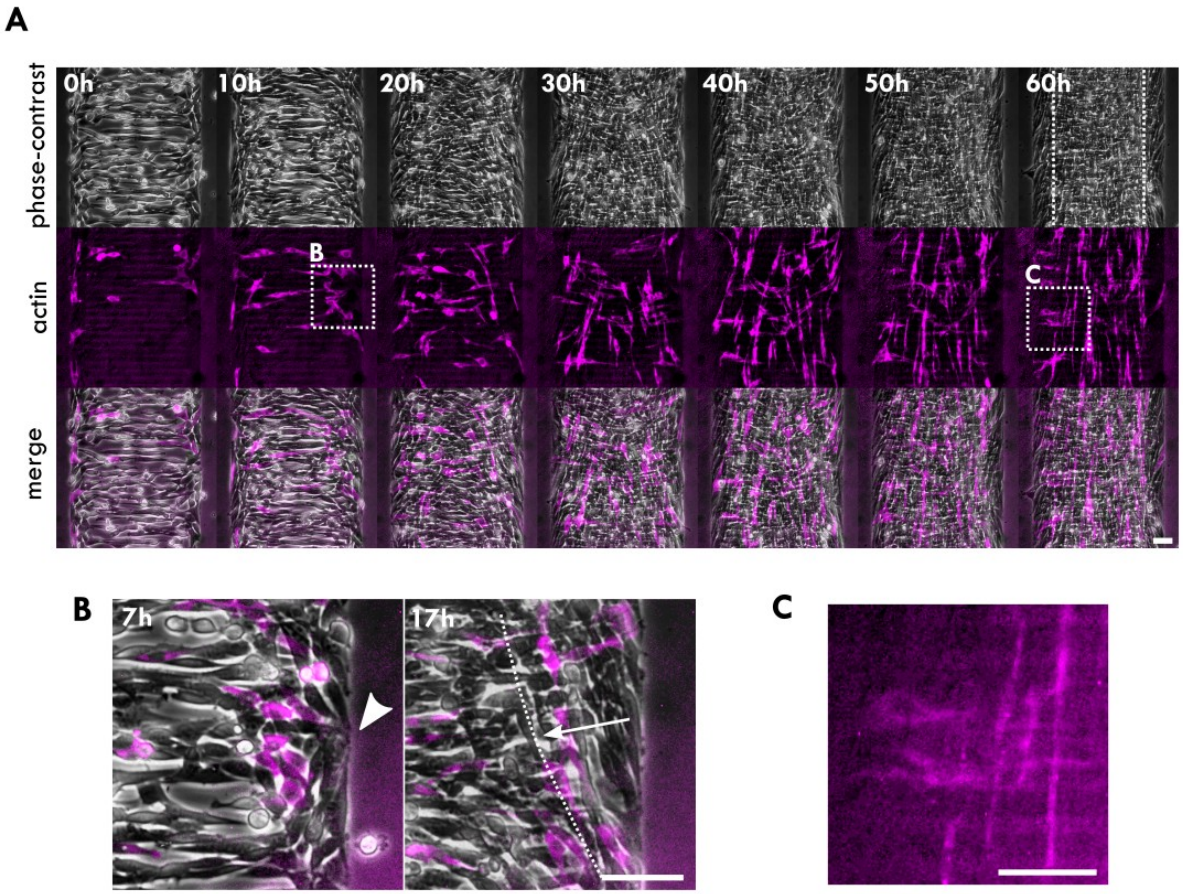

Figure 4 – 3. Individual cell motion during cell cord formation. (**A**) Images of C2C12 WT cells and 10% of C2C12 marked in actin during cell cord formation on LADDER10x5 pattern. At the end of the experiment, at least two layers of cells are perpendicularly oriented on top of each other. (**B**) Cell motion close to the edge. The second layer seems to form initially close to the edge (white arrow). Convergent flows then drive the cells inwards. Dashed lines show cell cord boundary. (**C**) Zoom on cells perpendicular on top of each other, at 60h. Scale bar = 50 µm.

1. 2. Architecture of cell cords

To better characterize the architecture of the cell cord, we observed its evolution by confocal microscopy. We seeded C2C12 cells on LADDER10x5 patterns and observed their actin cytoskeleton for 60h (Fig. 4 – 4A). Looking at a projection in the XZ plan, we observed that the cell cord looked like a flattened droplet whose height increased over the time of the experiment (Fig. 4 – 4B). We measured the height of the cord in the middle of the stripes, for stripes of several

widths (Fig. 4 – 4C). The height of the cell cord increased over the duration of the experiment but surprisingly, this increase was independent of the stripe width. By observing cell nuclei over the height of cell cord, we could observe the cell developing a layered 3D structure (Fig. 4 – 4D).

We measured the orientation of cells in the XY plane over the cord height (Fig. 4 – 5A). As long as the system remained monolayered, cells in the middle of the stripes oriented in the direction of the micropatterns. As the system multilayered, the upper layers oriented in the direction of the stripe's long axis, perpendicularly to the first layer where the cells remained oriented along the direction of the micropatterns (Fig. 4 – 5B,C).

Perpendicular orientation of cells on top of each other is an uncommon feature, yet it has already been observed in particular by Elsdale et al. on human foetal lung fibroblasts[197]. As we mentioned previously, cells formed the second layer by starting from the edges. It is likely that cell migration together with the secretion of oriented ECM proteins such as collagen or fibronectin, may possibly be at the origin of such perpendicular orientation. As cells on upper layers adhere to the apical side of the underlaying cells while cells of the first layer adhere to the glass pattern, another possible origin of the phenomenon could be the difference in cell-substrate adhesion. Finally, the difference in stiffness could explain the changes in actin organization and thus in cell orientation. For example, among the cytoskeletal changes, cells may not develop the so-called actin cap, particular actin stress fibers running on top of cells[36].

Our observations show that the cord height increased with time, rising to 40 μm, 60h after confluence. Cells in upper layers of the cord were aligned in the stripe direction perpendicularly to the bottom layer which was aligned along the μCG. Cell alignment as well as the adherence of upper layers on top of each others in this 3D structure has been shown to favor C2C12 differentiation. For these reasons, we hypothesized that our system may favorably impact the differentiation of C2C12 myoblasts in the cell cord.

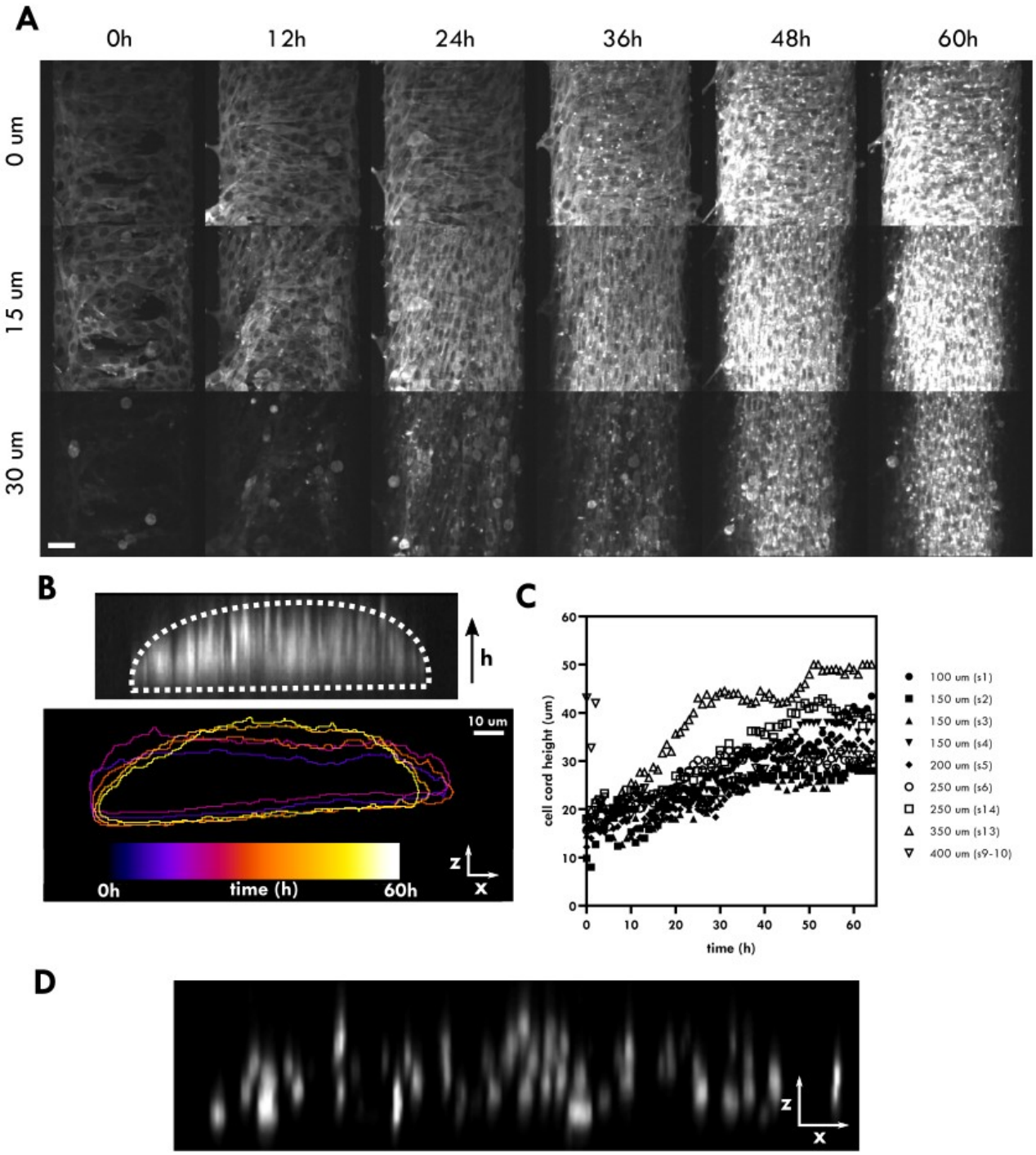

Figure 4 – 4. Cell cord height. (**A**) Fluorescent images in confocal microscopy of C2C12 seeded on LADDER10x5 pattern. Actin is marked with mCherry. Images are taken every 12h and three layers are shown, z= 0 μm, 15 μm and 30 μm. Width of the stripe = 250 μm. (**B**) Section in XZ plane of a stripe. Image of the XZ profile of the previous image across time. Scale bar = 10 μm; time t = 60h. (**C**) Cell cord height versus time for several stripes of different widths. The cell cord grows similarly independently of the stripe width. (**D**) Fluorescently marked nuclei of C2C12 cells on PERP 5x5 pattern show that cells in the cell cord organize in layers. Scale bar = 20 μm.

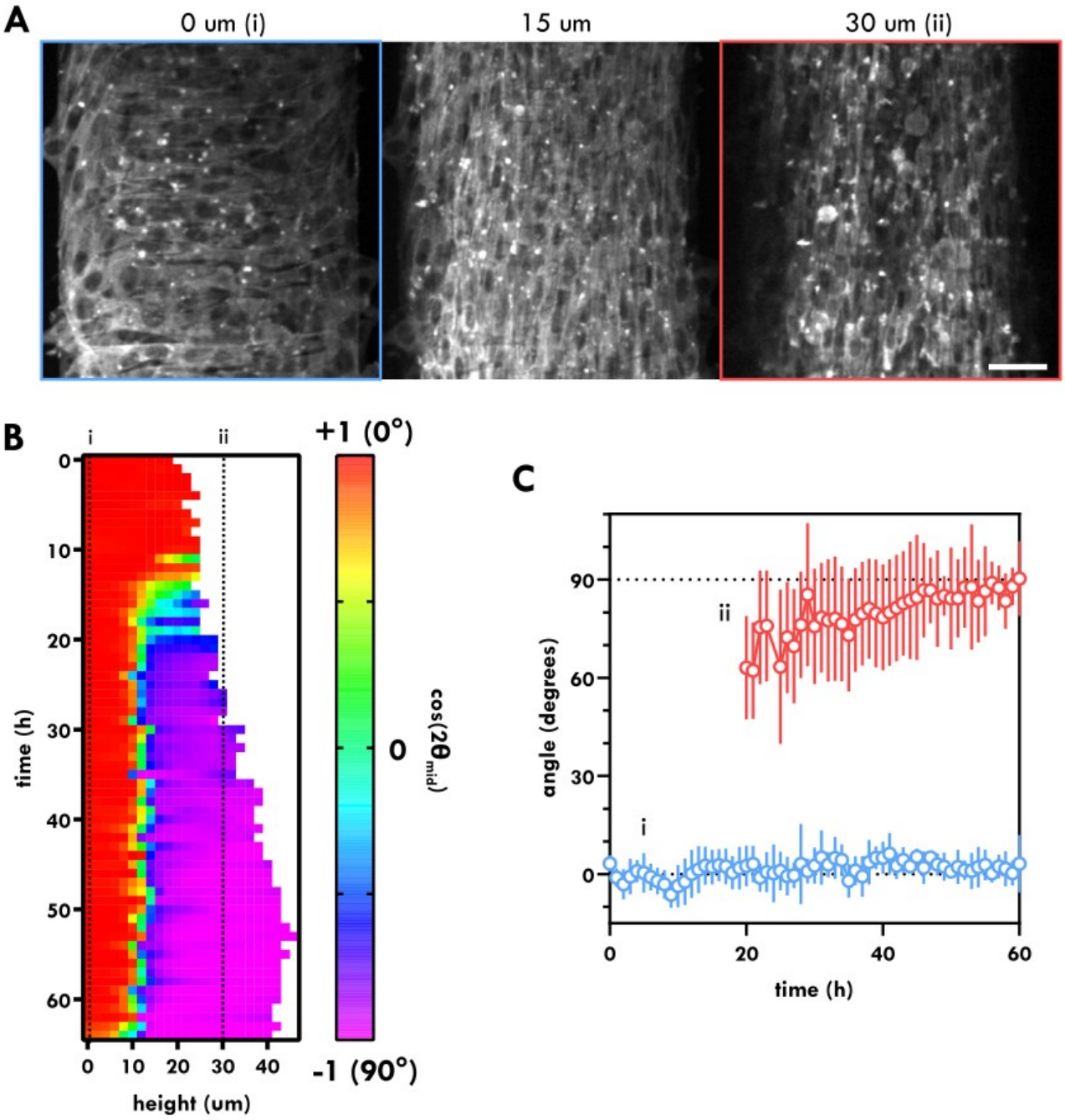

Figure 4 – 5. Orientation in layers of the cell cord. (**A**) Confocal images of C2C12 cells on LADDER10x5 pattern for several positions across the z-axis. Actin is marked. Scale bar = 50 µm. (**B**) Cell cord height and orientation of the cells in the middle of the cord over the duration of the experiment. Orientation is colorcoded. (**C**) Cellular orientation in the middle of the stripes for bottom (i; blue) and upper layer (ii; red). The first layer is oriented in the direction of the micropattern while the second layer is oriented in the stripe's direction.

2. Myoblasts differentiation on multiscale substrates

It is known that the C2C12 cells we used can be differentiated *in vitro*. The literature on this topic (see Chapter I. 1. 3. 2.) shows that prealignment of the cells favors their differentiation. So far, this alignment has been achieved by μCG or mG alone, and has been shown to positively act on the differentiation of monolayers. In addition, combining the physical cues, the cells develop in the third dimension which also favors differentiation[120]. All these observations led us to test our multiscale substrates to enhance differentiation and self-organization of C2C12 myoblasts into mature muscle fibers *in vitro*.

2. 1. Differentiation protocol

We followed the classical differentiation protocol summarized in Chapter II. 1. 3. Briefly, patterned coverslips were first coated with laminin 1:100 (from stock solution 1 – 2 mg/mL) at 37°C for at least 4h. Then C2C12 cells were seeded in proliferation medium (DMEM + 10% FBS + 1% penicillin/streptomycin). When the cells reached 70% confluence, we switched to differentiation medium (DMEM + 2% HS + 1% ITS + 1% penicillin/streptomycin). After 5 days, the sample was fixed and stained with antibodies. The whole process of differentiation is illustrated in Fig. 4 – 6.

Here we point out the key parameters that have to be considered to achieve maximal differentiation in our system:

- *Cells.* It was important to use C2C12 cells with very low passage number that expressed myoD. Indeed, after several passages, cells with proliferative phenotype, those that do not express myoD, tend to be overselected. To compare differentiation on different substrates, we made sure that we seeded cells with the same passage number. This procedure gave less biological variability between samples.

- *Substrate coating.* Coating of the substrate helped cells to differentiate as well as anchor them to the surface. We tried several coatings: none, gelatin 0,1% (from stock solution 1 mg/mL), polylysine (0.1% w/v_{H20}), laminin 1:10 to 1:100 (from stock solution 1 – 2 mg/mL). Only laminin

showed clearly positive results. On these coated substrates, cells differentiated well after 3 days. However, cells started to detach after 5 days of culture in differentiation medium, which is why we stopped the experiment 5 days after switching to differentiation medium.

- *Differentiation medium.* Several media were used in the literature to differentiate C2C12. We opted for DMEM + 2% HS + 1% ITS medium. Horse serum (HS) was meant to "starve" cells as it is less nutritive than FBS. Insulin-tranferrin-sodium selenite (ITS) is a factor that has been proven to enhance differentiation[51,198–200]. Finally, we optimized the time at which we switched to differentiation medium. From previous observations, a mature cell cord takes 2-3 days to form. Moreover, when the medium was changed, myoblasts started to fuse 2 days after the change. To have myoblasts fusing inside a developed cell cord structure, we then switched to the differentiation medium at 70% confluence.

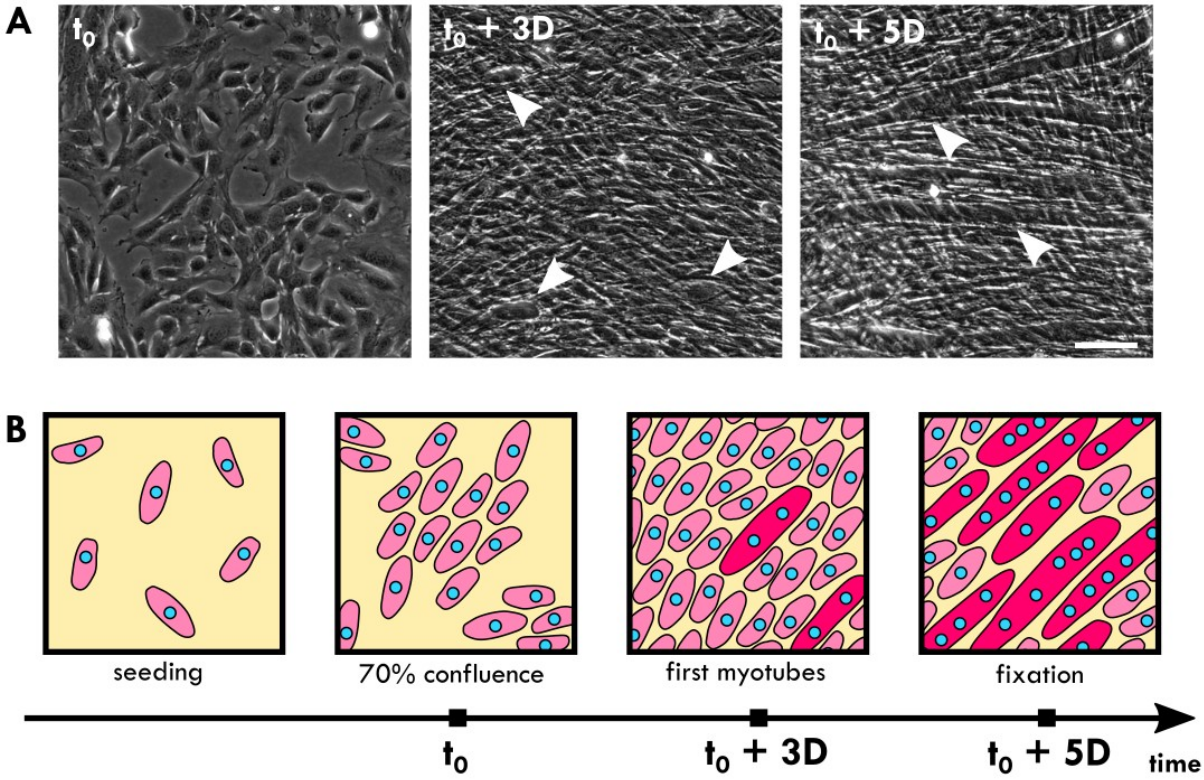

Figure 4 – 6. Differentiation of C2C12 cells. (**A**) Phase-contrast images of C2C12 cells in the process of differentiation. Myotubes are shown by white arrows. Scale bar = 100 µm. (**B**) Schematics of the differentiation process of C2C12 cells. Cells are seeded at low confluence then the culture medium is switched to differentiation medium at 70% confluence (t_0). After 2 – 3 days, first myotubes appear (dark pink). After five days, there are many myotubes. The sample is then fixed and imaged.

After five days, we prepared our samples for imaging. We took images with the spinning-disk confocal microscope to observe the tridimensional organization of the cell cord. We imaged cords over at least 0.5 mm in length, often by stitching FOVs together with the Fiji plugin "Pairwise Stitching". We analyzed our images with a homemade Fiji macro to quantify the variables of interest: the number of nuclei and the myotubes' shape. For all our experiments, we compared the three previously described patterns: S, PERP and PARR. We focused on patterns of width 100, 200, 300, 400 and 500 μm.

2. 2. A focus on upper layers of cell cords

For the particular case of PERP patterns, the multilayered cell cord structure is present. In the upper layers of the cell cord, we showed that cells orient in the direction of the stripe. This particular orientation may favor C2C12 differentiation. Here are few observations that support this hypothesis.

2. 2. 1. Nuclear shape changes in upper layers

Observations of cell nuclei in PERP10x5 patterns showed that they changed in shape and orientation between the bottom and the top layer of the cell cord (Fig. 4 – 7A and inserts). On the bottom layer cells' nuclei were rounder while on upper layers they were more elongated. Moreover, cell density seemed higher in the upper layers of the cell cord. We segmented our images and measured each individual nuclei shape and orientation to quantify this observation. Eccentricity of nuclei significantly changed between the two layers from 0.8 ± 0.12 to 0.73 ± 0.12 showing a real change of shape (Fig. 4 – 7B), an eccentricity of 1 meaning a perfectly round nucleus. As expected, the nuclei followed the same orientation as the cell body. In the upper layers nuclei were oriented in the direction of the stripes (Fig. 4 – 7C).

As nuclei are more elongated on upper layers, we think they could be laterally compressed. Several studies have shown that mechanical forces acting on nuclei can have an impact on cell behaviour, in particular on myoblasts differentiation[38,40]. When the nucleus is compressed, the YAP protein exports out of the nucleus to the cytoplasm and become inactivated, allowing genes linked to differentiation to be activated[40,201]. Further studies should then focus on the localization of YAP in our system, that should be in the nucleus (resp. in the cytoplasm) for the cells in the bottom layer (resp. upper layers).

2. 2. 2. Upper layers show different degrees of differentiation

To correlate nuclear compression and differentiation we took a closer look at images on PERP patterns and clearly see several layers of myotubes (Fig. 4 – 8). Myotubes in the first layer were oriented in the direction of the μCG while myotubes in upper layers were oriented in the direction of the mG (Fig. 4 – 11C,D). Myotubes in the bottom layer were round and contained few nuclei. In contrary, myotubes in upper layers were much longer, up to millimeter long. This shows that the differentiation of the myotubes in the bottom layer is not as good as in the upper layers. *For that reason, in the following, we will only consider the upper layers of the cell cord in PERP patterns.*

2. 3. Fusion and maturation index

To quantify cell differentiation, we compute the *fusion index* that is defined as the ratio of the number of nuclei inside myotubes[a] to the total number of nuclei. This index quantifies the proportion of cells involved in the differentiation process. To quantify how far is the tissue in the differentiation process, we compute the *maturation index*. This index is the ratio of the number of myotubes with 5 or more nuclei to the total myotube population. It quantifies how mature are the myotubes in the tissue and if there are in the process of developing sarcomeric structures. Finally, we measure the number of nuclei per myotube.

a From this point, we call a "myotube" a cell positive for MHC that contains 2 or more nuclei. Cells positive to MHC that contains only one nucleus will be called "myoblasts".

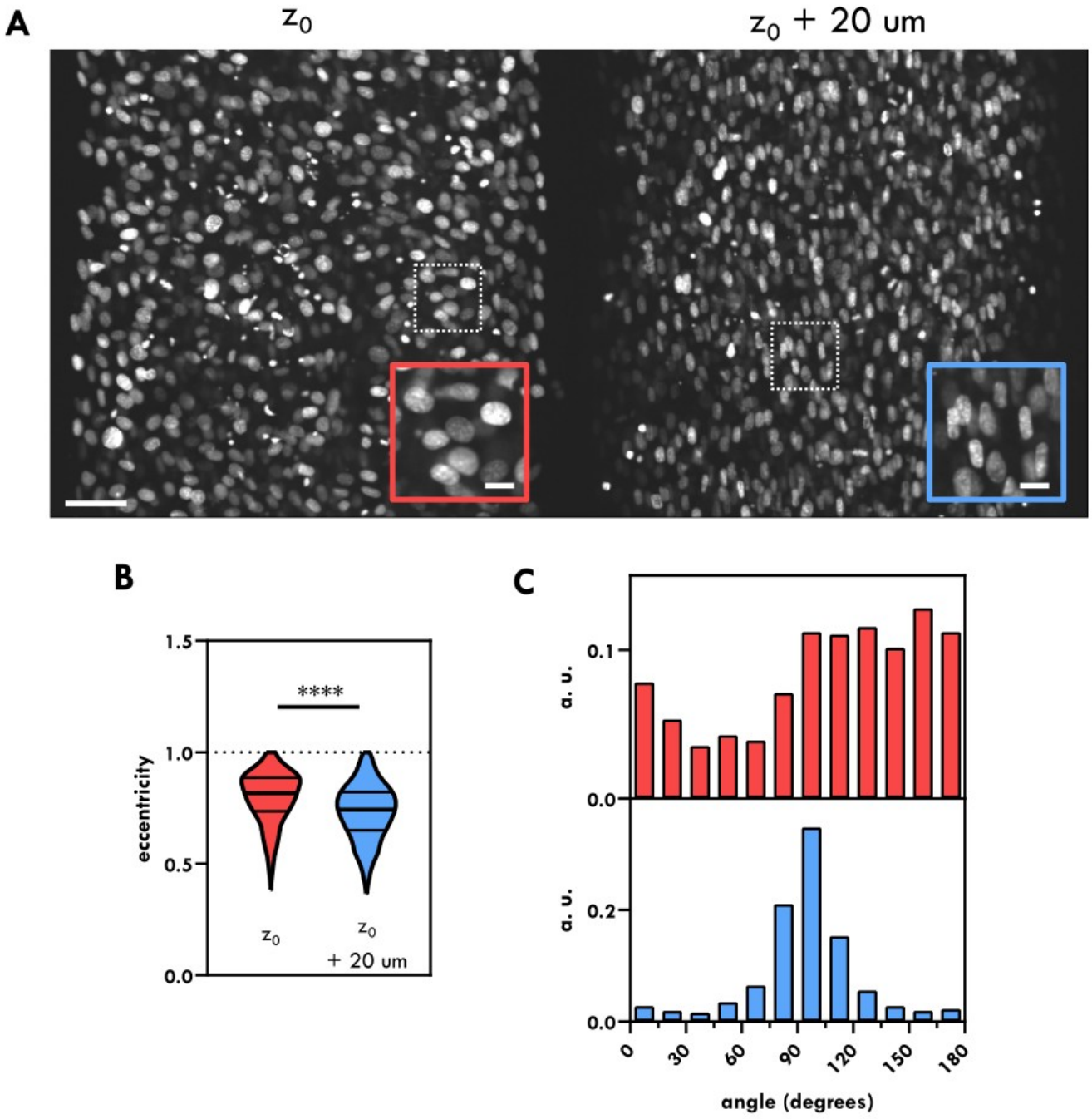

Figure 4 – 7. Changes in nuclear shape between bottom and top layers. (**A**) Confocal images of nuclei in bottom layer and 20 µm above the bottom layer (upper layer). Nuclei change shape and orientation (inserts). Images are taken 60h after the beginning of the experiment. Scale bar = 50 µm (insert: 10 µm). Nuclei eccentricity (**B**) and orientation (**C**) in bottom (red; n= 562) and upper (blue; n= 574) layer. Eccentricity significantly change between the two layers (Mann-Whitney test, p-value<0.0001). Nuclei follow stripes' direction, as do the cells' body.

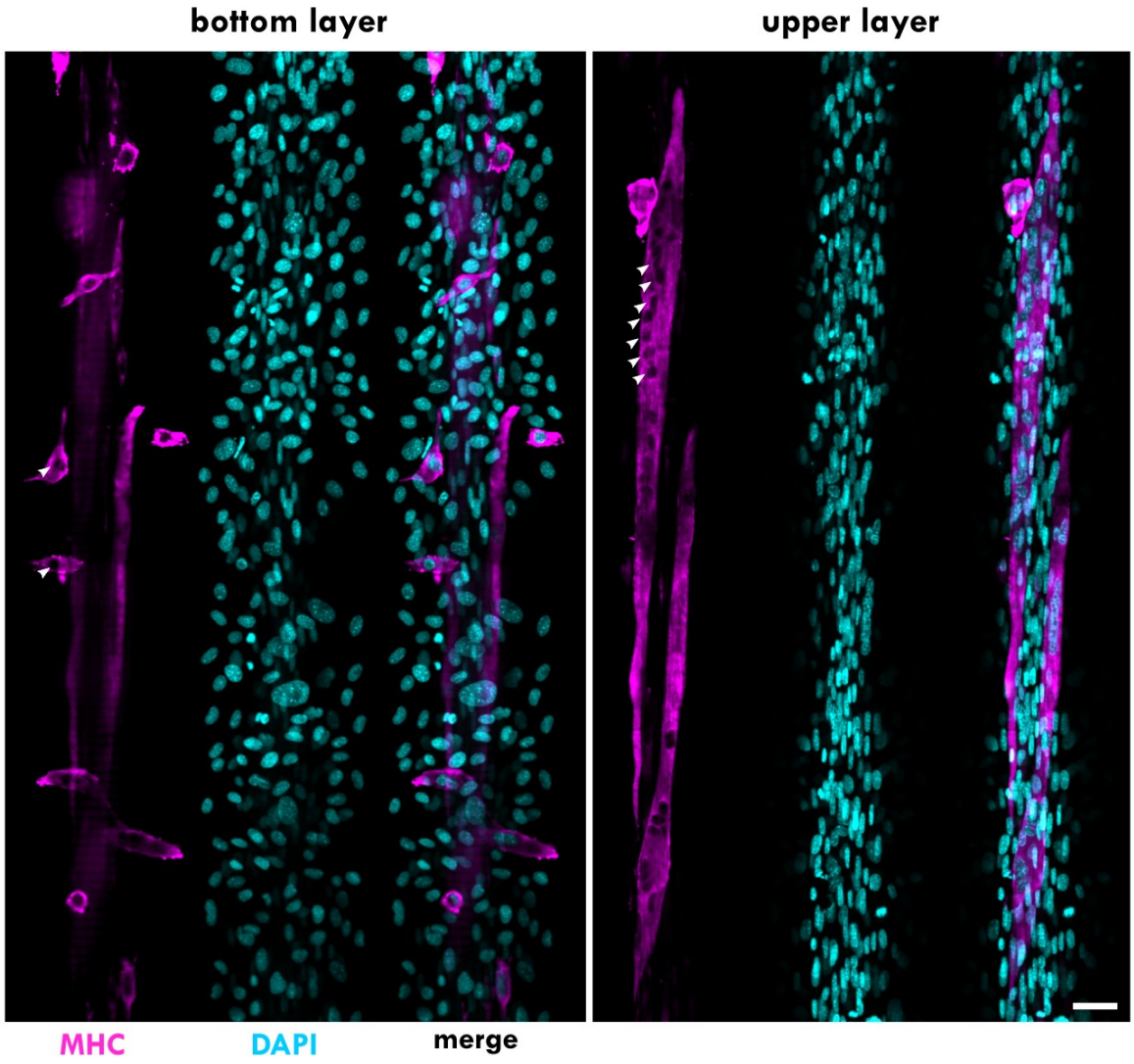

Figure 4 – 8. Myotubes in upper layer of cell cords show enhanced differentiation. Myotubes (MHC) and nuclei (DAPI) in bottom and top layer of a 200 µm PERP pattern. We clearly observe that the bottom layer contains few myotubes with one or two nuclei only while cells in the upper layer show longer myotubes with dozens of nuclei. We also observe a change of nucleus shape as described previously. White arrows point at nuclei. Scale bar = 50 µm.

On PERP patterns, the layered structure of the cell cord makes these indexes harder to define. We had to manually separate the bottom and upper layers of the cell cord in order to quantify the maturation index. *In the following the maturation index is shown for upper layers of the cell cord in PERP patterns.* Unfortunately, the fusion index cannot be calculated this way because it is practically impossible to assess if a nucleus is in an upper layer. *For that reason, the fusion index in PERP patterns is calculated for bottom and top layers combined (denoted PERP*).*

We compare all these indexes given the number of observed patterns (Table 4 – 1). Despite limited statistics, we observed that the fusion index (Fig. 4 – 9A) did not seem impacted by the type of pattern. This index was around 10 – 15% which is comparable to published data. For S patterns, Bajaj et al.[136] found a value of 5 – 10% (at 4 days), Sun et al.[132] a value of around 20% (at 6 days) and Zatti et al.[131] a value of 50 – 70% (at 6 days). Moreover, the maturation index (Fig. 4 – 9B) seemed larger on thinner stripes. Overall, this maturation index ranged from 15 to 30%, slightly larger than the values of 10 – 20% on S patterns at 4 days found by Bajaj et al.[136]

Number of observations	S (N = 4)	PERP (N = 2)	PARR (N = 2)
100 µm	7	3	4
200 µm	7	5	4
300 µm	7	5	4
400 µm	6	3	3
500 µm	5	3	3

Table 4 – 1. Number of observations. We observed differentiated C2C12 cells on S, PERP and PARR patterns of width ranging from 100 to 500 µm. N represents the number of different independent experiments.

Due to the variability and our limited number of observations, we could not conclude on the impact of the PERP pattern compared to the others. These results fall short of our expectations. Nonetheless, it is worth noticing that we still observe a larger maturation index when upper layers of cell cord were only taken in account (PERP* vs. PERP). Altogether, these indexes account for a global measurement of the advancement of the differentiation. So far, few studies in the literature looked at the extent of differentiation by characterizing individual myotube shape such as width or length.

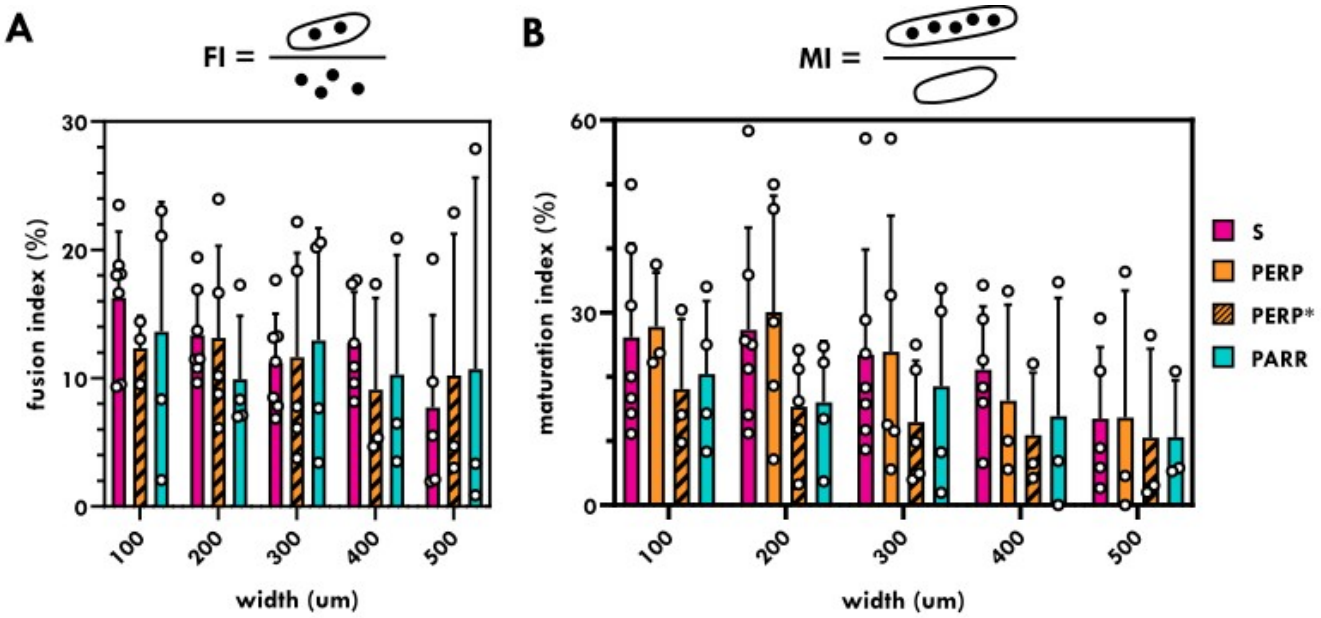

Figure 4 – 9. Fusion index and maturation index (**A**) Fusion index of C2C12 cells. This index seems independent of the pattern geometry. (**B**) Maturation index of C2C12 cells. PERP* is the PERP pattern with both bottom and upper layers taken in account while myotubes in upper layers are only considered in PERP. Maturation index is larger in upper layers of cell cords in PERP patterns. Thinner stripes help develop more mature myotubes.

2. 4. Myotubes

To complete our observations, we looked at myotubes from our confocal images following the protocol of Chapter II. 3. 3. To do so, we drew manually the contours of the myotubes. A Matlab algorithm fitted an ellipse to each contour. This gave parameters such as myotube width (the small-axis of the ellipse), length (the long-axis of the ellipse) and orientation. On top on this shape analysis, we counted the number of nuclei in each myotube.

2. 4. 1. Shape

Myotubes appeared in various shapes (Fig. 4 – 10A). Myotubes' widths ranged from 5 to 100 µm which is in accordance with the physiological expected value of 50 µm. Their length varied much more, from 20 µm to 3 mm occasionally. Myotubes width and length were logically correlated with their number of nuclei, myotubes containing a large number of nuclei being longer. We

measured the width and length of each individual myotube in our patterns (Fig. 4 – 10B,C). Average values of width and length helped us find tendencies for myotube shapes[b] depending on the pattern type and width. The width of the stripe impacted the myotubes' width, as wider myotubes were found on wider patterns. The pattern type did not influence the width of the myotubes. The length of myotubes had too much variability to show a clear trend. Even if we cannot compare the patterns together, we saw that myotubes on PERP patterns were at least as long as on other patterns and that those in upper layers of cell cords show a well differentiated phenotype.

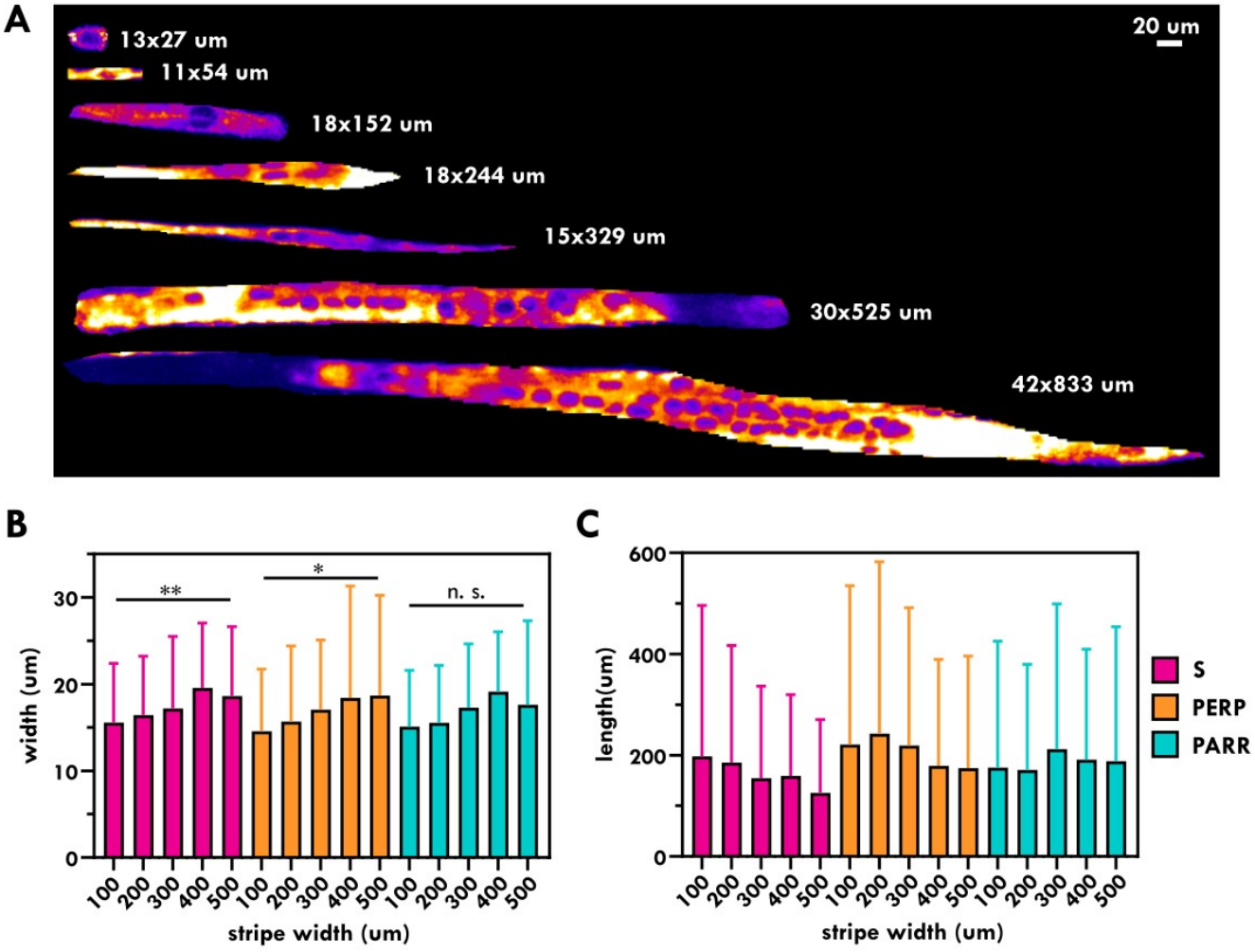

Figure 4 – 10. Myotubes shape. (**A**) Fluorescence images (MHC) of myotubes that can be found in one FOV on a PERP5x5-300 pattern. Myotubes appear with various width, length and contain different amount of nuclei. The size of the exemplified myotubes is noted (width x length). Scale bar = 20 µm. Myotubes width (**B**) and length (**C**) for different patterns. Widths slightly increase with pattern width for all conditions in contrary to lengths.

b For this analysis, we excluded myoblasts (myotubes with one nuclei).

2. 4. 2. Orientation

It has been previously shown that orientation of myotubes relative to the stripe direction hinders their elongation[132,134]. Indeed, if the myotube is tilted by an angle θ, because of the edges of the stripe pattern, its length cannot exceed w/cosθ with w the width of the stripe (Fig. 4 – 11A). We measured the myotube orientation in our patterns (Fig. 4 – 11B) and also observed a tilted orientation of the myotubes for S, increasing with the stripes' width. This observation was also in accordance with our study of Chapter III. as cell orientation on S saturates around 60° for large widths. Surprisingly, for PARR patterns, a tilt angle was also observed. However this tilt was much smaller than in S. As expected from our study of the cell cord, PERP showed the best alignment of myotubes with the direction of the stripe. For patterns thinner than 400 μm, a perfect parallel alignment was even observed.

Altogether, PERP patterns lead to long myotubes better aligned. These patterns are therefore good candidates to an efficient differentiation in the cell cord upper layers.

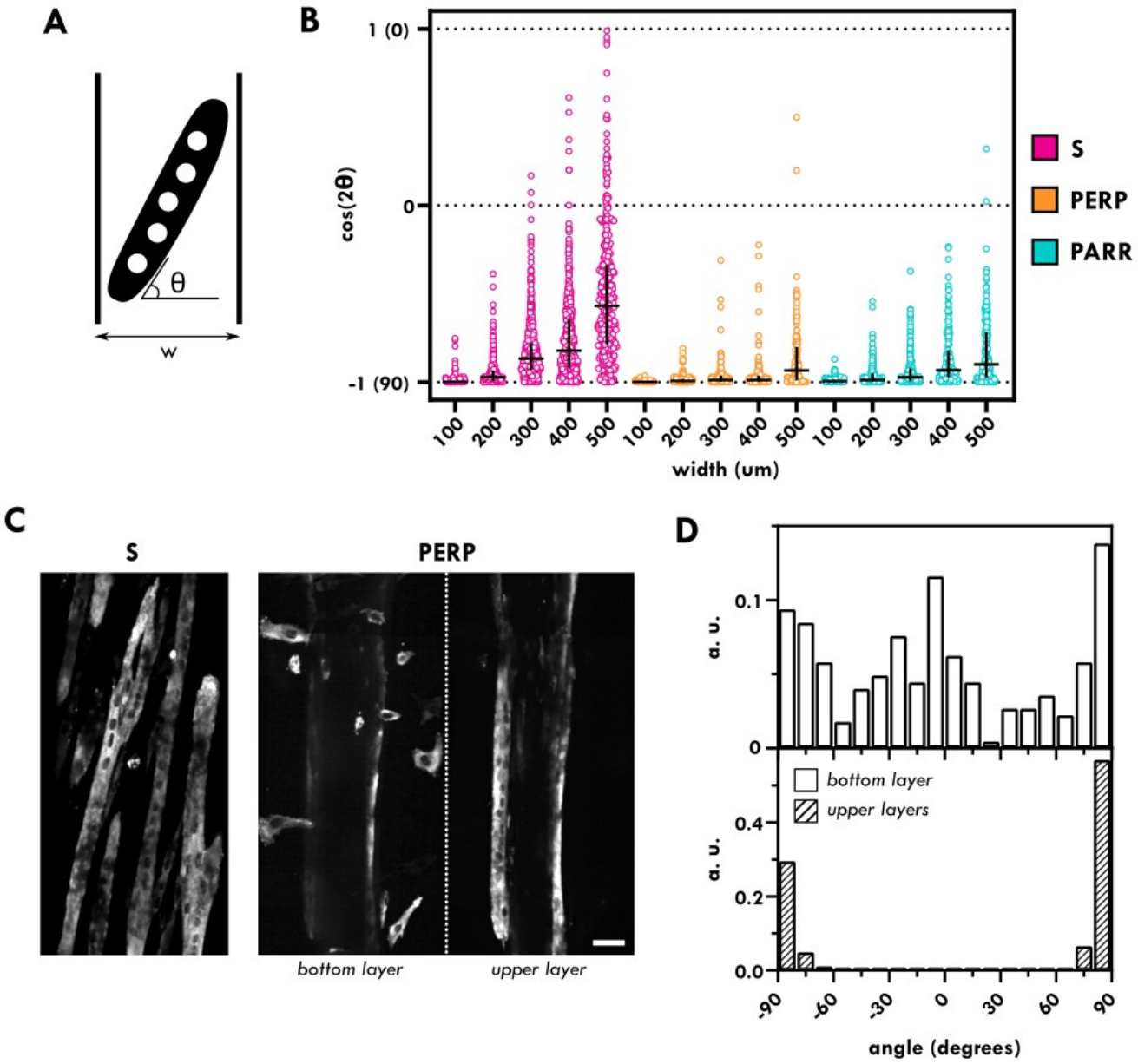

Figure 4 – 11. Myotubes orientation. (**A**) Schematics of how myotube orientation can hinder its elongation in stripes. The maximal myotube length cannot exceed w/cosθ. (**B**) Myotubes orientation (cos 2θ) for our different patterns. We observe a tilted angle for S and PARR pattern similarly as we previously described in Chapter III. In PERP patterns, cells are perfectly aligned with the stripes' direction. Median and first/third quartiles are shown. (**C**) Myotubes in S and PERP (bottom/upper layers) patterns. A clear tilt of the myotube appears in S pattern. MHC is stained. Scale bar = 50 µm. (**D**) Angle distribution in PERP-300 pattern. The bottom layer mostly composed of myoblasts orient along both µCG and mG cue while the upper layers perfectly orient along the stripe's direction.

3. Conclusion and perspectives

We used multiscale patterns to enhance the self-organization and differentiation of C2C12 myoblasts. This project was motivated by the observation that cells seeded on such patterns spontaneously form a three-dimensional well-aligned "cord".

At first, we described the architecture of the cell cord as well as the mechanisms leading to its formation (IV. 1. 1.). The cell cord formed around 20h after confluence for all the tested patterns. Cells started to build the second layer from the edges, via the convergent flows described in Chapter III. We established the cell cord architecture in confocal microscopy (IV. 1. 2.). The height increase of the cord over time was independent of the width of the mesoscale patterns. In terms of cell architecture, cells in the bottom layer followed the microscale pattern while cells in upper layers were always oriented in the direction of the mesoscale stripe. Cells' nuclei were oriented the same way and showed lateral compression. Surprisingly, cells in bottom and upper layers were oriented perpendicularly.

Our understanding of the cell cord formation and architecture helped us set a protocol for C2C12 differentiation in such patterns (IV. 2. 1.). We were able to measure indexes of differentiation and compare all conditions together and with the literature (IV. 2. 3.). Because of the variability of our experiments, we were not able to draw a significant conclusion on the differentiation of C2C12 cells on PERP patterns. Still, we observed a larger maturation index on upper layers of cell cords.
We got further insights by looking at the shape of the myotubes. Their widths slightly increased with pattern width while their length was highly variable from 20 μm to 3 mm. These rare cases were also shown in thinner PERP patterns that also allowed a better myotube alignment.
These results are not as good as what we expected when we started this project but are still preliminary. PERP patterns show C2C12 differentiation comparable to the other patterns and the literature. However, the cell cord structure on these patterns showed fusion and maturation index up to the levels obtained on S and PARR patterns. As expected from our observations of cell cord architecture that set all the conditions that favor differentiation (cell alignment, 3D structure, nucleus lateral compression, …) this pattern remains promising for C2C12 differentiation and 3D tissue engineering of entire muscles.

So far, we only observed myotubes under the scope of the terminal differentiation marker MHC, however it would be interesting to observe myoG, a protein expressed earlier in myogenic differentiation and to know if this protein expression is enhanced locally due to geometrical constraints. It would also be good to measure the localization of YAP in cells of the upper layers of the cell cord. These observations can be easily performed on fixed samples but only at a given timepoint of the experiment. To complete such study, a quantification by qPCR for example, of some MRFs over the course of the experiment would be a good indicator of how our substrates favor C2C12 differentiation. Lastly, we have not tested the role of the microscale geometry. 10x5 or 20x5 patterns would offer less adhesion surface but may enhance μCG which could eventually lead to enhanced differentiation in the upper layer of the cell cord. Finally, further work should go together with an effort on automation of image analysis. Presently, measurements of myotube shapes as well as nuclei counting are done manually. A less-time consuming method would be to segment each nuclei. However the high density of nuclei in our images makes this step very difficult. We have explored the possibility to use the deep-learning software *ilastik* for image analysis[202]. Although preliminary results were promising for counting nuclei in our 3D stacks, they are still far (20 to 30% difference) from manual counting, which hinders proper quantification for now.

Over the scope of this manuscript, several key results should be emphasized in the field of *in vitro* active nematics and tissue engineering.

We seeded active nematic cells on homemade multiscale substrates that put in competition multiple lengthscales (Chapter III.). Cells were confined in mesoscale stripes with an underlying perpendicular microscale abrasion topography. Depending on the width of the stripes, cells oriented along one or the other guiding cue. We identified a geometrical transition in orientation for a critical width that was independent of the cells' activity.

We built a theoretical model based on active gel theory to model our system. We took advantage of the competition between the two modes of guidance to measure the so-called flow-alignment parameter ν. This parameter couples the cellular flows and orientation and is involved to model several dynamical states of active nematics. To our knowledge, this parameter has never been measured in such active system.

Our physical model helped us understand what parameters were at stake in such multiscale systems. *In vivo*, cells in tissues are constrained in similar conditions, with the ECM surrounding them spanning several lengthscales. For this reason, we think our model can explain *in vivo* collective cell migration in such environments. Practically, we could implement a device where a 3D collagen stripe embedded with nematic cells would be confined (Fig. 5 – 1A). This would recapitulate more closely the environment cells interact with, *in vivo*. Moreover, we can think in a way to orient the collagen fibers within the collagen, for example by stretching the mold, then extrapolate our 2D model into this 3D configuration[203].

We used the understanding of such phenomenon to smartly engineering C2C12 mouse myoblasts tissues into fully grown muscles (Chapter IV.). At large experimental times, we observed the formation of a 3D cell cord with an architecture favoring C2C12 cell differentiation. Cells in upper layers were constrained and oriented along the stripes' direction. Quantification showed an enhancement of the maturation and length of myotubes compared to control patterns.

These results are a promising new way to control and enhance myoblasts differentiation for tissue engineering industry. We could think of smart way to industrially produce fully grown

myotubes by combining our protocol and patterns with microfluidics and specific surface chemistry (Fig. 5 – 1B). Thermoresponsive polymers such as pNIPAAm would allow to detach myotubes easily after differentiation. By cycling this process, one could harvest a significant quantity of myotubes for future applications like tissue engineering or cultured meat.

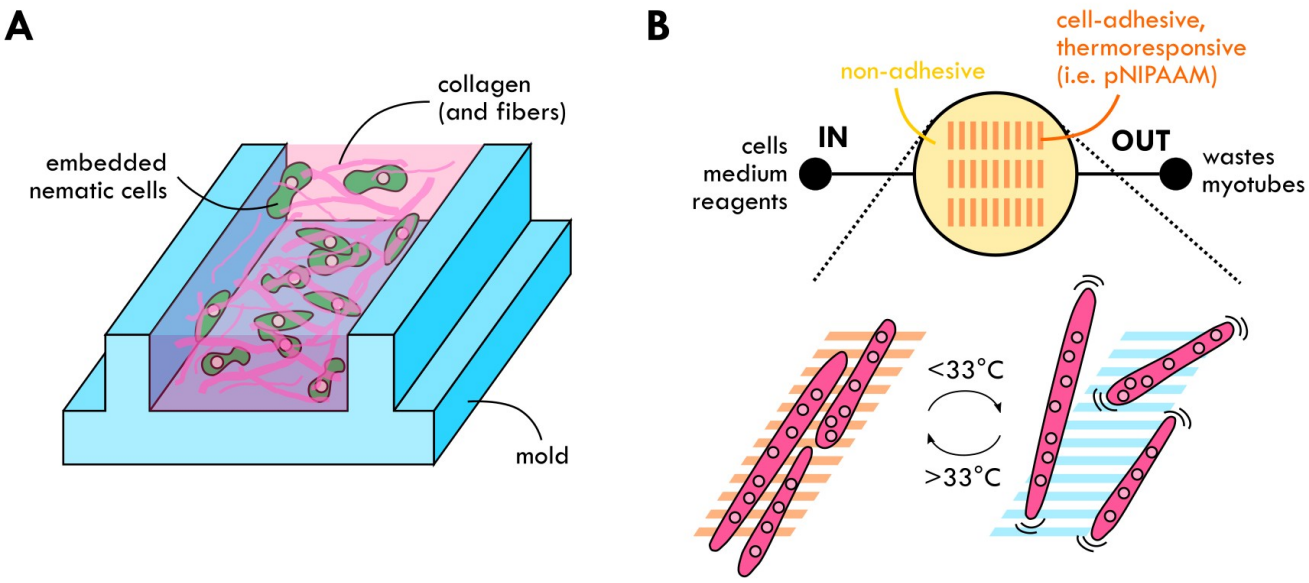

Figure 5 – 1. Perspectives of the thesis. (**A**) Schematics of a device to extrapolate our 2D system in a 3D physiological environment. Nematic cells are embedded in a 3D collagen gel constrained in stripes of given width. (**B**) Schematics of a reusable device for myotubes production. We could implement our protocol to grow myotubes then harvest them by detaching them using a thermoresponsive polymer attached to the surface.


Ap.

Appendix

A. Protocols

A. 1. Immunostaining

Step	Instruction	Time	Comment
1. Fixation (30 min)			
a.	Suck the medium and rince the sample with PBS.		It removes all floating impurities.
b.	Fix with 4% PFA in PBS (ex. 250 µL of PFA in 750 mL of PBS).	15 min	It preserves the tissue from autolysis.
c.	Rince with PBS x3.	3x 5min	
2. Permeabilization (25 min)			
a.	Permeabilize with Triton x100 0.1% or Tween 20.	10 min	It makes the cell membrane porous. Tween 20 is less aggressive for cells.
b.	Rince with PBS x3.	3x 5min	
3. Saturation (1h 15 min)			
a.	Prepare saturation solution (SS): 0.1% BSA in PBS (ex. 10 mg BSA in 10 mL PBS).		
b.	Saturate the sample with SS + 2.5% serum. Ideally, serum should be from the species of the antibody II (ex. 25 µL NGS for 1 mL of solution).	1h	It ensures all binding sites are saturated with BSA. This will lead to a better contrast of the staining.
c.	Rince with PBS x3.	3x 5min	
4. Antibody I (2h15+)			
a.	Incubate the sample with SS + Ab I following the dilution table.	2h+ (RT) OR overnight (4°C)	Ab I will fix on the target protein.
b.	Rince with PBS x3.	3x 5min	
5. Antibody II (45 min)			
a.	Incubate the sample with SS + Ab II following the dilution table. Cover the sample in aluminum to avoid contact with light.	30 min	Ab II will fix on Ab I. Be careful, light can destroy fluorophores of Ab II.
b.	Rince with PBS x3.	3x 5min	
6. DAPI (35 min)			
a.	Incubate with 0.1 – 10 µg/mL DAPI in SS.	20 min	DAPI marks the nucleus of cells. By fine tuning the amount of DAPI and incubation time, you can observe nucleoles.
b.	Rince with PBS x3.	3x 5min	

Step	Instruction	Time	Comment
7. Mounting (optionnal)			
a.	Add a drop of mounting reagent (ex. Prolong Gold Antifade reagent) on a clean glass slide.		Make sure there are no bubbles left.
b.	Gently drop the sample coverslip on the glass slide.		
c.	Let the mounting reagent to dry away from light.	overnight	

Table of dilutions

Antibody I	
MF-20 (for MHC)	1:50
Antibody II	
Alexa Fluor 546 (goat-anti-mouse)	1:500
Alexa Fluor 488 (goat-anti-mouse)	1:500
Fluorophores	
DAPI	1:1000
phalloidine	1:150

A. 2. Abrasions protocol

Step	Instructions	Comment
1. Scotch pad		
a.	Glue two foam tape (tesa® 4957) together.	
b.	On one face, glue a thermoresponsive tape (Nitto).	
c.	Cut scotch pad using a round cutter.	Make sure you protect the underlying surface when cutting the pads.
2. Preparation of the machine		
a.	Glue sandpaper on the bottom rail of the machine with classical double face tape.	The sandpaper should sit on a hard surface.
b.	Glue a scotch pad under the load cart. Make sure the thermoresponsive tape surface is facing the sandpaper.	
c.	Glue the coverslip at the center of the scotch pad.	
3. Abrasions		
a.	Put in contact the coverslip with the sandpaper.	The contact should be perfect as the scotch pad compensates for defaults in alignment between the cart and the bottom rail.
b.	Abrade the coverslip by doing back-and-forth movements.	N_p times.
c.	Separate the coverslip and the sandpaper once done.	
d.	Unglue delicately the coverslip by heating the thermoresponsive tape with a heat pistol.	

A. 3. Patterning protocol

List of chemicals

Name	Abbreviation
sulfuric acid 96%	-
hydrogen peroxide	-
allytrichlorosilane 95%	ATC-silane
acrylamide	Aam
N,N'-methylenebis(acrylamide)	BIS
benzophenone	-
poly(ethylene glycol)	PEG
S1813 positive photoresist (Shipley)	S1813
Microposit™ 351 developer	-
Sylgard® 184	PDMS

Following the protocol of Tourovskaia et al. and optimizations of our team [93,173,182,183].

Step	Instruction	Time	Comment
1. Clean the coverslip surfaces			
a.	Rince the coverslips in ethanol under sonication. Air dry them.		
b.	Prepare a piranha solution: 30 mL of pure sulfuric acid + 10 of hydrogen peroxide. Incubate the coverslips in this solution. Rince with distilled water and air dry.	5 min	Be careful when preparing the piranha solution, it is extremely corrosive. Be sure no metal touches the solution.
c.	Put the coverslips in air plasma.	5 min	
2. Covalent layer			
a.	Prepare the covalent layer: 15.5 mL ATC-silane + 200 mL toluene. Incubate the coverslips in this solution. Rince with toluene, distilled water and air dry.	5 min	Make sure no water touches the solution (otherwise the solution will become cloudy). After incubation, the coverslips should be highly hydrophobic.
b.	Heat the silanized coverslips at 90°C	1h	
3. Gel layers			
a.	Prepare the gel solutions: - A: 3g Aam, 0.03g BIS, 1.09g benzophenone in 20 mL acetone - B: 6g PEG, 0.9g BIS, 1.09g benzophenone in 20 mL methanol		Mix them well with the help of the sonicator.
b.	Incubate the coverslips in A.	5 min	Make sure the layer to coat is at the bottom. Indeed, solubilized oxygen destroy the polymerization reaction[204].

Step	Instruction	Time	Comment
c.	Illuminate them with UV light transilluminator (light from the bottom).	3 min	A thin white layer should appear at the end of the process.
d.	Rinse with acetone, distilled water and air dry.		Dry the center first. Blow on the coverslip to check the coated side. It should be hydrophilic (no condensation).
e.	Incubate the coverslips in B.	5 min	
f.	Illuminate them with UV light transilluminator (light from the bottom).	3 min	Small white crystals should float at the end of the process.
g.	Rinse with methanol, acetone, distilled water and air dry.		Dry the center first. Blow on the coverslip to check the coated side. It should be hydrophilic (no condensation).
4. Photolithography			
a.	Spincoat a layer of S1813 positive resin on the coated side of the coverslips: 4000 turns/min for 30s. Heat the coverslips for 1 min at 115°.	30s + 1 min	Make sure the inactinic light is on.
b.	Illuminate the coverslips through a clean mask for 8s under UV light (λ = 365 nm).		Turn on the lamp at least 10 minutes before illuminating the sample. The resin should touch the ink of the mask.
c.	Prepare the developing solution: 10mL of 351 developer + 40 mL distilled water. Develop the coverslips in this solution for exactly 10s. Rince with distilled water and air dry.		
d.	Put the coverslips in air plasma for 4x 5min.	4x 5 min	This will remove the unprotected cell-repellent layer up to the glass surface. Make sure coverslips do not heat too much (wait between plasmas).
e.	Incubate the coverslips with any ECM proteins.		Not mandatory.
f.	Remove the resin with acetone. Rince with water and air dry.		
5. Plate preparation			
g.	Prepare PDMS solution: 0.2g reticulant + 1.8g monomer. Mix well. Glue coverslips with PDMS at the bottom of plates.		
h.	Heat at 60°C for at least 1h	1h+	

B. Directional statistics

B. 1. Why using directional statistics ?

For many datasets using angular data, computing averages and standard deviations can become difficult because of the wrapping of angles around [0°, 360°] (or [0, 2π]). Mathematicians have uncovered these kind of problems using *directional statistics*. This field is in fact more general than just angular data and can also be applied or any cyclic dataset for example hourly or yearly data. Most topics uncovered in the following are updated form the book of Kanti Mardia and Peter Jupp [205].

B. 2. Representations

It is common to represent the dataset on a circle of radius 1 (Fig. B – 1A). This way, it is easy to see if all the points are concentrated around some angles or dispersed uniformly all around the circle. It can also be relevant to group data into histograms. This angle histogram can be shown again on a circle, which is commonly refereed as a "rose" histogram (Fig. B – 1B), or it can be unwrapped in a linear fashion (Fig. B – 1C). One must be careful with the latter representation as the histogram shape will depend on the angle where the unwrapping has been made, for example, unwrapping around the mean angle can lead to a linear histogram that look bimodal at the edges.

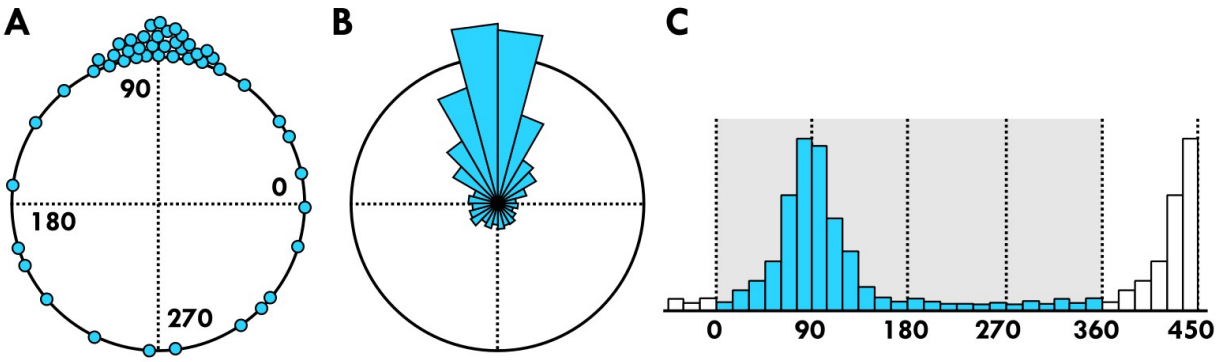

Figure B – 1. Different representations of circular data. (**A**) Points around a circle represent well how data concentrate around particular angles. Histograms around a circle, denotted as "rose" histogram (**B**) or linear (**C**) are good at representing bigger datasets. Be careful on linear histogram, depending on the position of the wrapping, the interpretation can be misleading.

B. 3. Circular mean and variance

For circular data, computing the average angle of a distribution could be difficult as the dataset is wrapped. For example, the mean of [15°, 330°] is not 172,5° but 337,5° (or -22,5°). We then need another definition of the average in order to given the correct result.

The method can be resumed graphically as in the Figure B – 2. On details, each point $\mathbf{x}_i$ sitting at angle θ_i on the unit circle, can be described in cartesian coordinates by its projections on x-axis and y-axis as $\mathbf{x}_i(\cos\theta_i,\ \sin\theta_i) = (c_i, s_i)$. For a distribution of N points $\mathbf{x}_1, \mathbf{x}_2, \ldots \mathbf{x}_N$, we can define the resultant vector $\mathbf{R}$ as

$$\boldsymbol{R}=\left(\sum_{i=1}^{N} c_i, \sum_{i=1}^{N} s_i\right)=\left(\sum_{i=1}^{N}\cos(\theta_i), \sum_{i=1}^{N}\sin(\theta_i)\right)=(C,S) \quad \text{of norm} \quad R=\sqrt{C^2+S^2}$$

Then the circular mean $\bar{\theta}$ is just the angle which the resultant vector is pointing at, or in mathematical words, the solution of the equations

$$\cos(\bar{\theta})=\frac{C}{R},\ \ \sin(\bar{\theta})=\frac{S}{R}$$

An easy way to compute $\bar{\theta}$ is to use complex numbers, the average angle will then be the argument of the complex resultant vector. Particular cases are apolar problems where only the direction of the vector is known. As angle distributions are perfectly symmetric, the resultant vector is thus $\vec{0}$ and the mean cannot be calculated. The trick is to double the angles in the distribution and wrap them so that they lie in the range [0°, 360°]. The detailed algorithm is explained in Appendix C. 1.

The equivalent for classical variance, is called circular variance and is defined as

$$V=1-\bar{R} \quad \text{where} \quad \bar{R}=\frac{R}{N}$$

Then the standard deviation will be $v=\sqrt{-2\ln(1-V)}\simeq\sqrt{2V}$, for small V.

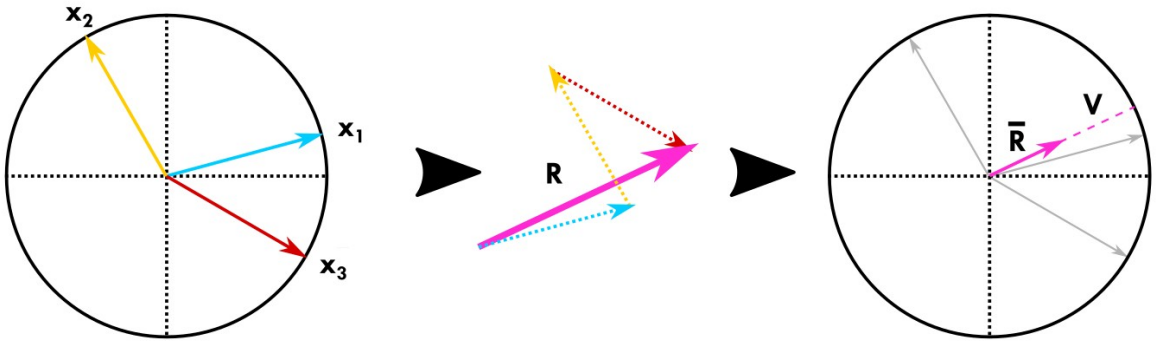

Figure B – 2. Averaging angles. The circular average of an angular distribution if the direction the resultant vector **R** is pointing at. The circular standard deviation is calculated using the norm of this vector.

B. 4. von Mises distribution

A common model for distribution of data around the circle is the von Mises distribution introduced in 1918. This distribution is also named the "circular normal distribution" as it is really close in its form and interpretation to the normal distribution (Fig. B – 3). The von Mises distribution M(μ, κ), has probability density function

$$f_{VM}(\theta|\mu,\kappa)=\frac{1}{2\pi I_0(\kappa)}e^{\kappa\cos(\theta-\mu)}$$

where I_0 is the modified Bessel function of the first kind.

The mean direction of the sample is μ and κ is called the concentration parameter and refers to how « concentrated » the points are on the unit circle. Large κ mean uniformly distributed angles while small κ, angles tightly distributed around μ. In fact, for large enough κ, von Mises distribution can be approximated as simple (wrapped) normal distribution of mean μ and variance $1/\kappa^2$.

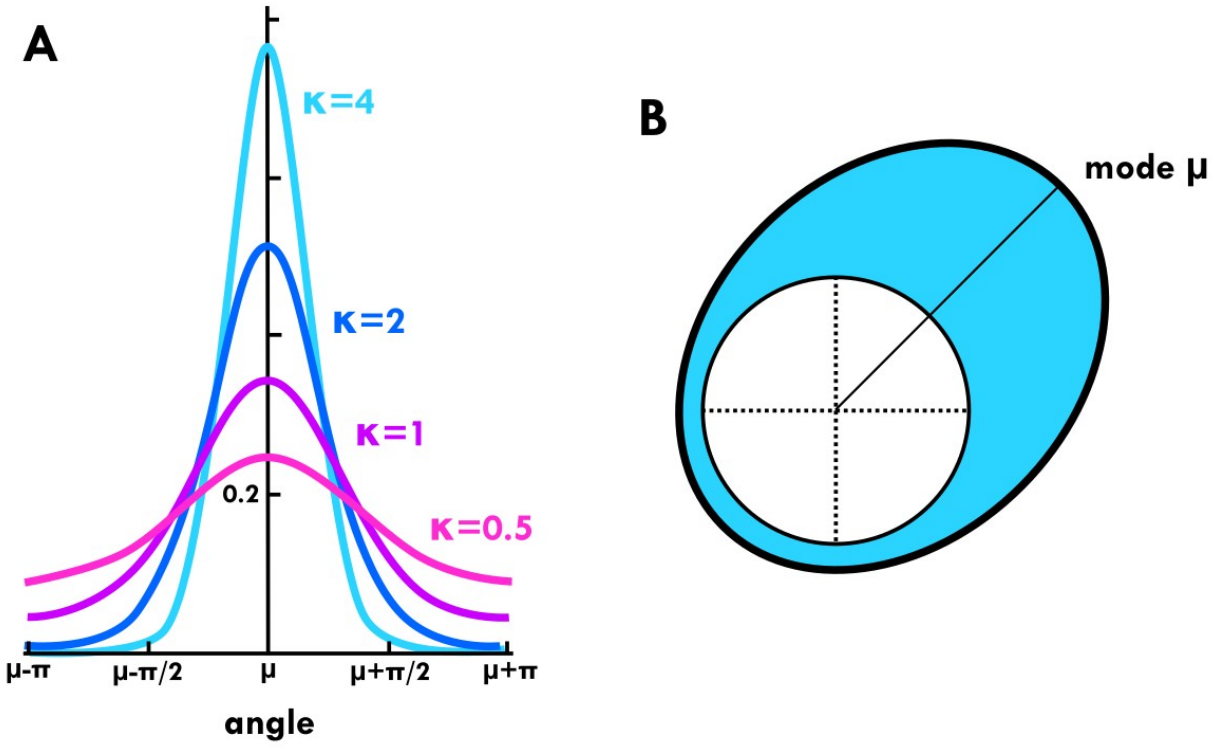

Figure B – 3. von Mises distribution. (**A**) Linear representation of the von Mises distribution around angle μ. For large κ, this distribution becomes close to a classical normal distribution N(μ,1/κ). (**B**) Circular representation of the von Mises distribution. Blue: dataset.

C. Algorithms

C. 1. Circular average of bimodal angle distributions

As our data represent directions, we will need to average perfectly symmetrical bimodal distributions. Using the circular average in this case is not possible because the result is not defined. A simple way to tackle this issue is to compute the average angle 2a using the algorithm described in Fig. C – 1.

- (i) OrientationJ data or more generally directional data are given for angles between [-90°, 90°]. For that reason, it is quite difficult to get average angle a of distributions peaked around 90°. For simplification for the following of the algorithm, we put the angle distribution on [0°, 180°] range.

- (ii) We duplicate the data over the all circle angle range [0°, 360°]. Our distribution is now bimodal and perfectly symmetric. This last point is quite important for the calculation.

- (iii) We double all the angles then remove 360° to all angles above 360°. As the data are wrapped, this will have for effect to create a single angle distribution but for the angle 2a. The trick is in this step.

- (iv) We now average our doubled distribution and get the average angle 2a. It is then simple to compute the average angle a of our data.

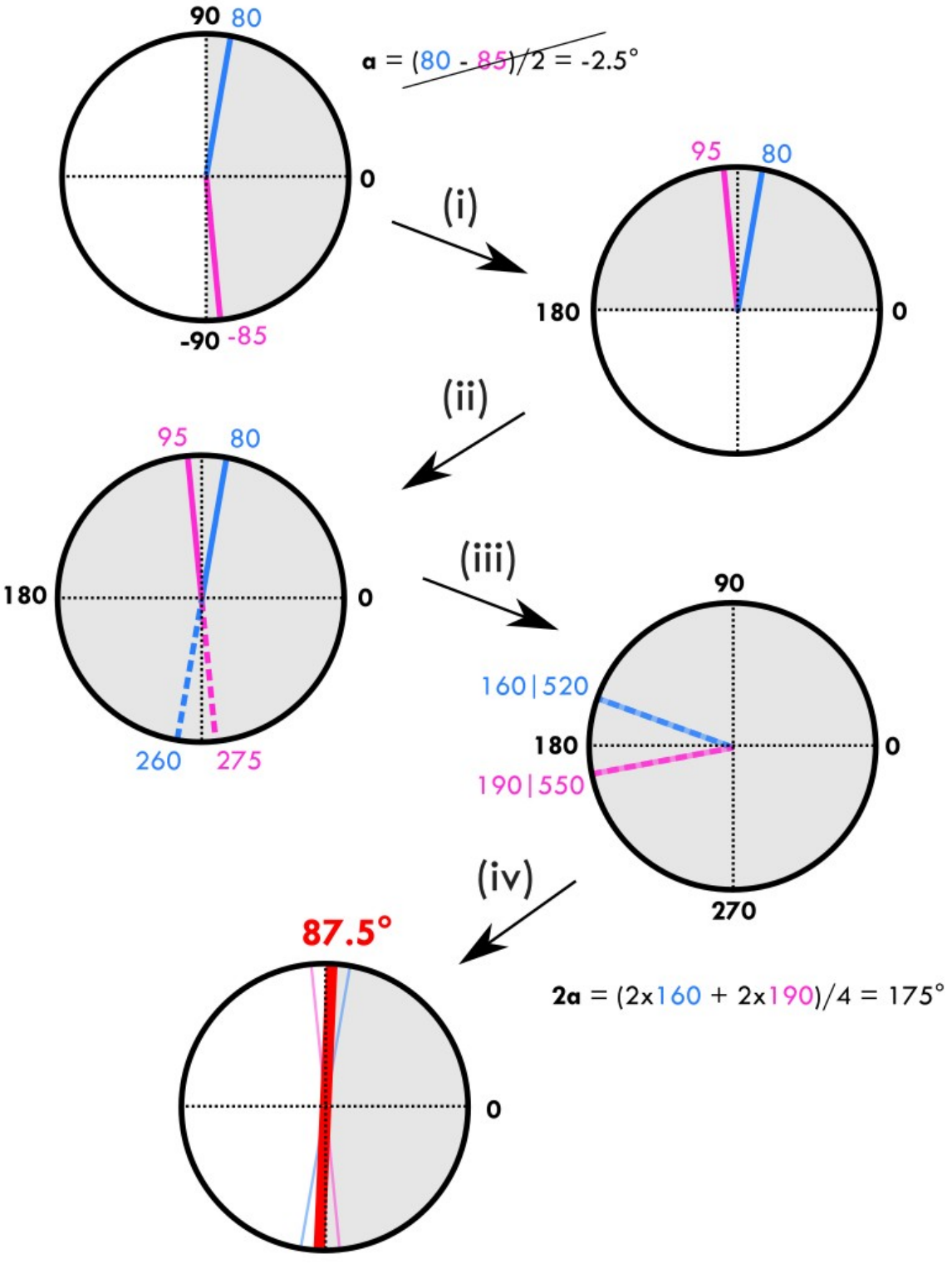

Figure C – 1. Algorithm for averaging angle of bimodal datatset. (i) Angles in the dataset are changed from [-90°, 90°] to [0, 180°]. (ii) Angles are mirrored so that the dataset range is [0, 360°]. (iii) Angles are doubled and wrapped. (iv) A circular mean gives the correct value of the average.

C. 2. Profile binning algorithm

We performed our experiments on many stripes with widths ranging from hundreds to thousands of micrometers. Due to the high noise of biological systems and as we wanted to make our data easily readable, we had to perform data binning and extract averaged value out of the hundreds of FOVs. For that purpose, we wrote an algorithm to sort and compute average profiles for each bin range. Most of the time, we chose to gather stripes of same width every 100 µm (w_{bin} = 0 – 100 µm, 100 – 200 µm, …) and displayed corresponding profile where each point is averaged every 20 µm (x_{bin} = 0 – 20 µm, 20 – 40 µm, …). The algorithm works as presented in Figure C – 2.

- (i) We create a 3D matrix filled with NaN values that we fill with our profile data: first column is the x values, second column the angle or velocity and third column, the standard deviation of this value.

- (ii) We gather all FOVs for which stripes width is included in the binning width. Then we remove unnecessary NaN values and create a 2D matrix containing all the points (x_i, y_i, s_i).

- (iii) We bin points that have x-value within the second binning range then average. The resulting ouput is an average profile (**x**, **y**, **s**) of all the FOVs (iv).

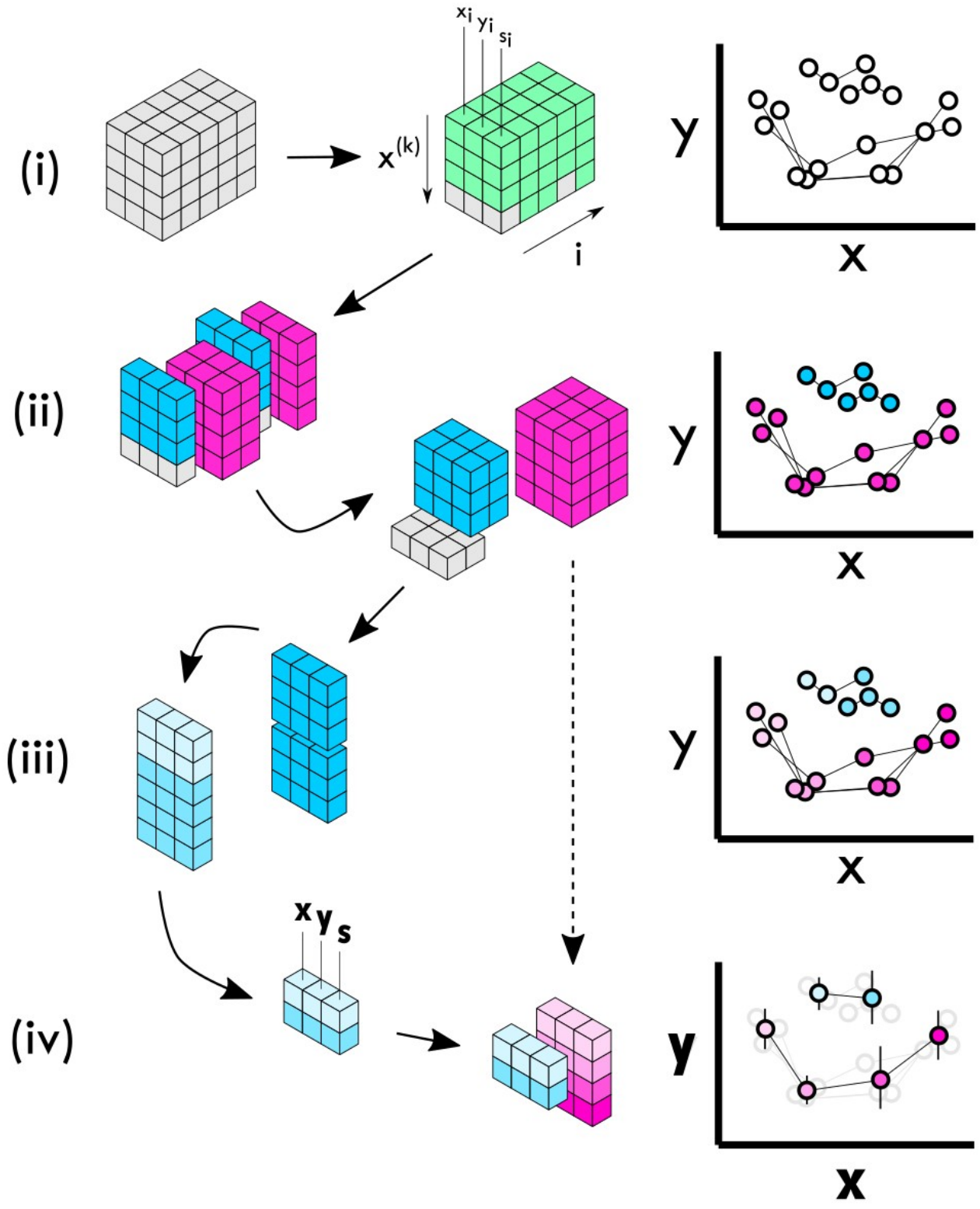

Figure C – 2. Binning algorithm. (i) Our dataset is ordered in a matrix (x_i, y_i, s_i) where i correspond to each observed stripe. (ii) The dataset is sorted by stripe width, for each binning range. (iii) In each binned dataset, x and y value are binned along the x-profile. (iv) The dataset is averaged in each bin. The result in an averaged profile (**x**, **y**, **s**).

C. 3. Topological defects analysis

We detected and characterized topological defects in our nematic system following the protocol of DeCamp et al. [189]. We used the dataset given by OrientationJ to compute position, charge and orientation of the defects following the algorithm illustrated in Figure C – 3.

- (i) From the angle map, we create an order parameter map. The defect sits at the center of low order parameter regions.

- (ii) We create a mask around the defect core. The mask is a disk of radius r_c divided into N_s slices. Angle is averaged in each slices and noted θ. Each slice orientation is noted α.

- (iii) Going in the trigonometric direction (increasing α), the defect will be a +1/2 (resp. -1/2) if θ is increasing (resp. decreasing). The orientation of the defect will be the point where $\theta = \alpha$ modulo the symmetry of the defect, that can be retrieved graphically.

- (iv) Altogether, we get the position, charge and orientation of the defect.

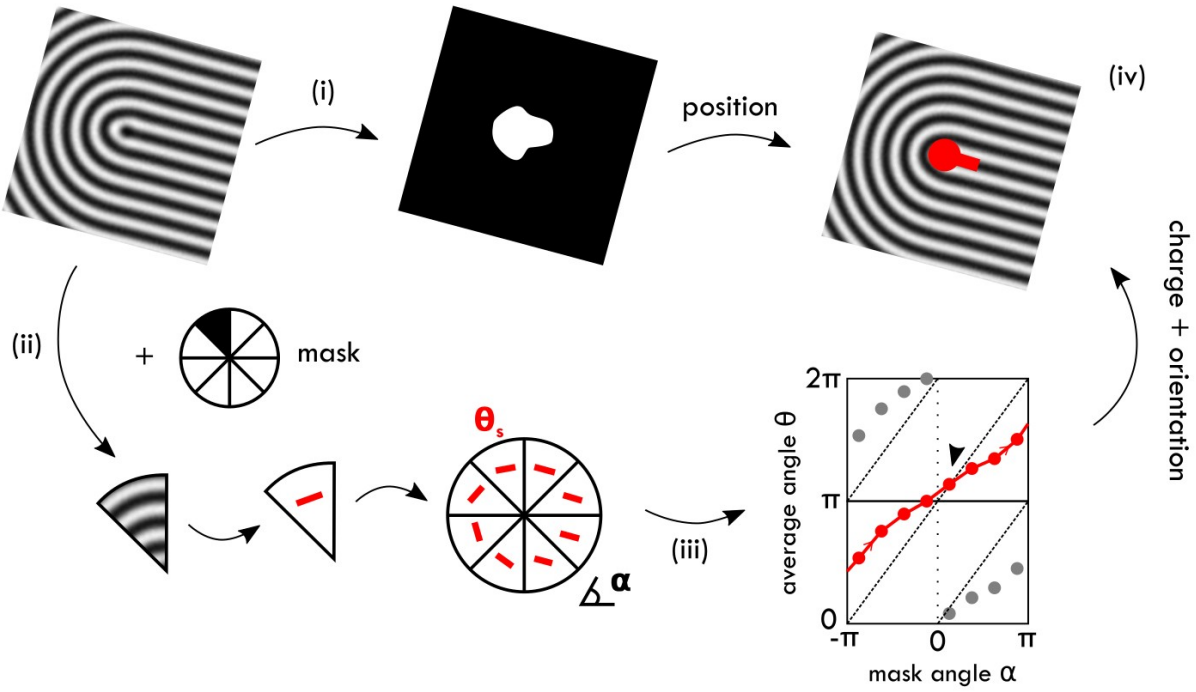

Figure C – 3. Algorithm for defect detection and characterization. (i) From the angle data of OrientationJ, we compute the order parameter map. The centroid of low order parameter region is the position of the defect core. (ii) We split a circular region around the defect and compute average angle θ in it. (iii). The change in angle θ in the trigonometric direction gives the charge of the defect. The orientation is given when θ = α (black arrow). (iv) Image of the defect and its calculated position, charge and direction.

D. Fun facts

This section gathers all kind of anecdotes linked to the topics present in my thesis. They are inspired by a friend of mine that became a running gag for us. Feel free to use them in dinners, parties or to overwhelm any audience with useless yet powerful science facts.

The word « cell »

Have you ever wondered why do we call a cell a « cell » ? The answer simply comes from the fact that Robert Hooke, the first person to observe cells (in this case onion skin cells) compared them to honeycomb cells in his book *Micrographia* [206]. The word then stayed in the language. Here is exact citation :

« I could exceedingly plainly perceive it to be all perforated and porous, much like a Honey-comb, but that the pores of it were not regular. (…) these pores, or **cells**, . . . were indeed the first *microscopical* pores I ever saw, and perhaps, that were ever seen, for I had not met with any writer or person, that had made any mention of them before this. »

The word « muscle »

This word comes from the latin *musculus* that literally means « little mouse ». But why should a muscle be compared with a mouse ? The answer is not clear and two hypothesis exist. The simplest one is that some muscles look like mice (I do not know which one by the way). The other hypothesis is similar, when some muscles contracts, for example biceps, it looks like a mouse under a rug [207].

The word « myosin »

This protein name comes from the simple fact that is was first discovered by W. Khüne in muscles where it is preponderant [208]. At first, it was though to be present only in muscles but in the 1970's, some myosins were found in non-muscle cells. At the same time, a one-headed myosin was found in the amoeba *Acanthamoeba castellanii* [209]. This made the distinction between this one-headed myosin I and muscle myosin II which are two-headed.

The secret of wrinkles

Aging comes from the fact that elastin, the component of ECM that gives elasticity to the tissue, starts to degrade. Indeed, this protein has a half-like time of 50 – 70 years and cannot be secreted by in adults [2].

Danders

Danders, the scientific word for hairs, nail, claw, feathers, scales, … are excrescence found in diverse animals. They come from highly keratinized cells that died. However, did you know keratins are part of the intermediate filaments family [2]?

How GFP was discovered

GFP is a well-known protein that has revolutionized the field of biology and even led the scientists responsible for its discovery to win a Nobel prize in 2008. The history of its discovery show how passionate, patient and hard-worker one need to become a Nobel prize one day. In their study Shimomura et al. [210] explained that they collected over 10000 samples of the medusa *Aequorea aequorea*. Because the organ containing the bioluminescent GFP is easily destroyed by squeezing, they were not able to use a net to collect all the sample at one time but rather had to fish for medusa at night, with an ultraviolet lamp and a hand fish net.

Dystrophin

Dystrophin is a protein part of an adhesion complex, the dystrophin-associated protein complex (DAPC), that links Z-disks of muscle cells to the ECM. This protein owns a record : its associated gene is one of the longest in human genome. It covers 2.3 megabases which corresponds to 0.08 % of human genome. A lack of expression of this protein leads to muscular distrophies which are severe myopathies. A total lack of expression is called a Duchenne Muscular Dystrophy while a partial lack of expression is a Becker Muscular Dystrophy. These diseases affect mostly boys as the dystrophin gene is present on X chromosome [211].

Cultured *in vitro* meat industry

In this thesis, I mentioned the tissue engineering industry. There is another possible application of *in vitro* myogenesis which is the cultured meat industry. This industry aims at recreating meat-like foods from cultivated animal cells rather than breeding full animals. It is expected to replace or be complementary to conventional food industry in order to serve both the growing need for meat/animal proteins as well as ecological purposes.

According to the 2019 report of The Good Food Institute [212], this industry has raised 77 M$ in 2019 with the creation of 20 start-ups distributed among 19 countries. One of the most famous among them, Mosa Meat (Maastricth, Netherlands), achieved the first cultivated beef burger in 2013 and plan to sell its product

starting 2021. Even Merck, a big actor of life science industry, created a team dedicated to cultured meat in 2019.

In order to develop, this industry still faces technological challenges. Upstream of commercialization, four main technical issues should be solved : the need for cell line development, the improvement of cell culture conditions, the scaffolding to retrieve physiological meat organization and finally the scaling-up to bioreactors. The last three issues can be easily tackled if efforts are made on understanding biophysic related problem for tissue self-organization and improved culture conditions.

Some world records linked to muscles

Biggest biceps	Mustafa Ismail (EGY) / Greg Valentino (USA)	79 cm perimeter / 69 cm perimeter	Controversial because of possible use of synthol.
Most « Mr. Olympia » titles [213] (bodybuilding)	Lee Haney (USA) & Ronnie Coleman (USA)	8 titles	Special mention of Arnold Schwarzenegger (USA) who won 7 titles.
Most « World's Stongest Man » titles [214]	Mariusz Pudzianowski (POL)	5 titles	Special mention to Hafþór Júlíus Björnsson (ISL) aka The Mountain in the TV show Games of Thrones, who won 1 title.
Powerlifting [215] : - Squat - Bench press - Deadlift	 Jezza Uepa (NRU) Jezza Uepa (NRU) Cameron McKenzie (AUS)	 460 kg 272 kg 355 kg	Record for cumulated weight lifted in all three events goes to Jezza Uepa (NRU) with 1042 kg.
Olympic weightlifting [216] : - Snatch - Clean and jerk	 Lasha Talakhadze (GEO) Lasha Talakhadze (GEO)	 220 kg 264 kg	
Heaviest bull	Fêtard (FRA)	1950 kg	

« The whole is more than the sum of its parts »

Meditate on this sentence. Two philosophical current of thought can be opposed on this sentence. Reductionism considers « the whole » can be explained by precisely describing each of its parts and nothing more. Holism considers « the whole » as indivisible and is more than the sum of its parts. A striking example opposing these two way of thinking is the question about the human person. Can it be described as an ensemble of biochemical reaction creating thoughts or is there on top of the physical entity a « soul » ?

In between these two visions, systemic approaches focus on describing « the whole » by its parts and their interactions that give rise to unexpected phenomenon. In this sense, active matter can be philosophically be seen under this prism.

Architecture for crowd control

This thesis used the framework of active matter to describe biological problems related to cell collective behaviour. However, this study should not be limited to this. We can emphasize the growing interest of physico-biology of active matter in the field of human crowd control [217]. Theories, simulations, experiments, algorithms,… could be used in the near future to understand and control more efficiently assemblies of people. This could help architects or urbanists building safer places for example to help evacuation of a building on fire. In the near future, more collaborative works between active matter specialists and crowd control engineers could give rise to unexpected architectures.


Bb.

1. de Gennes, P.-G. & Prost, J. *The physics of liquid crystals*. (Oxford University Press, 1993).

2. Alberts, B. *et al. Molecular Biology of the Cell*. (Garland Science, 2007).

3. Fletcher, D. A. & Mullins, R. D. Cell mechanics and the cytoskeleton. *Nature* **463**, 485–492 (2010).

4. Herrmann, H., Bär, H., Kreplak, L., Strelkov, S. V. & Aebi, U. Intermediate filaments: From cell architecture to nanomechanics. *Nat. Rev. Mol. Cell Biol.* **8**, 562–573 (2007).

5. Blanchoin, L., Boujemaa-Paterski, R., Sykes, C. & Plastino, J. Actin Dynamics, Architecture, and Mechanics in Cell Motility. *Physiol. Rev.* **94**, 235–263 (2014).

6. Berro, J., Michelot, A., Blanchoin, L., Kovar, D. R. & Martiel, J. L. Attachment conditions control actin filament buckling and the production of forces. *Biophys. J.* **92**, 2546–2558 (2007).

7. Chan, C. E. & Odde, D. J. Traction dynamics of filopodia on compliant substrates. *Science (80-.).* **322**, 1687–1691 (2008).

8. Naumanen, P., Lappalainen, P. & Hotulainen, P. Mechanisms of actin stress fibre assembly. *J. Microsc.* **231**, 446–454 (2008).

9. Sellers, J. R. Myosins: A diverse superfamily. *Biochim. Biophys. Acta - Mol. Cell Res.* **1496**, 3–22 (2000).

10. Hartman, M. A. & Spudich, J. A. The myosin superfamily at a glance. *J. Cell Sci.* **125**, 1627–1632 (2012).

11. Frantz, C., Stewart, K. M. & Weaver, V. M. The extracellular matrix at a glance. *J. Cell Sci.* **123**, 4195–4200 (2010).

12. Theocharis, A. D., Skandalis, S. S., Gialeli, C. & Karamanos, N. K. Extracellular matrix structure. *Adv. Drug Deliv. Rev.* **97**, 4–27 (2016).

13. Engler, A. J., Sen, S., Sweeney, H. L. & Discher, D. E. Matrix Elasticity Directs Stem Cell Lineage Specification. *Cell* **126**, 677–689 (2006).

14. Humphrey, J. D., Dufresne, E. R. & Schwartz, M. A. Mechanotransduction and extracellular matrix homeostasis. *Nat. Rev. Mol. Cell Biol.* **15**, 802–812 (2014).

15. Kadler, K. E., Baldock, C., Bella, J. & Boot-Handford, R. P. Collagens at a glance. *J. Cell Sci.* **120**, 1955–1958 (2007).

16. Durbeej, M. Laminins. *Cell Tissue Res.* **339**, 259–268 (2010).

17. Järveläinen, H., Sainio, A., Koulu, M., Wight, T. N. & Penttinen, R. Extracellular matrix molecules: Potential targets in pharmacotherapy. *Pharmacol. Rev.* **61**, 198–223 (2009).

18. Lutolf, M. P. & Hubbell, J. A. Synthetic biomaterials as instructive extracellular microenvironments for morphogenesis in tissue engineering. *Nat. Biotechnol.* **23**, 47–55 (2005).

19. McCullen, S. D., Ramaswamy, S., Clarke, L. I. & Gorga, R. E. Nanofibrous composites for tissue engineering applications. *Wiley Interdiscip. Rev. Nanomedicine Nanobiotechnology* **1**, 369–390 (2009).

20. Dutta, R. C. & Dutta, A. K. Cell-interactive 3D-scaffold; advances and applications. *Biotechnol. Adv.* **27**, 334–339 (2009).

21. Boudou, T., Crouzier, T., Ren, K., Blin, G. & Picart, C. Multiple functionalities of polyelectrolyte multilayer films: New biomedical applications. *Adv. Mater.* **22**, 441–467 (2010).

22. Barnes, C. P., Sell, S. A., Boland, E. D., Simpson, D. G. & Bowlin, G. L. Nanofiber technology : Designing the next generation of tissue engineering scaffolds ☆. **59**, 1413–1433 (2007).

23. Ayres, C. E., Jha, B. S., Sell, S. A., Bowlin, G. L. & Simpson, D. G. Nanotechnology in the design of soft tissue scaffolds : innovations in structure and function. (2010) doi:10.1002/wnan.055.

24. Lien, S. M., Ko, L. Y. & Huang, T. J. Effect of pore size on ECM secretion and cell growth in gelatin scaffold for articular cartilage tissue engineering. *Acta Biomater.* **5**, 670–679 (2009).

25. Murphy, C. M. & O'Brien, F. J. Understanding the effect of mean pore size on cell activity in collagen-glycosaminoglycan scaffolds. *Cell Adhes. Migr.* **4**, 377–381 (2010).

26. Nishida, T., Yasumoto, K., Otori, T. & Desaki, J. The network structure of corneal fibroblasts in the rat as revealed by scanning electron microscopy. *Investig. Ophthalmol. Vis. Sci.* **29**, 1887–1890 (1988).

27. Chen, V. J. & Ma, P. X. Nano-fibrous poly(L-lactic acid) scaffolds with interconnected spherical macropores. *Biomaterials* **25**, 2065–2073 (2004).

28. Boettiger, D. Mechanical control of integrin-mediated adhesion and signaling. *Curr. Opin. Cell Biol.* **24**, 592–599 (2012).

29. Wiesner, S., Legate, K. R. & Fässler, R. Integrin-actin interactions. *Cell. Mol. Life Sci.* **62**, 1081–1099 (2005).

30. Zaidel-Bar, R., Itzkovitz, S., Ma'ayan, A., Iyengar, R. & Geiger, B. Functional atlas of the integrin adhesome. *Nat. Cell* **9**, 858–867 (2007).

31. Orr, A. W., Helmke, B. P., Blackman, B. R. & Schwartz, M. A. Mechanisms of mechanotransduction. *Dev. Cell* **10**, 11–20 (2006).

32. Schwartz, M. A. Integrin signaling revisited. *Trends Cell Biol.* **11**, 466–470 (2001).

33. Hall, A. Rho GTPases and the Actin Cytoskeleton. *Science (80-.).* **279**, 509–514 (1998).

34. Hall, A. Rho family GTPases. *Biochem. Soc. Trans.* **40**, 1378–1382 (2012).

35. Defilippi, P. *et al.* Actin cytoskeleton organization in response to integrin-mediated adhesion. *Microsc. Res. Tech.* **47**, 67–78 (1999).

36. Tamiello, C., Bouten, C. V. C. & Baaijens, F. P. T. Competition between cap and basal actin fiber orientation in cells subjected to contact guidance and cyclic strain. *Sci. Rep.* **5**, 1–10 (2015).

37. Werner, M., Kurniawan, N. A. & Bouten, C. V. C. Cellular geometry sensing at different length scales and its implications for scaffold design. *Materials (Basel).* **13**, 1–18 (2020).

38. Dupont, S. *et al.* Role of YAP/TAZ in mechanotransduction. *Nature* **474**, 179–184 (2011).

39. Janmey, P. A. & McCulloch, C. A. From tissue mechanics to transcription factors. *Differentiation* **86**, 112–120 (2013).

40. Fischer, M., Rikeit, P., Knaus, P. & Coirault, C. YAP-mediated mechanotransduction in skeletal muscle. *Front. Physiol.* **7**, (2016).

41. Harrison, R. G. The cultivation of tissues in extraneous media as a method of morpho-genetic study. *Anat. Rec.* **6**, 181–193 (1912).

42. Weiss, P. Experiments on cell and axon orientation in vitro: The role of colloidal exudates in tissue organization. *J. Exp. Zool.* **100**, 353–386 (1945).

43. Curtis, A. S. G. & Clark, P. The effects of topographic and mechanical properties of materials on cell behavior. *Crit. Rev. Biocompat.* **5**, 343–362 (1990).

44. Curtis, A. S. G. Small is beautiful but smaller is the aim: Review of a life of research. *Eur. Cells Mater.* **8**, 27–36 (2004).

45. Kim, D.-H., Provenzano, P. P., Smith, C. L. & Levchenko, A. Matrix nanotopography as a regulator of cell function. *J. Cell Biol.* **197**, 351–360 (2012).

46. Li, Y. *et al.* Engineering cell alignment in vitro. *Biotechnol. Adv.* **32**, 347–365 (2014).

47. Nguyen, A. T., Sathe, S. R. & Yim, E. K. F. From nano to micro: topographical scale and its impact on cell adhesion, morphology and contact guidance. *J. Phys. Condens. Matter* **28**, 183001 (2016).

48. Tamiello, C., Buskermolen, A. B. C., Baaijens, F. P. T., Broers, J. L. V. & Bouten, C. V. C. Heading in the right direction: understanding cellular orientation responses to complex biophysical environments. *Cell. Mol. Bioeng.* **9**, 12–37 (2016).

49. Saez, A., Ghibaudo, M., Buguin, A., Silberzan, P. & Ladoux, B. Rigidity-driven growth and migration of epithelial cells on microstructured anisotropic substrates. *Proc. Natl. Acad. Sci. U. S. A.* **104**, 8281–8286 (2007).

50. Yang, P., Baker, R. M., Henderson, J. H. & Mather, P. T. In vitro wrinkle formation via shape memory dynamically aligns adherent cells. *Soft Matter* **9**, 4705–4714 (2013).

51. Greco, F. *et al.* Microwrinkled conducting polymer interface for anisotropic multicellular alignment. *ACS Appl. Mater. Interfaces* **5**, 573–584 (2013).

52. Bursac, N., Parker, K. K., Iravanian, S. & Tung, L. Cardiomyocyte Cultures With Controlled Macroscopic Anisotropy: A Model for Functional Electrophysiological Studies of Cardiac Muscle. *Circ. Res.* **91**, e45–e54 (2002).

53. Au, H. T. H., Cheng, I., Chowdhury, M. F. & Radisic, M. Interactive effects of surface topography and pulsatile electrical field stimulation on orientation and elongation of fibroblasts and cardiomyocytes. *Biomaterials* **28**, 4277–4293 (2007).

54. Ohara, P. T. & Buck, R. C. Contact guidance in vitro. *Exp. Cell Res.* **121**, 235–249 (1979).

55. Ray, A. *et al.* Anisotropic forces from spatially constrained focal adhesions mediate contact guidance directed cell migration. *Nat. Commun.* **8**, 14923 (2017).

56. Den Braber, E. T., De Ruijter, J. E., Ginsel, L. A., Von Recum, A. F. & Jansen, J. A. Quantitative analysis of fibroblast morphology on microgrooved surfaces with various groove and ridge dimensions. *Biomaterials* **17**, 2037–2044 (1996).

57. Dunn, G. A. & Heath, J. P. A new hypothesis of contact guidance in tissue cells. *Exp. Cell Res.* **101**, 1–14 (1976).

58. Teixeira, A. I. Epithelial contact guidance on well-defined micro- and nanostructured substrates. *J. Cell Sci.* **116**, 1881–1892 (2003).

59. Ramirez-San Juan, G. R., Oakes, P. W. & Gardel, M. L. Contact guidance requires spatial control of leading-edge protrusion. *Mol. Biol. Cell* **28**, 1043–1053 (2017).

60. Buskermolen, A. B. C. *et al.* Cellular Contact Guidance Emerges from Gap Avoidance. *Cell Reports Phys. Sci.* **1**, 100055 (2020).

61. Curtis, A. & Wilkinson, C. Topographical control of cells. *Biomaterials* **18**, 1573–1583 (1997).

62. Clark, P., Connolly, P., Curtis, A. S. G., Dow, J. A. T. & Wilkinson, C. D. W. Cell guidance by ultrafine topography in vitro. *J. Cell Sci.* **99 (Pt 1)**, 73–7 (1991).

63. Sutherland, J., Denyer, M. & Britland, S. Contact guidance in human dermal fibroblasts is modulated by population pressure. *J. Anat.* **206**, 581–587 (2005).

64. Kim, D.-H. *et al.* Nanoscale cues regulate the structure and function of macroscopic cardiac tissue constructs. *Proc. Natl. Acad. Sci.* **107**, 565–570 (2010).

65. Mathur, A., Moore, S. W., Sheetz, M. P. & Hone, J. The role of feature curvature in contact guidance. *Acta Biomater.* **8**, 2595–2601 (2012).

66. Grigola, M. S., Dyck, C. L., Babacan, D. S., Joaquin, D. N. & Hsia, K. J. Myoblast alignment on 2D wavy patterns: Dependence on feature characteristics and cell-cell interaction. *Biotechnol. Bioeng.* **111**, 1617–1626 (2014).

67. Kubow, K. E., Shuklis, V. D., Sales, D. J. & Horwitz, A. R. Contact guidance persists under myosin inhibition due to the local alignment of adhesions and individual protrusions. *Sci. Rep.* **7**, 1–15 (2017).

68. Provenzano, P. P., Inman, D. R., Eliceiri, K. W., Trier, S. M. & Keely, P. J. Contact guidance mediated three-dimensional cell migration is regulated by Rho/ROCK-dependent matrix reorganization. *Biophys. J.* **95**, 5374–5384 (2008).

69. Tabdanov, E. D. *et al.* Bimodal sensing of guidance cues in mechanically distinct microenvironments. *Nat. Commun.* **9**, 4891 (2018).

70. Charles-Orszag, A. *et al.* Adhesion to nanofibers drives cell membrane remodeling through one-dimensional wetting. *Nat. Commun.* **9**, (2018).

71. Driscoll, M. K., Sun, X., Guven, C., Fourkas, J. T. & Losert, W. Cellular contact guidance through dynamic sensing of nanotopography. *ACS Nano* **8**, 3546–3555 (2014).

72. Lawrence, B. D., Pan, Z. & Rosenblatt, M. I. Silk Film Topography Directs Collective Epithelial Cell Migration. *PLoS One* **7**, e50190 (2012).

73. Londono, C., Loureiro, M. J., Slater, B., Lücker, P. B. & Soleas, J. Nonautonomous contact guidance signaling during collective cell migration. *Proc. Natl. Acad. Sci.* **111**, 1807–1812 (2014).

74. Angelini, T. E., Hannezo, E., Trepat, X., Fredberg, J. J. & Weitz, D. A. Cell Migration Driven by Cooperative Substrate Deformation Patterns. *Phys. Rev. Lett.* **104**, 168104 (2010).

75. Scarpa, E. & Mayor, R. Collective cell migration in development. *J. Cell Biol.* **212**, 143–155 (2016).

76. Ladoux, B. & Mège, R. M. Mechanobiology of collective cell behaviours. *Nat. Rev. Mol. Cell Biol.* **18**, 743–757 (2017).

77. Trepat, X. & Sahai, E. Mesoscale physical principles of collective cell organization. *Nat. Phys.* **14**, 671–682 (2018).

78. Chen, T., Saw, T. B., Mège, R.-M. & Ladoux, B. Mechanical forces in cell monolayers. *J. Cell Sci.* **131**, jcs218156 (2018).

79. Hakim, V. & Silberzan, P. Collective cell migration : A Physics perspective. *Reports Prog. Phys.* (2017) doi:10.1042/BJ20101136>.

80. Alert, R. & Trepat, X. Physical Models of Collective Cell Migration. *Annu. Rev. Condens. Matter Phys.* **11**, 77–101 (2020).

81. Abercrombie, M. & Heaysman, J. E. M. Observations on the social behaviour of cells in tissue culture. I. Speed of movement of chick heart fibroblasts in relation to their mutual contacts. *Exp. Cell Res.* **5**, 111–131 (1953).

82. Mayor, R. & Carmona-Fontaine, C. Keeping in touch with contact inhibition of locomotion. *Trends Cell Biol.* **20**, 319–328 (2010).

83. Carmona-Fontaine, C. *et al.* Contact inhibition of locomotion in vivo controls neural crest directional migration. *Nature* **456**, 957–961 (2008).

84. Theveneau, E. *et al.* Chase-and-run between adjacent cell populations promotes directional collective migration. *Nat. Cell Biol.* **15**, 763–772 (2013).

85. Poujade, M. *et al.* Collective migration of an epithelial monolayer. (2007) doi:10.1073/pnas.0705062104.

86. Trepat, X. *et al.* Physical forces during collective cell migration. *Nat. Phys.* **5**, 426–430 (2009).

87. Tambe, D. T. *et al.* Collective cell guidance by cooperative intercellular forces. *Nat. Mater.* **10**, 469–475 (2011).

88. Petitjean, L. *et al.* Velocity Fields in a Collectively Migrating Epithelium. *Biophys. J.* **98**, 1790–1800 (2010).

89. Sadati, M., Taheri Qazvini, N., Krishnan, R., Park, C. Y. & Fredberg, J. J. Collective migration and cell jamming. *Differentiation* **86**, 121–125 (2013).

90. Fink, J. *et al.* External forces control mitotic spindle positioning. *Nat. Cell Biol.* **13**, 771–778 (2011).

91. Bosveld, F. *et al.* Epithelial tricellular junctions act as interphase cell shape sensors to orient mitosis. *Nature* **530**, 495–498 (2016).

92. Angelini, T. E. *et al.* Glass-like dynamics of collective cell migration. *Proc. Natl. Acad. Sci.* **108**, 4714–4719 (2011).

93. Deforet, M., Hakim, V., Yevick, H. G., Duclos, G. & Silberzan, P. Emergence of collective modes and tri-dimensional structures from epithelial confinement. *Nat. Commun.* **5**, 1–9 (2014).

94. Rossen, N. S., Tarp, J. M., Mathiesen, J., Jensen, M. H. & Oddershede, L. B. Long-range ordered vorticity patterns in living tissue induced by cell division. *Nat. Commun.* **5**, 1–7 (2014).

95. Ranft, J. *et al.* Fluidization of tissues by cell division and apoptosis. *Proc. Natl. Acad. Sci. U. S. A.* **107**, 20863–20868 (2010).

96. Doxzen, K. *et al.* Guidance of collective cell migration by substrate geometry. *Integr. Biol.* **5**, 1026–1035 (2013).

97. Vedula, S. R. K. *et al.* Emerging modes of collective cell migration induced by geometrical constraints. *Proc. Natl. Acad. Sci. U. S. A.* **109**, 12974–12979 (2012).

98. Leong, M. C., Vedula, S. R. K., Lim, C. T. & Ladoux, B. Geometrical constraints and physical crowding direct collective migration of fibroblasts. *Commun. Integr. Biol.* **6**, 2–5 (2013).

99. Alexander, S., Koehl, G. E., Hirschberg, M., Geissler, E. K. & Friedl, P. Dynamic imaging of cancer growth and invasion: A modified skin-fold chamber model. *Histochem. Cell Biol.* **130**, 1147–1154 (2008).

100. Weigelin, B., Bakker, G.-J. & Friedl, P. Intravital third harmonic generation microscopy of collective melanoma cell invasion. *IntraVital* **1**, 32–43 (2012).

101. Szabó, A. *et al.* In vivo confinement promotes collective migration of neural crest cells. *J. Cell Biol.* **213**, 543–555 (2016).

102. Cha, S. H., Lee, H. J. & Koh, W. G. Study of myoblast differentiation using multi-dimensional scaffolds consisting of nano and micropatterns. *Biomater. Res.* **21**, 1–9 (2017).

103. Gilchrist, C. L., Ruch, D. S., Little, D. & Guilak, F. Micro-scale and meso-scale architectural cues cooperate and compete to direct aligned tissue formation. *Biomaterials* **35**, 10015–10024 (2014).

104. Kim, J. *et al.* Multiscale patterned transplantable stem cell patches for bone tissue regeneration. *Biomaterials* **35**, 9058–9067 (2014).

105. López-Bosque, M. J. *et al.* Fabrication of hierarchical micro-nanotopographies for cell attachment studies. *Nanotechnology* **24**, (2013).

106. Moffa, M., Sciancalepore, A. G., Passione, L. G. & Pisignano, D. Combined nano- and micro-scale topographic cues for engineered vascular constructs by electrospinning and imprinted micro-patterns. *Small* **10**, 2439–2450 (2014).

107. Nam, K. H. *et al.* Multiscale cues drive collective cell migration. *Sci. Rep.* **6**, 1–13 (2016).

108. Werner, M., Kurniawan, N. A., Korus, G., Bouten, C. V. C. & Petersen, A. Mesoscale substrate curvature overrules nanoscale contact guidance to direct bone marrow stromal cell migration. *J. R. Soc. Interface* **15**, (2018).

109. MacIntosh, B., Gardinier, P. & McComas, A. *Skeletal Muscle: Form and Function*. (Human Kinetics, 2006).

110. Betts, G. *et al.* Anatomy and Physiology. *OpenStax* https://openstax.org/books/anatomy-and-physiology/pages/1-introduction (2013).

111. Bryson-Richardson, R. J. & Currie, P. D. The genetics of vertebrate myogenesis. *Nat. Rev. Genet.* **9**, 632–646 (2008).

112. Le Grand, F. & Rudnicki, M. A. Skeletal muscle satellite cells and adult myogenesis. *Curr. Opin. Cell Biol.* **19**, 628–633 (2007).

113. Bentzinger, C. F., Wang, Y. X. & Rudnicki, M. A. Building Muscle: Molecular Regulation of Myogenesis. *Cold Spring Harb. Perspect. Biol.* **4**, a008342–a008342 (2012).

114. Cadot, B., Gache, V. & Gomes, E. R. Moving and positioning the nucleus in skeletal muscle-one step at a time. *Nucleus* **6**, 373–381 (2015).

115. Abmayr, S. M. & Pavlath, G. K. Myoblast fusion: lessons from flies and mice. *Development* **139**, 641–656 (2012).

116. Bruyère, C. *et al.* Actomyosin contractility scales with myoblast elongation and enhances differentiation through YAP nuclear export. 1–14 (2019) doi:10.1038/s41598-019-52129-1.

117. Charrasse, S., Meriane, M., Comunale, F., Blangy, A. & Gauthier-Rouvière, C. N-cadherin-dependent cell-cell contact regulates Rho GTPases and β-catenin localization in mouse C2C12 myoblasts. *J. Cell Biol.* **158**, 953–965 (2002).

118. Kühl, U., Öcalan, M., Timpl, R. & von der Mark, K. Role of laminin and fibronectin in selecting myogenic versus fibrogenic cells from skeletal muscle cells in vitro. *Dev. Biol.* **117**, 628–635 (1986).

119. Menko, A. S. & Boettiger, D. Occupation of the extracellular matrix receptor, integrin, is a control point for myogenic differentiation. *Cell* **51**, 51–57 (1987).

120. Engler, A. J. *et al.* Myotubes differentiate optimally on substrates with tissue-like stiffness: Pathological implications for soft or stiff microenvironments. *J. Cell Biol.* **166**, 877–887 (2004).

121. Roberts, E. G. *et al.* Engineering Myocardial Tissue Patches with Hierarchical Structure. *Ann. Biomed. Eng.* **43**, 762–773 (2015).

122. Cezar, C. A. & Mooney, D. J. Biomaterial-based delivery for skeletal muscle repair. *Adv. Drug Deliv. Rev.* **84**, 188–197 (2015).

123. Ingber, D. E. Mechanical control of tissue growth: Function follows form. *Proc. Natl. Acad. Sci.* **102**, 11571–11572 (2005).

124. Kilian, K. A., Bugarija, B., Lahn, B. T. & Mrksich, M. Geometric cues for directing the differentiation of mesenchymal stem cells. *Proc. Natl. Acad. Sci.* **107**, 4872–4877 (2010).

125. Nelson, C. M. *et al.* Emergent patterns of growth controlled by multicellular form and mechanics. *Proc. Natl. Acad. Sci.* **102**, 11594–11599 (2005).

126. Smith, A. S. T., Davis, J., Lee, G., Mack, D. L. & Kim, D. H. Muscular dystrophy in a dish: engineered human skeletal muscle mimetics for disease modeling and drug discovery. *Drug Discov. Today* **21**, 1387–1398 (2016).

127. Liu, J. *et al.* Current Methods for Skeletal Muscle Tissue Repair and Regeneration. *Biomed Res. Int.* **2018**, (2018).

128. Hirt, M. N., Hansen, A. & Eschenhagen, T. Cardiac tissue engineering : State of the art. *Circ. Res.* **114**, 354–367 (2014).

129. Patel, N. G. & Zhang, G. Responsive systems for cell sheet detachment. *Organogenesis* **9**, 93–100 (2013).

130. Griffith, L. G. Tissue Engineering--Current Challenges and Expanding Opportunities. *Science (80-.).* **295**, 1009–1014 (2002).

131. Zatti, S. *et al.* Micropatterning topology on soft substrates affects myoblast proliferation and differentiation. *Langmuir* **28**, 2718–2726 (2012).

132. Sun, Y., Duffy, R., Lee, A. & Feinberg, A. W. Optimizing the structure and contractility of engineered skeletal muscle thin films. *Acta Biomater.* **9**, 7885–7894 (2013).

133. Denes, L. T. *et al.* Culturing C2C12 myotubes on micromolded gelatin hydrogels accelerates myotube maturation. *Skelet. Muscle* **9**, 1–10 (2019).

134. Jana, S., Leung, M., Chang, J. & Zhang, M. Effect of nano- and micro-scale topological features on alignment of muscle cells and commitment of myogenic differentiation. *Biofabrication* **6**, (2014).

135. Yeo, M. & Kim, G. H. Nano/microscale topographically designed alginate/PCL scaffolds for inducing myoblast alignment and myogenic differentiation. *Carbohydr. Polym.* **223**, 115041 (2019).

136. Bajaj, P. *et al.* Patterning the differentiation of C2C12 skeletal myoblasts. *Integr. Biol.* **3**, 897 (2011).

137. Ahmed, W. W. *et al.* Myoblast morphology and organization on biochemically micro-patterned hydrogel coatings under cyclic mechanical strain. *Biomaterials* **31**, 250–258 (2010).

138. Fujita, H., Shimizu, K. & Nagamori, E. Novel method for fabrication of skeletal muscle construct from the C2C12 myoblast cell line using serum-free medium AIM-V. *Biotechnol. Bioeng.* **103**, 1034–1041 (2009).

139. Neal, D., Sakar, M. S., Ong, L.-L. S. & Harry Asada, H. Formation of elongated fascicle-inspired 3D tissues consisting of high-density, aligned cells using sacrificial outer molding. *Lab Chip* **14**, 1907 (2014).

140. Shimizu, K., Fujita, H. & Nagamori, E. Alignment of Skeletal Muscle Myoblasts and Myotubes Using Linear Micropatterned Surfaces Ground With Abrasives. **103**, 631–638 (2009).

141. Yamamoto, D. L. *et al.* Myotube formation on micro-patterned glass: Intracellular organization and protein distribution in C2C12 skeletal muscle cells. *J. Histochem. Cytochem.* **56**, 881–892 (2008).

142. Nagamine, K., Kawashima, T., Ishibashi, T. & Kaji, H. Micropatterning Contractile C 2 C 12 Myotubes Embedded in a Fibrin Gel. **105**, 1161–1167 (2010).

143. Fréedericksz, V. & Repiewa, A. Theoretisches und Experimentelles zur Frage nach der Natur der anisotropen Flüssigkeiten. *Zeitschrift für Phys.* **42**, 532–546 (1927).

144. Laurent, J. *et al.* Convergence of microengineering and cellular self-organization towards functional tissue manufacturing. *Nat. Biomed. Eng.* **1**, 939–956 (2017).

145. Bain, N. & Bartolo, D. Dynamic response and hydrodynamics of polarized crowds. *Science (80-.).* **363**, 46–49 (2019).

146. Narayan, V., Ramaswamy, S. & Menon, N. Long-Lived Giant Number Fluctuations. *Science (80-.).* **317**, 105–109 (2007).

147. Dombrowski, C., Cisneros, L., Chatkaew, S., Goldstein, R. E. & Kessler, J. O. Self-Concentration and Large-Scale Coherence in Bacterial Dynamics. *Phys. Rev. Lett.* 2–5 (2004) doi:10.1103/PhysRevLett.93.098103.

148. Surrey, T., Nédélec, F., Leibler, S. & Karsenti, E. Physical Properties Determining Self-Organization of Motors and Microtubules. *Science (80-.).* **292**, 1167–1171 (2001).

149. Grill, S. W. Growing up is stressful: Biophysical laws of morphogenesis. *Curr. Opin. Genet. Dev.* **21**, 647–652 (2011).

150. Camley, B. A. & Rappel, W. J. Physical models of collective cell motility: From cell to tissue. *J. Phys. D. Appl. Phys.* **50**, (2017).

151. Vicsek, T., Czirok, A., Ben-Jacob, A., Cohen, I. & Shochet, O. Novel Type of Phase Transition in a System ofSelf-Driven Particles. *Phys. Rev. Lett.* **75**, 4–7 (1995).

152. Toner, J. & Tu, Y. Flocks, herds, and schools: A quantitative theory of flocking. *Phys. Rev. E - Stat. Physics, Plasmas, Fluids, Relat. Interdiscip. Top.* **58**, 4828–4858 (1998).

153. Glazier, J. A. & Graner, F. Simulation of the differential adhesion driven rearrangement of biological cells. *Phys. Rev. E* **47**, 2128–2154 (1993).

154. JULICHER, F., KRUSE, K., PROST, J. & JOANNY, J. Active behavior of the Cytoskeleton. *Phys. Rep.* **449**, 3–28 (2007).

155. Ramaswamy, S. The Mechanics and Statistics of Active Matter. *Annu. Rev. Condens. Matter Phys.* **1**, 323–345 (2010).

156. Marchetti, M. C. *et al.* Hydrodynamics of soft active matter. *Rev. Mod. Phys.* **85**, 1143–1189 (2013).

157. Prost, J., Jülicher, F. & Joanny, J.-F. Active gel physics. *Nat. Phys.* **11**, 111–117 (2015).

158. Donald, A. M. & Windle, A. H. *Liquid crystalline polymers*. *Liquid crystalline polymers* vol. 1 (1992).

159. Wikipedia Contributors. Elliptical integral. *Wikipedia, The Free Encyclopedia* https://en.wikipedia.org/wiki/Elliptic_integral (2020).

160. Brochard, F. Mouvements de parois dans une lame mince nématique. *J. Phys.* **33**, 607–611 (1972).

161. Thampi, S. P., Golestanian, R. & Yeomans, J. M. Instabilities and topological defects in active nematics. *EPL (Europhysics Lett.* **105**, 18001 (2014).

162. Thampi, S. P., Golestanian, R. & Yeomans, J. M. Velocity correlations in an active nematic. *Phys. Rev. Lett.* **111**, 2–6 (2013).

163. Vromans, A. J. & Giomi, L. Orientational properties of nematic disclinations. *Soft Matter* **12**, 6490–6495 (2016).

164. Giomi, L., Bowick, M. J., Mishra, P., Sknepnek, R. & Cristina Marchetti, M. Defect dynamics in active nematics. *Philos. Trans. R. Soc. A Math. Phys. Eng. Sci.* **372**, 20130365 (2014).

165. Blanch-Mercader, C. *et al.* Turbulent Dynamics of Epithelial Cell Cultures. *Phys. Rev. Lett.* **120**, 208101 (2018).

166. Doostmohammadi, A., Adamer, M. F., Thampi, S. P. & Yeomans, J. M. Stabilization of active matter by flow-vortex lattices and defect ordering. *Nat. Commun.* 7, 10557 (2016).

167. Guillamat, P., Ignés-mullol, J. & Sagués, F. Control of active liquid crystals with a magnetic field. *Proc. Natl. Acad. Sci.* **113**, 1–5 (2016).

168. Kawaguchi, K., Kageyama, R. & Sano, M. Topological defects control collective dynamics in neural progenitor cell cultures. *Nature* **545**, 327–331 (2017).

169. Saw, T. B. *et al.* Topological defects in epithelia govern cell death and extrusion. *Nature* **544**, 212–216 (2017).

170. Duclos, G., Erlenkämper, C., Joanny, J.-F. & Silberzan, P. Topological defects in confined populations of spindle-shaped cells. *Nat. Phys.* **13**, 58–62 (2016).

171. Guillamat, P., Blanch-Mercader, C., Kruse, K. & Roux, A. Integer topological defects organize stresses driving tissue morphogenesis. (2020) doi:https://doi.org/10.1101/2020.06.02.129262.

172. Norton, M. M. *et al.* Insensitivity of active nematic liquid crystal dynamics to topological constraints. *Phys. Rev. E* **97**, 012702 (2018).

173. Duclos, G., Garcia, S., Yevick, H. G. & Silberzan, P. Perfect nematic order in confined monolayers of spindle-shaped cells. *Soft Matter* **10**, 2346–2353 (2014).

174. Duclos, G. *et al.* Spontaneous shear flow in confined cellular nematics. *Nat. Phys.* **14**, 728–732 (2018).

175. Voituriez, R., Joanny, J. F. & Prost, J. Spontaneous flow transition in active polar gels. *Europhys. Lett.* **70**, 404–410 (2005).

176. Wahl, J. & Fischer, F. Elastic and Viscosity Constants of Nematic Liquid Crystals from a New Optical Method. *Mol. Cryst. Liq. Cryst.* **22**, 359–373 (1973).

177. Chandragiri, S., Doostmohammadi, A., Yeomans, J. M. & Thampi, S. P. Active transport in a channel: Stabilisation by flow or thermodynamics. *Soft Matter* **15**, 1597–1604 (2019).

178. Thijssen, K., Metselaar, L., Yeomans, J. M. & Doostmohammadi, A. Active nematics with anisotropic friction: The decisive role of the flow aligning parameter. *Soft Matter* **16**, 2065–2074 (2020).

179. Yaffe, D. & Saxel, O. Serial passaging and differentiation of myogenic cells isolated from dystrophic mouse muscle. *Nature* **270**, 725–727 (1977).

180. Jainchill, J. L., Aaronson, S. A. & Todaro, G. J. Murine Sarcoma and Leukemia Viruses: Assay Using Clonal Lines of Contact-Inhibited Mouse Cells. *J. Virol.* **4**, 549–553 (1969).

181. Képiró, M. *et al.* Para-nitroblebbistatin, the non-cytotoxic and photostable myosin II inhibitor. *Angew. Chemie - Int. Ed.* **53**, 8211–8215 (2014).

182. Tourovskaia, A. *et al.* Micropatterns of Chemisorbed Cell Adhesion-Repellent Films Using Oxygen Plasma Etching and Elastomeric Masks. *Cell* 4754–4764 (2003).

183. Tourovskaia, A., Figueroa-Masot, X. & Folch, A. Long-term microfluidic cultures of myotube microarrays for high-throughput focal stimulation. *Nat. Protoc.* **1**, 1092–1104 (2006).

184. Püspöki, Z., Storath, M., Sage, D. & Unser, M. Transforms and Operators for Directional Bioimage Analysis: A Survey. in *PLoS ONE* (ed. Neves, N. M.) vol. 7 69–93 (2016).

185. Sage, D. OrientationJ. http://bigwww.epfl.ch/demo/orientation/.

186. Berens, P. CircStat: A MATLAB Toolbox for Circular Statistics. *J. Stat. Softw.* **31**, 293–295 (2009).

187. Deforet, M. *et al.* Automated velocity mapping of migrating cell populations (AVeMap). *Nat. Methods* **9**, 1081–1083 (2012).

188. Sveen, J. K. An introduction to MatPIV v. 1.6.1. *World Wide Web Internet Web Inf. Syst.* 27 pp (2004).

189. DeCamp, S. J., Redner, G. S., Baskaran, A., Hagan, M. F. & Dogic, Z. Orientational order of motile defects in active nematics. *Nat. Mater.* **14**, 1110–1115 (2015).

190. Sahoo, P. *Surface topography*. *Tribology for Engineers* (Woodhead Publishing Limited, 2011). doi:10.1533/9780857091444.1.

191. Brézin, L. Tissues as active materials: spontaneous flows and topological defects in active cellular nematics. (Sorbonne Univesité, 2020).

192. Aigouy, B. *et al.* Cell Flow Reorients the Axis of Planar Polarity in the Wing Epithelium of Drosophila. *Cell* **142**, 773–786 (2010).

193. Hoffmann, L. A., Schakenraad, K., Merks, R. M. H. & Giomi, L. Chiral stresses in nematic cell monolayers. *Soft Matter* **16**, 764–774 (2020).

194. Kawaguchi, K., Kageyama, R. & Sano, M. Topological defects control collective dynamics in neural progenitor cell cultures - Supplementary informations. *Nature* **545**, 327–331 (2017).

195. Guochen, Y., Jianru, S. & Ying, L. Surface anchoring energy and the first order Fréedericksz transition of a NLC cell. *Liq. Cryst.* **27**, 875–882 (2000).

196. Sarkar, T. *et al.* Crisscross multilayering of cell sheets. *unpublished* (2021).

197. Elsdale, T. & Bard, J. Cellular Interactions in Mass Cultures of Human Diploid Fibroblasts. *Nature* **236**, 152–155 (1972).

198. Charest, J. L., García, A. J. & King, W. P. Myoblast alignment and differentiation on cell culture substrates with microscale topography and model chemistries. *Biomaterials* **28**, 2202–2210 (2007).

199. Ricotti, L. *et al.* Proliferation and skeletal myotube formation capability of C2C12 and H9c2 cells on isotropic and anisotropic electrospun nanofibrous PHB scaffolds. *Biomed. Mater.* 7, 035010 (2012).

200. Kodaka, Y., Rabu, G. & Asakura, A. Skeletal Muscle Cell Induction from Pluripotent Stem Cells. *Stem Cells Int.* **2017**, (2017).

201. Chen, T. H. *et al.* YAP promotes myogenic differentiation via the MEK5-ERK5 pathway. *FASEB J.* **31**, 2963–2972 (2017).

202. Berg, S. *et al.* Ilastik: Interactive Machine Learning for (Bio)Image Analysis. *Nat. Methods* **16**, 1226–1232 (2019).

203. Dickinson, R. B., Guido, S. & Tranquillo, R. T. Biased cell migration of fibroblasts exhibiting contact guidance in oriented collagen gels. *Ann. Biomed. Eng.* **22**, 342–356 (1994).

204. Bhanu, V. A. & Kishore, K. Role of Oxygen in Polymerization Reactions. *Chem. Rev.* **91**, 99–117 (1991).

205. Mardia, K. & Jupp, P. *Directional Statistics*. (1972).

206. Hooke, R. *Micrographia*. (1665).

207. muscle. *Online Etymology Dictionary* www.etymonline.com.

208. Khüne, W. *Lehrbuch der Physiologischen Chemie*. (1868).

209. Pollard, T. & Korn, E. Acanthamoeba Myosin: Isolation from acanthamoeba castellanii of an enzyme similar to muscle myosin. *J. Biol. Chem.* **248**, 4682–4690 (1973).

210. Shimomura, O., Johnson, F. H. & Saiga, Y. Extraction, Purification and Properties of Aequorin, a Bioluminescent Protein from the Luminous Hydromedusan,Aequorea. *J. Cell. Comp. Physiol.* **59**, 223–239 (1962).

211. Wikipedia Contributors. Dystrophin. *Wikipedia, The Free Encyclopedia* https://en.wikipedia.org/wiki/Dystrophin (2020).

212. Crosser, N. *et al. 2019 State of the Industry Report - Cultivated Meat*. (2020).

213. Mr. Olympia official webpage. https://mrolympia.com/.

214. World's Strongest Men official webpage. http://www.theworldsstrongestman.com/.

215. World Powerlifting men's world records. https://worldpowerlifting.com/records/mens-world-records/.

216. Olympic weightlifting official webpage. https://www.olympic.org/weightlifting.

217. Kok, V. J., Lim, M. K. & Chan, C. S. Crowd behavior analysis: A review where physics meets biology. *Neurocomputing* **177**, 342–362 (2016).

RÉSUMÉ

In vivo, les groupes de cellules ont besoin de se déplacer de façon coordonnée pour pouvoir développer des fonctions physiologiques. Certaines cellules sont entourées d'une matrice extracellulaire, un réseau de protéines allant du nanomètre aux centaines de micromètres. Dans un tel environnement, les cellules peuvent se déplacer ensemble, guidées par l'orientation du réseau. Ce comportement a été étudié *in vitro* dans des systèmes simplifiés utilisant des guides de différentes tailles. Ces études montrent que la taille du guide contrôle le mouvement collectif des cellules. Cependant, ce mouvement collectif et les mécanismes associés sont encore flous dans les systèmes où coexistent des guides de plusieurs tailles.

Dans cette thèse, nous avons cultivés des cellules sur des substrats présentant deux échelles de tailles: des microabrasions subcellulaires orientées selon un angle par rapport à des bandes mésoscopiques plus larges. Nous montrons que la largeur de la bande contrôle une transition d'orientation des cellules entre les deux modes de guidage, et ce, pour une largeur critique. Plus précisément, l'angle au centre dans les bandes larges est stabilisé par un effet de "contact guidance" indépendant de l'activité cellulaire, alors même que la migration collective des cellules montre un écoulement de cisaillement aux bords de la bande. Ces observations ont été reliées à un modèle théorique que nous avons développé, basé sur la matière active. De plus, en changeant l'orientation des microabrasions, nous avons mesuré le "flow-alignment parameter" pour la première fois dans de tels systèmes.

Ces mécanismes généraux peuvent s'appliquer à d'autres contextes *in vivo*, en particulier pendant la myogénèse. En cultivant des myoblastes de souris, les cellules C2C12, sur nos substrats multi-échelles, nous avons observé leur auto-organisation en une "corde cellulaire" tridimensionnelle. Grâce à cette structure particulière, la différentiation a été favorisée par rapport aux méthodes classiques de la littérature. Ceci montre un impact réel de la géométrie du substrat sur le processus de différentiation. Nous proposons donc une méthode simple de myogénèse basée seulement sur l'auto-organisation cellulaire. Cette thèse peut avoir des applications dans l'ingénierie tissulaire.

MOTS CLÉS

nématiques actifs, comportements collectifs cellulaires, contact guidance, multiéchelle, différentiation

ABSTRACT

Group of cells *in vivo* need to move together in order to achieve physiological function. In particular, some cells are surrounded by extracellular matrix, a meshwork of proteins displaying sizes ranging from nanometers to hundreds of micrometers. In such environments, cells can move altogether directed by mesh orientation. This behaviour has been studied *in vitro* for simplified systems using guiding cues of different sizes. These studies show that the size of the cue controlled the cell collective motion. However, cell collective motion and the mechanisms involved in systems displaying a mix of different lengthscale cues are still unclear.

In this thesis, we plated cells on substrates that have been textured at two lengthscales: subcellular microridges making an angle with a wider mesoscopic stripe. We show that the stripe's width controls a transition at a critical width for the orientation angle of the cells between the two limiting cases. More precisely, middle angle in wider stripes is stabilized by a simple contact guidance effect independent of cell activity while collective cell migration display shear flows close to the edge of stripes. These observations fit a theoretical model we developed based on the active matter framework. More interestingly, changing the microscale field orientation allowed us to measure the so-called "flow-alignment parameter" for the first time in such systems.

Understanding these general mechanisms can be relevant in other several contexts *in vivo*, in particular during myogenesis. By seeding C2C12 mouse myoblasts cells on our previous multiscale system, we observed the self-organization of a 3D "cell cord" in the center of stripes. Due to their particular structures, differentiation was favored compared to classical patterns of the literature showing a real impact of geometrical conditions on cell differentiation processes. We then managed to provide a simple method of muscle differentiation based on cellular self-organization only. This thesis could have outcomes in the tissue engineering field.

KEYWORDS

active nematics, collective cell behaviour, contact guidance, multiscale, differentiation